Silicon nanowire solar cells : from single and double to triple and quadruple radial junctions for unassisted water splitting

Chaoqi Wang

To cite this version:

Chaoqi Wang. Silicon nanowire solar cells : from single and double to triple and quadruple radial junctions for unassisted water splitting. Physics [physics]. Institut Polytechnique de Paris, 2022. English. NNT : 2022IPPAX085 . tel-04105555

HAL Id: tel-04105555
https://theses.hal.science/tel-04105555
Submitted on 24 May 2023

NNT : 2022IPPAX085

Thèse de doctorat

Silicon nanowire solar cells: from single and double to triple and quadruple radial junctions for unassisted water splitting

Thèse de doctorat de l'Institut Polytechnique de Paris
préparée à École Polytechnique

École doctorale n°626 Ecole Doctorale de l'Institut Polytechnique de Paris (ED IP Paris)
Spécialité de doctorat: Physique

Thèse présentée et soutenue à Palaiseau, le 19 Septembre 2022, par

Chaoqi Wang

Composition du Jury :

Pedro Alpuim Professeur, University of Minho (INL)	Président
Jean-Paul Kleider Directeur de recherche, Université Paris-Saclay (GEEPS)	Rapporteur
Antonin Fejfar Professeur, Czech Academy of Sciences	Rapporteur
Linwei Yu Professeur, Nanjing University	Examinateur
Erik Johnson Directeur de recherche, École polytechnique (LPICM)	Directeur de thèse
Pere Roca i Cabarrocas Directeur de recherche, École polytechnique (LPICM)	Invité
Martin Foldyna Chargé de recherche, École polytechnique (LPICM)	Invité

Acknowledgements

I am glad to finish my PhD at LPICM and it is my great experience to study at here when I was in France. I want to thank all people who gave me help during these precious time.

Firstly, I want to thank my supervisor Erik. It is my great pleasure to meet Erik during my PhD. I appreciate his patience on showing me how to do fitting, his clear logical on designing experiments for the next step, his kind suggestions on electric circuit... I also thank Erik for his good organization on manuscripts and presentations. In addition, his optimistic attitude and humorous character have a profound influence on me.

Secondly, I would thank my supervisor Pere for his diligent and positive toward work which always ignite me. He teaches classes, participates meetings and conferences, does experiment by himself and leads internship students, PhDs and postdocs. His specialized knowledge in this field helps me improve the thesis a lot. I enjoy every discussion with him and always obtain very helpful suggestions. Moreover, his hospitality is proverbial. He always invite lab members to go to his garden for barbecue. He grows vegetables by himself in the garden. I also like his enthusiasm toward life.

Thirdly, I thank my supervisor Martin for giving me this such challenge topic. I would like to thank Yvan for giving me support when I met difficulty. Thank Dmitri, Pavel, Jacqueline, Cyril, Jerome, Jean-Charles, BEER... for training and maintenance on thermal evaporator, sputtering machine, Plasfil and SEM... Thank Denis for the ultrasonic machine.

I specially thank Weixi and Zhengyu for their help when I was in hard time. Hope their lovely babies healthy growth. Thank Junkang for answering me many professional questions. Thank Marc, Fabrice and Debashrita for their help on experiment about electrochemistry. Thank Eric for his help on equipment. Thank Pingping for helping me on some trivial matters during my defense. Thank Shenming for giving me some masks. Thank Xinlei and Guili for their help on cleaning. Thank Shiwei and Qiqiao for their help in the chemical lab. Thank Amir for his suggestions on defense and assistance on AFM. Thank Antonio for the experiment about Arcam. Talking with Ghewa and Loan, I felt very light and airy. It is also nice to meet many other lab members: Jean-Luc, Aleix, Michel, Hindia, Toan, Haeyeon, Martine, Monalisa, Deyan, Lakshman, Lise, Aram...

In addition, thank you to my friends in France: Sylvie, Tianjiao, Hongwei, Ouyang, Jiuxiang, Lu, Yichen... This list cannot be the completed... I enjoy every moments traveling with you. I feel grateful that I can meet you. I also thank my friends in other countries: Yang, Mei, Pengfei, Min, Yuzhi, Fanlu, Hao, Jingxuan... It is also very lovely to meet you.

I would also like to thank Pedro, Jean-Paul, Antonin and Linwei for being my jury members. I appreciate that you give me a lot of useful suggestions and comments.

Finally, I acknowledge my parents for the persistent care. More than 8000 km straight distance between Paris and Harbin, it has been three years since I last went home, but I still can feel their concern.

Abstract

Photoelectrochemical (PEC) cells are promising devices to convert solar energy to chemical energy (by splitting water and obtaining hydrogen) so that it can be stored and transported. However, according to thermodynamic calculations, a 1.23 V potential is required for water splitting, which exceeds the open-circuit voltage (V_{OC}) of most single junction solar cells. In practice, the required potential for maximum splitting efficiency can be even higher for non-optimal catalysts and electrolytes, and would require multijunction solar cells to drive the reaction. Single and double radial junction silicon nanowire (SiNW) solar cells have been previously studied as their improved light trapping ability allows for thinner hydrogenated amorphous silicon (a-Si:H) absorber layers, and thus decreased light-induced degradation. In this thesis, radial junction SiNW solar cells are fabricated consisting of single and double junctions (1RJ, 2RJ), and for the first time, triple and quadruple junction (3RJ, 4RJ). The 3RJ solar cells – which display a V_{OC} of more than 2 V - are fabricated using a one-pump-down plasma-enhanced chemical vapor deposition process. We investigated the 3RJ SiNW diode performance and the effect of the NW density on the triple junction solar cell performance, showing that a higher V_{OC} correlates with a lower NW density. An efficiency optimum in NW density is found, as an S shape in the J-V curve occurs at the lowest NW density. This occurs due to a contact issue concerning the p-a-Si:H deposited at 600 °C in-between the NWs and the ZnO:Al substrate. Using a higher density of SiNWs can improve the S shape, benefiting from the superior contact between the SiNWs themselves and the substrate, but at the tradeoff of V_{OC}. We then compare the performance of 1RJ, 2RJ and 3RJ with an eye towards water-splitting and not just absolute efficiency.

In a second section, in order to know where the randomness in the performance of 3RJ solar cells comes from, the growth processes of SiNW solar cells are checked step-by-step, which includes changes in the ZnO:Al substrate, the H_2 plasma treatment, and initial growth of the SiNW. We find that the ZnO:Al roughness change and the Sn droplet coalescence are the reasons. From ellipsometry measurements during NW growth, we also show a relationship between the final NW density and the position in time of the peak in the signal intensity curve. A later peak time corresponds to lower NW density.

In a final section, we investigate the performance of the 4RJ SiNW solar cell for water splitting. Different scan speeds, electrolyte pH, and distances between anode and cathode for water splitting are investigated. The first RJ SiNW unassisted PEC cell is demonstrated in the thesis. The 4RJ SiNW solar cells with a V_{OC} of 2.75 V are fabricated, and we use the earth-abundant Ni catalyst (deposited by thermal evaporation) to construct the photocathode for hydrogen evolution. With a Pt photoanode, PEC cell operation is demonstrated. Furthermore, the performance of this PEC cell with a RJ SiNW photocathode in different kinds of solution are studied. The unassisted water splitting by PEC cell runs stably for 90 min in 1M KBi electrolyte. The PEC efficiency has an initial value of 0.98% when using 0.1 M KOH as electrolyte, and a stabilized value of 0.43% when using 1 M KBi.

Keywords: radial junction; silicon nanowire; triple and quadruple junction solar cell; photoelectrochemical cell

Résumé

Les cellules photo-électrochimiques (PEC) sont des dispositifs prometteurs pour convertir l'énergie solaire en énergie chimique via l'électrolyse de l'eau pour obtenir du H_2, que l'on peut stocker et transporter. Cependant, selon le calcul thermodynamique, un potentiel de 1,23 V est nécessaire pour l'électrolyse de l'eau, ce qui dépasse la tension en circuit ouvert (V_{OC}) de la plupart des cellules solaires monojonction. En pratique, la tension nécessaire est supérieure 1.23 V à cause des pertes dans les catalyseurs et les electrolytes, et donc des cellules multijonctions sont nécessaires pour la réaction. Les cellules solaires à base de nanofils de silicium (SiNW) à jonction radiale simple et double ont été étudiées précédemment car leur capacité de piégeage lumineux permet des couches absorbantes en silicium amorphe hydrogéné (a-Si:H) plus fines, et donc un photo-dégradation réduite. Dans cette thèse, les cellules solaires SiNW à jonction radiale sont fabriquées, d'abord des simple et double jonctions (1RJ, 2RJ), et pour la première fois, en triple et quadruple jonction (3RJ, 4RJ). Les cellules solaires à triple jonction radiale – qui montrent une tension en circuit ouvert (V_{OC}) supérieure à 2 V - sont fabriquées par dépôt chimique en phase vapeur assisté par plasma avec une seule étape de pompage. Nous avons étudié les performances des diodes 3RJ SiNW, et l'effet de la densité des NWs sur les performances des cellules solaires à triple jonction, et nbous avons montré qu'un V_{OC} plus élevée est corrélé avec une densité de NWs plus faible. Néanmoins, une diminution dans la densité de NWs conduit à des caractéristiques J-V en forme de S que nous avons attibué à un problème de contact entre le couche p-a-Si:H qui se dépose à 600 °C entre les NWs et le substrat en ZnO:Al. Un optimum en efficacité en termes de densité de NWs est ainsi trouvé. Nous comparons ensuite les performances de 1RJ, 2RJ et 3RJ en tenant compte d'application visée et pas seulement de l'efficacité absolue.

Dans une deuxième section, afin de savoir d'où vient le caractère aléatoire des performances des cellules solaires 3RJ, les processus de croissance des cellules solaires à base de SiNWs sont vérifiés étape par étape, ce qui inclut des changements dans le substrat ZnO:Al, l'effet du traitement du ZnO:Al par un plasma H_2 et les étapes initiales de la croissance des SiNWs. Nous constatons que le changement de rugosité du ZnO:Al et la coalescence des gouttelettes de Sn en sont les principales raisons. À partir de mesures d'ellipsométrie pendant la croissance des NWs, nous montrons également une relation entre la densité finale de NWs et la position dans le temps du pic dans la courbe d'intensité du signal. Un pic plus tardif correspondant à une densité NW plus faible.

Dans la dernière section nous étudions les performances de la cellule solaire 4RJ SiNW pour la séparation de l'eau. L'effet de la vitesse de balayage de la caractéristique J-V, le pH de l'électrolyte et les distances entre l'anode et la cathode sur l'efficacité de la séparation de l'eau sont étudiés. La première cellule PEC non assistée RJ SiNW est démontrée. Les cellules solaires 4RJ SiNW avec un V_{OC} de 2,75 V sont fabriquées et nous utilisons le Ni (matériau abondant) déposé par évaporation thermique sur la cellule 4RJ comme catalyseur pour construire la photocathode pour le dégagement d'hydrogène. Avec une photoanode Pt, le fonctionnement de la cellule PEC est démontré. De plus, les performances de cette cellule PEC avec une photocathode RJ SiNW dans différents types de solution sont étudiées. La séparation de l'eau non assistée par la cellule PEC fonctionne de manière stable pendant 90 min dans l'électrolyte 1M KBi. L'efficacité PEC a une valeur initiale de 0,98% lors de l'utilisation de 0,1 M KOH comme électrolyte, et une valeur stabilisée de 0,43% lors de l'utilisation de 1 M KBi.

Mots clés: jonction radiale ; nanofil de silicium; triple et quadruple jonction cellule solaire; cellule photoélectrochimique

Contents

List of acronyms and abbreviations

c-Si	Crystalline silicon
a-Si:H	Hydrogenated amorphous silicon
μc-Si:H	Hydrogenated microcrystalline silicon
μc-SiO$_x$:H	Hydrogenated microcrystalline silicon oxide
CG	Corning glass
PECVD	Plasma enhanced chemical vapor deposition
SEM	Scanning electron microscope
AFM	Atomic force microscopy
QCM	Quartz crystal microbalance
SE	Spectroscopic Ellipsometry
CCP	Capacitively Coupled Plasma
FF	Fill factor
RF	Radio frequency
RJ	Radial junction
sccm	Standard cubic centimeters per minute
VLS	Vapor liquid solid
SiNW	Silicon nanowire
PEC	photoelectrochemical
LSV	Linear sweep voltammetry

Chapter 1 Introduction

1.1 Clean Energy and Chemical Energy Storage

1.1.1 Fossil Fuels and Non-Fossil Fuels

In 2020, the primary energy needs of mankind totaled 14200 Mtoe (million tons of oil equivalent). Of this, oil constituted ~30%, natural gas ~25% and coal ~27%, thus a total of 82% from fossil fuels, with the rest coming from nuclear or renewable sources, which encompasses energy from hydroelectric dams, wind, tidal/ocean-wave, solar, and biomass. Of this total energy input (removing other uses and conversion losses) about 16% (2300 MToe) is used as electricity [1]. This form of usage represents a significant opportunity to reduce humanity's dependence on fossil fuels, as it does not depend on the original energy source (unlike gasoline, for example).

Solar energy is one of the most promising forms of renewable energy. A total of 173000 terawatts of solar energy strikes the earth continuously, which exceeds by 1000 times that of human use [2]. One way that the flow of solar energy can be captured is through the use of photovoltaic (PV) devices, which directly transform solar illumination into electrical power. The contribution of PV to electricity generation increased from 11.9 TWh to 821 TWh between years 2008 and 2020, and currently, PV accounts for the production of 3.1% of electrical energy [3]. However, 64% of electrical power still originates from fossil fuels.

The continued growth of PV as an electrical power source faces a major challenge due to the variation of solar production, both by location, and in time. Because the Earth is a sphere, at every moment, rays from the Sun strike the surface at various angles ranging from 0° (sun just above the horizon) to 90° (sun directly overhead), causing a strong variation in available solar power per unit of ground surface area. The closer the sun's rays to vertical, the greater the received energy per unit of ground surface area, benefiting regions close to the equator, while the frigid polar regions never get a high irradiation, and due to the Earth's tilted axis of rotation, some areas at the North and South Pole get no sun at all for a portion of the year.

Of course, the rotation of the Earth also causes PV production to vary throughout the day, not just falling to zero at night, but decreasing in the morning and evening for solar panels that do not track the sun.[1] The amount of electricity produced by solar power systems varies also with the seasons, as the tilt of the Earth's axis relative to its orbital path again influencing the incident angle of the sun's rays. Indeed, some solar systems can generate twice as much electricity in the summer as they can in the winter due to the shorter days and increased incidence angle [4]. On top of all these sources of intermittence, one must also consider weather effects, such as clouds and snow, which are more difficult to predict.

It is clear that although the total available solar energy greatly exceeds human usage, its variation over minutes, hours, days and seasons poses a great challenge. Therefore, how to storage and transport solar energy is also of great importance. One way to do so is by converting the solar energy to chemical energy, as discussed in the next sections.

1.1.2 Photosynthesis

Through evolution, plants have long solved the issue of solar intermittency by converting solar energy to chemical energy, to feed themselves and fuel their growth during nighttime hours. As shown in figure 1.1, the plant uses energy from sunlight to cause a chemical reaction which can break down the molecules of water and carbon dioxide to produce oxygen and sugar [5], which can be stored as needed for the plant. This process is called photosynthesis, and from an energy point of view, solar energy is converted into chemical energy by the photosynthesis process. The photosynthesis can be expressed as an overly simplified equation:

$$6CO_2 + 6H_2O + \text{Light} \rightarrow C_6H_{12}O_6\,\text{(sugar)} + 6O_2$$

---

[1] Solar irradiance is also modified by the path length through the atmosphere, adding another degree of variance.

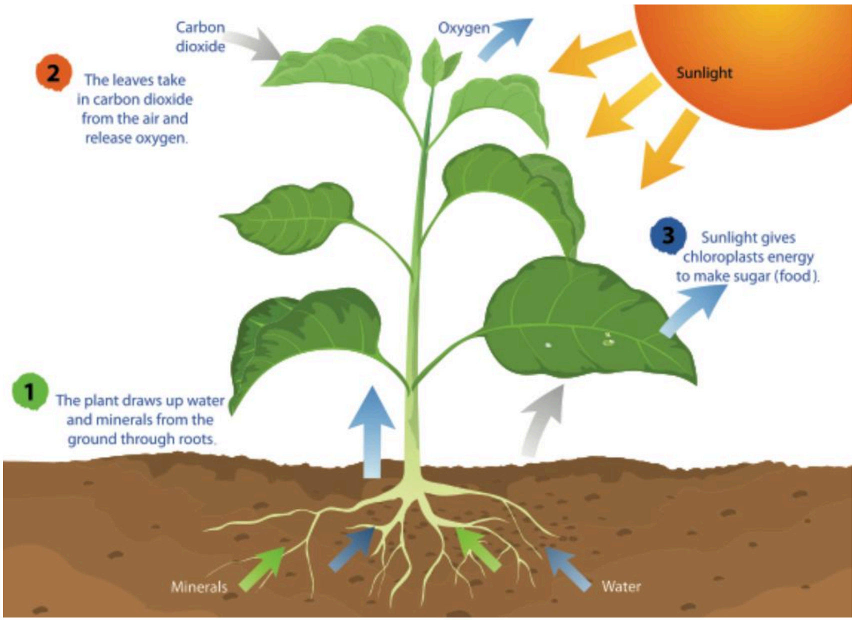

Figure 1.1 Plant photosynthesis process, extracted from [5].

1.1.3 Water Splitting and Artificial Photosynthesis

Mankind has long sought to emulate photosynthesis to convert solar energy into a storable chemical fuel, but more efficiently than natural photosynthesis (which is around 3-6% energy efficient). Artificial photosynthesis can be described as a process that converts water to hydrogen and oxygen, or converts carbon dioxide into high-value compounds such as ethylene, methanol and ethanol, using the energy received from sunlight to simulate natural photosynthesis [6, 7]. Artificial photosynthesis was first put forward by G. Ciamcian in 1912. He proposed to use photochemical devices to perform water splitting to power human civilization [7]. As well, light driven carbon dioxide reduction is a desirable process for carbon fixation. Y. Hori published the first study to quantify both gaseous and liquid products, accounting for 100% Faradaic efficiency [8]. Constant-current electrolysis of CO_2-saturated 0.5 M $KHCO_3$ at 5 mA cm^{-2} was performed as a batch experiment on a variety of polycrystalline metal electrodes for up to an hour. They found that $HCOO^-$ can be produced by Cd, In, Sn, and Pt cathodes, CO can be obtained by Ag and Au, CH_4 can be formed by Cu.

Water splitting by electrolysis using solar power is another form of artificial photosynthesis. Solar water splitting for the production of hydrogen as a fuel by using water and sunlight (an omnipresent and sustainable resource), is obviously very attractive for humankind. Hydrogen is non-toxic, environmentally friendly (non-greenhouse gas), and produces only water after combustion. Although the use of solar power to drive the electrolysis reactions somewhat complicates the devices, the processes can first be discussed looking at the water-splitting process itself.

1.1.4 Water-Splitting in Two Half-Reactions

The electrically driven water splitting process will convert water into hydrogen and oxygen once the electrical potential difference appearing at the two electrodes is sufficient to drive the reaction (and overcome any other undesired energy barriers present). This is represented in Figure 1.2, showing the electrical current flow for an electrode in water (voltage applied relative to an infinite reference electrode in water) with no other energetic barriers present. In reality, this behavior will depend strongly on the materials (due to electron transfer energetic barriers) and architectures (due to ion transport through the electrolyte) used to make the electrolysis device. As shown in Figure 1.2, the electrically driven water-splitting reaction ($2H_2O \rightarrow 2H_2 + O_2$) contains two half reactions; the hydrogen evolution reaction (HER) and the oxygen evolution reaction (OER). These two half reactions are discussed in the next section.

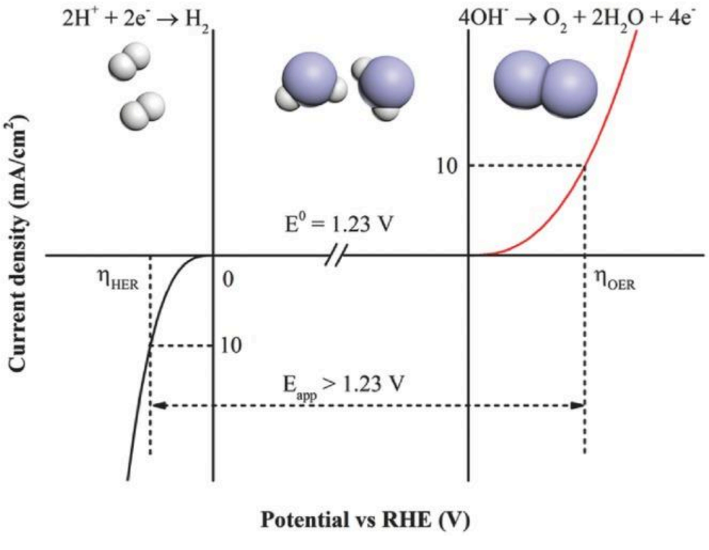

Figure 1.2 Current density-voltage curves for HER and OER. The thermodynamic equilibrium potential for water splitting is 1.23 V [9].

1.1.4.1 Hydrogen Evolution Reaction

The hydrogen evolution reaction (HER) is of great practical significance to produce clean and sustainable hydrogen energy during electrochemical water splitting. This process involves a two-electron-transfer reaction, through either the Volmer–Heyrovsky mechanism ($H^{+}+e^{-}\rightarrow H_{ads}$, $H_{ads} + H^{+}+e^{-}\rightarrow H_2$) or the Volmer–Tafel mechanism ($H^{+}+e^{-}\rightarrow H_{ads}$, $H_{ads} + H_{ads}\rightarrow H_2$). The kinetics of these two pathways are determined by the free energy of hydrogen adsorption ΔG_{Hads}. The ideal electrocatalyst would have a ΔG_H close to 0 eV, which means the adsorbed H can undergo an easy charge transfer and hence desorb. Precious-metal (Pt, Ru, etc.) based catalysts are ideal for HER, as they have small absolute ΔG_{Hads} values. However, their high cost and scarcity hamper their extensive applications [10].

The acidity/alkalinity of the electrolyte also plays a role in the reaction. In acidic electrolyte conditions, catalysts such as platinum group metals are often used for HER, despite their relatively high price. Efforts have been made to reduce the amount of Pt used in the device. N. Dasgupta presented atomic layer deposition (ALD) of platinum catalysts on silicon nanowire surfaces as HER catalyst for photoelectrochemical water reduction in 0.5 M H_2SO_4. Pt particles with size from 0.5 nm to 3 nm were deposited on Si. This method afforded a precise control of the mass of Pt loading. Pt was deposited by ALD and they changed the number of Pt ALD cycles to find the optimal thickness, found to be 10 ng/cm^2. The maximum photocurrent obtained was 7 mA/cm^2. This ALD technique gave the most suitable ratio for catalyst deposition on Si and reduced the cost of noble-metal catalyst [11].

Furthermore, acid proton membranes and strong acids further add costs. Highly corrosive reaction conditions also bring safety hazards and stability problems; the hydrogen produced may be contaminated by the acidic electrolyte evaporating, and the cell may be corroded by the strong acid. HER in alkaline conditions can avoid the above problems in acidic HER. If using alkaline HER, the price of HER can be reduced and the stability of HER can be enhanced. Moreover, using more common metals (such as Co, Fe, Ni) as catalysts can reduce costs. However, the much slower reaction kinetics of alkaline HER limits its practical application; the kinetics of HER in an alkaline electrolyte is 2-3 orders of magnitude lower than that of an acidic electrolyte.

1.1.4.2 Oxygen Evolution Reaction

The oxygen evolution reaction (OER) – the other of the two half-reactions of water splitting - is vital to renewable energy conversion technologies, such as water electrolysers, where the OER is driven on the electrode surface during the charging process [12]. The four proton-coupled electron transfer processes (Acidic conditions: $2H_2O \rightarrow O_2(g)+4H^{+}+4e^{-}$; Alkaline conditions: $4OH^{-} \rightarrow O_2+2H_2O+4e^{-}$) demonstrate intrinsically sluggish kinetics, which require a high over-potential to break O–H bonds and form O=O bonds. To date, Ir/Ru-based materials are commonly used as electrocatalysts for OER, although their high cost and scarcity severely hinder their widespread application. It is hence critically important to develop cost-effective, efficient, and highly durable non-precious-metal-based electrocatalysts to replace noble-metal-based materials. Earth-abundant 3d transition-metal metals involved in particular, have been considered as promising catalysts used in electrocatalytic OER applications. There are also challenges for the high-performance application in OER, such as high driving force over 1.23 V, undesirable metal loadings, and support stacking, which can be addressed by the strategies of doping, molecular ligands, morphology engineering, and more.

In OER, possible reaction mechanisms of acid and alkaline OER involve the formation of intermediates (OOH*, OH* and O*), an indirect path that certainly requires more energy and overpotential, leading to lower activity and slower dynamics [10]. The catalytic activity of OER in alkaline conditions is better than that in acidic conditions, in contrast to HER. Because the OER process begin with the formation of OH* and O*on the surface of catalyst, and a lot of -OH are in alkaline, these -OH can promote the reaction rate of OER [12].

1.1.4.3 Technical strategies for water splitting

The chemical reactions describing water splitting can be driven in a number of ways. Most simply, they may be driven in the dark by an electrical power source, and this power source can be of any type (including photovoltaic).

A first step towards avoiding the need for an external power source is directly using solar energy to drive the reaction. The difference in potential to drive the splitting can also be provided directly by energetic photons through illumination. Photocatalytic water splitting involves using only a catalytic effect driven by illumination. However, photocatalytic water splitting has the disadvantage of only using the UV portion of the solar spectrum, which contains a tiny fraction of the total available power.

One way to make use of the full solar spectrum for water-splitting is the photovoltaic (PV) effect, which uses a carrier collection asymmetry to create a voltage across a device. By using a PV device that produces a voltage greater than 1.23V, such a device can be used to directly drive the two half-reactions.

In short, driving the two water-splitting half reactions requires an electrical potential (Figure 1.2), which can be supplied externally by an electrical power source, or as an integrated renewable source. Keeping with our goal, one option is photovoltaic devices, with a preference for lower cost and more robust technologies. The next section gives a reminder of the operation and design of such devices.

1.2 Classical Silicon Photovoltaics

1.2.1 Crystalline Silicon Photovoltaics

Crystalline silicon (c-Si) – in either multicrystalline or monocrystalline form – is the most important material for the current photovoltaics industry. As of 2021, c-Si solar cells dominate the PV market with over a 90% share. The schematic structure of a classical c-Si solar cell is shown in figure 1.3. In this example, the 150-200 μm thick crystalline silicon wafer is p-type, the front electron collecting layer is formed by phosphorus diffusion, and the rear, hole collecting layer is formed by aluminum-doping. The front surface is passivated with a hydrogenated amorphous silicon nitride layer, which also performs the role of an antireflection coating. Aluminum is used both as the back contact and as a dopant source during the firing process, and silver is used for the front metallic fingers [13]. The output current density (continuous line) and output power density (dashed line) vs. voltage under one-sun illumination for the ideal (black line) and the world-record (red line) solar cells are shown in figure 1.4. The open-circuit voltage (V_{OC}) is the value of voltage when the current density is zero. The short-circuit current (J_{SC}) is the current density value when the applied voltage is zero. The maximum output power is P_{max}, the voltage at the point of P_{max} is V_{MPP}.

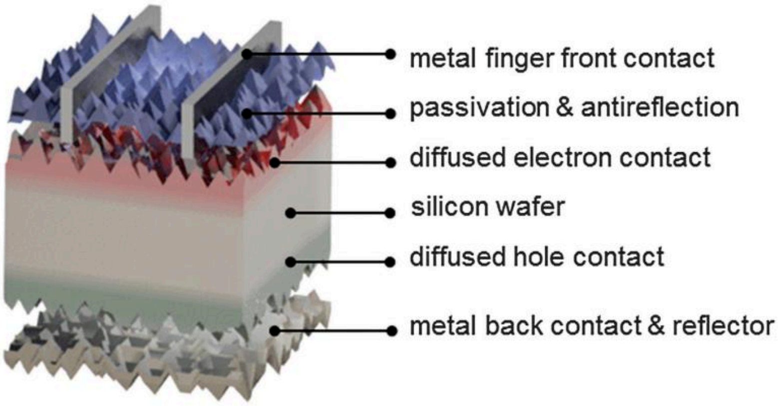

Figure 1.3 Schematic figure of classic c-Si homojunction solar cell [13]

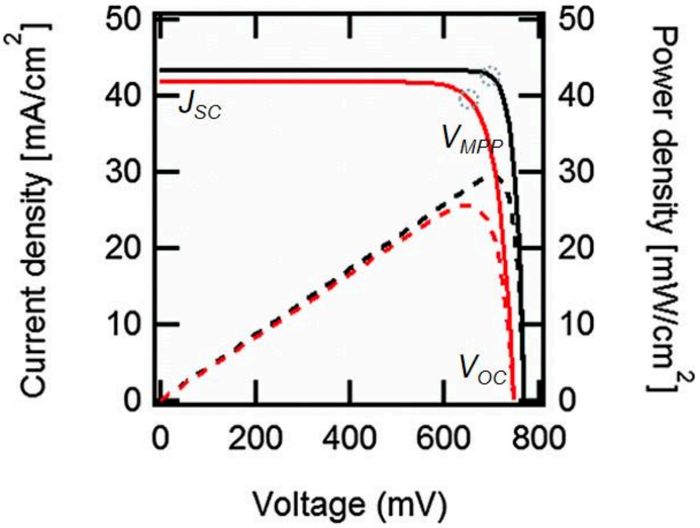

Figure 1.4 Output current density (continuous line) and output power density (dashed line) vs. voltage under one-sun illumination for the ideal (black line) and the world-record (red line) solar cells [13].

1.2.2 Thin film silicon PV

Thin film solar cells have been called the second generation of solar cells. In this architecture, one deposits thin films of photovoltaic materials on the substrate, and the active layers are much thinner than the first generation c-Si solar cell (c-Si wafer is around 150-200 μm). Industrial thin film technologies include cadmium telluride (CdTe), copper indium gallium diselenide (CIGS), and amorphous silicon (a-Si) thin film. Solar cells using thin film technology are cheaper per m^2, but less efficient than c-Si technology.

Amongst these, amorphous silicon (a-Si) is a form of non-crystalline silicon; it does not have strict periodicity and long range order. Hydrogenating this material and making amorphous silicon (a-Si:H) can reduce the number of dangling bonds in a-Si and thus reduce the defect density of the material. Due to hydrogenation and disorder, the optical band gap of a-Si:H is around 1.7 eV (compared to 1.12 eV for c-Si). The a-Si thin film is one of the most well-developed thin film technology, and is viewed positively as it has lower toxicity problem due to a lack of cadmium.

Hydrogenated amorphous silicon solar cells are fabricated using a plasma-enhanced chemical vapor deposition (PECVD) method. This method uses a gaseous mixture of silane (SiH_4) and other gases to deposit a-Si:H thin films, creating reactive species through the presence of a plasma. Solar cells are formed using a PIN structure, with thin doped layers (15 nm) sandwiching an undoped, intrinsic layer (200-300 nm) as shown in figure 1.5. However, a metastable defect creation mechanism [called the Staebler-Wronski (SW) effect] limits absolute a-Si:H solar cell performance. If the solar cell is subjected to extended light exposure, the defect density will increase and the efficiency will be reduced due to recombination. The schematic of a-Si:H solar cell is shown in figure 1.5. The PIN a-Si:H is grown on transparent conductive oxide (TCO) covered glass. The metallization is top contact. The light shines through TCO side.

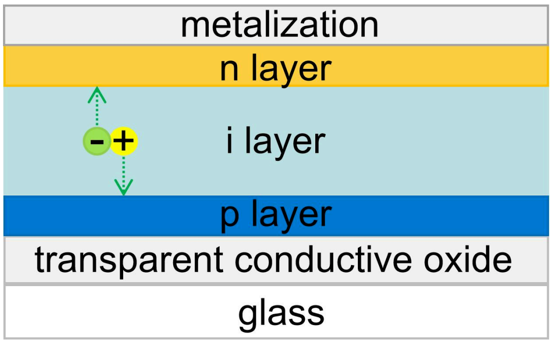

Figure 1.5 Schematic of a-Si:H solar cell

A closely related material is micro-crystalline silicon (μc-Si), whose grain size is intermediate between poly-crystalline silicon and amorphous silicon. The optical band gap of μc-Si is around 1.12 eV (like crystalline silicon), but it can be deposited by PECVD. Because there are a lot of crystalline grains in μc-Si, the conductivity is better than that of a-Si:H and the light-introduced degradation is reduced [14]. In addition, a-Si combined with μc-Si can create a tandem solar cell. The top a-Si:H solar cell absorbs light in the visible range, and the near infrared light is absorbed by the μc-Si solar cell [15].

1.3 Silicon nanowires and SiNW PV

Crystalline silicon is usually used in wafer form, and a-Si:H is typically deposited as a smooth, planar film with low roughness. However, some advantages can be obtained from forming more complicated structures, such as silicon nanowires (SiNWs) [16-18]. The first advantage to using SiNWs is to reduce the effect of lattice mismatch when growing crystalline silicon objects on different substrates. SiNWs can be grown on a wide variety of substrates, without perfect lattice matching. Secondly, the nanowire has an elevated surface to volume ratio. The effective surface area is maximized and the interactions between the SiNW and the surrounding volume is increased. In particular, for some surface-based chemical reactions, the reactivity can be greatly enhanced due to the large surface area of nanowires. Finally, for light-absorbing devices (such as PIN junction solar cells), coating them on SiNWs can enhance their light trapping ability. Typically, for a solar cell to absorb more light, it needs a thicker absorber layer. But if the absorber layer is too thick, the carriers will recombine before escaping the absorber layer. The SiNW solar cell can solve this problem. Although the absorber layer is thin, it can still have good light absorption, because of its 3D structure, while not increasing the problem of recombination in thicker absorber layer. These advantages will be discussed after an overview of SiNW fabrication techniques.

1.3.1 Approaches to grow SiNWs

For fabricating SiNWs, there are many approaches, such as chemical vapor deposition (CVD), lithographic technique with reactive ion etching, wet chemical etching, molecular beam epitaxy. The SiNW can be crystalline, polycrystalline or amorphous. The fabrication processes can be classified into two categories: (1) a top-down approach and (b) a bottom-up approach [19-22].

1.3.1.1 Top-down approach

The top-down approach can provide highly uniform vertical SiNWs from a c-Si bulk substrate by selective etching with a mask [23, 24]. Lithographic technologies can be used to define a mask, and then an etching process (such as deep reactive ion etching (DRIE) using SF_6) can be applied to remove the unwanted material. Perfectly organized arrays of nanowires can be realized by lithographic technologies, but they are limited to the laboratory scale, because of their high-cost and low throughput. In place of a lithographic mask, self-assembled nanospheres or nano-imprint lithography patterning can be used. For example, a silica bead solution for dip coating can be used to fabricate the mask, as shown in figure 1.6 [21].

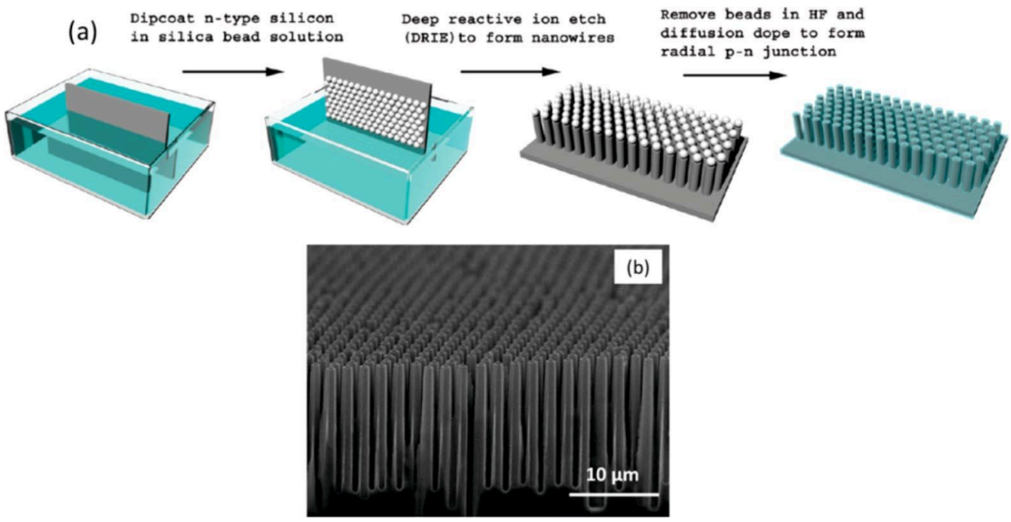

Figure 1.6 (a) NW fabrication by silica bead assembly via dip coating and DRIE; (b) tilted cross-sectional scanning electron microscope (SEM) image of a SiNW array. Figure extracted from [21].

Metal-assisted etching is an alternate wet chemical-etching method, where the presence of a noble metal in the salt solution catalyzes the Si dissolution reaction. J. Peng fabricated NW arrays by immersing a Si substrate in an HF + $AgNO_3$ solution [25]. In this solution, Ag particles are deposited on Si substrate and oxidation under the Ag particles is promoted. The oxide layer (SiO_2) is removed by HF, pits with the same size as the Ag particles are produced, and nanowire-like pores are formed.

1.3.1.2 Bottom-up approach

The second approach to growing SiNWs is bottom-up. The most common method demonstrating a bottom-up approach to synthesizing SiNWs is a vapor-liquid-solid (VLS) process with chemical vapor deposition (CVD) [26]. As described in the name of VLS, the atoms go from their gaseous state into the catalyst liquid, and end up as a solid phase after precipitation. Growing SiNWs by this method on c-Si wafer using Au catalyst was first proposed by R. S. Wagner [19]. In the VLS process of SiNW growth, the precursor gases [for instance, silicon tetrachloride ($SiCl_4$) or silane (SiH_4)] are absorbed and decomposed on the liquid surface as the temperature reaches the eutectic temperature of the catalyst. Then the Si atoms form a liquid eutectic alloy with the catalyst. If the precursor gases are supplied without interruption, the Si-catalyst alloy becomes supersaturated and Si starts to precipitate out at the liquid-solid interface, aiming to minimize the free energy of the system. As time progresses, this leads to the formation of c-SiNWs though bottom-up growth [27]. Although Au is the most used catalyst for SiNW growth, Au will introduce contamination and defects, which can become a problem for electronic devices [28].

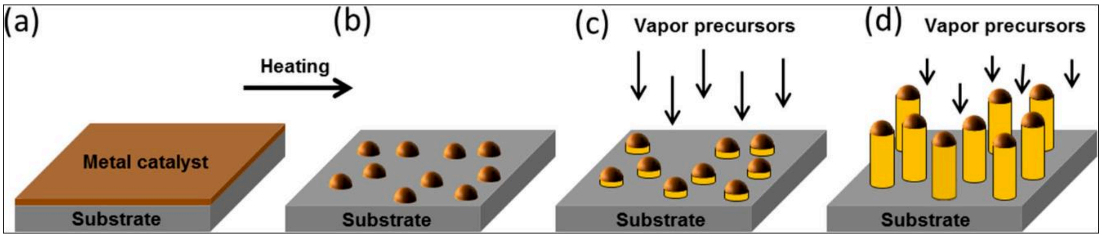

Figure 1.7 VLS method for SiNWs growth. (a) Metal catalyst layer deposition; (b) Small droplet forming after heating; (c) Vapor precursor dissolve into catalyst droplet and precipitation at the droplet-substrate interface; (d) SiNWs growth [27].

Similar to VLS, the vapor-solid-solid method is also possible. Instead of the liquid catalyst droplet, the catalyst for VSS growth is solid. For instance, Cu can be used for growing SiNWs by the VSS method. Whether the VLS or VSS route is preferred for SiNW growth depends on the catalyst composition and temperature [29, 30].

1.3.1.3 SiNWs grown by plasma assisted VLS method

To grow SiNWs by CVD via the VLS method, the catalyst normally needs to be at high temperature (600 to 700°C) to dissociate the gas precursors [31]. However, if the precursor gases are dissociated by electron impact during plasma-enhanced chemical vapor deposition (PECVD), no catalytic dissociation effect is necessary. Therefore, this makes the SiNWs possible to grow via PECVD.

Many kinds of metal can be used as catalysts for SiNW growth by PECVD, although some kinds of metal will also introduce recombination through their contaminating presence. The recombination depends on the location of the impurity level in the band gap of the host semiconductor. According to the Shockley-Read-Hall model for recombination, the closer the energy level to middle of the band gap, the higher the recombination rate [32].

In figure 1.8, we can see that Au, Zn, Cu, Fe, Co and Cr have energy levels close to the band gap of Si, so they are not good candidates for growing SiNWs for photovoltaics (PV) [33]. A further problem when growing SiNWs using Au is contamination, as it is hard to clean due to its stability. Growing SiNWs using metal catalysts like Ga, In, Tl, and Al results in p-type doping, because their impurity levels are close to the valence band. Growing SiNW by Bi, Li, Sb and Te leads to n-type doping, due to the fact that their impurity levels are close to conduction band.

In figure 1.8, the x-axis is the minimum temperature for SiNW growth (bulk melting point of a metal catalyst). Ga, In, Sn and Bi allow one to grow SiNWs at temperatures below 300°C, which is compatible with using an industrial PECVD reactor for SiNW VLS growth.

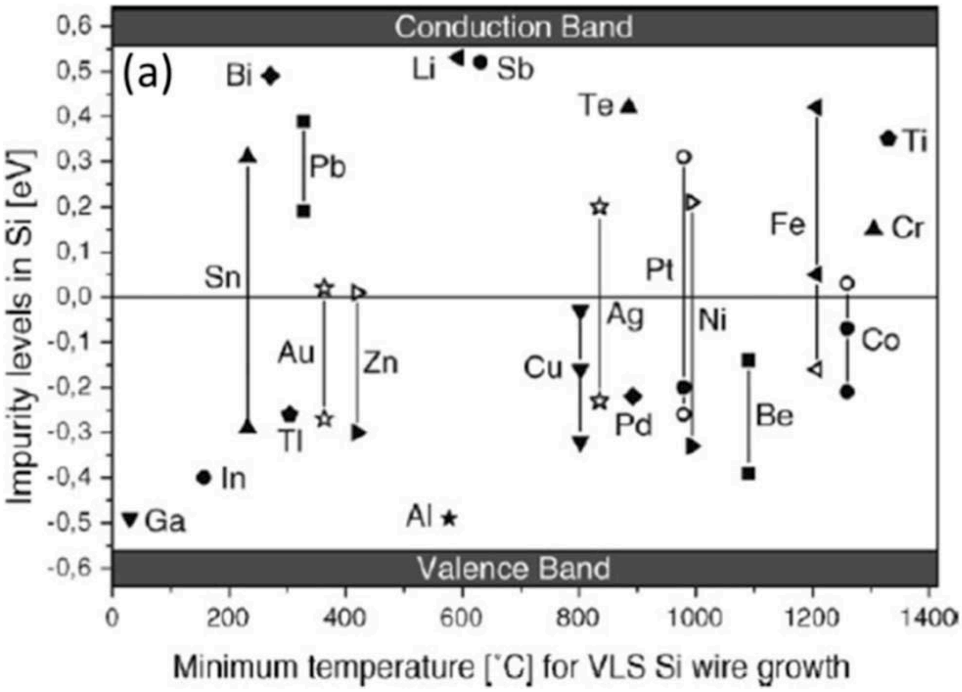

Figure 1.8 Various impurity levels in Si with respect to middle of bandgap as a function of minimum temperature for VLS growth.

1.3.2 SiNW solar cells

A p-n junction solar cell based on SiNWs (also called a radial junction) was proposed by E. Garnett in 2008 as shown in figure 1.9 [34]. Their radial junction solar cell was a core/shell structure; the core was fabricated by wafer etching and the shell by low temperature chemical vapor deposition. A power conversion efficiency of 0.5% was demonstrated. The performance was limited by interfacial recombination and high series resistance, and so surface passivation and contact optimization were needed to improve the performance.

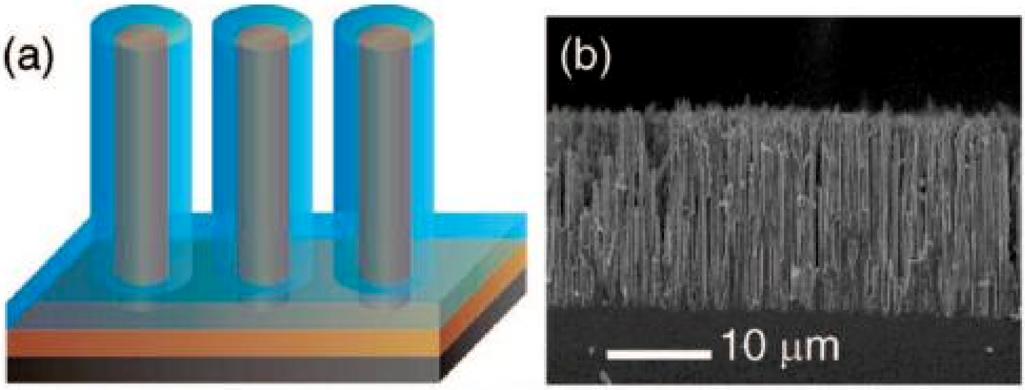

Figure 1.9 p-n RJ SINW solar cell. (a) Schematic of solar cell with core-shell structure; (b) SEM of cross section of p-n RJ solar cell. Figures extracted from [34].

L. Yu fabricated a-Si:H RJ solar cell by forming the Sn catalyst in-situ from an indium tin oxide (ITO) layer, growing the SiNWs by VLS growth, then depositing a PIN a-Si:H solar cell on them. In that work, different temperatures were explored for the H_2 plasma treatment that led to the Sn catalyst droplet formation, and a series of RJ SiNW solar cells with different thickness of absorber layer were investigated [35]. S. Misra further developed a-Si:H RJ SiNW solar cells grown from a Sn catalyst, achieving a higher efficiency and stable performance. The efficiency achieved reached 8.14% with short circuit current density (J_{SC}) of 16.1 mA/cm^2. Moreover, a J_{SC} of 13.46 mA/cm^2 could be generated from only a 50 nm thick absorber layer, which emphasizes the good light trapping from RJ SiNW solar cells. Finally, the solar cell performance did not significantly change after a 120 h light-soaking test; the light-induced degradation is limited to 6%, likely due to the 100nm thick absorber layer, as shown in figure 1.10 [36].

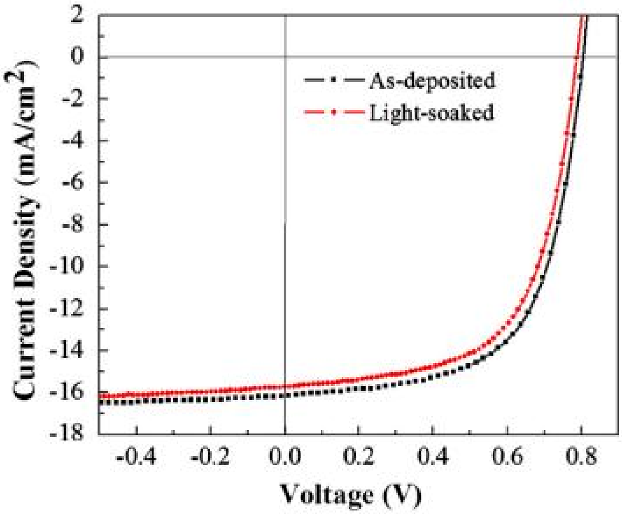

Figure 1.10 J-V performance of RJ SiNW solar cell before and after 120h light-soaking test. Figure extracted from [36].

RJ SiNW solar cells have also been grown on flexible Al foil, with a bending radius of 5 mm. These flexible RJ SiNW solar cells had an open circuit voltage (V_{OC}) of 0.71 V and J_{SC} of 14.2 mA/cm^2, giving an efficiency of 5.6% [37]. Flexible radial tandem junctions were first demonstrated by S. Zhang, with a V_{OC} of 1.2 V and efficiency of 8.1 % achieved with ~55 nm a-Si:H and ~45 nm a-SiGe:H absorber layers. When grown on Al foil, it has a power-to-weight ratio of ~1628 W/kg [38].

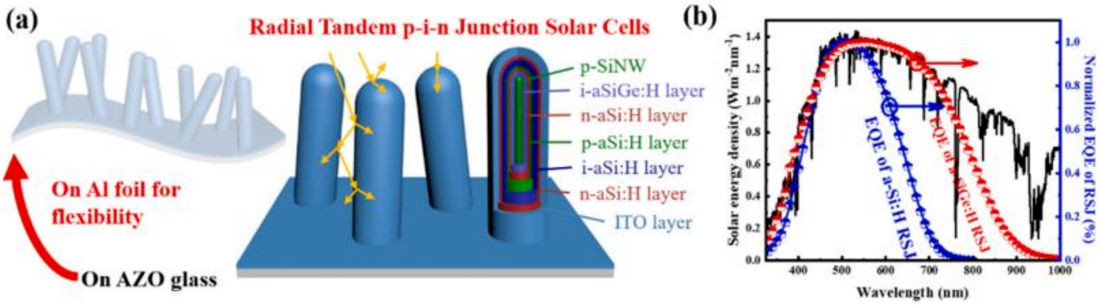

Figure 1.11 The tandem RJ SiNW solar cell. (a) Schematic diagram of tandem RJ SiNW solar cell; (b) EQE of the tandem RJ SiNW solar cell [38].

1.3.3 Other application of SiNWs

Many more applications for SiNWs (other than solar cells) have been proposed, such as MOS capacitors, photodetectors, and sensors. These other applications are briefly reviewed in this section.

1.3.3.1 Photodetector

An a-SiGe:H p-i-n junction based on c-SiNWs grown on a "soft" Al foil substrate can be used as a near-infrared (NIR) photodetector, as shown in figure 1.12 [39]. The device operates at 800 nm, where skin has high optical transparency and which overlaps with the absorption of oxyhemoglobin and deoxyhemoglobin. The device displayed a high responsivity of ≈140 mA/W at wavelength of 800 nm and good flexibility, undergoing 1000 bending cycles of 10 mm radius while maintaining rise/fall time scales of 5.4 μs/17.6 μs. It can therefore detect sphygmic signals at the wrist, which vary with significant changes in arterial blood volume. As an added bonus, it can be fabricated without toxic or heavy metal elements.

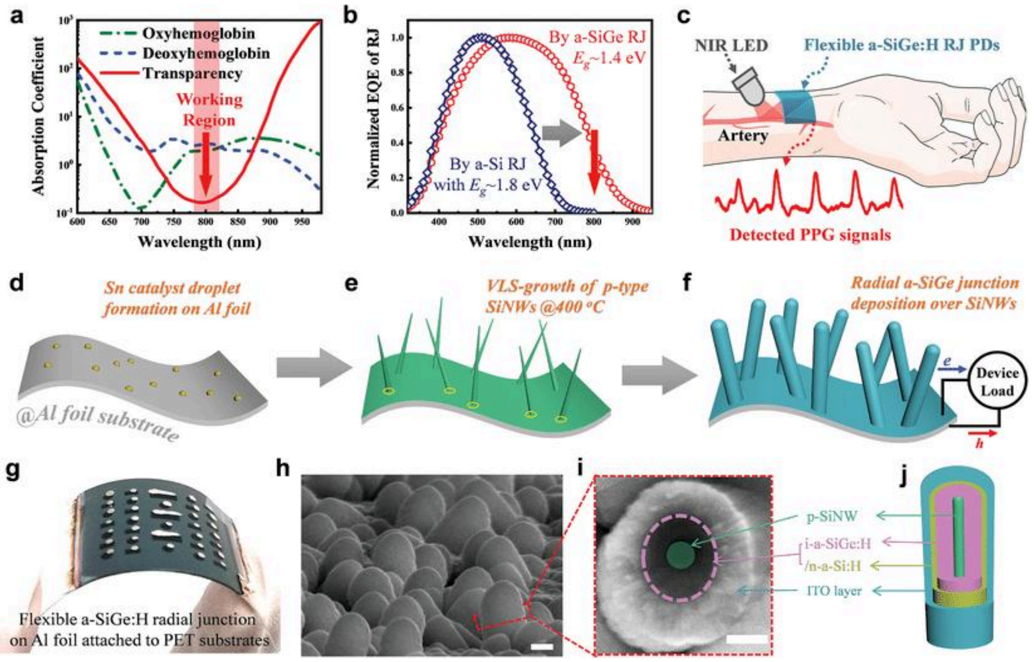

Figure 1.12 a-SiGe:H radial junction (RJ) as near-infrared photodetector. (a) Absorption coefficient of oxyhemoglobin and deoxyhemoglobin in human blood as function of wavelength; (b) EQE of a-Si:H and a-SiGe:H (RJ); (c) Configuration of detecting pulse from artery by a-SiGe:H RJ; (d-f) Fabrication of process of a-SiGe:H on soft Al foil; (g) Photograph of flexible a-SiGe:H RJ NIR gown on soft Al foil attached to polyethylene terephthalate (PET) substrates. (h) Side view of SEM image of a-SiGe:H RJ with SnO_2:In top contact; (i) Cross section of a-SiGe:H RJ; (j) Diagram of RJ SiNW. Scale bar in (h) is 100 nm, (i) is 300 nm. Figures extracted from [39].

Further developing this concept, as presented in figure 1.13, an a-Si/a-Ge:H absorber layer RJ also has been developed as a NIR photodetector with an even faster response time of 2.62 µs [40]. Using a-Ge:H can further expand the absorption range to 1050 nm, and an a-Si:H passivation layer was grown between the p-type SiNWs and a-Ge:H layer to reduce the interface defect state density.

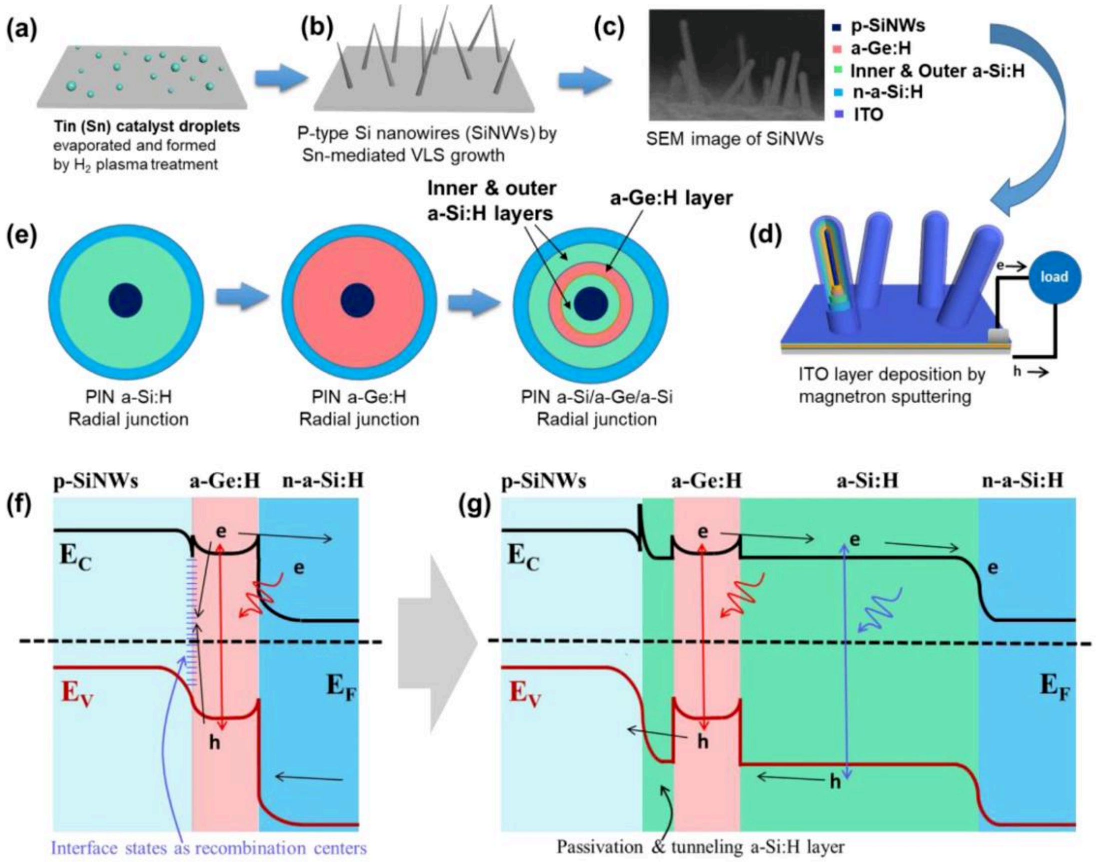

Figure 1.13 a-Si:H passivation layer/a-Ge:H/a-Si:H RJ as NIR photodetector. (a-d) fabrication process of a-Si:H passivation layer/a-Ge:H/a-Si:H RJ as NIR photodetector; (e) a-Si:H PIN RJ, a-Ge:H PIN RJ and a-Si:H/a-Ge:H/a-Si:H PIN RJ; (f) band diagram of a-Ge:H PIN RJ; (g) band diagram of a-Si:H/a-Ge:H/a-Si:H PIN RJ. Figures extracted from [40].

1.3.3.2 Field effect Transistor

In 2009, L. Yu *et al* discovered an in-plane, solid-liquid-solid (IPSLS) silicon nanowire growth phenomenon [41]. Then, a liquid In droplet is first formed during the H_2 plasma treatment process, followed by an a-Si:H layer deposition by PECVD at low temperature (below the melting point of In) everywhere on the substrate, including on the solid In droplet. During a subsequent annealing process (done in vacuum), c-SiNWs will start to grow in plane as the droplet moves on the surface.

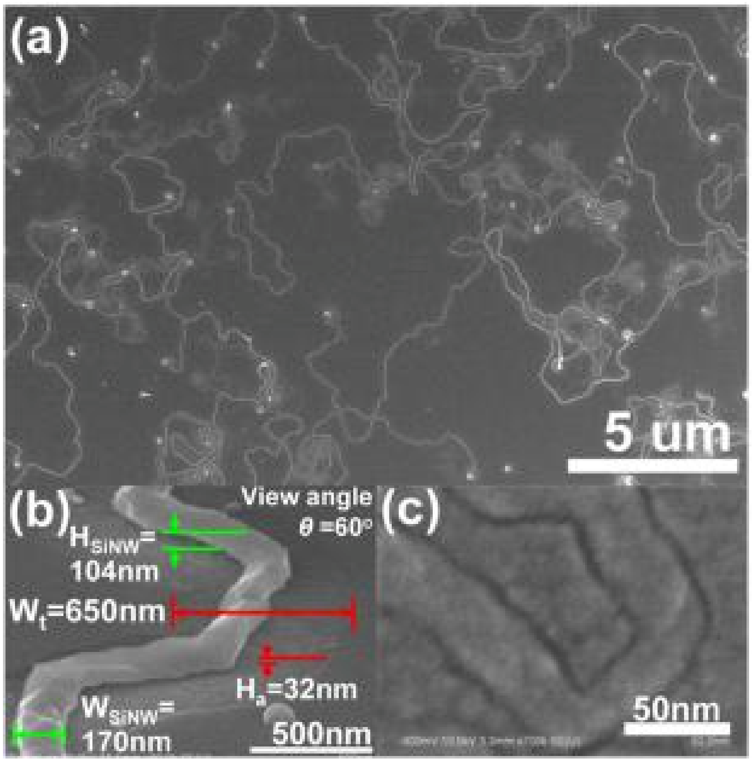

Figure 1.14 In-plane SiNWs. (a) SEM image of in-plane SiNW; (b) a side-view of SiNW trench structure; (c) one of the smallest in-plane SiNWs. Figure extracted from [41].

Recently, the IPSLS method was used to grow SiNWs with diameters less than 80 nm and with high order by using trenches [42]. An array of field effect transistor was then fabricated and transferred to flexible polydimethylsiloxane (PDMS) substrate. In that work, they also designed a discrete FET scheme where each FET is on an individual "island", such that when the whole substrate is bent, each small FET device can be supported by its island, as shown in figure 1.15.

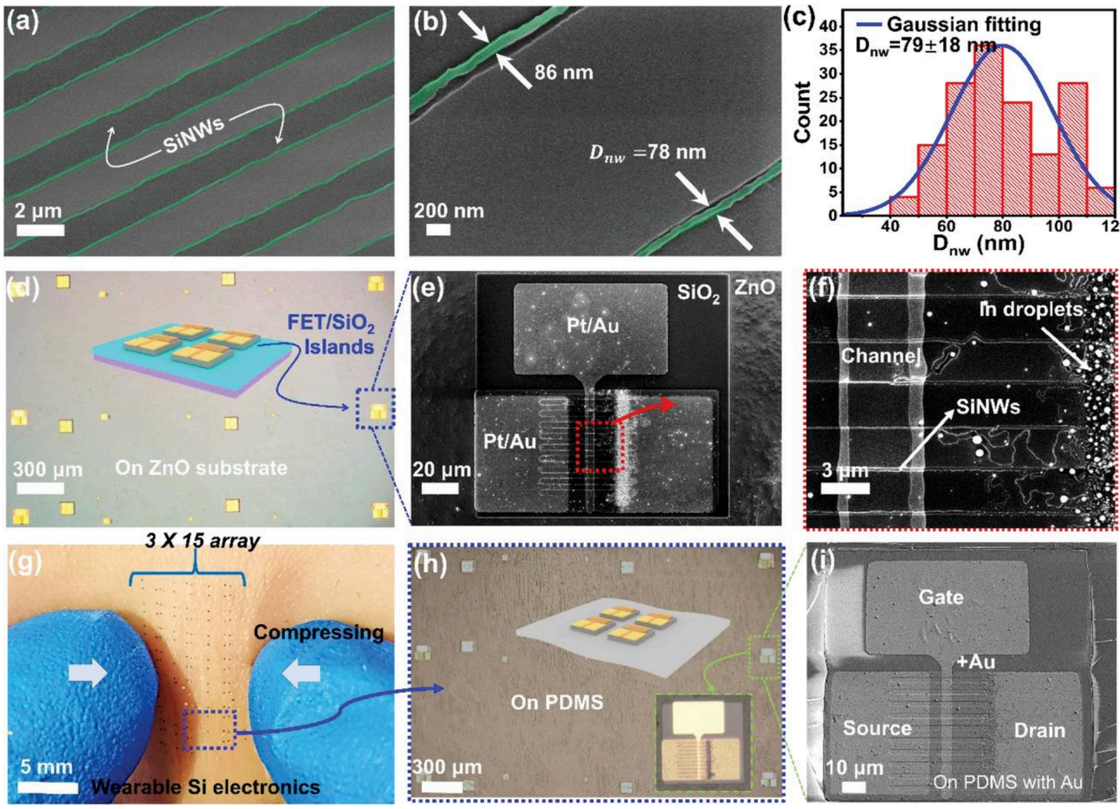

Figure 1.15 (a) SEM image of edge-guided in-plane SiNWs; (b) Close view of edge-guided in-plane SiNWs; (c) SiNW diameter distribution; (d) Schematic figure and microscope image of SiO_2 hard islands. FET units are on the top of SiO_2 islands, which are on a ZnO substrate; (e) enlarged SEM image of FET unit on SiO_2; (f) enlarged SEM image of channel, only the slim guided SiNWs away from the In are used as channels; (g) Photograph of SiNW FET transferred to PDMS substrate and attached on human skin; (h) and (i) Scrutiny of the discrete islands by microscope and SEM. Figures extracted from [42].

1.3.3.3 Field effect gas detector

X. Song recently demonstrated the feasibility of a FET-based gas detector using edge-guided in-plane SiNWs, as presented in figure 1.16 [43]. The SiNW based device achieved a field-effect sensitivity of 75.8% in 100 ppm NH_3 and a 100 ppb detection limit. This performance was attributed to the quick charge transfer between NH_3 gas molecules and the SiNWs. The device displayed good repeatability and a stability of around 6 months at room temperature.

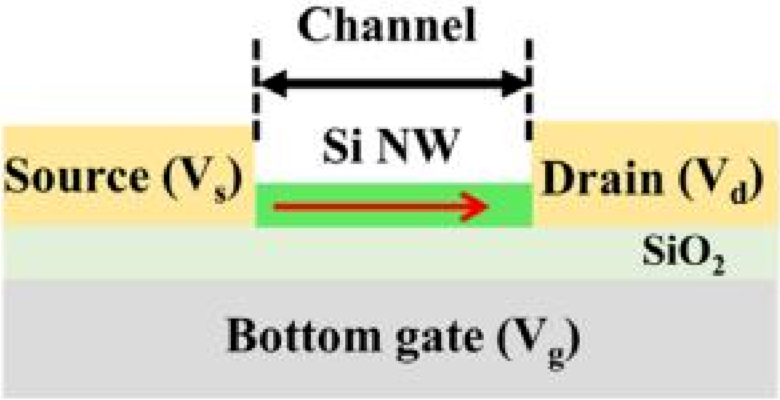

Figure 1.16 Schematic figure of FET using SiNWs. Figure extracted from [43].

1.4 Systems for Solar to Fuel Conversion

The previous section provided an overview of silicon photovoltaics, including a specific architecture using SiNWs as the contact and scaffold for a-Si:H PIN devices. In this section, we will discuss how PV devices can be used in photoelectrochemical (PEC) devices to perform water splitting for solar energy to fuel conversion.

Figure 1.17 depicts three different strategies for using solar energy to split water: photocatalysis, a photoelectrochemical cell, and a photovoltaic-electrolysis system [44]. Figure 1.17 (a) displays the process of photocatalysis. In this architecture, the photocatalyst (PC) material is dispersed in liquid and the charge transfer distance (several micrometers) is much shorter than that in other systems (which can be tens of millimeters). However, the H_2 and O_2 are generated on the same surface in the same time and the gases are not separated, limiting the usefulness of such a device.

A more useful architecture is obtained by separating the OER and HER reaction in space in a Photo-Electro-Chemical (PEC) system, shown in figure 1.17 (b). Such a system is constructed using photoanode and a photocathode, as determined by the nature of each of the liquid-semiconductor/metal junctions. Charge transfer occurs through a wire (by electrons) and through the electrolyte (by ions). The gases can now be separated, because H_2 and O_2 are produced at two different electrodes.

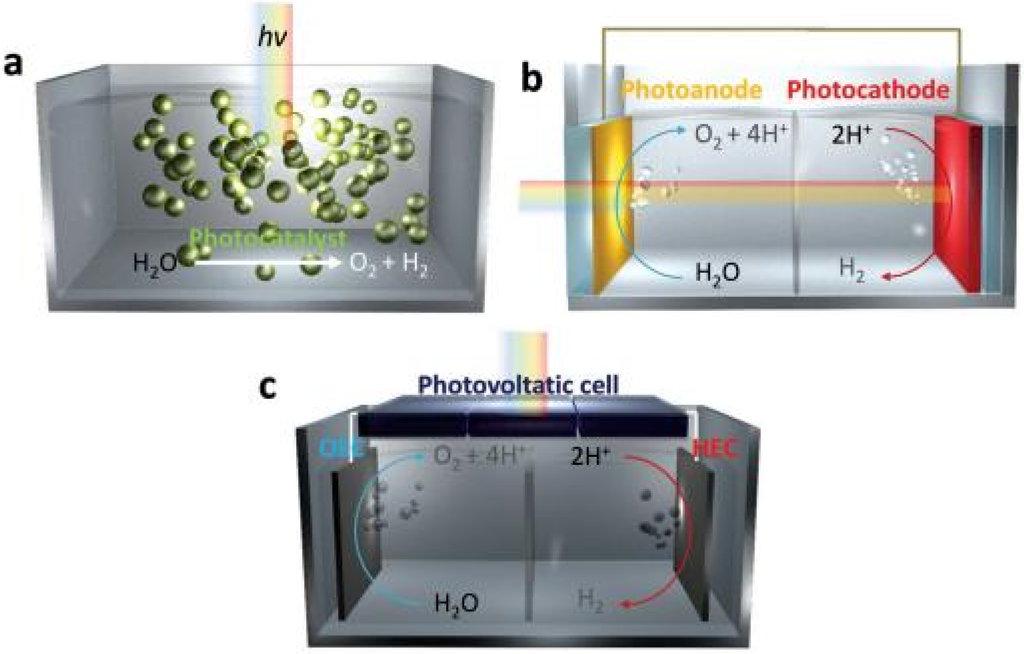

Figure 1.17 Different solar water splitting systems. (a) Photocatalysis; (b) Photoelectrochemical cell; (c) Photovoltatic-electrolysis systems. Figures extracted from [44].

Titanium dioxide (TiO_2) was first used for photocatalytic water splitting by A. Fujishima during the 1960s [45]. The TiO_2 is excited by UV light and produces holes and electrons. At the TiO_2 electrode (the photoanode), the valence band potential is appropriate for accepting electrons (into holes) and causing oxygen evolution, and the conduction band edge potential (which is tied electrically to the Pt cathode) is appropriate for proton reduction. Electrons flow through the external wire to the Pt counter electrode (photocathode), where H_2 is formed.

As previously mentioned, however, photocatalytic water splitting has the disadvantage of only using the UV portion of the solar spectrum. To make full use of the solar spectrum for water-splitting requires exploiting the photovoltaic (PV) effect, which uses a carrier collection asymmetry to create a voltage across a device. Photovoltaic electrolysis systems use a multi-junction photovoltaic device to generate the voltage needed to split the water [44]. The simplest version of a photovoltaic-electrolysis (PV-EC) system is presented in figure 1.17 (c). An independent PV device generates the voltage difference necessary for electrolysis. The PV device is placed out of the electrolyte, giving better stability against corrosion in alkaline and acidic electrolyte. The disadvantage of such PV-EC systems is higher complexity.

For example, as shown in figure 1.18, Spontaneous solar water splitting by DSSC/CIGS tandem solar cells [46]. The J-V curve and water splitting curve are compared. We can note that the potential for water splitting exceeds the single junction solar cell V_{OC}. The tandem solar cell or the solar cell modules are required for sufficient unassisted water splitting.

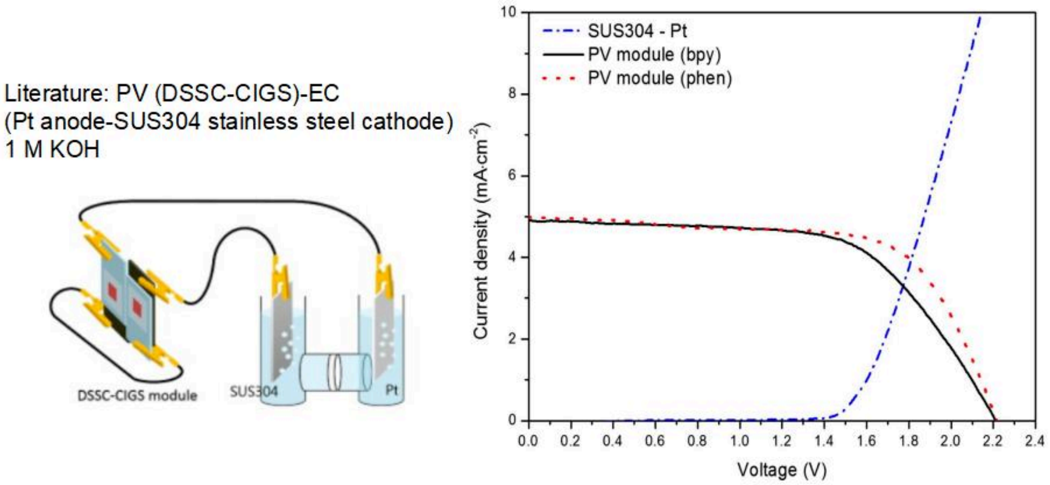

Figure 1.18 J-V performance of DSSC-CIGS tandem PV module and water splitting curves of photovoltaic-electrolysis [46].

A hybrid version of this strategy integrates the photovoltaic device with the two electrodes in contact with the electrolyte, but while keeping the active layers out of the electrolyte. Such a structure was demonstrated by Licht *et al* [47]; employing, $Al_{0.15}Ga_{0.85}As$ and Si layers together to form a hybrid junction, which then connects to sidewalls extending down into the electrolyte, they demonstrated an efficiency over 10% using RuO_2.

Full integration implies immersing the photovoltaic junction into the electrolyte and illuminating it underwater. Doing so, for example, O. Khaselev reported a p/n junction of $GaInP_2$/GaAs with a Pt activated layer as photocathode which reached a 12.4% energy conversion efficiency [48]. Both of these last two examples display good performance concerning energy conversion, but use one of the most expensive type of solar cells (III-V materials).

Combing the two concepts of photocatalysis and photovoltaic electrolysis, F.

Abdi used a CoPi/W:$BiVO_4$ photoanode with a double-junction amorphous Si solar cell in a tandem configuration, as shown in figure. 1.19 (a) [49]. In this structure, the absorbed light can be separated into short and long wavelengths. The PEC photoanode on the top absorbs the solar light of short wavelengths and the Si solar cell at the bottom absorbs the long wavelengths. This tandem solar water-splitting cell achieved a stable short-circuit photocurrent of ≈ 4 mA cm^{-2}, which corresponds to a solar to hydrogen (STH) efficiency of 4.9%.

Y. Pihosh fabricated a similar tandem device [50]. This cell had a CoPi/BiVO4/WO_3 photoanode and the voltage was produced by a double-junction stacked GaAs/AlGaAsP solar cell as shown in figure 1.19 (b). In their device, the solar cell was located parallel to the incident light to absorb the light reflected from the photoanode and optical losses caused by the inferior transparency could be avoided in this configuration. This coupling system exhibited a sustainable water splitting photocurrent of 6.56 mA cm^{-2}, which was corresponding to an STH efficiency of 8.1%.

Different from the above-mentioned two systems that immersed all the elements into the aqueous solution, Y. Qiu demonstrated a tandem device that was fabricated by direct connection between a Fe(Ni)OOH/Mo:$BiVO_4$ photoanode and a perovskite solar cell, as in figure 1.19 (c). A beam splitter was introduced to separate the standard solar light into two wavelength ranges of >515 nm and <515 nm, which was respectively absorbed by the perovskite cell and the photoanode. This device exhibited a short-circuit photocurrent of 5.01 mA cm^{-2} and an STH efficiency of 6.2% [51].

The above PEC water splitting devices are all comprised of a photovoltaic cell and a photoanode, which are connected by external wires. The artificial leaf is another configuration of PEC water splitting cells which is characterized by its wireless nature. In 1983, W. Ayers patented a configuration of the artificial leaf, which they fabricated with an amorphous silicon thin film solar cell [52]. A permeable barrier above the device was used to separate the two electrolytes and for proton transport. Aiming for lower cost catalytic layers, in 2008, D. G. Nocera created an "artificial leaf" with earth-abundant catalysts containing cobalt and phosphate, towards the goal of low-cost water splitting. A typical modern example of artificial leaf comprises a triple junction silicon photoabsorber (3jn-a-Si) with Co-based OER catalyst on the indium tin oxide (ITO) side and NiMoZn HER catalyst on the stainless steel side, as in figure 1.19 (d). An STH efficiency up to 2.5% in a 9.2 pH value solution was measured in the wireless PEC cell [53].

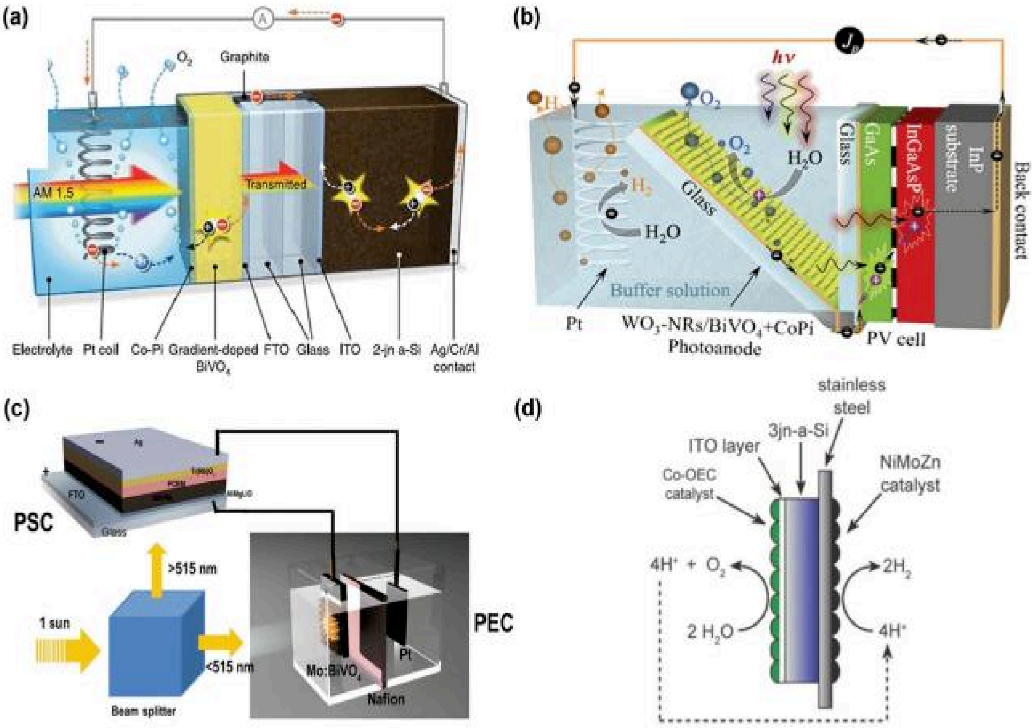

Figure 1. 19 Diagrammatic figure of (a) CoPi/W:$BiVO_4$ photoanode with a double-junction amorphous Si solar cell; (b) CoPi/BiVO4/WO_3 photoanode biased by a double-junction mechanically stacked GaAs/AlGaAsP solar cell; (c) a tandem device fabricated by direct connection of Fe(Ni)OOH/Mo:$BiVO_4$ photoanode and a perovskite solar cell; (d) a triple-junction silicon photoabsorber (ITO/3jn-a-Si/stainless steel) with Co-based OER catalyst on the indium tin oxide (ITO) side and NiMoZn HER catalyst on the stainless steel side [49-51, 53].

In addition, some RJ architectures have been applied for water splitting such as Si/TiO_2 tandem-junction microwire arrays or silicon microwire arrays modified with isolated Pt nanoparticles and conformal TiO_2 ultrathin film [54, 55]. The previous examples provide demonstrations of various PV technologies and radial junctions being used to perform water splitting. However, SiNW-based solar cells could be interesting for unassisted water splitting. Such devices have several advantages: (1) compared with planar solar cells, the SiNW RJ solar cell has a larger surface area, (2) the fabrication of SiNW RJ solar cells is simple, consisting of a one-pump-down process, (3) SiNW RJ solar cells are robust and can work in water, and (4) SiNW RJ solar cells are low-cost per m^2.

1.5 Thesis outline

The objective of this thesis is to fabricate RJ SiNW solar cells, improving the existing single and double junctions, and going to triple and quadruple junctions to obtain a high voltage to drive efficient water splitting. This will be used to develop an unassisted solar to hydrogen and oxygen PEC device using RJ SiNW solar cells as the voltage source. The work will be shown in the following sequence.

Chapter 2 will introduce the equipment and processes for RJ SiNW solar cell fabrication, how to fabricate substrate, deposit catalyst, grow SiNWs, deposit radial junction on SiNWs and coat top contact. Afterwards, the performance measurement and characterizations for solar cells and PEC cells will be presented.

Chapter 3 will investigate RJ SiNW solar cell performance. It will present results from trying to optimize the single, double and triple RJ SiNW solar cell performance by several strategies, such as doped layer changes, layer thickness, tunnel junction design, and SiNW density. The RJ SiNW diode performance is discussed. Moreover, the origin of the S shape observed in the J-V curves of RJ SiNW solar cells is studied. We also compare the 1RJ, 2RJ and 3RJ solar cells performance.

Chapter 4 will study the repeatability of the 3RJ SiNW solar cell fabrication process. It will first show the types of randomness that are present. The growth process is investigated step-by-step, from ZnO:Al to Sn evaporation to H_2 plasma treatment and SiNW growth to check where the randomness comes from. In-situ ellipsometry is used to observe the growth process of RJ SiNW solar cells.

Chapter 5 will present the performance of water splitting by our home-made electrodes. We fabricated 4RJ SiNW solar cell and deposited Ni catalyst by thermal evaporation for unassisted water splitting. We will investigate performance of PEC cell with RJ SiNW solar cells in different electrolytes.

References

[1] *World total final consumption by source*, https://www.iea.org/reports/key-world-energy-statistics-2020/final-consumption.

[2] *Shining brightly*, https://news.mit.edu/2011/energy-scale-part3-1026.

[3] *Solar ETFs: Zero-Carbon Investing Solution*, https://www.trackinsight.com/en/article/solar-etfs-zero-carbon-investing-solution.

[4] *How does solar work,* https://ohrenergy.com/how-does-it-work/solar-w/.

[5] *What is Photosynthesis*, https://ssec.si.edu/stemvisions-blog/what-photosynthesis.

[6] W. Lee, C. Lim, E. Ban, S. Bae, J. Ko, H. Lee, Byoung K. Min, K. Lee, J.Yu, H. Oh, *W@Ag dendrites as efficient and durable electrocatalyst for solar-to-CO conversion using scalable photovoltaic-electrochemical system*, Applied Catalysis B: Environmental, 2021, **297**:p. 120427.

[7] G. Ciamician, *The Photochemistry of the Future*, Science, 1912, 36 (926):p. 385-394.

[8] Y. Hori, K. Kikuchi, S. Suzuki, *Production of CO and CH_4 in Electrochemical Reduction of CO_2 at Metal Electrodes in Aqueous Hydrogencarbonate Solutions,* Chemistry Letters, 1985, **14**(11): 1695-1698.

[9] F. Lu, M. Zhou,Y. Zhou, X. Zeng, *First-Row Transition Metal Based Catalysts for the Oxygen Evolution Reaction under Alkaline Conditions: Basic Principles and Recent Advances*, Small, 2017, **13**:p. 1701931.

[10] Z. Shi, W. Yang, Y. Gu, T. Liao, Z. Sun, Metal-Nitrogen-Doped Carbon Materials as Highly Efficient Catalysts: Progress and Rational Design, Advance Science, 2020.

[11] N. Dasgupta, C. Liu, S. Andrews, F. Prinz, P. Yang, *Atomic Layer Deposition of Platinum Catalysts on Nanowire Surfaces for Photoelectrochemical Water Reduction*, Journal of The American Chemical Society, 2013, **135**(35):p. 12932-12935.

[12] L Li, P Wang, Q Shao and X Huang, *Metallic nanostructures with low dimensionality for electrochemical water splitting*, Chemical Socirty Reviews, 2020, **10**(49):p. 3072-3106.

[13] C. Battaglia, A. Cuevas, S. Wolf, *High-efficiency crystalline silicon solar cells:*

status and perspectives, Energy & Environmental Science, 2016, 9, 1552.

[14] Robert A. Meyers, *Encyclopedia of Physical Science and Technology (Third Edition)*, 2003.

[15] H. Keppner, J. Meier, P. Torres, D. Fischer, A. Shah, *Microcrystalline silicon and micromorph tandem solar cells*, 1999, **69**(2):p. 169-177.

[16] T. Zhang, J. Wang, L. Yu, J. Xu, P. Roca i Cabarrocas, *Advanced radial junction thin film photovoltaics and detectors built on standing silicon nanowires*. Nanotechnology, 2019, **30**:p. 302001.

[17] V. Khayrudinov, M. Remennyi, V. Raj, P. Alekseev, B. Matveev, H. Lipsanen, T. Haggren, *Direct Growth of Light-Emitting IIIV Nanowires on Flexible Plastic Substrates*, ACS Nano, 2020, **14**:p. 7484–7491.

[18] M. Zhang, K. Peng, X. Fan, J. Jie, R. Zhang, S. Lee, N. Wong, *Preparation of Large-Area Uniform Silicon Nanowires Arrays through Metal-Assisted Chemical Etching*, The Journal of Physical Chemistry C, 2008, **112**:p. 4444–4450 .

[19] R. S. Wagner, W. C. Ellis, *Vapor-Liquid-Solid Mechanism of single crystal growth, Applied Physics Letters*, 1964, **4**:p. 89.

[20] A. Hsu, Stephen T. Connor, M. X. Tang, Y. Cui, *Wafer-scale silicon nanopillars and nanocones by Langmuir–Blodgett assembly and etching*, Applied Physics Letters, 2008, **93**:p. 133109.

[21] E. Garnett, P. Yang, *Light Trapping in Silicon Nanowire Solar Cells*, Nano Letters, 2010, **10**(3):p. 1082-1087.

[22] P. Kanungo, N. Zakharov, J. Bauer, O. Breitenstein, P. Werner, U. Goesele, *Controlled in situ boron doping of short silicon nanowires grown by molecular beam epitaxy*, Applied Physics Letters, 2008, **92**:p. 263107.

[23] J. S. Ha, K. Park, K. Park, W. S. Yun, *STM investigation of nano-structures fabricated on passivated Si surfaces*, Korean Journal of Chemical Engineering, 2003, **20**: p. 169-173.

[24] E. Auzelyte, H. H. Solak, Y. Ekinci, R. MacKenzie, J. Voros, S. Olliges, R. Spolenak, *Large area arrays of metal nanowires*, Microelectron Engineering, 2008, **85**:p. 1131–1134.

[25] J. Peng, Y. Yan, S. Gao, J. Zhu, *Synthesis of Large-Area Silicon Nanowire Arrays via Self-Assembling*, Nanoelectrochemistry, Advanced Materials, 2002, **14**(16):p. 1164-1167.

[26] S. Misra, L. Yu, W. Chen, M. Foldyna, P. Roca i Cabarrocas, *A review on plasma-assisted VLS synthesis of silicon nanowires and radial junction solar cells*, Journal of Physics D: Applied Physics, 2014, **47**:p. 393001.

[27] S. Misra, L. Yu, W. Chen, M. Foldyna, P. Roca i Cabarrocas, *A review on plasma-assisted VLS synthesis of silicon nanowires and radial junction solar cells*, Journal of Physics D: Applied Physics, 2014, **47**:p. 393001.

[28] J. Hannon, S. Kodambaka, F. Ross, R. Tromp, *The influence of the surface migration of gold on the growth of silicon nanowires*, Nature, 2006, 440:p. 69-71.

[29] J. Arbiol, B. Kalache, P. Roca i Cabarrocas, J. Ramon Morante, A. Fontcuberta i Morral, Influence of Cu as a catalyst on the properties of silicon nanowires synthesized by the vapour–solid–solid mechanism, Nanotechnology, 2018, **18**:p. 305606.

[30] J. Arbiol, A. Fontcuberta i Morral, S. Estradé, F. Peiró, B. Kalache, P. Roca i Cabarrocas, J. Ramon Morante, Influence of the (111) twinning on the formation of diamond cubic/diamond hexagonal heterostructures in Cu-catalyzed Si nanowires, Journal of Applied Physics, 2008, **104**:p. 064312.

[31] V. Nebol'sin, A. Shchetinin, A. Dolgachev, V. Korneeva, *Effect of the Nature of the Metal Solvent on the Vapor–Liquid–Solid Growth Rate of Silicon Whiskers*, Inorganic Materials, 2005, **41**(12): p. 1256-1259

[32] W. Shockley, W. Read, *Statistics of the Recombinations of Holes and Electrons*, Physical Review, 1952, **87**:p. 835.

[33] V. Schmidt, J. Wittemann, S. Senz, U. Gösele, *Silicon Nanowires: A Review on Aspects of their Growth and their Electrical Properties*, Advanced Materials, 2009, **21**:p. 2681-2702.

[34] E. Garnett, P. Yang, *Silicon Nanowire Radial p−n Junction Solar Cells*, Journal of the American Chemical Society, 2008, **130**(29):p. 9224-9225.

[35] L. Yu, B. O'Donnell, M. Foldyna, P. Roca i Cabarrocas, *Radial junction*

amorphous silicon solar cells on PECVD-grown silicon nanowires, Nanotechnology, 2012, **23**:p. 194011.

[36] S. Misra, L. Yu, M. Foldyna, P. Roca i Cabarrocas, *High efficiency and stable hydrogenated amorphous silicon radial junction solar cells built on VLS-grown silicon nanowires*, Solar Energy Materials & Solar Cells, 2013, **118**:p. 90-95.

[37] X. Sun, T. Zhang, J. Wang, F. Yang, L. Xu, J. Xu, Y. Shi, K. Chen, P. Roca i Cabarrocas, L. Yu, *Firmly standing three-dimensional radial junctions on soft aluminum foils enable extremely low cost flexible thin film solar cells with very high power-to-weight performance*, Nano Energy, 2018, **53**:p. 83-90.

[38] S. Zhang, T. Zhang, Z. Liu, J. Wang, L. Yu, J. Xu, K. Chen, P. Roca i Cabarrocas, *Highly flexible radial tandem junction thin film solar cells with excellent power-to-weight ratio*, Nano Energy, 2021, **86**:p. 106121.

[39] S. Zhang, T. Zhang, Z. Liu, J. Wang, J. Xu, K. Chen, L. Yu, *Flexible and Robust 3D a-SiGe Radial Junction Near-Infrared Photodetectors for Rapid Sphygmic Signal Monitoring*, Advanced Functional Materials, 2022, **32**(2):p. 2107040.

[40] X. Sun, T. Zhang, L. Yu, L. Xu, J. Wang, *Three-dimensional a-Si/a-Ge radial heterojunction near-infrared photovoltaic detector*, Scientific Reports, 2019, **9**:p. 19752.

[41] L. Yu, P. Alet, G. Picardi, P. Roca i Cabarrocas, *An In-Plane Solid-Liquid-Solid Growth Mode for Self-Avoiding Lateral Silicon Nanowires*, Physical Review Letters, 2009, **102**:p. 125501.

[42] X. Song, T. Zhang, L. Wu, R. Hu, W. Qian, Z. Liu, J. Wang, Y. Shi, J. Xu, K. Chen, L. Yu, *Highly Stretchable High-Performance Silicon Nanowire Field Effect Transistors Integrated on Elastomer Substrates*, Advanced Sciences, 2022, **9**(9):p. 2105623.

[43] X. Song, R. Hu, S. Xu, Z. Liu, J. Wang, Y. Shi, J. Xu, K. Chen, L. Yu, *Highly Sensitive Ammonia Gas Detection at Room Temperature by Integratable Silicon Nanowire Field-Effect Sensors*, ACS Applied Materials & Interfaces, 2021, **13**(12):p. 14377-14384.

[44] J. Kim, D. Hansora, P. Sharma, J. Jang, J. Lee, *Toward practical solar hydrogen*

production - an artificial photosynthetic leaf-to-farm challenge, Chemical Society Reviews, 2019, **48**:p. 1908-1971.

[45] A. Fujishima, K. Honda, *Electrochemical Photolysis of Water at a Semiconductor Electrode*, Nature, 1972, **238**:p. 37-38

[46] S. Chae, S. Park, O. Joo, B. Min, Y. Hwang, *Spontaneous solar water splitting by DSSC/CIGS tandem solar cells*, Solar Energy, 2016, **135**:p. 821-826.

[47] S. Licht, B. Wang, S. Mukerji, T. Soga, M. Umeno, H. Tributsch, *Efficient Solar Water Splitting, Exemplified by RuO_2-Catalyzed AlGaAs/Si Photoelectrolysis*, The Journal of Physical Chemistry B, 2000, **104**(38): p. 8920-8924.

[48] O. Khaselev, J. Turner, *A Monolithic Photovoltaic-Photoelectrochemical Device for Hydrogen Production via Water Splitting*, Science, 1998, **280**(5362):p. 425-427.

[49] F. Abdi, L. Han, A. M. Smets, M. Zeman, B. Dam, R. Krol, *Efficient Solar Water Splitting by Enhanced Charge Separation in a Bismuth Vanadate-silicon Tandem Photoelectrode*, Nature Communications, 2016, **6**(15):p. 1600602.

[50] Y. Pihosh, I. Turkevych, K. Mawatari, J. Uemura, Y. Kazoe, S. Kosar, K. Makita, T. Sugaya, T. Matsui, D. Fujita, M. Tosa, M. Kondo, T. Kitamori, Photocatalytic generation of hydrogen by core-shell WO_3/$BiVO_4$ nanorods with ultimate water splitting efficiency, Scientific Reports, 2015, **5**:p. 11141.

[51] Y. Qiu, W. Liu, W. Chen, W. Chen, G. Zhou, P. Hsu, R. Zhang, Z. Liang, S. Fan, Y. Zhang, *Efficient solar-driven water splitting by nanocone BiVO4-perovskite tandem cells*, Science Advances, 2016, **2**(6): p. 1-8.

[52] William Ayers, US Patent 4,466,869 Photolytic Production of Hydrogen. *"Designing A Better Catalyst for Artificial Photosynthesis'"*.

[53] S. Reece, J. Hamel, K. Sung, T. Jarvi, A. Esswein, J. Pijpers, D. Nocera, *Wireless Solar Water Splitting using Silicon–Based Semiconductors and Earth Abundant Catalysts*, Science, 2011, **334** (6056):p. 645–648.

[54] M. Shaner, M. McDowell, A. Pien, H. Atwater, N. Lewis, *Si/TiO_2 Tandem-Junction Microwire Arrays for Unassisted Solar-Driven Water Splitting*, Journal of the Electrochemical Society, **163**(5):p. H261-H264.

[55] J, Yan, S. Wu, X. Zhai, X. Gao, X Li, *Si microwire array photoelectrochemical*

cells: Stabilized and improved performances with surface modification of Pt nanoparticles and TiO_2 *ultrathin film*, Journal of Power Sources, 2017, **342**:p. 460-466.

Chapter 2 Experimental setups and characterization

The goal of this thesis is to fabricate radial junction (RJ) silicon nanowire (SiNW) solar cells with a sufficiently high operating voltage to perform unassisted solar water splitting. A low-cost method, PECVD, has been chosen to grow SiNW solar cells composed of single, double, triple and quadruple junctions. Using the VLS method, the Sn catalyst droplet will determine the location of SiNW growth. To fabricate the SiNW solar cell, the Sn catalyst is first deposited on ZnO:Al/Ag/Corning glass (CG, standard 7059 borosilicate glass) substrate by thermal evaporation. Section 2.1 will introduce the Sn catalyst deposition. After that, the Sn/ZnO:Al/Ag/CG substrate is transferred into a PECVD chamber for SiNW growth, as described in section 2.2, and for thin film silicon layer deposition, explained in 2.3.1. Throughout, the in-situ ellipsometer will be used for investigating the state of the substrate and stack, especially during the SiNW growth. Section 2.3.2 will provide an overview of sputtering deposition, which is used twice during the fabrication: (1) before RJ SiNW solar cell growth, to coat the Corning glass with ZnO:Al, and (2) after the RJ SiNW solar cell growth, to deposit the ITO transparent contact. The solar cell is then measured in the dark and in the light using a AAA solar simulator, explained in section 2.4. Also in that section, measurements concerning the performance of water splitting setups are also explained.

A few other characterization techniques have been used to evaluate the state of the sample after certain steps. After the RJ SiNW solar cell growth and performance evaluation, the morphology of the RJ SiNW solar cell has been characterized by scanning electron microscopy (explained in section 2.4.4). The morphology of the evaporated catalyst has been characterized by atomic force microscopy (section 2.4.5). The thickness of a-Si:H thin film will be characterized by spectroscopic ellipsometry (section 2.4.6).

2.1 Catalyst deposition

2.1.1 Thermal Evaporator

The metal Sn used as catalyst for growing SiNWs is prepared using either a FL

400 Boc Edwards Auto 306 Evaporator, or a custom-made bell jar thermal evaporator. Figure 2.1 presents the evaporator and its internal components. The samples are fixed on the substrate holder and the catalyst pellet is loaded into the tungsten crucible. Different substrates - such as ZnO:Al/Ag/CG, ZnO:Al/CG, SnO_2:F/Soda lime glass, and c-Si wafer - are fixed on the substrate-holder. A quartz crystal microbalance (QCM) is used for in-situ measurement of the nominal thickness of the evaporated catalyst during evaporation, using the density of the metal, ρ, as set in the control panel. The system works once a base-pressure under 5×10^{-6} mbar is achieved. The current flowing through the crucible is then increased to heat and evaporate the catalyst metal. The QCM measures the thickness by measuring the change in the resonance frequency of a quartz crystal [1]. The thickness change Δ_h can be expressed as:

$$\Delta_h = \frac{\Delta_m}{\rho s}, \tag{2-1}$$

Where Δ_m is the change in mass of deposited material, ρ is the material density, and s is the quartz surface area. Δ_m follows the equation:

$$\Delta_m = \frac{-c\left(\frac{1}{f_0^2}\right)}{\Delta f^2}, \tag{2-2}$$

where c is a constant of the quartz crystal, f_0 is the intrinsic frequency of the quartz crystal and Δf is the frequency variation. When the value of Δ_h reaches the desired one, the shutter is closed to stop the evaporation, and the current is turned down to zero.

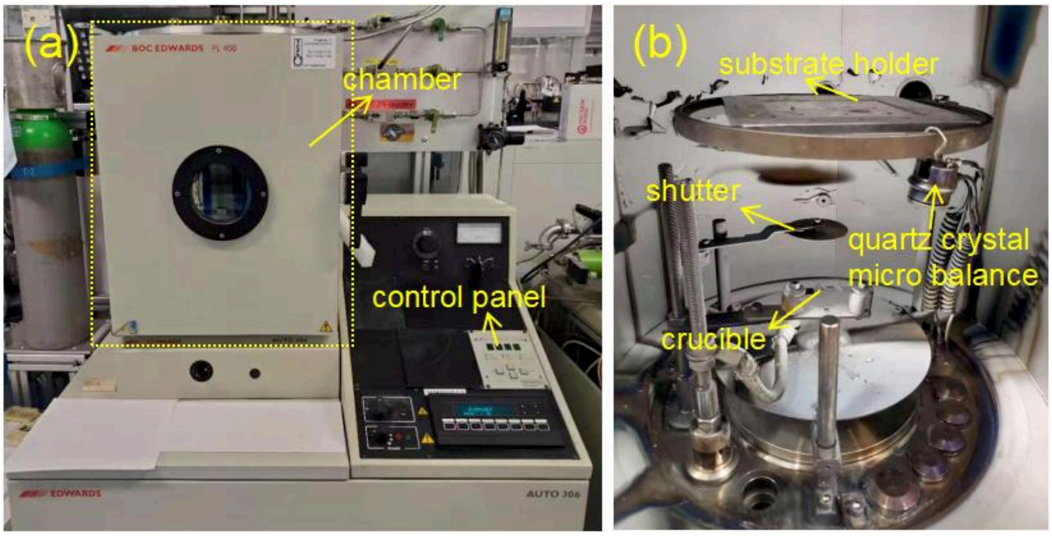

Figure 2.1 Photographs of thermal evaporator (a) Boc Edwards Auto 306 Evaporator FL 400. (b) shows internal compositions.

The density of SiNWs can be controlled by the amount of Sn catalyst. The minimum measurable thickness of Sn for the thermal evaporator is 0.1 nm due to available digits on the display. In order to deposit less Sn catalyst, two workarounds can be used. First, we can change the compensation factor (nominal vs actual) to some value "n", for example, by turning or moving the substrate holder. Thus, for a nominal thickness of 0.1 nm Sn as shown on the control panel, the thickness of the evaporated metal can be reduced to 0.1/n nm. By doing so, the deposited Sn can be controlled for thicknesses below 0.1 nm, as long as the evaporation rate is slow. Another method to gain more precision is to change the metal density ρ. If we put a smaller value $\rho_1=\rho/n$ in the control panel, as the control panel shows 0.1 nm, the actual nominal thickness is 0.1/n nm. Using these workarounds, we can controllably achieve a nominal thickness of Sn catalyst below 0.1 nm.

2.2 Plasma-enhanced chemical vapor deposition

In this work, plasma-enhanced chemical vapor deposition (PECVD) is used for growing the SiNW solar cells, as was done in the work of Tang [2] and Wang [3]. Plasma is an ionized gas, in our case, created by applying an RF voltage to two electrodes in a chamber at low pressure. As the RF power is turned on, an electric field is generated between the two electrodes which causes the residual electrons to be accelerated to the top and bottom electrodes. These initial electrons are produced by particles ionized by existing photoelectrons. Electrons with enough kinetic energy can ionize and dissociate gas molecules, and the newly generated electrons will ionize more gas molecules, and a chain reaction begins. As the level of ionization builds up to a new steady state value, the medium changes from gas to plasma (conductive).

Only the electrons can respond to the instantaneous electric field produced by the applied voltage, because of their higher mobility and lower mass compared to other charged species (10 μs). The electron plasma frequency and ion plasma frequency can be defined as [4]:

$$\omega_{\mathrm{e}} = q\sqrt{\frac{n_e}{m\varepsilon_0}}, \tag{2-3}$$

$$\omega_{\mathrm{i}} = q\sqrt{\frac{n_i}{\mathrm{M}\varepsilon_0}}, \tag{2-4}$$

Where q is the charge, n_e is the electron density, n_i is the ion density, m is the mass of electron, M is the mass of the ion and ε_0 is the vacuum permittivity. Species can only respond at frequencies below their plasma frequency. The excitation frequency of the plasma is typically in the range of

$$\omega_i << \omega << \omega_e, \tag{2-5}$$

In the capacitively-coupled plasma (CCP) process, the central part of discharge is quasi-neutral. However, close to the electrode and reactor walls, quasi-neutrality no longer exists. This area has an excess of ions, and is named the plasma sheath, across which a DC voltage drop builds up. Under the action of this DC electric field, positive ions are accelerated to the substrate and bombard the substrate.

A Plasma Enhanced Chemical Vapor Deposition (PECVD) process consists of creating a plasma (in our case, using a radio frequency voltage), which in turn dissociates a gas containing atoms of the desired film components, which stick to the local area [5]. Compared to the conventional CVD method to grow films, one of the advantages of PECVD is that reactions can be promoted at lower temperatures and avoid substrate damage. Moreover, a wide range of precursors can be used in PECVD technique, because of the improved reactivity of the precursors. In this thesis, the SiNW solar cells are grown in a PECVD reactor which is named Plasfil, as shown in Figure 2.2. Its schematic is presented in Figure 2.3.

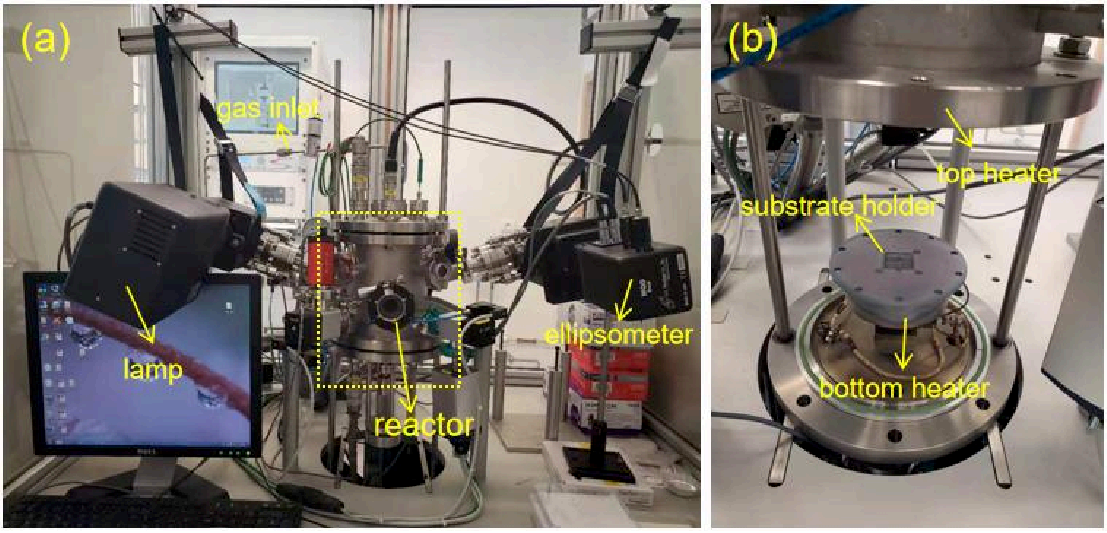

Figure 2.2 PECVD Plasfil (a) front view and (b) inside view.

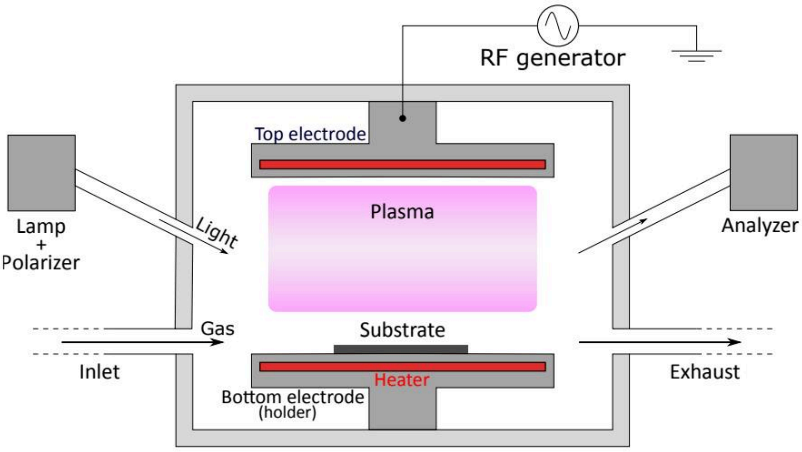

Figure 2.3 Schematic of Plasfil reactor, extracted from [6].

Plasfil is a capacitively-coupled plasma (CCP) chemical vapor deposition reactor. Plasfil has two electrodes, the top electrode is a radio frequency powered electrode (13.56 MHz) and the bottom is grounded. The distance between electrodes can be changed from 10 mm to 40 mm. The chamber containing these electrodes is linked with a pumping system and a precursor gas inlet. The gases of H_2, SiH_4, $(CH_3)_3B$ (TMB for p type doping), SiH_4, GeH_4, N_2 and Ar are available. An in-situ ellipsometer is used for monitoring the deposition process. Both the RF electrode and substrate holder are heated. The top electrode is connected to the gas injection system and the bottom electrode works as the substrate holder. Before usage, the reactor must be pumped to a vacuum level below 5 × 10^{-5} mbar, and the working process pressure is in the range of 0.1 to 2 mbar. The pressure of the gases in the chamber is controlled by a butterfly valve. The flow of the gases is controlled by the software in the control panel.

The temperature of each electrode in Plasfil can be controlled independently. The top heater nominal temperature can be changed from room temperature to 220 °C, and the bottom heater nominal temperature can be changed from room temperature to 650 °C. The temperature of the substrate is monitored with thermocouples, but a notable discrepancy has been noted between the displayed nominal temperature of the heater and the real temperature of the sample, which can be more accurately measured with a PT100 sensor probe connected to the substrate [7]. Figure 2.4 presents the relationship between the nominal temperature and substrate holder temperature of Plasfil. A PT100 sensor was placed on the surface of a piece of CG on the substrate holder to measure the temperature. Above 100 °C, the calibrated substrate temperature is always lower than the set substrate temperature.

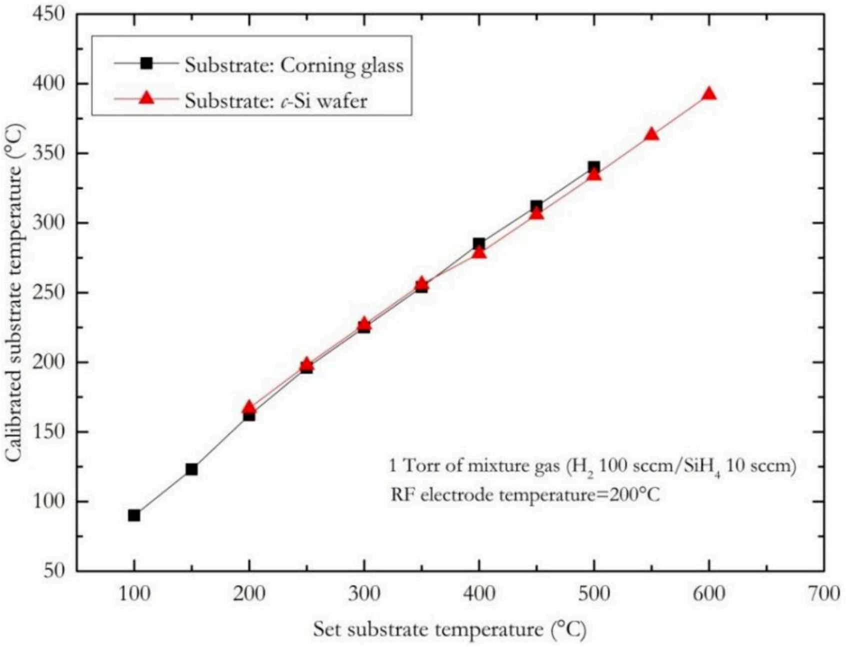

Figure 2.4 Temperature of sample measured by thermocouple as a function of nominal temperature of heater in Plasfil PECVD chamber, extracted from [7].

2.3 Solar cell fabrication

2.3.1 Overview of process of SiNW growth and solar cell fabrication

In this thesis, we fabricated a-Si:H planar and SiNW based solar cells on ZnO:Al/Ag/ Corning glass (CG) substrates or commercial fluorine doped SnO_2 (FTO) substrates. The steps for SiNW solar cell fabrication on ZnO:Al/Ag/CG are shown in Figure 2.5. The Ag back reflector contact is deposited by sputtering, and is present in order to increase light absorption in the solar cell due to better reflection at the back contact [8-10]. The ZnO:Al is also then sputtered on the Ag reflector. The ZnO:Al is used as the back contact for solar cell and to protect the Ag from the plasma. As a first step, the Ag and ZnO:Al layers are deposited on 1 inch×1 inch CG substrates by sputtering in an Alliance Concept DP 650 RF magnetron sputtering machine. Compared to FTO or ITO, ZnO:Al is more stable in an H_2 plasma [11], which is important for subsequent steps.

After ZnO:Al deposition, Sn is deposited on the substrate by thermal evaporation (as previously described). The substrate is then transferred into the PECVD chamber. In the PECVD chamber, firstly, a H_2 plasma is used to first reduce the SnO_2 layer formed on the evaporated Sn (upon its exposure to air during the transfer from evaporator to PECVD chamber) to Sn, and then to form Sn droplets.

After the H_2 plasma treatment, the PIN junction fabrication process steps are presented in Fig. 2.5. H_2, TMB and SiH_4 are used for growing p type c-SiNWs, according to the VLS growth method [12-14]. Then, the p layer, i layer and n layer are consecutively deposited on the c-SiNWs by changing the doping gases. The intrinsic layer and doped layer are established on the p type c-SiNWs to form a PIN junction [15-17].

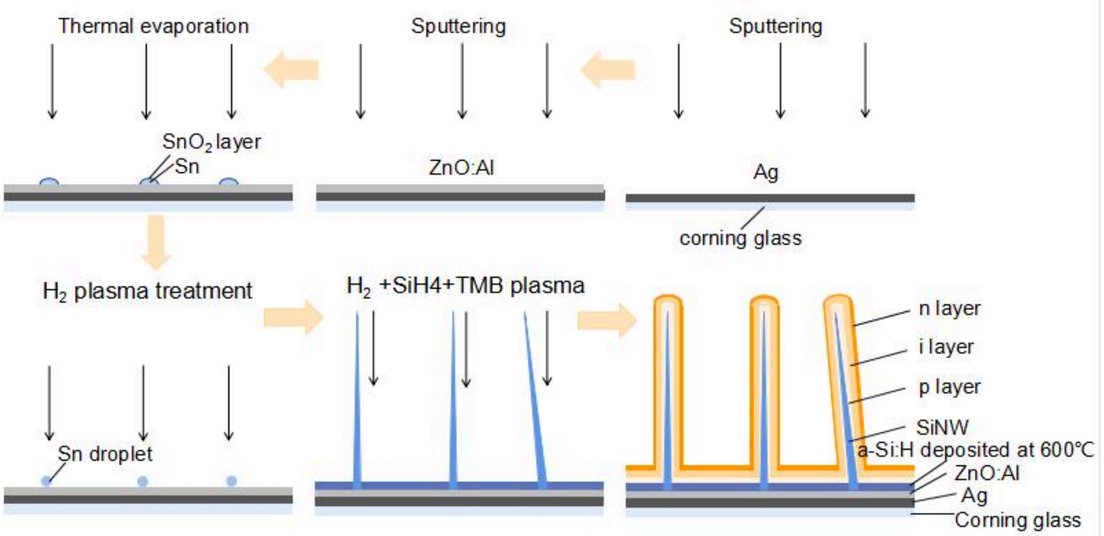

Figure 2.5 The fabrication process of SiNW radial junction solar cells with Sn catalyst deposited by evaporation.

Another way to obtain a Sn catalyst source to grow SiNW is by reducing it from a FTO (SnO_2:F) layer using a H_2 plasma treatment [18-20], which will be used in chapter 5. The steps for growing SiNW starting from a FTO substrate are presented in Figure 2.6. First, a H_2 plasma is used for reducing and forming the Sn droplet from the FTO layer. Detailed parameters concerning the temperature evolution of one sample during SiNW radial junction solar cell fabrication is shown in Figure 2.7. The nominal temperature for H_2 plasma, c-SiNWs growth and a-Si:H PIN junction deposition are 250, 600, and 220 °C, respectively. The time of the whole process of SiNW single radial junction growth is ~2 h.

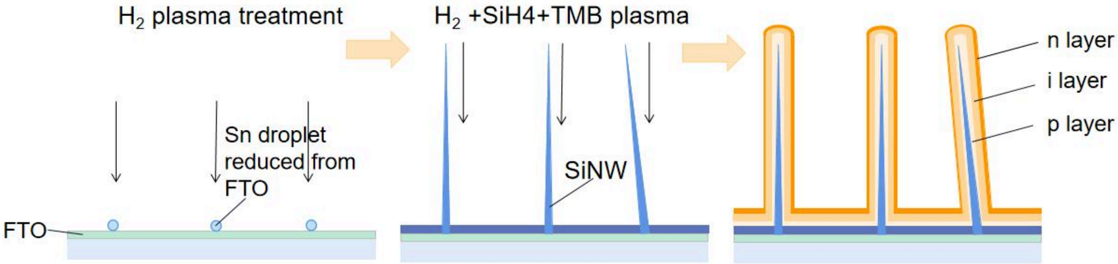

Figure 2.6 The fabrication process of SiNW radial junction solar cells using FTO as Sn source.

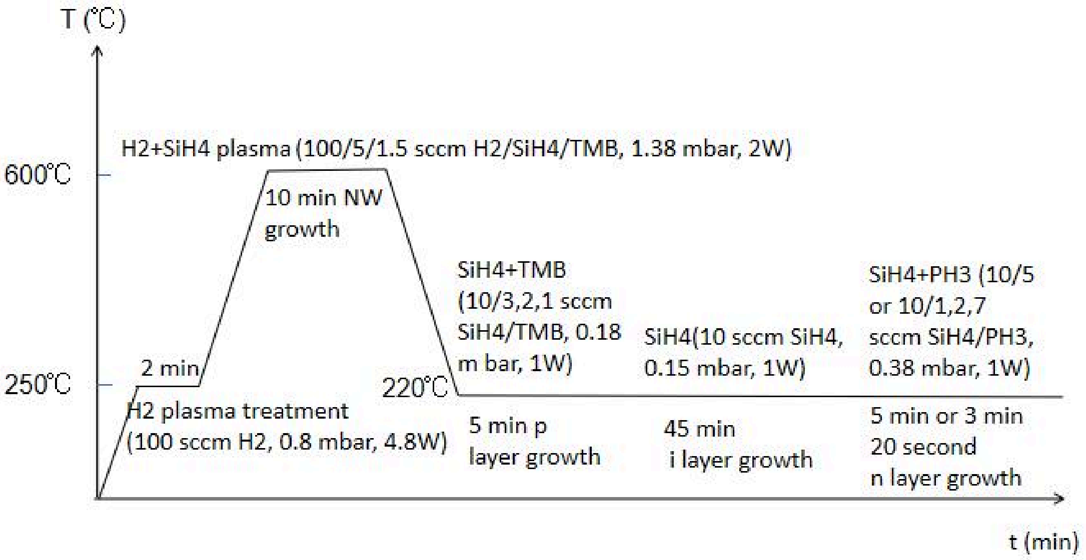

Figure 2.7 Chronogram for growing SiNW radial junction solar cell.

Figure 2.8 shows an example of SiNWs grown from nominal Sn catalyst of thickness 0.2 nm for 10 min with gas flow of H_2, SiH_4 and TMB. The length of longest SiNW is around 400 nm to 500 nm. Straight and long conical SiNWs are obtained. At the tip, some SiNWs still have tiny Sn catalyst droplets left, which can be removed by H_2 plasma treatment. Some SiNWs do not have Sn droplets, indicating that the catalyst has been consumed while the nanowire was growing. After the catalyst is consumed, an a-Si:H shell will be deposited on the c-SiNWs. Because of TMB gas doping, in this case, the c-SiNW is p type [21].

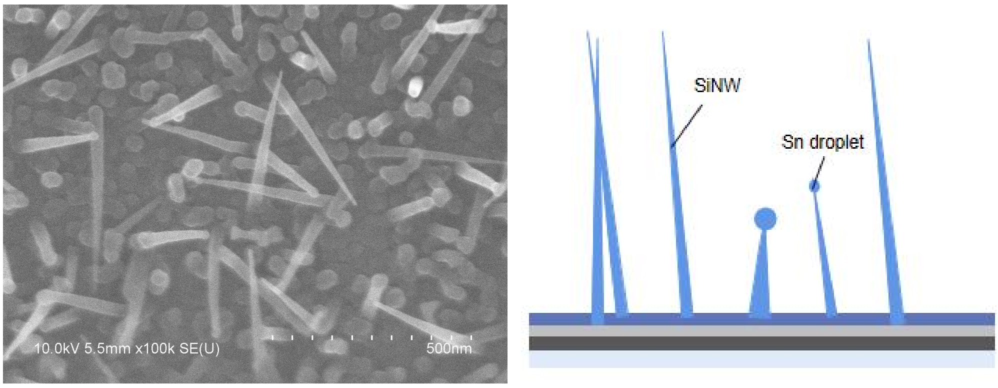

Figure 2.8 SEM images and schematic figure of SiNWs.

Indium Tin Oxide (ITO) thin films are widely used as transparent conducting oxides for solar cells [22-24]. They have good conductivity and optical transparency. After the solar cell growth in PECVD reactor, the samples are transferred to a sputtering machine for depositing ITO as the top transparent contact of solar cell.

2.3.2 Contact sputtering

In this thesis, the Alliance Concept DP 650 RF magnetron sputtering machine (as shown in Figure 2.9) was used to prepare the contacts for solar cells. Sputter deposition is a physical vapor deposition technique by which atoms in a solid target are knocked out by high-energy ions, generated by an Ar plasma [25]. The advantage of sputtering is that films of high melting point materials can be prepared at low temperatures and at very high rates.

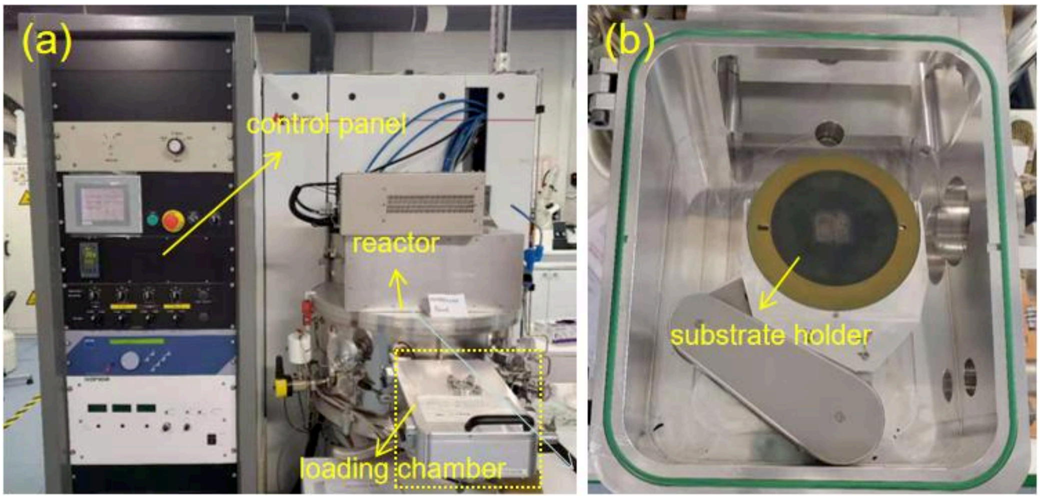

Figure 2.9 Photograph of sputtering (a) Alliance Concept DP 650 RF magnetron sputtering and (b) details of the load lock.

As previously described, the bottom and top contacts of our solar cells are both deposited by sputtering. For the bottom contact, Ag is used as the back reflector contact [26-28]. The Ag is first sputtered on CG substrates with Ar gas in flow rate of 43 sccm and at a RF power of 50 W for 3 min at room temperature. In order to improve reflection at the back side of solar cell, a low refractive index ZnO:Al layer is always deposited between the solar cell and the Ag reflector [28-31]. The ZnO:Al layer is deposited on Ag with Ar gas flow rate of 30 sccm and a RF power of 250 W for 3 min at room temperature. These two back contact layers (Ag sputtering and ZnO:Al sputtering) are deposited in one process, without vacuum break.

Sputtering is also used to deposit the front, ITO contact. Before ITO deposition, a shadow mask is placed on the top of the solar cell, so that the area of the solar cell is determined by the hole in the mask. Plasma parameters for ITO sputtering are 43 sccm of Ar gas and 3 sccm of H_2 gas at temperature of 180 °C and a pressure of 4.4×10^{-3} mbar and RF power of 200 W for 7 min. Under these conditions, the thickness of ITO deposited on CG glass is around 240 nm. As shown in figure 2.10, after ITO deposition through the shadow mask, we have 15 small cells with a diameter of ~2 mm diameter and 6 large cells with diameter of ~4 mm on a 1-inch×1-inch substrate. Some small Ag spots are placed on the top of ITO using silver paste to provide a good electrical contact between the probes and ITO during light and dark J-V measurements. The corner of the substrate is scraped using a diamond pen in order to expose the bottom contact and then covered with silver paste for good contact while measuring the solar cell.

Figure 2.10 Photographs of solar cell before and after ITO deposition through shadow mask (16 cells with ITO pad area of 0.0314 cm^2, 6 cells with ITO pad area of 0.125 cm^2).

Figure 2.11 shows SEM images of radial junction solar cells with and without their ITO top contacts (as well as a schematic illustration of both cases). Note that the orientation of the nanowires is random. The diameter of the radial junctions is around 220 nm. After ITO top contact sputtering, the diameter becomes around 360 nm. Comparing Figure 2.8 with Figure 2.11, one can notice that the radial junction density is much lower than the initial density of SiNWs. This phenomenon is explained by the fact that the shorter NWs get buried during the subsequent PECVD steps.

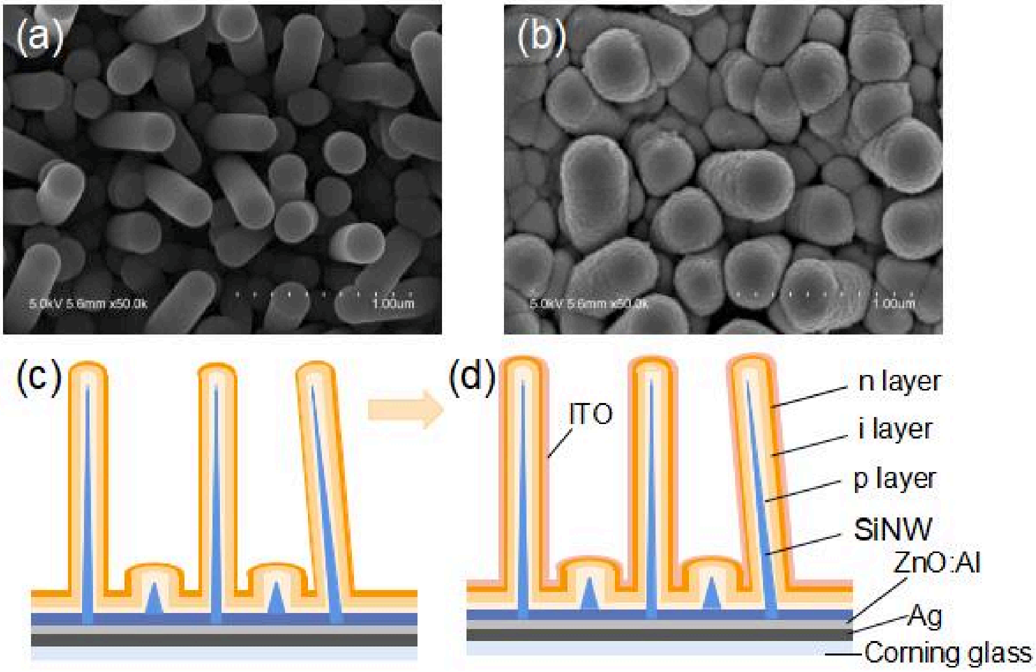

Figure 2.11 SEM images of (a) radial junction (a-Si:H PIN junction is coated on the c-SiNW of Figure 2.8); (b) after ITO sputtering; (c) schematic figure of SiNW radial junction corresponding to (a); (d) schematic figure of SiNW radial junction with ITO contact corresponding to (b).

2.4 Characterization

2.4.1 Thickness measurements

To know the thickness of the sputtered contacts, a stylus profilometer Dektak 150 is used. The stylus is fixed on the core of an electromechanical sensor named a linear variable differential transformer. The core will move vertically as the stylus moves vertically. An inductance change in the coil is induced by its movement. This is recorded by a resistor bridge excited by an oscillator. As presented in Figure 2.12, the sample is placed on a moving table that can be displaced over larger distances. Using an optical assembly and a camera, one can focus on and visualize the tip and the sample to ensure an accurate measurement position [32].

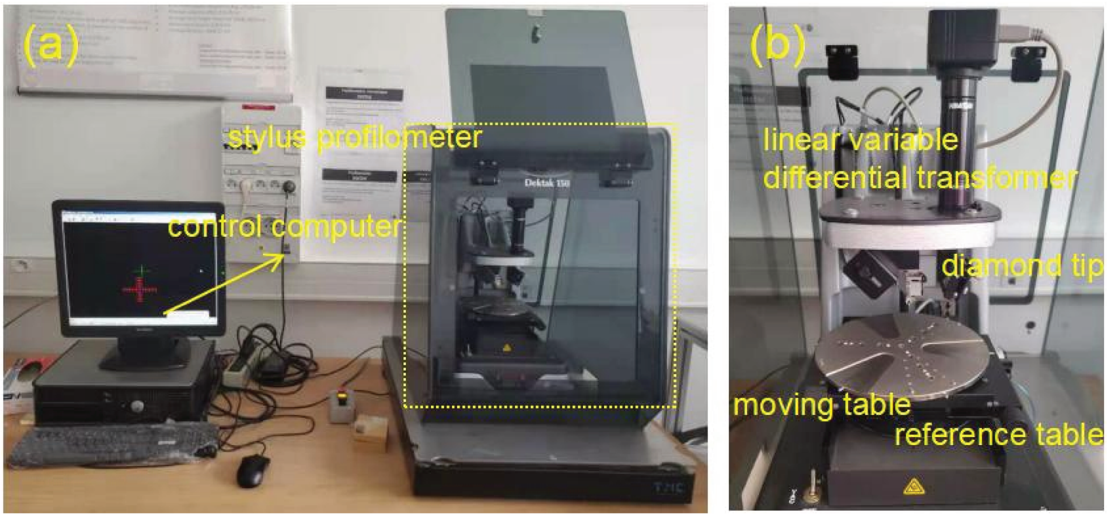

Figure 2.12 Photograph of (a) stylus profilometer Dektak 150 and (b) its interior structures. (b) provides a closer view of the dashed line part of (a).

After sputtering Ag and ZnO:Al bottom contacts on the CG substrates, the thicknesses of these layers has been measured by the stylus profilometer, as shown in figure 2.13 and 2.14. As the diamond tip moved from deposited layer to the CG area, there is jump in the profile, corresponding to a change in thickness. During deposition, we aimed for a thickness of Ag of ~70 nm and a thickness of ZnO:Al of ~100 nm, and these two thicknesses are approximately confirmed.

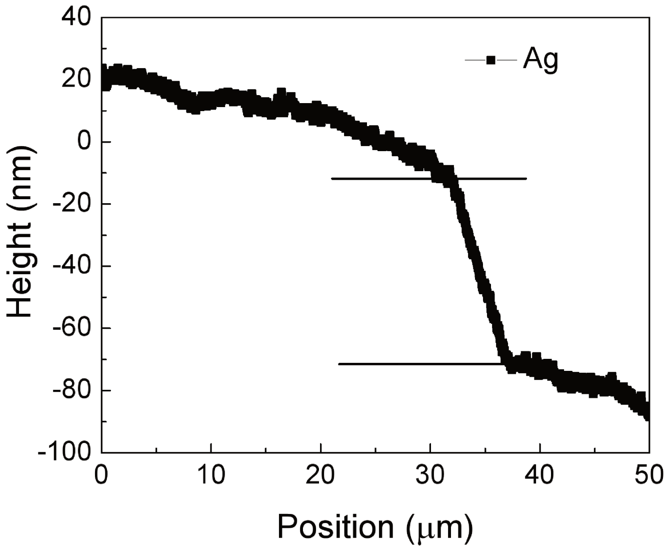

Figure 2.13 Profile of Ag deposited on CG by sputtering.

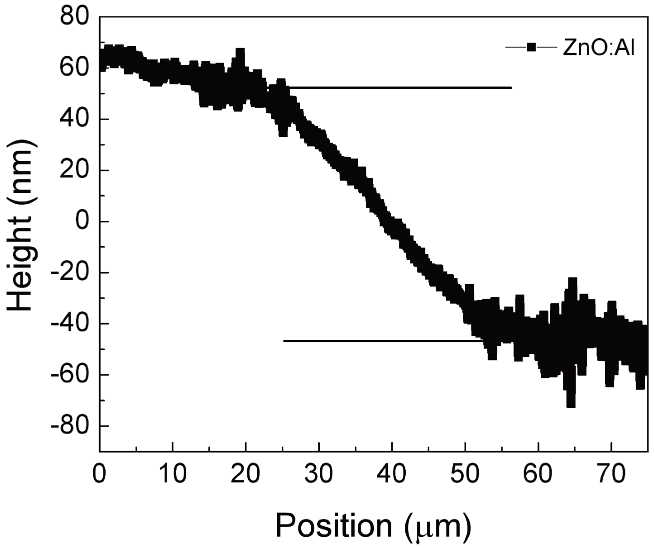

Figure 2.14 Profile of ZnO:Al deposited on CG by sputtering.

2.4.2 J-V characterization

To investigate the performance of solar cells after fabrication, measurement of current density vs. applied voltage (J-V) measurements are the important tool to quantify the various parameters of solar cells. A solar simulator Newport Oriel Sol3A was used as light source and a Keithley 2460 Source Meter is used for measuring the J-V characteristics of the solar cell under one sun illumination (AM 1.5, 100 mW/cm^2), as presented in Figures 2.15 and 2.16. Before measurement, we preheat the solar simulator for 30 min until the power density produced by the lamp remains stable. Afterwards, we set the power density to the standard 100 mW/cm^2. The light is shined through the top contact on the solar cell, and a sweeping voltage is applied while the current flow through the solar cell is measured. Figure 2.17 compares the J-V characteristic of a SiNW solar cell under dark and light illumination. V_{OC} is the voltage when the current density is zero, also called open-circuit voltage. J_{SC} is the current density when the applied voltage is zero, also named short-circuit current. P_{max} is the maximum output power, V_{MPP} is the voltage at the point of P_{max}, J_{MPP} is the current density at the point of $P_{max.}$

The fill factor (FF) is related to V_{max}, J_{max}, V_{OC} and J_{SC}, FF is defined as:

$$FF = \frac{V_{MPP} J_{MPP}}{V_{oc} J_{sc}}. \qquad (2\text{-}6)$$

The power conversion efficiency (PCE) is defined as the maximum output power divided by the incident power from light (100 mW/cm^2, AM 1.5):

$$PCE = \frac{|P_{\max}|}{P_{in}} \times 100\%. \qquad (2\text{-}7)$$

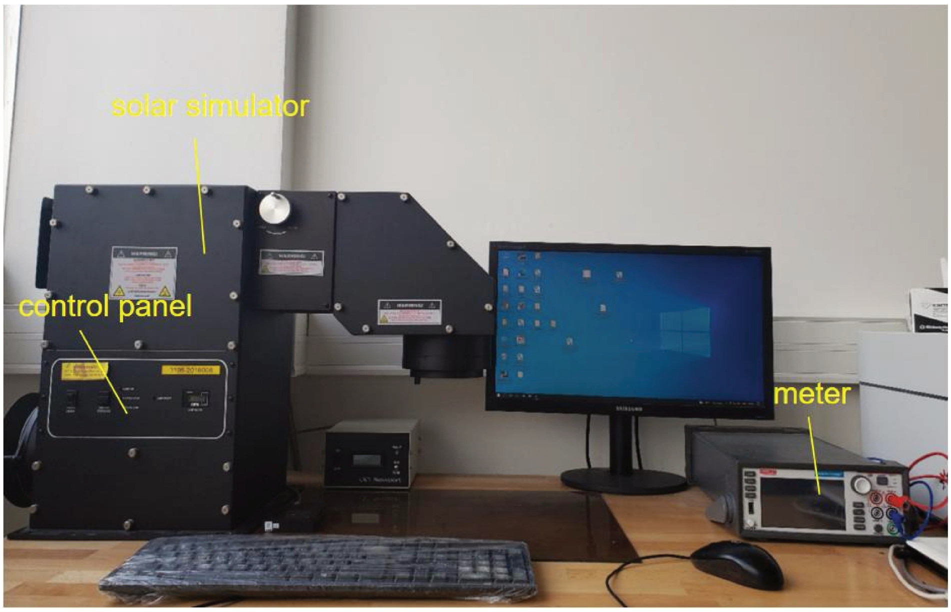

Figure 2.15 Photograph of equipment for measuring solar cell.

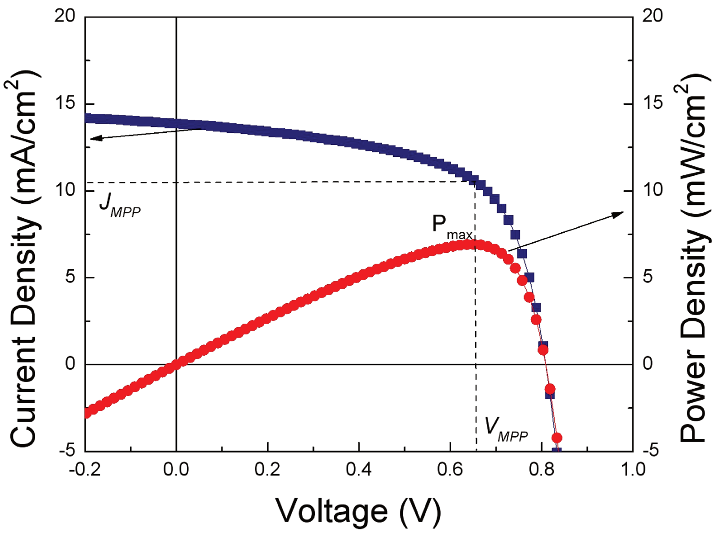

Figure 2.16 J-V curve of SiNW RJ solar cell measured under one sun (AM 1.5, 100 mW/cm^2).

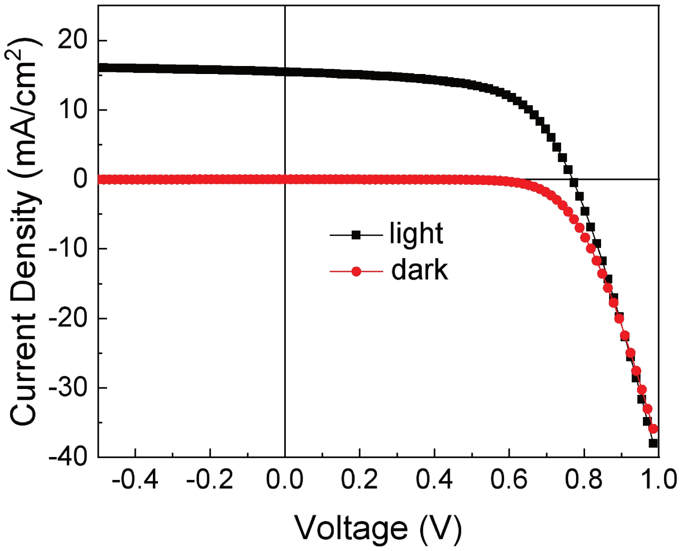

Figure 2.17 Current density-voltage characteristic of SiNW solar cell in the dark and light illumination (AM 1.5, 100 mW/cm^2).

The simplest model of a solar cell is a diode described by the Shockley diode equation:

$$I(V) = I_0[\exp(\frac{qV}{nkT}) - 1], \tag{2-8}$$

where I is the current which goes through the diode, q is the fundamental charge constant, V is the voltage across the diode, I_0 is the dark saturation current, n is the diode ideality factor, k is the Boltzmann constant, and T is the temperature in Kelvins. When V is above 50 mV at room temperature, the equation can be simplified as:

$$I(V) = I_0 \exp(\frac{qV}{nkT}). \tag{2-9}$$

After taking the logarithm on both sides of the equation, the equation becomes:

$$\ln(I) = \frac{qV}{nkT} + \ln(I_0). \tag{2-10}$$

From the plots of ln(I) as a function of V, the ideality factor n can be calculated from the slope, and the value of I_0 can be determined by the intercept from (2-3). The value of I_0 can be connected to the carrier recombination in the solar cell, and it provides the information on the quality of a solar cell. A low I_0 value represents a reduced recombination. Typical values of the saturation current J_0 (I_o divided by the area of the device) for a-Si:H solar cells is of the order of 10^{-10} mA/cm^2, the typical J_0

for c-Si is 10^{-15} mA/cm^2, but the typical J_0 for RJ is at the level of 10^{-6} mA/cm^2.

While the solar cell is under illumination, the I-V characteristic of the diode can be superimposed to a photo-generated current I_{ph} as follows:

$$I = I_{ph} - I_0[\exp(\frac{qV}{nkT}) - 1]. \tag{2-11}$$

In this model, the series resistance (R_S) and shunt resistance (R_{SH}) should be taken into account. The more realistic equivalent circuit with R_S and R_{SH} for solar cell under illumination is presented in Figure 2.18. The equation can be expressed as:

$$I = I_{ph} - I_0[\exp(\frac{q(V + IR_S)}{nkT}) - 1] - \frac{V + IR_S}{R_{SH}}. \tag{2-12}$$

R_S and R_{SH} can be obtained from fitting the curve of dark I-V. R_S originates from the bulk resistance of devices, contact resistance, and wire resistance. R_S does not impact the V_{OC} (as it only affects the solar cell performance when a photocurrent is going through) and only impacts the J_{SC} of a solar cell in extreme cases. The R_{SH} represents the current leakage of a device. R_{SH} is reduced in the presence of defects, junction edges, and pinholes.

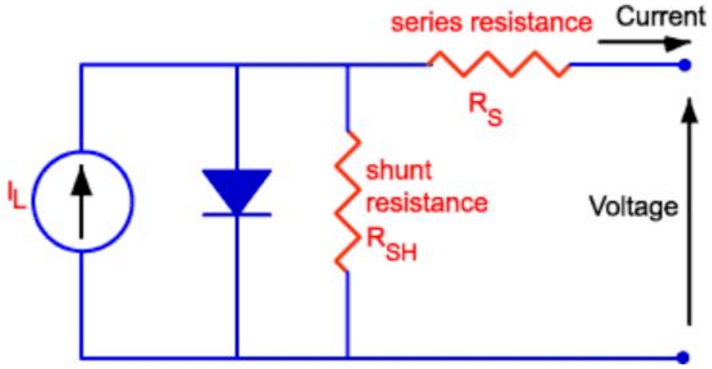

Figure 2.18 Equivalent circuit with parasitic resistance R_S and R_{SH} for solar cell device under illumination, from [33].

As shown in figure 2.19, the real R_S and R_{SH} can be obtained from the slope of fitting curves of sloping part and gentle part in figure 2.19 (a). Figure 2.19 (b) gives an example of fitting curve for ideality factor n and reverse saturation current density I_0 as (2-10).

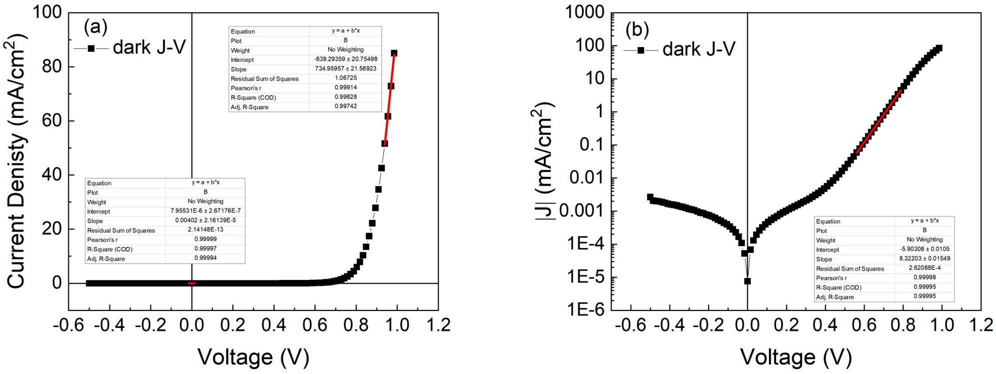

Equation	y = a + b*x
Plot	B
Weight	No Weighting
Intercept	-639.29359 ± 20.75498
Slope	734.95957 ± 21.56923
Residual Sum of Squares	1.06725
Pearson's r	0.99914
R-Square (COD)	0.99828
Adj. R-Square	0.99742

Equation	y = a + b*x
Plot	B
Weight	No Weighting
Intercept	7.95531E-6 ± 2.67176E-7
Slope	0.00402 ± 2.16139E-5
Residual Sum of Squares	2.14148E-13
Pearson's r	0.99999
R-Square (COD)	0.99997
Adj. R-Square	0.99994

Equation	y = a + b*x
Plot	B
Weight	No Weighting
Intercept	-5.90308 ± 0.0105
Slope	8.32203 ± 0.01549
Residual Sum of Squares	2.62088E-4
Pearson's r	0.99998
R-Square (COD)	0.99995
Adj. R-Square	0.99995

Figure 2.19 (a) Typical dark J-V curve of SiNW solar cell, fit for R_s is shown at highest value of current, and fit for R_p around V=0, both in red. (b) Typical dark J-V curve of SiNW solar cell (semilog plot). Fit for section of curve where J_0 and n are extracted is shown in red.

2.4.3 Linear sweep voltammetry and chronoamperometry

The performance of catalysts in an electrolyte has been evaluated by the linear sweep voltammetry (LSV) method using a Keithley 2460 Source Meter. The scan range is from 0 V to 2.5 V or 3 V with scan rate of 1 V/s, 25 mV/s or 5 mV/s. A 100 nm thick Pt film deposited on CG substrate is used as the reference electrode. Ti layer (10 nm) was deposited between CG and Pt to prevent the Pt from peeling off. The electrolyte used is 0.1 M KOH (pH=13.2, 20 mS/cm) or 1 M KBi (pH=9.2, 26 mS/cm). The distance between anode and cathode can be varied between 1, 2 or 5 cm. In Figure 2.20, the LSV curves shows the relationship between voltage and current density while water splitting is occurring. Chronoamperometry is an electrochemical test method. The current response is measured as a function of time after a single or double voltage step is applied to electrode, which can be used to evaluate the stability of PEC cell.

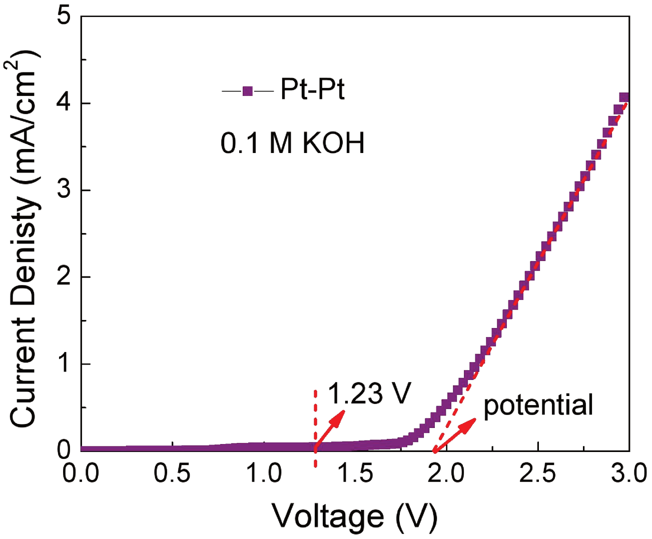

Figure 2.20 LSV curve of symmetrical Pt-Pt thin film electrodes with distance of 5 cm for water splitting in 0.1 M KOH electrolyte solution.

2.4.4 pH meter

The pH values (the negative of the log of the hydrogen ion concentration) of the electrolyte solutions mentioned above have been measured using an Atlas Scientific ENV-40 pH meter as shown in Figure 2.21, which uses the potentiometric method. The main components of the pH meter are a glass electrode and a reference electrode [34-36]. The glass electrode is sensitive to pH, but the potential of the reference electrode remains stable. Two electrodes of the pH meter are placed in the same solution together and form a galvanic cell. The potential of the galvanic cell is the sum of the potential of the glass electrode and the reference electrode. Therefore, if the temperature remains constant, changes in the potential of the galvanic cell are only related to the potential of the glass electrode, and the potential of the glass electrode depends on the pH value of the solution to be measured. Hence, through the change of potential measurement, the pH value of the solution can be obtained.

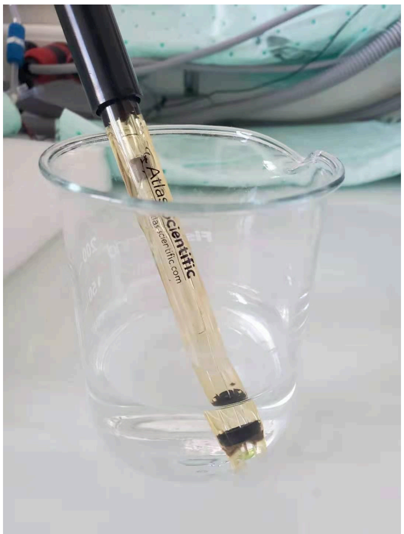

Figure 2.21 Photograph of pH meter.

2.4.5 Scanning electron microscopy

After PECVD growth and solar cell measurement, the size, density and morphology of SiNWs is investigated using a Hitachi S800 field emission scanning electron microscope (SEM). SEM focuses a high energy electron beam on the sample to obtain its surface topography [37]. In secondary electron imaging mode, the electron beam rapidly scans the substrate surface and produces secondary electrons from surface atoms. Therefore, the surface morphology of the sample can be displayed very effectively. However, there is no obvious dependence between the yield of secondary electrons and atomic number, therefore it cannot be used for compositional analysis. In the back-scattered electron imaging mode, back-scattered electrons are collected, which are a fraction of the incident electrons that have bounced off the nucleus of a solid sample within a depth range of several hundred nanometers from the surface of the sample. Because the back-scattered electron yield increases with atomic number, it can be used both for morphology analysis and for qualitative compositional analysis. Many forms of solid samples (block, film, particle) of different sizes can be directly observed in vacuum by SEM.

Comparing with optical microscopy, SEM provides much greater resolution; it can magnify images by 80000 times and achieve a resolution of 1~2 nm, in theory. The real resolution depends on the material charging effects and the size of the electron beam. The electron beam in the SEM used can be accelerated from 0.5 to 30 keV. We have used 5~10 keV for studying our solar cells grown on ZnO:Al/Ag/CG and FTO substrates. Higher acceleration voltages lead to serious charging effects, and the quality of the images deteriorates. We can count the number of NWs and get the NW diameter as shown in figure 2.23.

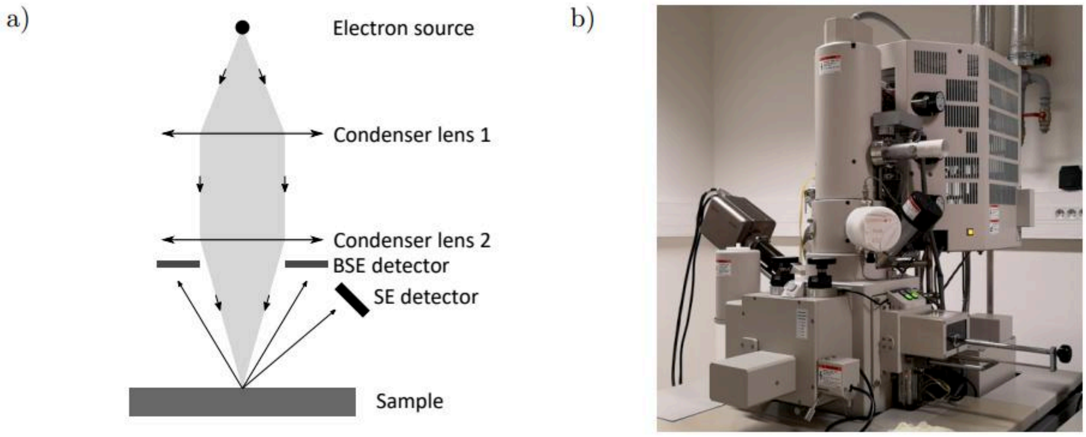

Figure 2.22 (a) Schematic of SEM; (b) Photograph of SEM Hitachi S-4700 [6].

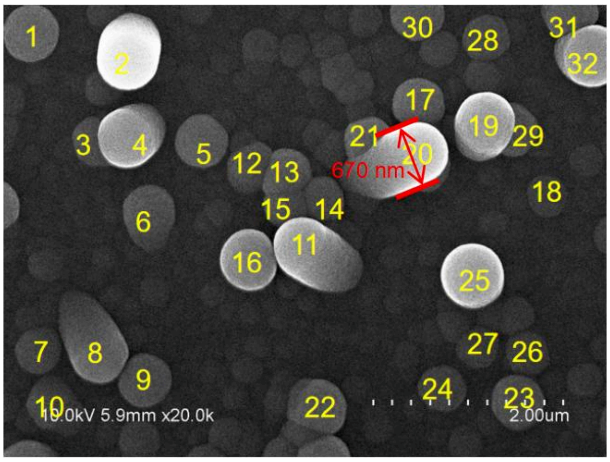

Figure 2.23 SEM image of RJ solar cell.

2.4.6 Atomic force microscopy

The morphology and roughness of the samples is evaluated using a Bruker Dimension Icon atomic force microscope (AFM) as shown in figure 2.24. The principle of AFM is based on the forces between a microprobe and surface atoms, which increase rapidly when the distance decreases below a certain value. Therefore, the height of the sample surface can be directly calculated by the force on the microprobe, so as to obtain information about the sample surface topography. Figure 2.25 shows the AFM image of 2 nm Ni (nominal thickness) deposited on c-Si wafer. We can see that the diameter of Ni particle is less than 10 nm.

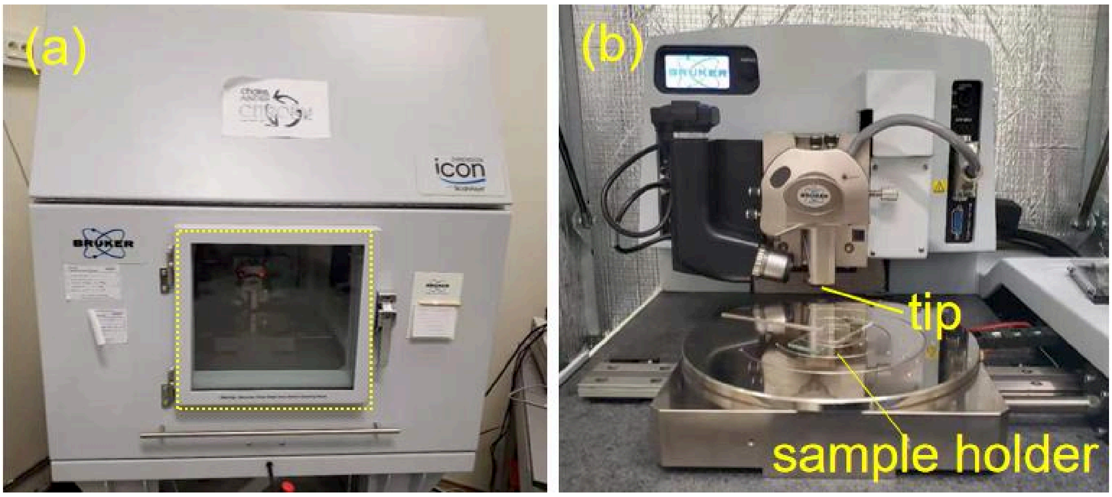

Figure 2.24 Photograph of (a) atomic force microscope Bruker Dimension Icon and (b) its interior structures. (b) is the internal structure of the dashed line part of (a).

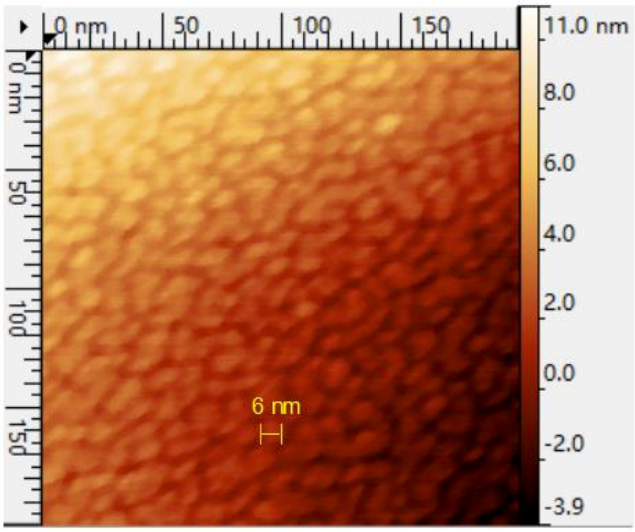

Figure 2.25 AFM images of a 2 nm Ni (nominal thickness) deposited on c-Si wafer.

There are four operating modes for AFM: contact mode, non-contact mode, tapping mode, and phase shift mode [38]. For contact mode, the force perceived is due to exchange forces due to the Pauli exclusion principle of electrons (being fermions). This method can stably obtain the high-resolution surface micro-topography of samples. The disadvantage of this method is that when a soft sample with low elastic modulus is analyzed, the sample surface will be deformed or even scratched under the action of the AFM tip. The tip and the sample contact and slide over each other, and it is easy to wear down the tip of the probe or even damage the surface. For the non-contact method, the force measured is the attractive force dominated by van der Waals forces, and the distance between tip and sample is about 5-20 nm. In non-contact mode, the tip will not deform the sample surface and will not suffer wear, but the sensitivity of non-contact mode is lower.

In the tapping mode, the system uses a small piezoelectric ceramic element driven micro cantilever vibration. The vibration frequency is chosen to be higher than the mechanical resonance frequency of the probe to drive the following signal amplification effect. When the probe (undergoing forced vibrations) approaches the sample surface, a weak attraction occurs that will decrease the probe's resonant frequency. As the driving frequency was already greater than the non-interacting resonant frequency, the amplitude of oscillation will decrease. Thus, changes in the height of the sample surface can be observed by detecting changes in the amplitude using a laser. The method effectively overcomes the disadvantages of scratching the sample by the tip and the influence of friction when the tip is dragged over the sample.

The phase shift mode is an important extension of the tapping mode. The phase shift mode is based on the detection of the change of the phase angle between the signal source driving the vibration of the micro-cantilever probe and the actual vibration of the probe.

2.4.7 Spectroscopic ellipsometry

In order to determine a sample's surface roughness, thickness, material composition and optical constants, we use spectroscopic ellipsometry, which is a non-destructive and fast optical measurement that can be applied either in-situ or ex-situ. The technique is based on the detection of the change in polarization of a light beam interacting with a sample. The UVISEL phase shift modulated ex-situ ellipsometry in Figure 2.26 is from Horiba Jobin-Yvon and it was used with the photon energy range from 1.5 eV to 4.5 eV (corresponding to wavelengths from 826.7 nm to 275.5 nm) with an energy step of 0.02 eV. The in-situ ellipsometer is from J. A.

Wollam as shown in Figure 2.2 (a) and used with the photon energy range from 1.2 eV to 5.5 eV.

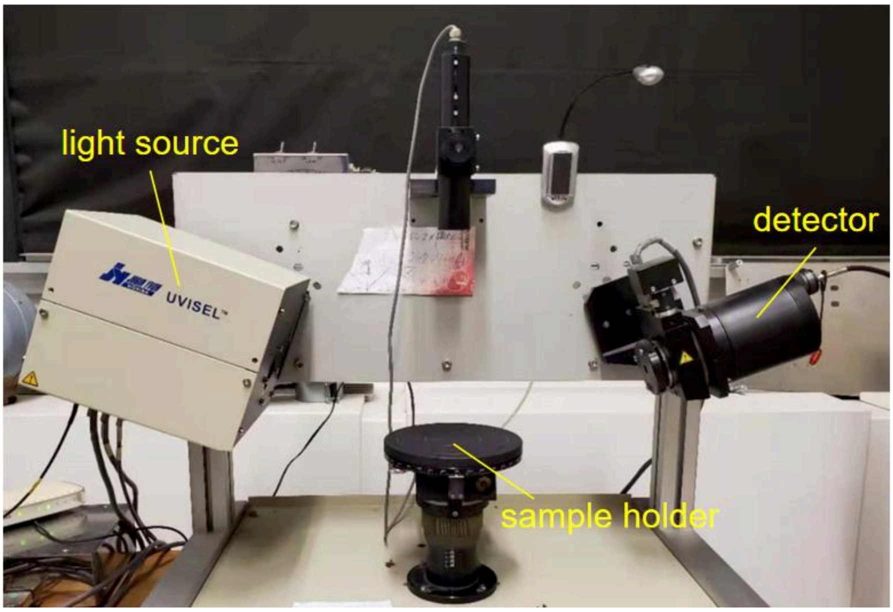

Figure 2.26 Photograph of ex-situ UVISEL Horiba Jobin-Yvon ellipsometer.

An ellipsometry system typically contains a light source, polarizer, modulator, analyzer, and detection system. The light beam is polarized, and consists of components parallel (p-polarized) and perpendicular (s-polarized) to the incidence plane. After reflection from the sample, the reflection coefficients of p and s-polarized components at the air/sample surface can be expressed as:

$$r_s = \left|r_s\right| e^{i\delta p}, \tag{2-13}$$

$$r_p = \left|r_p\right| e^{i\delta p}, \tag{2-14}$$

where $|r_s|$, δ_s and $|r_p|$, δ_p are the absolute phases and amplitude attenuation changes for s and p components after the reflection, respectively. The change of polarization state can be characterized by the ratio ρ defined as follows:

$$\rho = \frac{r_p}{r_s} = \frac{\left|r_p\right|}{\left|r_s\right|} e^{i(\delta_p - \delta_s)} = \tan\varphi \cdot e^{i\Delta}, \tag{2-15}$$

$$\tan\varphi = \frac{\left|r_p\right|}{\left|r_s\right|}, \tag{2-16}$$

$$\Delta = \delta_p - \delta_s, \tag{2-17}$$

where tan φ is the ratio of amplitude attenuation and Δ is the phase change difference.

The pseudo-dielectric function can be defined as:

$$\langle\varepsilon\rangle = \sin^2\theta\left[\tan^2\theta\frac{(1-\rho)^2}{(1+\rho)^2}+1\right], \tag{2-18}$$

$$\langle\varepsilon\rangle = \langle\varepsilon_r\rangle + i\langle\varepsilon_i\rangle, \tag{2-19}$$

where θ is the incidence angle, and $\langle\varepsilon_r\rangle$ and $\langle\varepsilon_i\rangle$ are the real part and imaginary part of $\langle\varepsilon\rangle$, respectively. By calculating these values from the ellipsometry measurements acquired, they can be used to characterize the optical properties of the thin film material stacks.

To better understand the properties of a sample, it can be modeled as a multilayer stack using the parameters of each layer's thickness, dielectric function and volume fraction. The modeled layer stack is then fitted to the experimental spectra to determine useful information about the sample. A useful tool when doing so is the Bruggeman effective medium approximation method [39]. The dielectric function ε_b for a layer is calculated from the dielectric functions of the different materials composing that layer by solving the equation:

$$\textstyle\sum_i f_i\frac{\varepsilon_i-\varepsilon_b}{\varepsilon_i+2\varepsilon_b}=0, \tag{2-20}$$

where ε_i is the dielectric function of the material with a volume fraction f_i. The dielectric functions of known materials are obtained as parametric dispersion curves or are tabulated function from references [40, 41].

Figure 2.27 shows the measurement and fitting result of a-Si:H deposited on CG at 600°C by a phase-modulated ellipsometry from 1.5 eV to 4.5 eV. The surface roughness is modelled by a thin layer (3 nm) of 50% a-Si:H and 50% void, and the thickness of the a-Si:H layer (without void) is 33 nm.

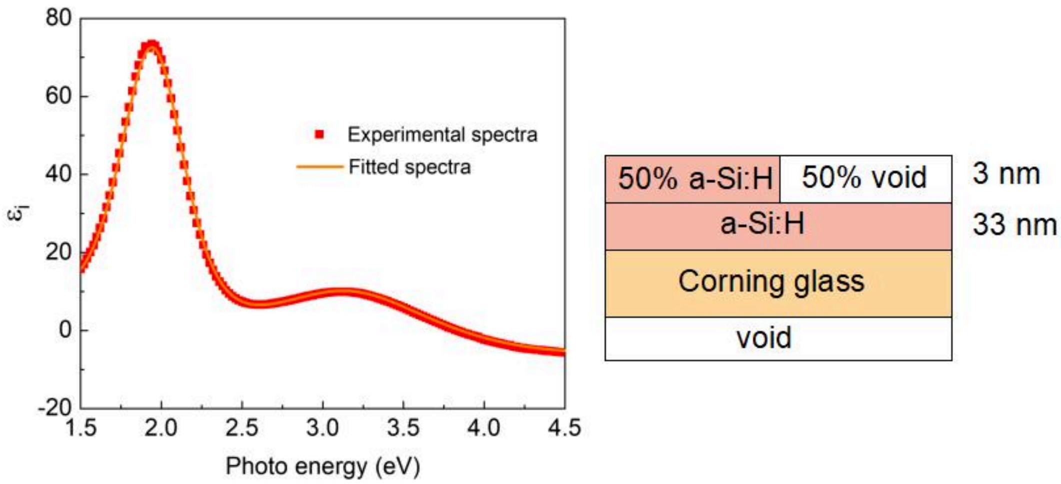

Figure 2.27 Ellipsometer spectra and its fitting mode of a-Si:H deposited at 600°C from 1.5 eV to 4.5 eV with incident angle of 70°.

References

[1] U. Latif, S. Can, O. Hayden, P. Grillberger, F. L. Dickert, *Sauerbrey and anti-Sauerbrey behavioral studies in QCM sensors—Detection of bioanalytes,* Sensors and Actuators B: Chemical, 2013, **176**: p. 825-830.

[2] J. Tang, J. Maurice, W. Chen, S. Misra, M. Foldyna, E. V. Johnson, P. Roca i Cabarrocas. *Plasma-Assisted Growth of Silicon Nanowires by Sn Catalyst: Step-by-Step Observation,* Nanoscale Research Letters, 2016, **11**: p. 455.

[3] W. Wang, E. Ngo, I. Florea, M. Foldyna, P. Roca i Cabarrocas, J. Maurice. *High Density of Quantum-Sized Silicon Nanowires with Different Polytypes Grown with Bimetallic Catalysts,* ACS Omega, 2021, **6** (40): p. 26381-26390.

[4] M. A. Lieberman, A. J. Lichtenberg, *Principles of Plasma Discharges and Materials Processing,* New Jersey: Wiley, 2005.

[5] H. F. Sterling, R. C. G. Swann, *Chemical vapour deposition promoted by r.f. discharge. Solid-State Electronics,*Solid-State Electronics, 1965, **8** (8): p. 653–654.

[6] E. Ngo. *In situ growth of silicon and germanium nanowires in the metastable hexagonal-diamond phase,* PhD thesis, Ecole Polytechnique, 2021.

[7] F. Zheng, *Study of in-plane silicon nanowires obtained via a solid-liquid-solid growth process and their self-organization for electronic applications,* PhD thesis, Ecole Polytechnique, 2015.

[8] E. Moulin, U. Paetzold, H. Siekmann, J. Worbs, A. Bauer, R. Carius. *Study of thin-film silicon solar cell back reflectors and potential of detached reflectors,* Energy Procedia, 2011, **10**: p. 106-110.

[9] K. Söderström, F.-J. Haug, J. Escarré, C. Pahud, R. Biron, C. Ballif. *Highly reflective nanotextured sputtered silver back reflector for flexible high-efficiency n–i–p thin-film silicon solar cells,* Solar Energy Materials and Solar Cells, 2011, **95** (12): p. 3585-3591.

[10] M. I. Hossain, W. Qarony, M. K. Hossain, M. K. Debnath, M. J. Uddin, Y. H. Tsang. *Effect of back reflectors on photon absorption in thin-film amorphous silicon solar cells,* Applied Nanoscience, 2017, **7**: p. 479-497.

[11] B. Drevillon, S. Kumar, P. Roca i Cabarrocas, J.M. Siefert, *In situ investigation of the optoelectronic properties of transparent conducting oxide/amorphous sincon interfaces*, Applied Physics Letters, 1989, 54:p. 2088-2090.

[12] L. Yu, B. O'Donnell, J. Maurice,P. Roca i Cabarrocas, *Core-shell structure and unique faceting of Sn-catalyzed silicon nanowires,* Applied Physics Letters, 2010, **97** (2): p. 023107.

[13] L. Yu, F. Fortuna, B. O'Donnell, G. Patriache, P. Roca i Cabarrocas, *Stability and evolution of low-surface-tension metal catalyzed growth of silicon nanowires,* Applied Physics Letters, 2011, **98** (12): p. 123113.

[14] E. I. Givargizov, *Fundamental aspects of VLS growth,* Journal of Crystal Growth, 1975, **31**: p. 20-30.

[15] J. Cho, B. O'Donnell, L. Yu, K. Kim, I. Ngo, P. Roca i Cabarrocas, *Sn-catalyzed silicon nanowire solar cells with 4.9% efficiency grown on glass,* Progress in Photovoltaics: Research and Applications, 2013, **21** (1): p. 77-81.

[16] X. Sun, T. Zhang, J. Wang, F. Yang, L. Xu, J. Xu, Y. Shi, K. Chen, P. Roca i Cabarrocas, L. Yu, *Firmly standing three-dimensional radial junctions on soft aluminum foils enable extremely low cost flexible thin film solar cells with very high power-to-weight performance,* Nano Energy, 2018, **53**: p. 83-90.

[17] L. Yu, B. O'Donnell, M. Foldyna and P. Roca i Cabarrocas, *Radial junction amorphous silicon solar cells on PECVD-grown silicon nanowires,* Nanotechnology, 2012, **23** (19): p. 194001.

[18] L. Yu, P. Alet, G. Picardi, I. Maurin, P. Roca i Cabarrocas, *Synthesis, morphology and compositional evolution of silicon nanowires directly grown on* SnO_2 *substrates,* Nanotechnology, 2008, **19** (48): p. 485605.

[19] B. O'Donnell, *Plasma grown silicon nanowires catalyzed by post-transition metals and applications in radial junction solar cells,* Ph.D thesis, Ecole Polytechnique, 2012.

[20] M. A. Ghzaiwat, *Fabrication and study of solar cell modules based on silicon nanowire based radial junction solar cells,* Ph.D thesis, Ecole Polytechnique, 2018.

[21] S. Misra, L. Yu, W. Chen, Pere Roca i Cabarrocas, *Wetting Layer: The Key*

Player in Plasma-Assisted Silicon Nanowire Growth Mediated by Tin, The Journal of Physical Chemistry C, 2013, **117**(34):p. 17786-17790.

[22] D. Pan, L. Jianya, T. Ming, W. Qingsong, W. Yuanyuan, J. Lian, B. Lifeng, L. Shulong, Y. Hui. *Transparent conducting indium-tin-oxide (ITO) film as full front electrode in III–V compound solar cell,* Chinese Physics B, 2017, **26** (3): p. 037305.

[23] J. Gwamuri, A. Vora, J. Mayandi, D. Ö. Güney, P. L. Bergstrom, J. M. Pearce. *A new method of preparing highly conductive ultra-thin indium tin oxide for plasmonic-enhanced thin film solar photovoltaic devices,* Solar Energy Materials and Solar Cells, 2016, **149**: p. 250.

[24] D. Zhang, A. Tavakoliyaraki, Y. Wu, R. A. C. M. M. van Swaaij, M. Zeman. *Influence of ITO deposition and post annealing on HIT solar cell structures,* Energy Procedia, 2011, **8**: p. 207.

[25] S. Swann, *Magnetron sputtering,* Physics in Technology, 1988, **19**: p. 67.

[26] E. Moulin, U. W. Paetzold, H. Siekmann, J. Worbs, A. Bauer, R. Carius. *Study of thin-film silicon solar cell back reflectors and potential of detached reflectors,* Energy Procedia, 2011, **10**: p. 106.

[27] U. W. Paetzol, E. Moulin, D. Michaelis, W. Bottler, C. Wachter, V. Hagemann, M. Meier, R. Carius, U. Rau. *Plasmonic reflection grating back contacts for microcrystalline silicon solar cells,* Applied Physics Letters, 2011, **99** : p. 181105.

[28] G. Yue, L. Sivec, J. M. Owens, B. Yan, J. Yang, S. Guha, *Optimization of back reflector for high efficiency hydrogenated nanocrystalline silicon solar cells,* Applied Physics Letters, 2009, **95** : p. 263501.

[29] Sai H, Fujiwara H, Kondo M. *Back surface reflectors with periodic textures fabricated by self-ordering process for light trapping in thin film microystalline silicon solar cells,* Solar Energy Materials and Solar Cells, 2009, **93**: p. 1087.

[30] L. R. Dahal, D. Sainju, N. J. Podraza, S. Marsillac, R. W. Collins. *Real time spectroscopic ellipsometry of Ag/ZnO and Al/ZnO interfaces for back-reflectors in thin film Si:H photovoltaics,* Thin Solid Films, 2011, **519** (9): 2682.

[31] B. Yan, G. Yue, L. Sivec, J. Owens-Mawson, J. Yang, S. Guha. *Correlation of texture of Ag/ZnO back reflector and photocurrent in hydrogenated nanocrystalline*

silicon solar cells, Solar Energy Materials and Solar Cells, 2012, **104**: p. 13.

[32] Dektak 150 profiler user’s manual, https://www.equipx.net/uploads/Veeco/Veeco-Dektak-150-user-manual.pdf.

[33] PV education, pveducation.org.

[34] H. Sigel, A. Zuberbühler, O. Yamauchi, *Comments on potentiometric pH titrations and the relationship between pH-meter reading and hydrogen ion concentration*, Analytica Chimica Acta, 1991, **1**:p. 63-72.

[35] W. McBryde, *The pH meter as a hydrogen-ion concentration probe*, Analyst, 1969, 1118.

[36] D. Tarbell, A. Tarbell, *The development of the pH meter*, Journal of Chemical Education, 1980, **57**(2):p. 133.

[37] K. Akhtar, S. Khan, S. Khan, A. Asiri, *Scanning Electron Microscopy: Principle and Applications in Nanomaterials Characterization*, Handbook of Materials Characterization, 2018, p. 113-145

[38] B. Voigtländer, *Atomic Force Microcopy*, 2019.

[39] D. Stroud, *The effective medium approximations: Some recent developments,* Superlattices and Microstructures, 1998, **23**(2-3):p. 567-573.

[40] E. Garcia-Caurel, A. De Martino, J-P. Gaston, L.Yan, *Application of spectroscopic ellipsometry and mueller ellipsometry to optical characterization*, Applied Spectroscopy, 2013, **67**(1): p. 1-21.

[40] H. G. Tompkins, J. N. Hilfiker*, Spectroscopic ellipsometry: practical application to thin film characterization,* 2015.

Chapter 3. “Efficient” Optimization of hydrogenated amorphous silicon triple radial junction solar cells for water splitting

Hydrogenated amorphous silicon (a-Si:H) deposited by PECVD has been much investigated as a low-cost material for photovoltaics. Its deposition at lower temperature leads to a non-equilibrium structure in which atomic bonds will be random [1-3]. Although covalent bonds between Si atoms are still present, there is no crystalline order in their positions beyond lengths of a few atoms [4-8]

The main weakness of a-Si:H is that prolonged light exposure produces dangling bonds, which degrades conductivity and increases recombination, an effect named the Stabler-Wronski (S-W) effect. In solar cells, the impact of this effect is reduced for thinner silicon layers (due to a stronger electric field), although thinner layers lead to less light absorption. Therefore, the question is how to increase the electric field, enhance the charge collection, but also maximize light absorption, and thus minimize the impact of the S-W effect for a better performance of solar cell [9-16].

The silicon nanowire (SiNW) radial junction solar cell provides a possible solution. It consists of a-Si:H layers built over a SiNW, and has excellent light trapping and anti-reflection properties [17-21]. Although the SiNW solar cell has a very thin intrinsic layer, its unique structure enhances light absorption and carrier collection ability [21]. The strong built-in electric field due to thinner devices means ^{2}&that the light degradation is reduced. In addition, the substrates do not need to be textured to increase the light absorption, which is always necessary for planar solar cells [22].

Going further with this architecture, radial multijunction SiNW solar cells have been fabricated in recent years at the LPICM, with different absorber layer materials being used for bottom and top cell. S. Misra fabricated a pm-Si:H/a-Si:H tandem device, for which the V_{OC} increases to 1.5 V and J_{SC} reaches 7 mA/cm^2, the fill factor is 0.6, the efficiency is 6.5%. He also attempted a-Si:H/μc-Si:H devices, whose PV performance are: V_{OC} = 1.02V, J_{SC} = 8.3 mA/cm^2, efficiency of 5.5% [23]. L. Dai also attempted an a-Si:H/μc-Si:H tandem SiNW solar cell after improving the μc-Si:H RJ performance, but was less successful, achieving efficiencies of 2.62% (V_{OC} = 0.77 V, J_{SC} = 7.2 mA/cm^2, FF = 0.47) [24]. Finally, J. Tang prepared an a-SiGe:H/pm-Si:H tandem silicon nanowire solar cell with efficiency of 4.93%, V_{OC} of 1.41 V and J_{SC} of

6.6 mA/cm^2 [25]. One can note that no RJ tandem device has surpassed the efficiency of the best single RJ device, around 9.7 % initial efficiency [23].

These devices all aimed for efficient use of the solar spectrum and the highest possible power conversion efficiency. In this thesis, with the goal of water-splitting in mind, we aim to achieve the highest possible operating **voltage** by using identical, wide band gap (1.7 eV) materials (a-Si:H) as absorber layers.

In this chapter, all a-Si:H single, double and triple radial junction solar cells are fabricated and investigated. Some strategies are used to improve the solar cell performance, such as changes to doping levels in the n layer, SiNW density, gradient layers, layer thicknesses, and tunnel junction properties.

Figure 3.1 shows a photograph of the RJ SiNW solar cell substrate design used for all samples in this chapter. On each 25 mm x 25 mm substrate, there are 15 cells with an area of 0.031 cm^2 and 6 cells with area of 0.125 cm^2, as defined by the areas of ITO deposition. The corner of sample is scraped by diamond pen to expose the bottom contact. Ag paste is placed on the corner as well as on the ITO for better contact while measuring the solar cells.

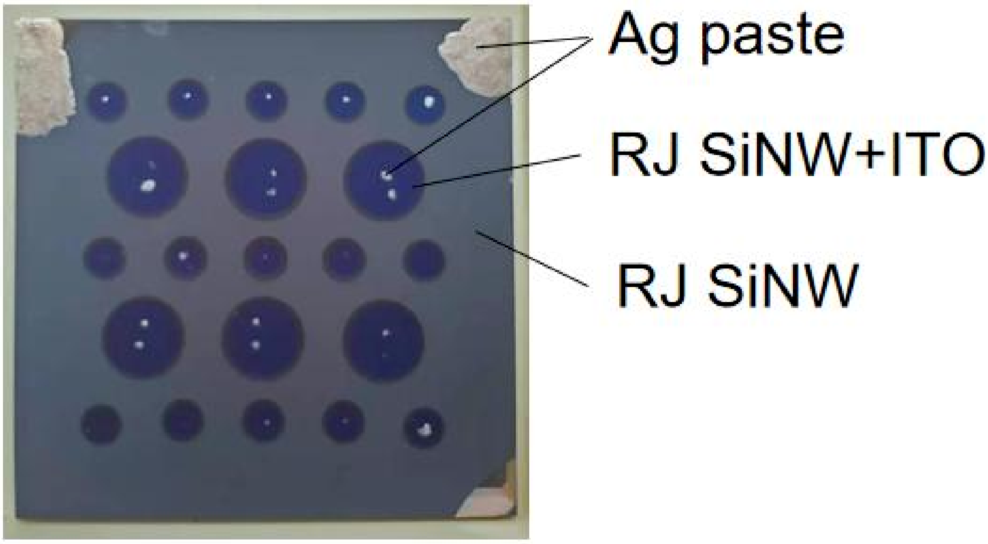

Figure 3.1 Photograph of RJ SiNW solar cells

3.1 SiNW RJ solar cells

3.1.1 Different n layer for SiNW RJ solar cells

Two samples of SiNW radial junction solar cells with low doping n layer and high doping a-Si:H n-layer have been prepared. From bottom to the top, the structure of these solar cells is Cg/Ag/ZnO:Al/c-SiNW/p type a-Si:H/intrinsic a-Si:H/n type a-Si:H/ITO. Two kinds of doping method are used for n layer deposition of SiNW radial junction solar cell. One doped n layer is grown by 1.5 sccm SiH_4, 0.9 sccm PH_3, 9 sccm H_2 under 0.31 mbar for 13 min, another doped n layer is grown by 10 sccm SiH_4, 5 sccm PH_3 under 0.44 mbar for 5 min.

The J-V of these samples were measured after sample annealing at 240 °C for 20 min in air. Fig. 3.2 and Table. 3.1 show the performance of SiNW solar cells with different doping ratio of n layer. The V_{OC} of SiNW solar cell with the first higher doping n layer is 0.71 V. The V_{OC} of SiNW solar cell with the second lower doping a-Si:H n layer is 0.77 V, which is larger than that with high doping n layer. 8.5% enhancement of V_{OC} is achieved by low doping a-Si:H n layer. This may be due to the fact that high dopant concentration creates more defects than active dopants and reduces the V_{OC}. Meanwhile, the series resistance (R_s) becomes larger with higher n-layer dopant concentration. Moreover, the current density of solar cell with lower doping n layer is 14.27 mA/cm^2, which is higher than that of solar cell with high doping n layer, 13.27 mA/cm^2. The solar cell with lower doping n type top layer exhibit a J_{SC} improvement of 7.5 %. Fill factor of solar cell with low doping n layer is 0.64, fill factor with high doping n layer is 0.53. As a result, the SiNW radial junction solar cell with doping n layer exhibit better efficiency of 7.03 % compared to that with higher n layer.

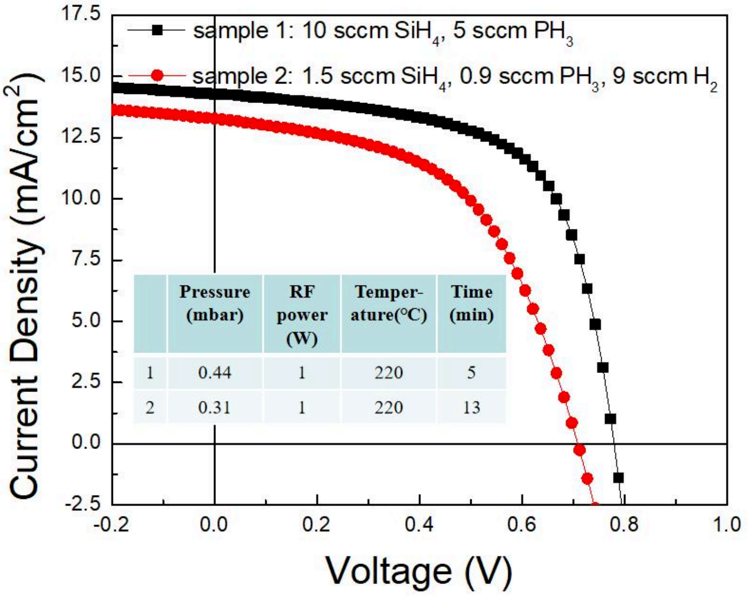

Figure 3.2 J-V curves of SiNW radial junction solar cell with different n-layer doping ratio

Table 3.1 V_{OC}, J_{SC}, FF, η of SiNW 1RJ solar cell with different n-layer doping

n layer	V_{OC} **(V)**	J_{SC} **(mA/cm^2)**	**FF**	**Efficiency (%)**
10 sccm SiH_4, 5 sccm PH_3	0.77	14.27	0.64	7.03
1.5 sccm SiH_4, 0.9 sccm PH_3, 9 sccm H_2	0.71	13.27	0.53	4.99

3.1.2 SiNW RJ solar cells with gradient doping n layer

The recombination always existed in the radial junction SiNW solar cell. Figuring out how to minimize the effect of recombination is important for solar cell performance improvement. Doping creates defects in the a-Si:H solar cell, particularly at the p-i and i-n interfaces, so gradient doping layers have been applied for improving SiNW solar cell. As shown in thesis of S. Misra, for PIN structure, the p a-Si:H layer growth on p type c-SiNWs can improve the voltage of SiNW solar cell from 0.8 V to 0.85 V, furthermore, coating a gradient doping p layer can improve the voltage to as high as 0.9 V. The defects from p-a-Si:H annealed at high temperature in the residual area without SiNWs growth are buried due to a p-layer coated on p-type SiNW. The a-Si:H deposited at higher temperature on planar is with low quality. A p type a-Si:H layer deposition at lower temperature reduces the recombination between planar area and intrinsic layer [23].

In order to obtain a better performance of the SiNW solar cell, we grow a gradient doping n layer to reduce the defects between i layer and n layer. As shown in Figure 3.3, the n layer consists of three sublayers, the first n layer is doped with 10 sccm SiH_4 and 1 sccm PH_3, the second n is layer doped with 10 sccm SiH_4 and 2 sccm PH_3, the third n is layer doped with 10 sccm SiH_4 and 7 sccm PH_3. Thus the n layer has a gradient doping. In the Figure 3.4 and Table 3.2, the voltage of solar cell is improved from 0.77 V to 0.79 V, because the gradient doping reduces the recombination. In the meantime, if the n layer become thinner, more light can go through the n layer and be absorbed by the i layer, therefore, the resistance is reduced by a thinner n layer, meanwhile, the current density of 14.83 mA/cm^2 is achieved. The gradient n layer leads to the efficiency improved from 6.72 % to 7.62 %. Almost 1 % efficiency improvement (absolute) is realized by gradient n layer growth for radial junction SiNW solar cell.

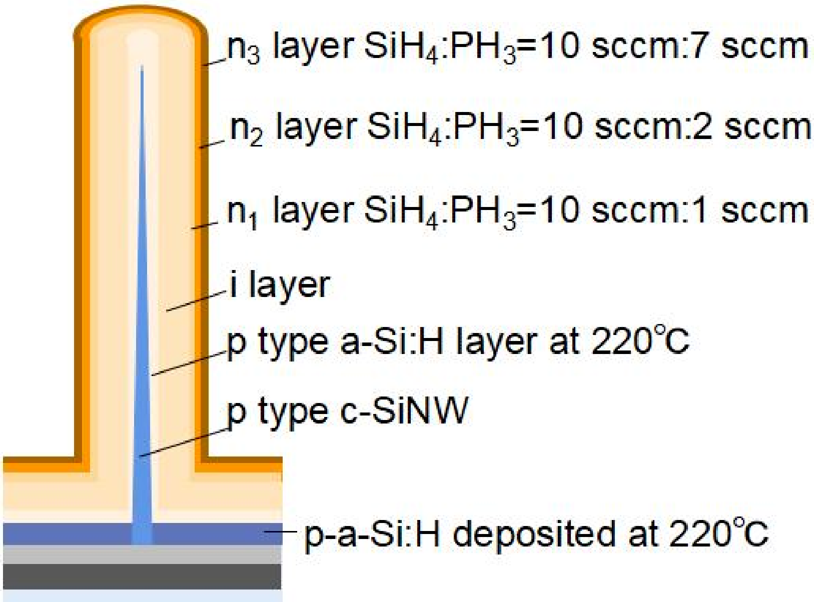

Figure 3.3 Configuration of SiNW with gradient doping n layer.

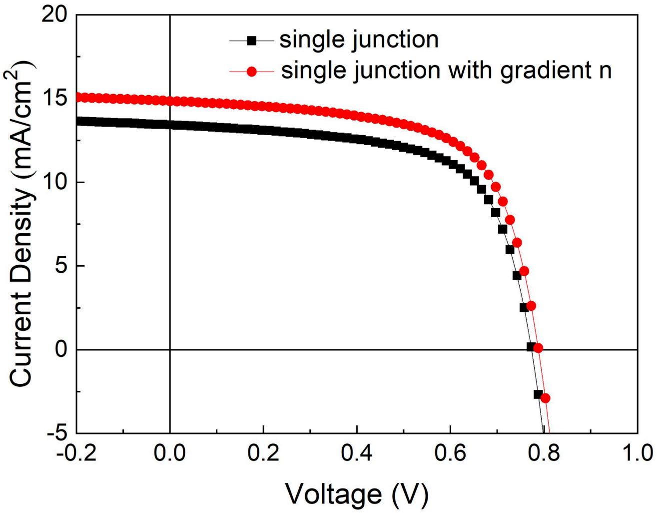

Figure 3.4 Comparison of the J-V curves for solar cells fabricated with gradient doping n layer and constant doping n layer.

Table 3.2 Comparison of different parameters extracted from J-V characteristics.

Type	V_{OC} **(V)**	J_{SC} **(mA/cm^2)**	**FF**	**Efficiency (%)**
Single junction	0.77	13.43	0.65	6.72
Single junction with gradient n layer	0.79	14.83	0.65	7.62

3.1.3 Influence of areal density of RJ on silicon nanowire solar cell performance

According to previous work, the silicon nanowire density has an important impact on the performance of radial junction solar cells [26]. A conformal and uniform coating will only occur for a suitable nanowire density. A radial junction density varying from $0.7\times10^8/cm^2$ to $4.8\times10^8/cm^2$ was obtained by using different nominal thickness of deposited Sn catalyst. SEM images of silicon nanowire radial junction with different nanowire densities are shown in Figure 3.5. The density was calculated by counting the radial junctions without ITO sputtering and is written into images in the left column. Solar cells after ITO sputtering are shown in the right column of Figure 3.5. Probably, shorter SiNWs get buried after the a-Si:H coating and do not form the radial junction. For example, some small balls are shown figure 3.5 (b) with density of $0.7\times10^8/cm^2$.

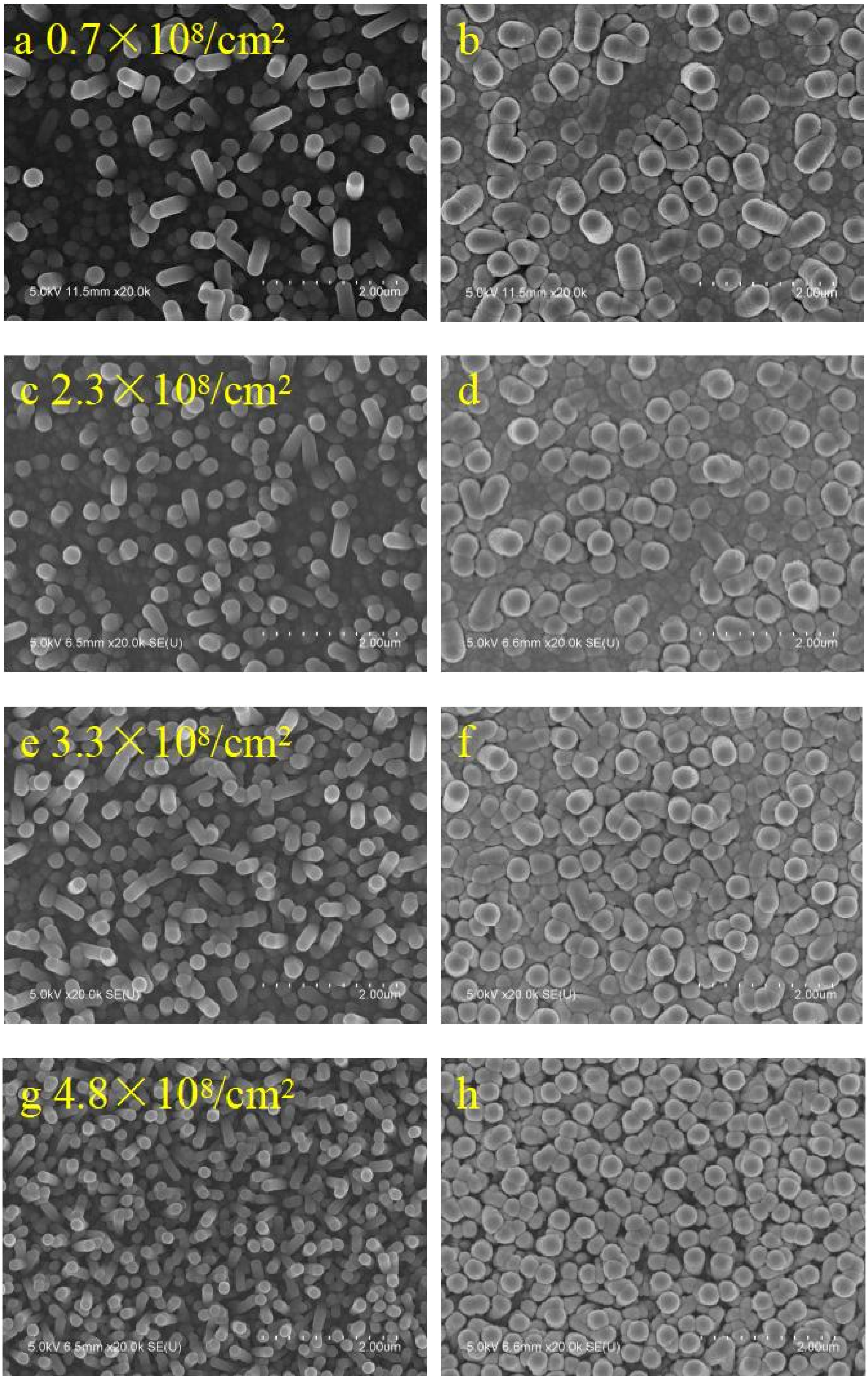

Figure 3.5 SEM images of RJ solar cell built over SiNWs with varying density from 0.7×10^8/cm^2 to 4.8×10^8/cm^2 (top view). Left column is the radial junction without ITO top contact, right column is the radial junction with ITO top contact.

The standard air mass 1.5 global (AM 1.5G) illumination (Newport solar simulator) is used for measuring the J-V characteristics of radial junction solar cells. The light is shined through the ITO top contact on n layer of the solar cell. The J-V curves of best efficiency solar cells are shown in Figure 3.6 while Table 3.3 shows the cell parameters of single junction SiNW solar cell.

The V_{OC} of SiNW radial junction solar cell decreases from 0.82 V to 0.65 V as the silicon nanowire density increases from $0.7 \times 10^8/\text{cm}^2$ to $4.8 \times 10^8/\text{cm}^2$. The short circuit current (J_{SC}) also increases with NW density due to better light trapping [26-28], but the reverse dark saturation current (J_0) also increases due to the larger effective surface area. I will show the dark J-V later. One notes that there are 100's of millions of NWs per square centimeter in such devices, so the increase in effective surface area is dramatic. The optimum efficiency results from the tradeoff between J_{SC} and V_{OC}, as approximated by V_{OC} = kT ln (J_{SC}/J_0). In the meantime, the V_{OC} rapid decrease can be assigned to the problem of conformal junction coating on silicon nanowire array.

For the lowest density silicon nanowires of 0.7×10^8 cm^{-2}, the J_{SC} is 12.8 mA/cm^2, furthermore, the J_{SC} increases to 13.89 mA/cm^2 and 15.49 mA/cm^2 as the density rises up to 2.3×10^8 cm^{-2} and 3.3×10^8 cm^{-2}, respectively. However, a further increase of the areal density of silicon nanowires to 4.8×10^8 cm^{-2}, leads to a J_{SC} decrease to 13.59 mA/cm^2. The J_{SC} increase can be explained by the light trapping enhancement as the SiNW density becomes higher. On the other hand, too much NW makes the solar cell form a planar-like structure as Figure 3.4 (g), which causes J_{SC} decreasing.

The fill factor increases from 0.6 for density of $0.7\times10^8/\text{cm}^2$ to 0.62 with density of $2.3\times10^8/\text{cm}^2$. This can be due to the improvement of the electrical contact between p-type ZnO:Al and crystalline silicon nanowires. As the nanowire density rises up, more connection area is established by crystalline silicon nanowires. Because the crystalline silicon has better conductivity and narrower band gap than amorphous silicon, the electrical contact between p type a-Si:H and ZnO:Al will be improved by crystalline SiNWs. When the density of silicon nanowires rises up to $4.8\times10^8/\text{cm}^2$, the fill factor decreases to 0.47, a larger series resistance is shown in the solar cell. For the SiNW radial junction solar cell, the solar cell with SiNW density of 3.3 × 10^8/cm^2 shows the best efficiency of 7.25 % with V_{OC} of 0.77 V, J_{SC} of 14.27 mA/cm^2 and FF of 0.64.

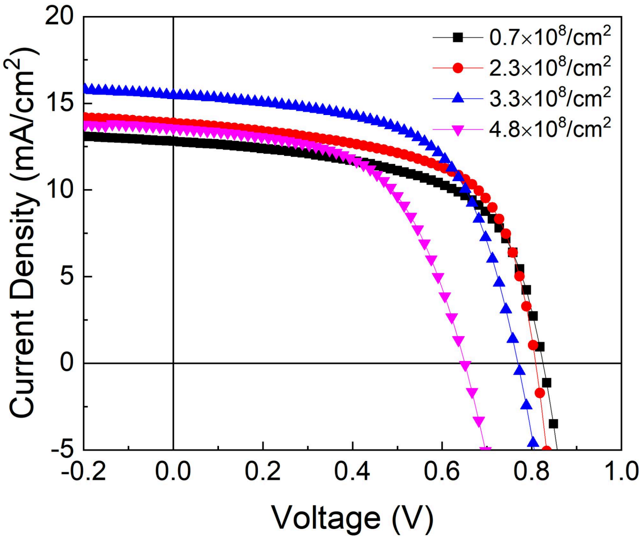

Figure 3.6 J-V characteristics of radial junction silicon nanowire solar cell built over SiNWs with density varying from 0.7 × 10^8/cm^2 to 4.8 × 10^8/cm^2.

Table 3.3 V_{OC}, J_{SC}, FF and efficiency of silicon nanowires solar cells with density varying form 0.7 × 10^8/cm^2 to 4.8 × 10^8/cm^2.

Nanowire Density	**V_{OC} (V)**	**J_{SC} (mA/cm^2)**	**FF**	**Efficiency (%)**
0.7 × 10^8/cm^2	0.82	12.8	0.6	6.3
2.3 × 10^8/cm^2	0.8	13.9	0.62	6.89
3.3 × 10^8/cm^2	0.77	15.49	0.61	7.25
4.8 × 10^8/cm^2	0.65	13.59	0.56	4.95

3.1.4 Comparison of light and dark J-V curves of different density SiNW RJ solar cells

In figure 3.7, the light and dark J-V curves of different density (from 0.7×10^8/cm^2 to 4.8×10^8/cm^2) SiNW solar cells are compared. In the region where the voltage is higher than V_{OC}, the light and dark J-V curve almost overlap. But for the region of voltage below zero, the dark and light J-V do not overlap. The shift is caused by the photo generated current. Comparing with dark J-V curve in this area, the shape of light J-V curve become steep. This is owing to recombination generated in the SiNW solar cells. Future work is to investigate high quality a-Si:H coating method in order to improve the recombination in the material.

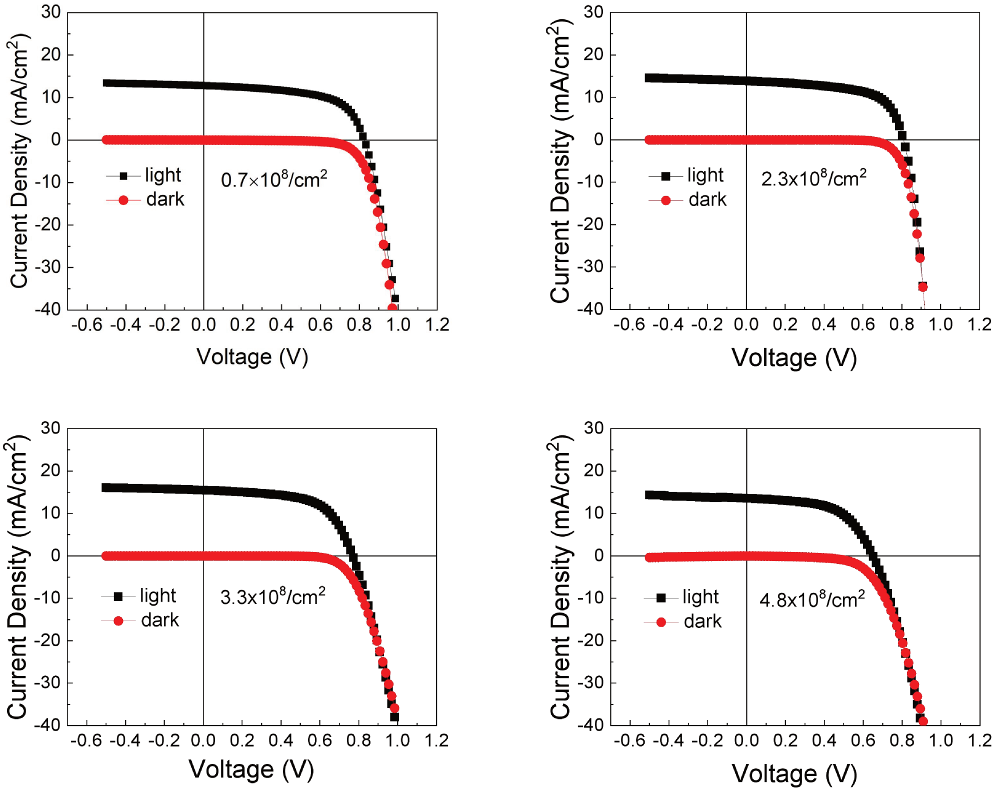

Figure 3.7 Light and dark J-V curves comparison of different NW density SiNW solar cells.

3.2 Double RJ SiNW solar cells

For water splitting, a single junction voltage of around 0.8 V is not enough for the reaction to occur. The required potential for water splitting is 1.23 V, not taking into account an overpotential to drive the HER and OER. Cheng et al. fabricated a 19.3% solar to hydrogen conversion efficiency III-V semiconductor based tandem solar cell with Rh and RuO_x catalysts [29]. However, the high cost of the III-V semiconductor materials precludes the widespread use of this system. To achieve the highest possible operating voltage, in the following section, a-Si:H/a-Si:H tandem radial junction solar cells are investigated for driving water electrolysis. Furthermore, one should note that the radial junction has a larger surface area, which may be good for water splitting catalyst density.

The V_{OC} of a tandem solar cell will be the sum of the V_{OC}'s of each subcell, but the J_{SC} will be the minimum J_{SC} amongst the subcells (due to current flow continuity). Therefore, the total photocurrent must be evenly shared between all the subcells to obtain the maximum output J_{SC}. Furthermore, in a multi-junction PIN/PIN tandem solar cell, the n layer of the bottom cell and the p layer of the top cell form an NP reverse biased junction, which can block the passage of current. This NP junction must allow the passage of current under reverse bias, and should therefore form a tunnel or recombination junction when used in a multijunction solar cell. Hence, a good quality of tunnel junction for better performance tandem solar cell is required. Therefore, the main issues for tandem solar cells are current matching and good quality tunnel junctions. They will be investigated in this section.

3.2.1 Different tunnel junction thickness for tandem RJ SiNW solar cells

A tunnel or recombination junction is a very highly doped p/n junction. For the normal p/n junction, when applying a forward bias voltage, the depletion region becomes narrow and the barrier height becomes lower at the same time. However, electrons in n-type material cannot go through the depletion region, because the built-in electric field is opposite to the direction of electron flow. If the applied voltage is more than the built-in electric field, the electrons from the n-layer can overcome the opposite force from depletion region, and then go into p layer. In brief, the energy of electron becomes greater than the height of barrier, and the electron can overcome the barrier. Under reverse bias, the barrier becomes ever higher, electrons and holes cannot overcome it, and little current flows.

The tunnel junction architecture allows the accumulated charges to pass through the barrier by quantum mechanical tunneling rather than going over their respective barriers. As shown in figure 3.8, in tunnel diodes, the conduction band energy levels in the n-type semiconductor are lower than the valence band levels in the p-type semiconductors, as one or both sides are doped degenerately. If the depletion region is narrow enough (a few nanometers), the electron can directly go through the narrow depletion region from the conduction band of the n-type material to recombine with a hole in the valence band of the p-type material, generating current flow.

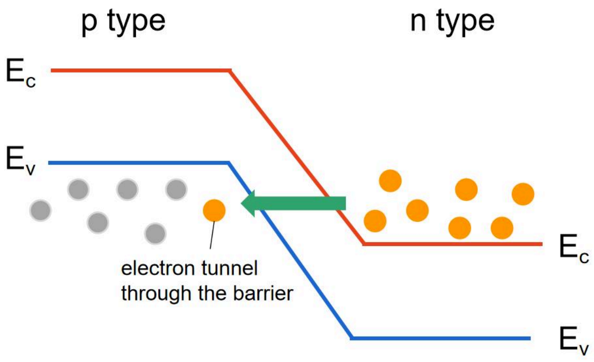

Figure 3.8 Schematic figure of tunnel junction

Compared to ordinary PN diodes, in a tunnel diode, a voltage which is smaller than that of depletion region is enough to generate current flow. A slight variation on this is for recombination junctions, where instead of tunneling all the way through to the other side, both types of carrier only tunnel halfway before recombining at the midpoint of the junction. When used in a solar cell, holes from the p layer of the top cell and electrons from the n layer of the bottom cell will recombine in the tunnel/recombination junction, giving uninterrupted current flow.

To develop materials to fabricate recombination junctions, we have first deposited n type and p type materials on CG and measure their thicknesses by ellipsometer. The deposition rates are 1.17 Å/s for n++ material and 1.67 Å/s for p++ material, respectively. SiH_4:PH_3=4 sccm: 10 sccm. These materials were then incorporated into a-Si:H/a-Si:H solar cells. The structure of all the double RJ SiNW solar cells in this chapter is the following: Corning glass/Ag/ZnO:Al/p type SiNW core/p-type a-Si:H/intrinsic a-Si:H/n-type a-Si:H/ n++ a-Si:H/p++ a-Si:H/p type a-Si:H/intrinsic a-Si:H/n type a-Si:H/ITO transparent top contact. The deposition rate of i-Si:H on CG is 0.67 Å/s. The deposition times are 45 min for bottom cell and 20 min for top cell. Fig. 3.9 shows the comparison of the J-V curves for tandem SiNW solar cells fabricated with different thickness of tunnel junction (of p and n layers). Table 3.7 presents the detailed V_{OC}, J_{SC}, FF and η from the figure 3.12. The V_{OC} of the tandem radial junction SiNW solar cell increases from 1.24 V to 1.32 V as the deposition time increases from 1 min to 2 min. The J_{SC} follows the same trend, the J_{SC}

is improved from 6.33 mA/cm^2 to 6.56 mA/cm^2. However, the voltage goes down to 1.2 V and the J_{SC} decreases to 5.95 mA/cm^2 as deposition time increases to 3 min. The fill factors are 0.61, 0.62 and 0.63 for 1 min, 2 min and 3 min sample, respectively. The best efficiency is 5.37% for the 2 min deposition.

This optimum in tunnel junction thickness (2 min + 2 min) may have some physical explanation. If the tunnel junction cannot provide enough recombination centers, the charges will accumulate in the junction, which will change the electric field distribution near the junction, resulting in the opposite dipole layer, generating a reverse current and voltage. Furthermore, too many defects are created in the thicker tunnel junction. If the tunnel junction is too thick, light will be lost in the tunnel junction.

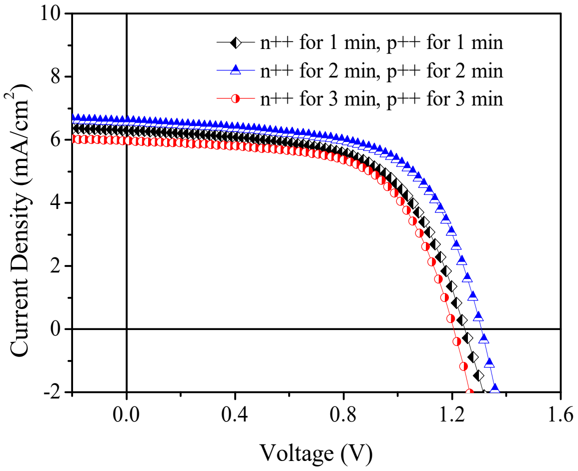

Fig. 3.9 Comparison of the J-V curves for tandem SiNW solar cells fabricated with different deposition times of p++ and n++ layers forming tunnel junction.

Table 3.4 Comparison of different parameters extracted from J-V characteristics shown above.

Time of growing n++ layer and p++ layer (min)	**V_{OC} (V)**	**J_{SC} (mA/cm^2)**	**FF**	**η (%)**
1	1.24	6.33	0.61	4.79
2	1.31	6.56	0.62	5.37
3	1.2	5.95	0.63	4.5

3.2.2 Effect of doping on double junction SiNW RJ solar cells

In a second set of experiments, we have used different doping ratios to grow the tunnel junction, SiH_4:PH_3=4 sccm: 6 sccm and SiH_4:PH_3=4 sccm: 10 sccm. As shown in Figure 3.10 and table 3.5, the V_{OC} of two samples are almost the same. The current density is improved from 4.87 mA/cm^2 to 6.56 mA/cm^2. The difference in the J_{SC}, however, can be attributed to a non-uniformity on the substrate. In the J-V curves of double junction with different doping ratio, the R_S of lower doping ratio is higher than that of higher doping ratio. Consequently, the higher doping of the layers of the tunnel junction makes it easier for the electrons and holes to tunnel through.

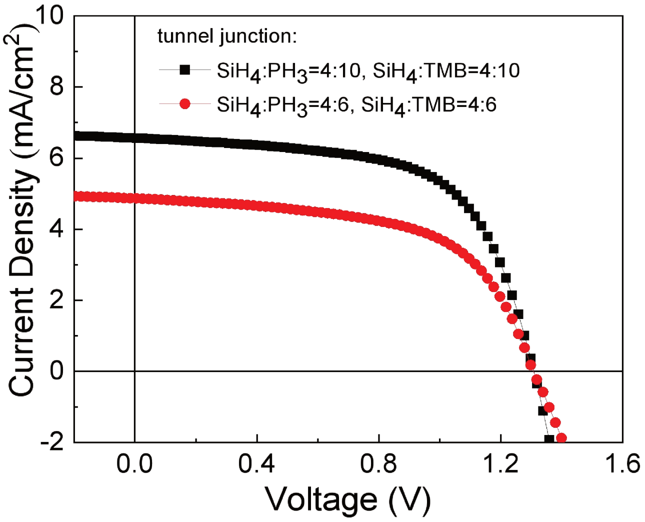

Fig. 3.10 Comparison of the J-V curves for tandem SiNW solar cells fabricated with different doping ratios of the p++ and n++ layers forming.

Table 3.5 Comparison of different parameters extracted from J-V characteristics shown above.

Tunnel junction	V_{OC} **(V)**	J_{SC} **(mA/cm^2)**	**FF**	**η (%)**
SiH_4:PH_3=4:10, SiH_4:TMB=4:10	1.31	6.56	0.62	5.37
SiH_4:PH_3=4:6, SiH_4:TMB=4:6	1.3	4.87	0.59	3.74

3.2.3 Double junction SiNW solar cells with different top and bottom absorber layer thickness

Current matching is important for tandem solar cell performance, as in a tandem solar cell, the photocurrent will be limited to that of the minimum sub cell. In this section, we change the thickness of top a-Si:H i layer and bottom a-Si:H i layer to balance the current density of top and bottom junctions. The deposition rate of i layer material on CG substrate is 0.67 Å/s. We keep the total device deposition time the same, and change top and bottom i layer thickness by changing their individual deposition times.

Figure 3.11 and table 3.6 show the performance of double RJ SiNW solar cells with different thickness of bottom and top absorber layer. The J_{SC} increases as the thickness of the top i layer decreases (or that of the bottom i layer increases), and reaches 7.36 mA/cm^2 with 15 min top i-layer deposition and 50 min bottom i-layer deposition. This illustrates that the double junction SiNW solar cell is current limited by the bottom cell. As for the V_{OC}, the greatest value of 1.34 V is achieved for the 20 min top i layer deposition and 45 min bottom i layer deposition. These conditions also achieve the best fill factor of 0.62 and efficiency of 5.87%.

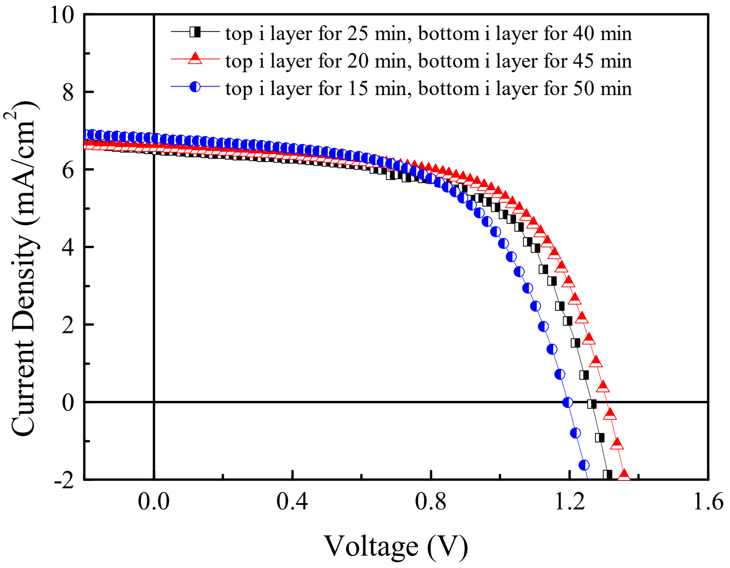

Fig. 3.11 Comparison of the J-V curves for double RJ SiNW solar cells fabricated with different thickness of bottom and top absorbed layer.

Table 3.6 Comparison of different parameters extracted from J-V characteristics shown above.

i layer growing time	V_{OC} **(V)**	J_{SC} **(mA/cm^2)**	**FF**	**η (%)**
Top cell 25 min, bottom cell 40 min	1.27	6.48	0.6	4.94
Top cell 20 min, bottom cell 45 min	1.34	7.07	0.62	5.87
Top cell 15 min, bottom cell 50 min	1.2	7.36	0.58	5.12

3.2.4 Gradient n layer for double RJ SiNW solar cells

As shown in section 3.1.2, a graded n-layer can improve the solar cell performance of a single junction SiNW solar cell. We can also use this strategy for tandem SiNW radial junction solar cells. Both top and bottom cell n layers were grown using a gradient doping. The deposition time for constant doping is 5 min, for the gradient doping is 3 min 20 seconds. Figure 3.12 and Table 3.7 show that the voltage of double junction is improved from 1.31 V to 1.34 V, the current density becomes better and reaches up to 7.07 mA/cm^2, the fill factor of tandem solar cell with and without gradient n layer does not change, the efficiency is improved from 5.37 % to 5.87 %, thus a 9.3 % improvement of double junction RJ SiNW solar cell from gradient doping n layer is achieved. These results can be explained, as the thickness of n-layers becomes thinner, more light will pass through them and could be absorbed by the i layer for both bottom and top cells.

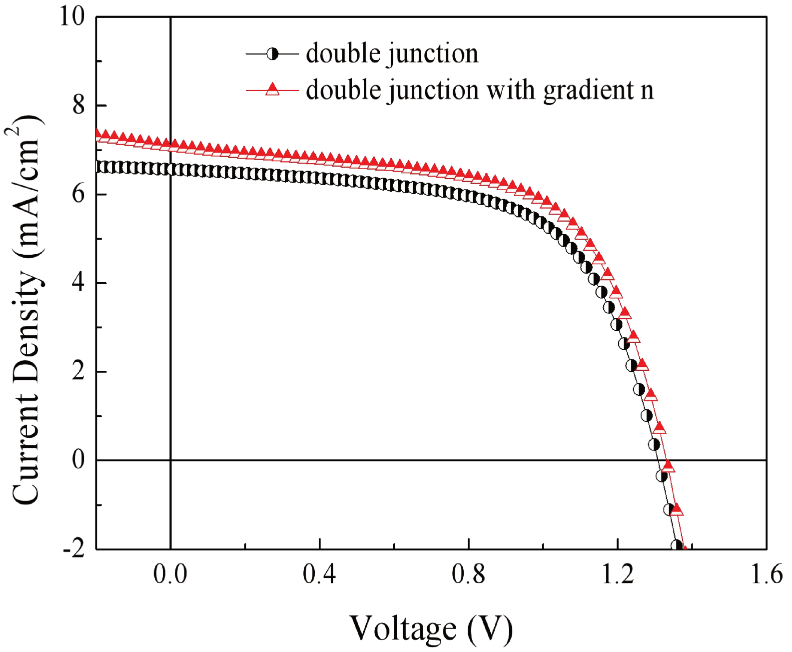

Fig. 3.12 Comparison of the J-V curves for tandem SiNW solar cells fabricated with gradient doping and constant doping n layer.

Table 3.7 Comparison of different parameters extracted from J-V characteristics shown above.

Type	**V_{OC} (V)**	**J_{SC} (mA/cm^2)**	**FF**	**η (%)**
Double junction	1.31	6.56	0.62	5.37
Double junction with gradient n layer	1.34	7.07	0.62	5.87

3.2.5 Influence of NW density on double junction SiNW solar cell performance

Another parameter to optimize is the NW density, which is controlled in our process by the Sn layer nominal thickness (and thus the Sn droplet density). We deposited different thicknesses of Sn on ZnO:Al/Ag/Cg substrates, and then grew double junction SiNW solar cells with different densities ranging from 6×10^7/cm^2 to 4×10^8/cm^2. The density was calculated by counting the radial junctions in the images without ITO top contact as presented in Figure 3.13. We can also see that the diameter of the SiNWs becomes lower as the density increases. The diameter changes from 500 nm to 340 nm, 320 nm, 300 nm and 280 nm; the same trend was observed in single junction SiNW solar cells, from 240 nm to 220 nm, 200 nm and 170 nm. Because a higher density of SiNWs generates a larger surface area, for the same plasma condition, the deposited thickness will be smaller.

From Figure 3.14 and Table 3.8, we see that as the SiNW density increases, the V_{OC} of the solar cell decreases, most likely because the larger surface area of the high density SiNW sample has more defects, which will affect the J_0 and further affect V_{OC} of the solar cell. The J_{SC} for the lowest density SiNW solar cell is 6.67 mA/cm^2. J_{SC} increases to a maximum of 7.27 mA/cm^2 for a SiNW density of 2.4×10^8/cm^2. Further increasing the areal density of radial junctions leads to a saturation of J_{SC}. The J_{SC} drops to 6.78 mA/cm^2 for a radial junctions density of 3.2×10^8/cm^2 and to 6.48 mA/cm^2 with an even higher SiNW density of 4.3×10^8/cm^2. Moreover, it can be found that the fill factor almost follows the same trend as J_{SC}. The density of around 2.4×10^8/cm^2 shows the best efficiency of 5.87%.

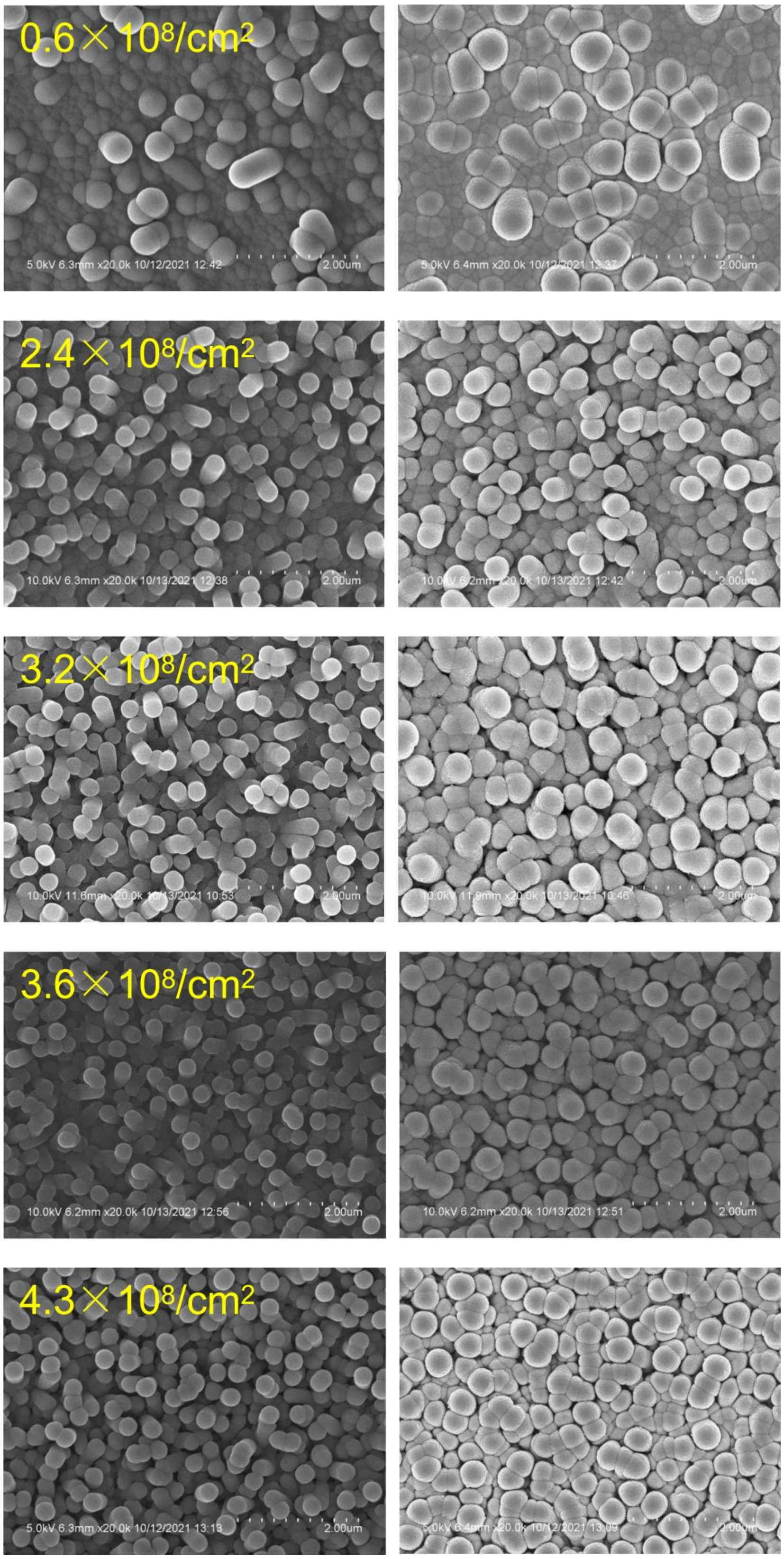

Figure 3.13 SiNW double radial junction solar cells with different NW density ranging from $0.6\times10^8/cm^2$ to $4.3\times10^8/cm^2$. Left column is the double PIN a-Si:H junction coated SiNWs, right column is the radial junction with ITO top contact.

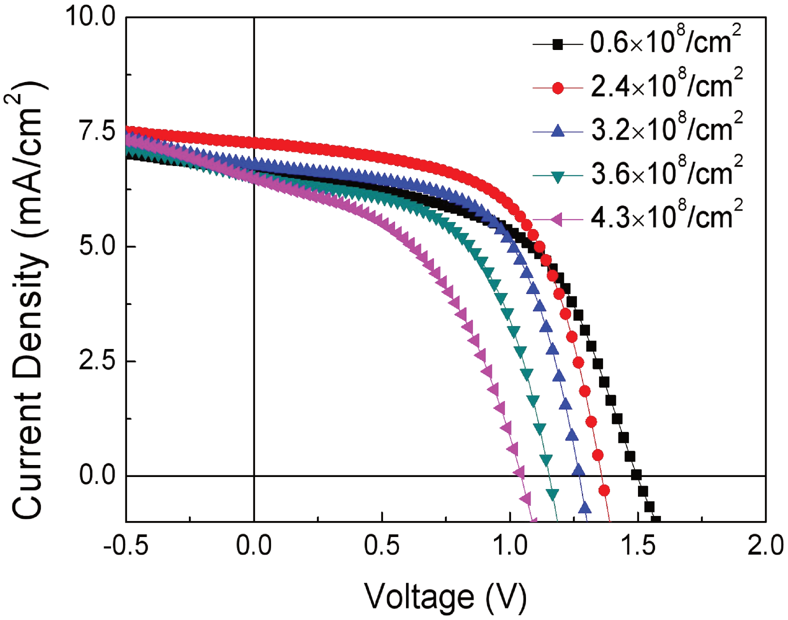

Figure 3.14 J-V characteristics of double radial junction SiNW solar cells with different densities ranging from 0.6×10^8/cm^2 to 4.3×10^8/cm^2.

Table 3.8 Comparison of solar cell parameters extracted from J-V characteristics shown in figure 3.12.

SiNW Density	**V_{OC} (V)**	**J_{SC} (mA/cm^2)**	**FF**	**η (%)**
0.6×10^8/cm^2	1.5	6.67	0.54	5.42
2.4×10^8/cm^2	1.37	7.27	0.59	5.87
3.2×10^8/cm^2	1.27	6.78	0.6	5.17
3.6×10^8/cm^2	1.17	6.53	0.56	4.28
4.3×10^8/cm^2	1.04	6.48	0.47	3.17

3.3 Triple RJ SiNW solar cells with different NW density

Having optimized 1RJ and 2RJ solar cells, we now move to optimizing more complex triple radial junction (3RJ) devices to achieve the higher possible operating voltage by using identical, wide band gap (1.7 eV) materials (a-Si:H) as absorber layers for water-splitting.

3.3.1 Different area 3RJ SiNW solar cells and J_{SC} uncertainty

After the fabrication of the first samples, the (in)dependence of the cell performance on the size of the cell has been verified, as there are two different sizes of solar cell on every substrate. As described previously, a 1-inch by 1-inch substrate is used for deposition, and 15 cells with area of 0.0314 cm^2 and 6 cells with area of 0.125 cm^2 are defined by the sputtering of ITO. The J-V curves of six solar cells with the two different areas are presented as Figure 3.15. The deposition time of the absorbed layer in each subcell are 32 min, 16 min and 8 min, respectively.

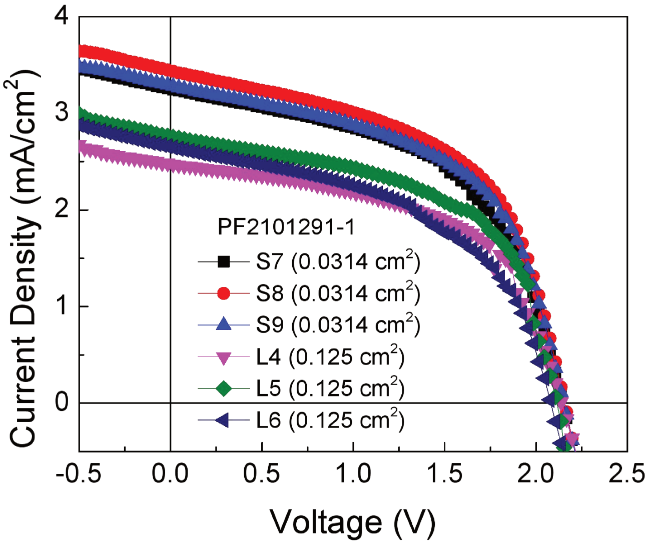

Figure 3.15 3RJ SiNW solar cells with different areas on the same substrate, 0.125 cm^2 and 0.0314 cm^2.

We can make some conclusions: (1) The V_{OC} of both same and different area solar cells are almost the same, with good repeatability. (2) The smaller solar cells have higher J_{SC} comparing with larger solar cell. This is because the area, A, used to calculate the $J_{SC} = I_{SC}/A$ is the area of the mask aperture as shown in section 2.3.2 (mask used for ITO deposition). However, some collection is made outside of this area because of ITO deposition outside the mask area, and collection through the doped layers. For the smaller solar cells this leads to underestimation of area, and thus overestimation of J_{SC}. (4) Finally, none of the J_{SC} are verified by EQE, and rely on the calibration of the solar simulator. For all these reasons, an absolute and relative error in J_{SC} of at least 10 % should be assumed throughout.

3.3.2 Optimizing SiNW density for triple junction devices

As was shown in Section 3.1.3, the optimum density of SiNWs for single radial junction solar cells grown under these conditions is ~3.3×10^8/cm^2. We now examine whether a similar optimum exists for 3RJ solar cells, where other effects may be at play. For 3RJ SiNW solar cells, the total thickness of the stack is obviously greater than that of the single junction. In addition, at higher SiNW densities, non-uniform radial deposition along the length of the SiNW was also observed, which may impact the device performance [26]. Therefore, the optimum density of SiNWs remains to be determined for 3RJ solar cells.

In Figure 3.16, SEM images of the SiNWs and complete 3RJ a-Si:H solar cells (without ITO top contact) are presented. The density of silicon nanowire solar cells was calculated by counting the radial junctions without sputtered ITO top contact, as shown in the right row of images in Figure 3.19. The densities are 1.2×10^8/cm^2, 1.7×10^8/cm^2, 2.2×10^8/cm^2, 3.5×10^8/cm^2 and 4.3×10^8/cm^2. From Figure 3.19 one can see that the diameter of the silicon nanowire solar cells decreases from 670 to 540, 470, 420 and 340 nm as their density increases. This is expected because the flux of reactive species supplied by the plasma is constant while the total surface of the radial junctions increases with SiNW density. The same phenomenon has been observed in the single and double junction devices.

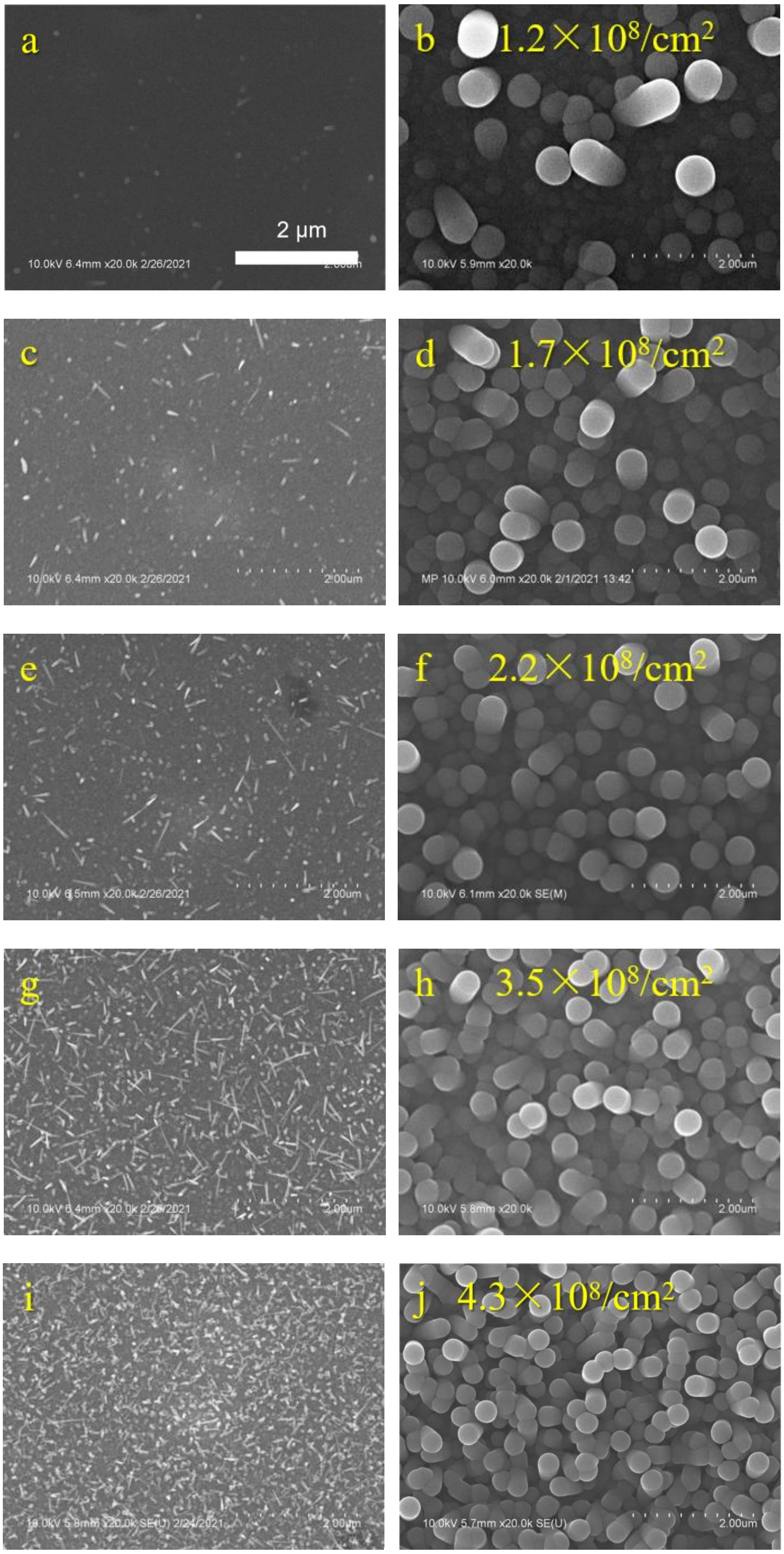

Figure 3.16 SEM images of SiNWs and 3RJ solar cells. Left row: SiNWs after VLS growth Right row: 3RJ solar cells with densities ranging from $1.2\times10^8/\text{cm}^2$ to $4.3\times10^8/\text{cm}^2$.

The J-V characteristics of 3RJ solar cells with different SiNW densities are presented in Figure 3.17. The V_{OC}, short circuit current density J_{SC}, FF and η of the best 3RJ solar cells are plotted as functions of SiNW densities in Figure 3.21(a)-(d), respectively. As expected, Figure 3.18 (a) shows that V_{OC} decreases as the density of SiNWs increases. At low SiNW density of $1.2\times10^8/\text{cm}^2$, a V_{OC} of 2.2 V is obtained but V_{OC} drops to 1.35 V for a density of $4.3\times10^8/\text{cm}^2$.

As discussed at the start of this section, a higher density of NWs increases the effective surface area of the devices. This increases the dark saturation current, I_0, compared to a planar device. Once this effect is not fully compensated by the increased short circuit current density J_{SC}, this will lead to a decreased V_{OC} (V_{OC} = kT ln (J_{SC}/J_0)) [30-32]. Indeed, light trapping is more efficient with increased SiNW density. Figure 3.18(b) shows a step increase in J_{SC}, but it flattens out for SiNW densities above $2.2\times10^8/\text{cm}^2$ reaching a maximum of 3.9 mA/cm^2 for a density of $4.3\times10^8/\text{cm}^2$. Surprisingly, Figure 3.18(c) shows that the fill factor of 3RJ solar cells increases quickly with SiNW densities from $1.2\times10^8/\text{cm}^2$ to $2.2\times10^8/\text{cm}^2$. Afterwards, the FF has a slow increase from SiNW density of $2.2\times10^8/\text{cm}^2$ to $4.3\times10^8/\text{cm}^2$. This can be attributed to poor electrical contact between the absorber layers and the planar areas between NWs, which increases in importance at low NW density. The devices with the lowest density of SiNWs ($1.2\times10^8/\text{cm}^2$) display an "S-curve", with a change of inflection around V_{OC}. This behavior is addressed in more detail in the next section.

The calculated efficiency of 3RJ solar cells as a function of SiNW density is shown in Figure 3.18(d), with a clear maximum at $2.2\times10^8/\text{cm}^2$, giving the best efficiency of 4.44%. At this point, the J_{SC} has increased to a higher value, but V_{OC} has not yet begun to dramatically decrease.

As expected, the SiNW density corresponding to the best performance is different in single and triple junction. The best density value decreases from $3.3\times10^8/\text{cm}^2$ in the case of the SJ in section 3.1.3 to $2.2\times10^8/\text{cm}^2$ in the case of the 3RJ. For 3RJ silicon nanowire solar cells, the optimum density is expected to be lower because they have a larger diameter than SJ.F

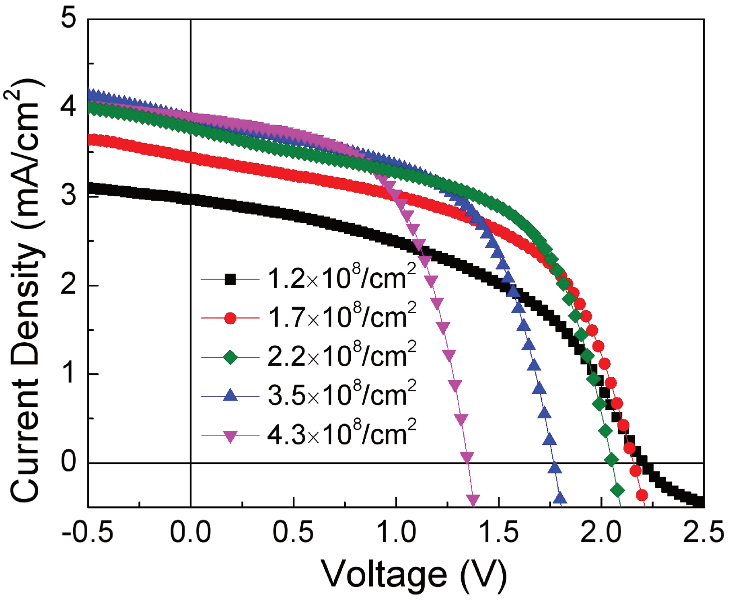

Figure 3.17. J-V characteristics of 3RJ solar cells with different SiNW densities ranging from $1.2\times10^8/\text{cm}^2$ to $4.3\times10^8/\text{cm}^2$.

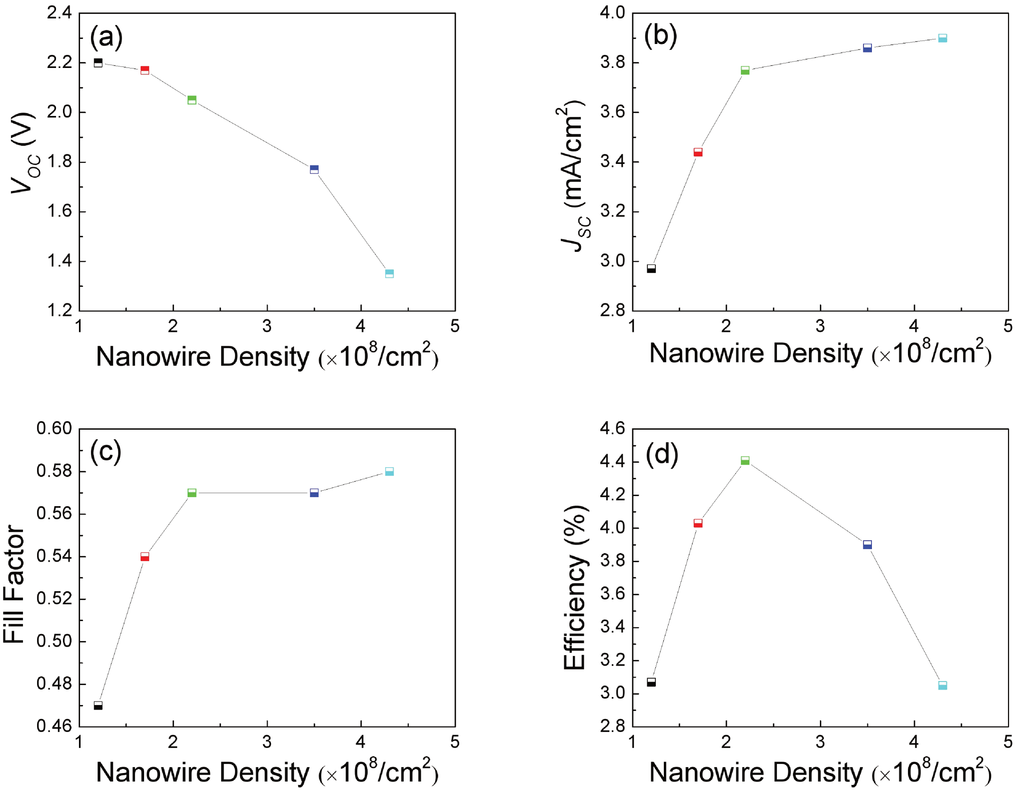

Figure 3.18 (a)-(d) V_{OC}, J_{SC}, FF and η of a-Si:H 3RJ solar cells as functions of SiNW density.

3.3.3 Top layer thickness and SiNW density effect in high V_{OC} 3RJ devices

For the devices shown above, a first guess was made that the ratios of the layer thicknesses in the 3J should go as 1:2:4 to approach current matching conditions. However, this estimation vastly oversimplifies the optimized choice possible of layer thicknesses for 3RJ solar cells. To nevertheless analyze the dependence of the device behavior based on this ratio, a set of samples have been fabricated, varying the thicknesses of the top layers. As already seen in Figure 3.17 above, the PV parameters achieved depend very strongly on the value of the NW density, particularly around the local efficiency optimum. Therefore, we have chosen devices with similar, elevated values of V_{OC} (2.11 to 2.2 V), as a proxy for local NW density, as this parameter is the hardest to control in this technology.

Two representative J-V curves of devices with areas of 0.125 cm^2 from each substrate are presented in Figure 3.19(a). Furthermore, the statistical spread of V_{OC} and J_{SC} for all working 0.125 cm^2 cells on each substrate are presented in Figures 3.19(b) and 3.19(c).

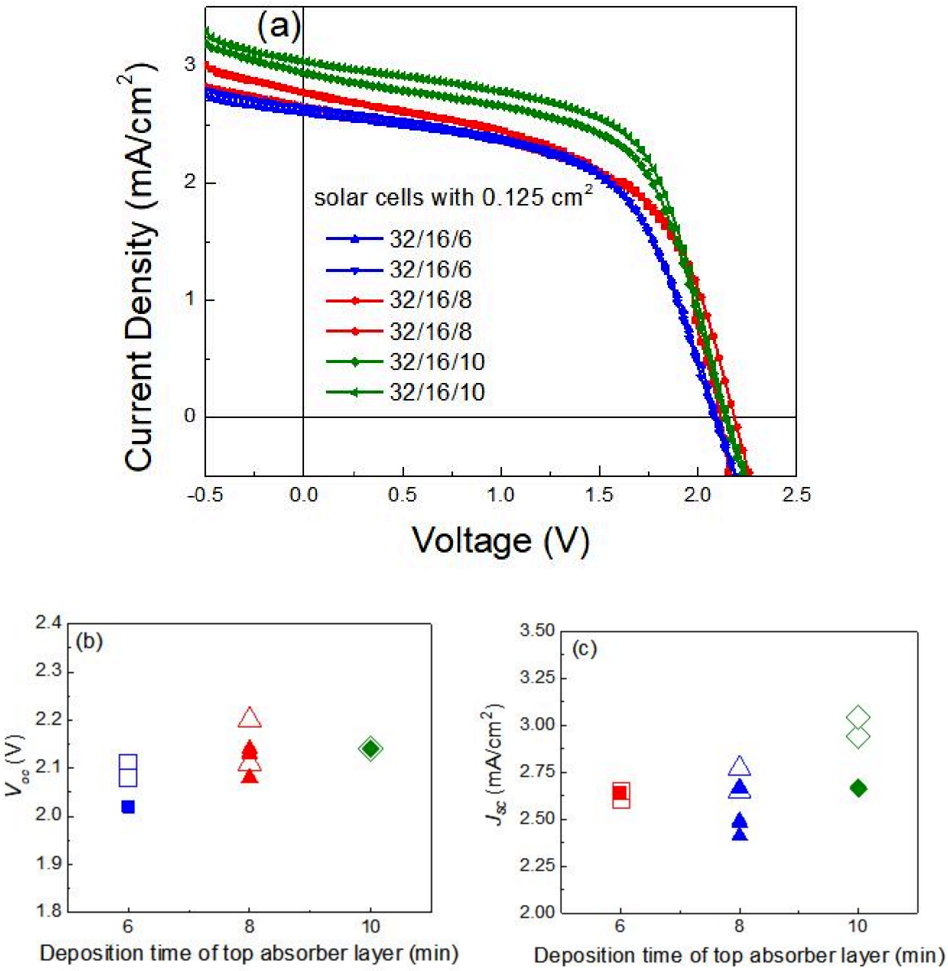

Figure 3.19 (a) J-V curves for SiNW 3RJ solar cells for three different deposition times (thicknesses) of the top cell. (b) V_{OC} and (c) J_{SC} values of all working cells on substrate, with cells of (a) highlighted as larger, open symbols.

The J-V curves of Figure 3.22(a) highlight two important facts: firstly, the elevated V_{OC} underlined in this work (targeted towards applications such as water splitting) is shown to be quite robust to variations in top layer thickness. Values above 2V are consistently produced. Secondly, the increasing thickness of the top i-layer seems to increase the overall J_{SC} (and the overall performance). As the J_{SC} in such structures is determined by the current-limiting cell [33-37], this suggests that the top-cell is limiting in the present design. One should also note that the ratio of deposition times should not be interpreted as a thickness ratio, as it would be for planar devices. Due to the RJ architecture, under constant plasma conditions, deposition rate will decrease with time as the SiNW increases in diameter and develops a larger surface area. Furthermore, the spread in values of J_{SC} on a single substrate (Figure 3.22c) shows the difficulty of optimizing such high V_{OC} devices. As one can infer from Figure 3.21, when targeting high V_{OC} values, one must use lower densities of NWs ($< 2\times10^8/\text{cm}^2$), and in this range of densities, the short circuit current density is very sensitive to NW density. In addition, process variations due to ZnO roughness, NW length, ITO contacts, and Ag spot placement will impact J_{SC}, while V_{OC} remains quite stable.

3.3.4 Comparison of light and dark J-V curves of SiNW 3RJ solar cells with different densities

Figure 3.20 presents the light and dark J-V curves of 3RJ solar cells with different SiNW densities. Normally, for a c-Si solar cell, the light and dark J-Vs are shifted versions of each other. But in figure 3.20, for the lowest SiNW density of $1.2\times10^8/\text{cm}^2$ (which give the highest V_{OC}) it is obvious to see that the J-V curves in the light and dark are very different. In particular, an S shape appears around V_{OC} in the light J-V curve, which may contribute to this effect. The origin of this S-shape phenomenon may be the non-ohmic contact between the ZnO:Al and SiNW solar cell. This will be addressed in the next section.

In addition, one can note that the value of J_{SC} measured does not represent a plateau in the J-V curve, especially for the higher densities of nanowires. This is due to the high level of recombination generated in the i-a-Si:H absorber layers. This is especially surprising, as for the higher density SiNW devices, these are the thinnest i-layers, and so should give the lowest recombination. In future work, a new strategy about improving deposition to achieve higher quality a-Si:H is worthy to be consider. Finally, for some curves, one can note some non-monotonicity in the curves around J_{SC} as Figure 3.21 (a). This indicates that the individual sub-cells are not well-matched, a further route for improvement.

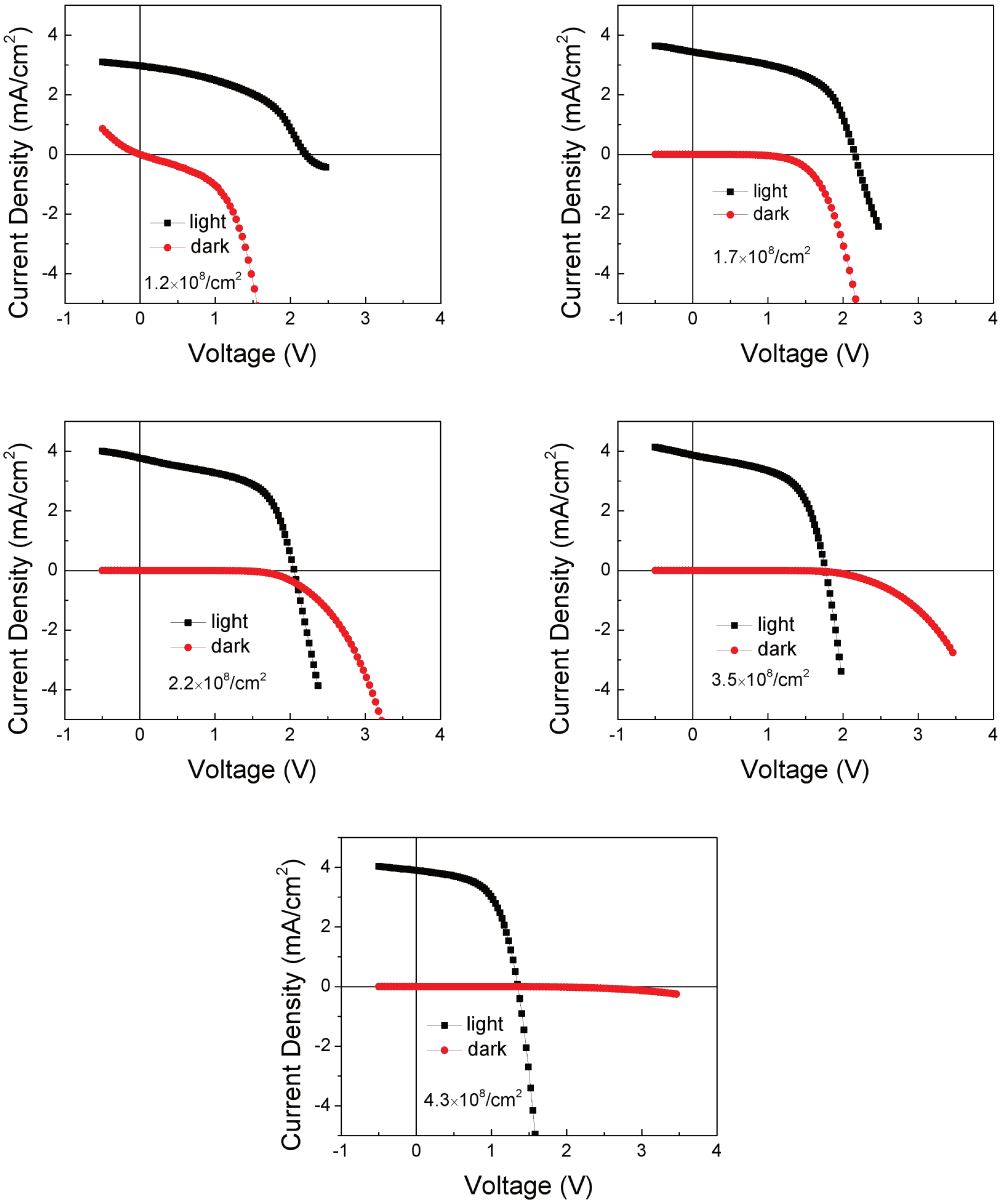

Figure 3.20 Light and dark J-V characteristics of 3RJ solar cells with different densities of SiNWs.

3.3.5 Larger scan range of 3RJ SiNW solar cells

To better understand the behavior of 3RJ solar cells, the J-V curves of some cells (with intermediate values of V_{OC} of 1.7 V and 1.98 V) have been acquired over a larger voltage range. The lower V_{OC} 3RJ solar cell is corresponding to a slightly higher SiNW density. Figure 3.21 (a) is the comparison of light and dark J-V of a 3RJ with V_{OC} of 1.7 V. We can see that the light J-V curve has “moguls”, or bumps, for the section where the voltage is under reverse bias. The dark J-V curve also has a "turn-on" in reverse bias, where the diode begins to fail. Indeed, Figure 3.21 (b) also shows an activated current in reverse bias (linear in log scale). However, around V_{OC}, neither the light nor the dark J-V have S shapes. In figure 3.21 (c), for the 3RJ with V_{OC} of 1.98 V, the dark J-V curve shows no interesting features, and an R_P like behavior in reverse bias. However, it shows both the bumps in reverse bias, and an S shape around V_{OC} under light. Comparing Figures 3.21 (b) and (d), the high V_{OC} SiNW solar cell has smaller J_0 and larger n value. We attribute the bumps and the S shape in the light J-V curves to the photo-generated minority carrier collection phenomena – the bumps to current mismatch between then cells, and the S-shape to a poor contact between the p-a-Si:H and the ZnO:Al at areas in between the SiNWs.

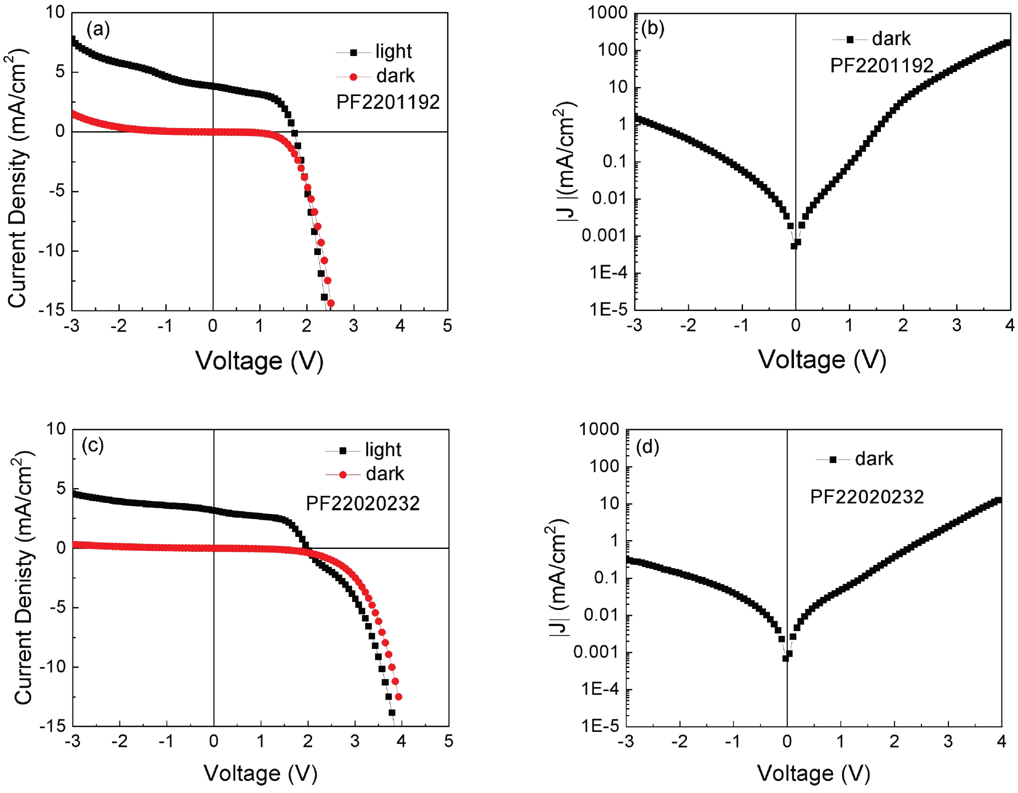

Figure 3.21 Larger scan range of light and dark J-V curves of 3RJ solar cells with different V_{OC}. (a) Comparison of light and dark J-V of 3RJ with V_{OC} of 1.7 V, (b) dark J-V of 3RJ with V_{OC} of 1.7 V ($\log_{10}|J_{0}|$ as a function of voltage). (c) Comparison of light and dark J-V of 3RJ with V_{OC} of 1.98 V. (d) dark J-V of 3RJ with V_{OC} of 1.98 V ($\log_{10}|J|$ as a function of voltage).

The device of Figure 3.21 (a) has been measured over an expanded current range, shown in Figure 3.22. Despite using voltages much higher than V_{OC} part, no S shape appears in the J-V curve at any point [whereas it showed up in Figure 3.21(c) just above V_{OC}]. Therefore, we can get the conclusion that more SiNWs can improve the S shape of solar cell, comparing with lower density SiNW solar cell. We also note that if the measurements of Figures 3.21(a) and 3.21(c) had only been done from J_{SC} to V_{OC}, these cells would be considered to be very similar, but their detailed physics are very different.

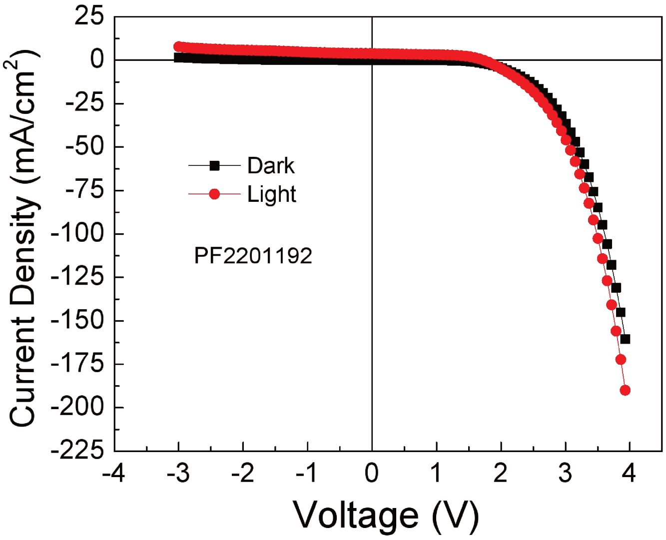

Figure 3.22 Current range expansion of figure 3.25(a), light and dark J-V curves of 3RJ with V_{OC} of 1.7V.

3.4 S-shape exploration

3.4.1 Planar solar cells with S shape in the J-V characteristics

In the previous section, we observe that S shaped curves occur frequently for low SiNW density 3RJ solar cells (with higher V_{OC}), but not for high SiNW density 3RJ solar cells. At this point of the chapter, we digress slightly to explore the origin of the S shape. The following results would not be limited to 3RJ cells but are applicable to architectures of cell.

In a low density SiNW solar cell, the structure approaches a planar one as the distance between NWs is so great. Therefore, we deposit planar PIN or NIP junction solar cells to investigate the origin of the S shape in our solar cells. The deposition conditions of planar PIN junction solar cells are the same as those of PIN radial junction, but without the p layer deposited at high temperature (600°C).

Figure 3.23 shows the J-V characteristics of planar solar cells with PIN and NIP structure, with the structure of the cell in the legend. We immediately note the S shape in the J-V curve for the PIN cell. The efficiency of the planar solar cell with NIP structure is better than that of PIN structure. For the V_{OC} of these two cells, the V_{OC} of PIN (0.85 V) is higher than that of NIP (0.77 V). But for J_{SC} and FF, the NIP structure is better than the PIN one.

The S shape may come from a number of sources. One possible source is a non-ohmic contact between the n type ZnO:Al and the bottom doped layer of the solar cell; another could be between the top doped layer and the ITO. As p-type a-Si:H is much more poorly doped than n-type, it seems probably that it is this layer giving a poor contact with the ZnO:Al that gives the S-curve for the PIN, and although the contact is better with the ITO, it still presents a small S-curve when in NIP configuration.

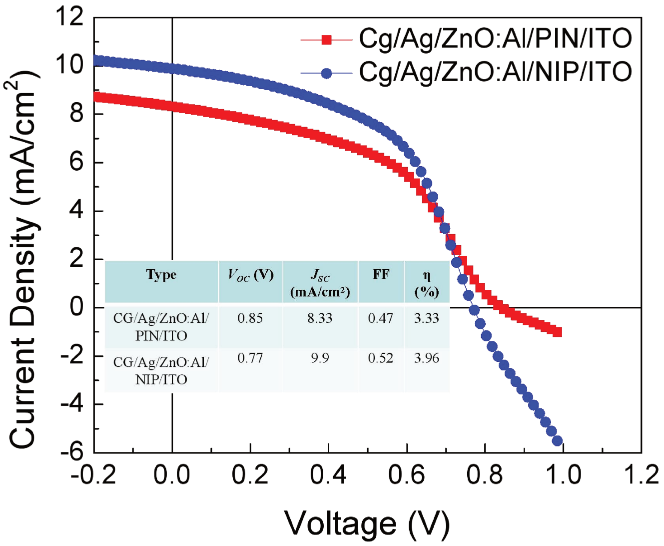

Type	V_{OC} (V)	J_{SC} (mA/cm^2)	FF	η (%)
CG/Ag/ZnO:Al/ PIN/ITO	0.85	8.33	0.47	3.33
CG/Ag/ZnO:Al/ NIP/ITO	0.77	9.9	0.52	3.96

Figure 3.23 J-V characteristics of PIN and NIP structure planar solar cells

To test this hypothesis, we reproduced the solar cells changing only the thickness of the ZnO:Al and nothing else. Figure 3.24 shows the J-V characteristics of planar solar cells with different thickness of ZnO:Al (100 nm and 300 nm). If the thickness of ZnO:Al becomes larger (300 nm), the V_{OC} and J_{SC} remain almost unchanged (9.4 to

9.7 mA/cm^2) but the FF is improved from 0.53 to 0.59, which results in the efficiency improvement from 3.83% to 4.42%. The change in FF is due to the decrease in the severity of the S-shape.

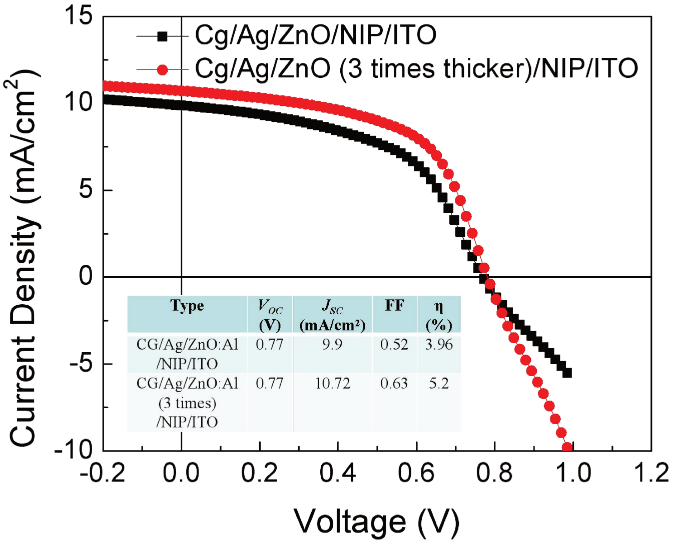

Type	V_{OC} (V)	J_{SC} (mA/cm²)	FF	η (%)
CG/Ag/ZnO:Al /NIP/ITO	0.77	9.9	0.52	3.96
CG/Ag/ZnO:Al (3 times) /NIP/ITO	0.77	10.72	0.63	5.2

Figure 3.24 J-V characteristics of planar solar cells with different thickness ZnO:Al substrate.

Table 3.9 The extracted parameters of planar solar cells with different thickness ZnO:Al substrate from figure 3.23

Type	V_{OC} (V)	J_{SC} (mA/cm^2)	FF	η (%)
Cg/Ag/ZnO/nip/ITO	0.77	9.9	0.52	3.96
Cg/Ag/ZnO (3 times) /nip/ITO	0.77	10.72	0.63	5.2

An explanation for the change in the contact quality between the ZnO:Al and the p-layer stems from the growth dynamics of ZnO:Al, as described in Figure 3.25, which shows the morphological properties of ZnO:Al growth related to the Ar pressure and substrate temperature. As the ZnO:Al film starts to grow, the grain size is small, the orientation of nuclei is random, and voids appear. The quality of thinner ZnO:Al is not good in the early stages. If the layer of ZnO:Al becomes thicker, the grain size will become larger, and the quality of crystal is improved. As this will improve doping efficiency and carrier mobility, the Schottky barrier with the solar cell will become a recombination junction, the R_S is improved and S shape is diminished.

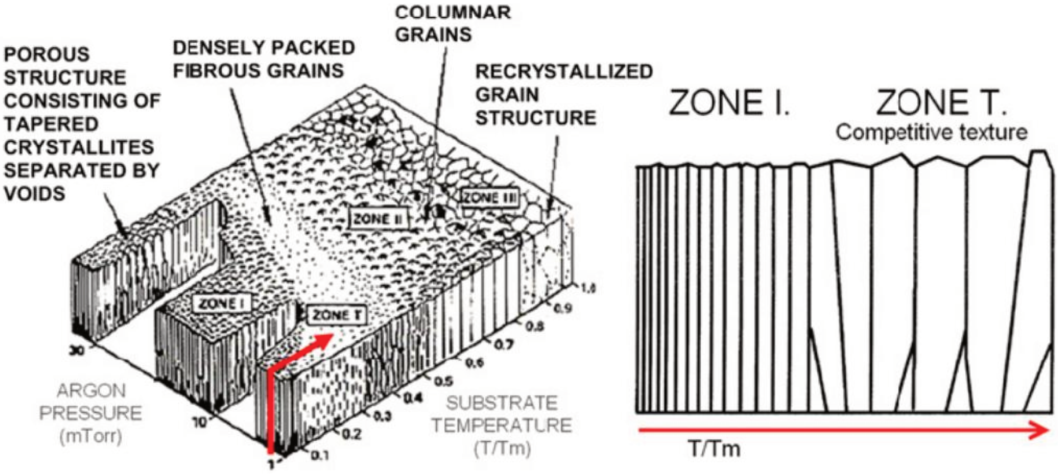

Figure 3.25 Relation between the argon pressure, substrate temperature and the films morphological properties of Thornton structure zone model extracted from [38].

Figure 3.26 shows the J-V characteristics of planar solar cells with different substrates, Cg/Ag/ZnO and soda lime glass/FTO. Table 3.10 shows the V_{OC}, J_{SC}, FF and η of planar PIN junction solar cells grown on different substrates. The solar cells with two kinds of substrates have almost the same V_{OC}. The solar cell with FTO substrate has current density of 11.55 mA/cm^2, which is higher than that with Cg/Ag/ZnO substrate of 8.33 mA/cm^2. It is notable that the S shape disappears in the solar cell with FTO substrate. This also illustrates that the S shape comes from the substrate or the interface between substrate and p layer of the solar cell.

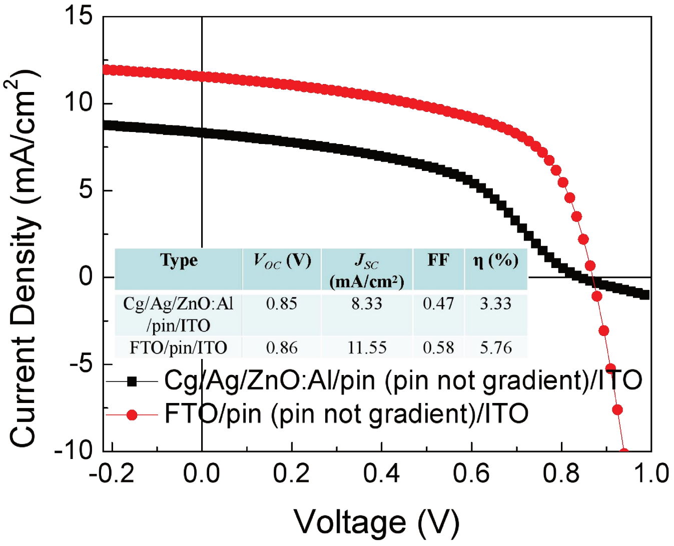

Type	V_{OC} (V)	J_{SC} (mA/cm^2)	FF	η (%)
Cg/Ag/ZnO:Al /pin/ITO	0.85	8.33	0.47	3.33
FTO/pin/ITO	0.86	11.55	0.58	5.76

Figure 3.26 J-V characteristics of planar PIN junction solar cells with different substrates

Table 3.10 The extracted parameters of planar PIN junction solar cells with different substrates from figure 3.25

Type	V_{OC} (V)	J_{SC} (mA/cm^2)	FF	η (%)
Cg/Ag/ZnO/pin/ITO	0.85	8.33	0.47	3.33
FTO/pin/ITO	0.86	11.55	0.58	5.76

In a word, the origin of the S curve becomes clear. When decreasing the density of SiNWs, the amount of absorber layer conducting current through an ohmic ZnO:Al/p type c-Si NW contact is replaced by planar layers going through a direct ZnO:Al/p-a-Si:H contact, which is not ohmic. This is graphically illustrated in Figure 3.27.

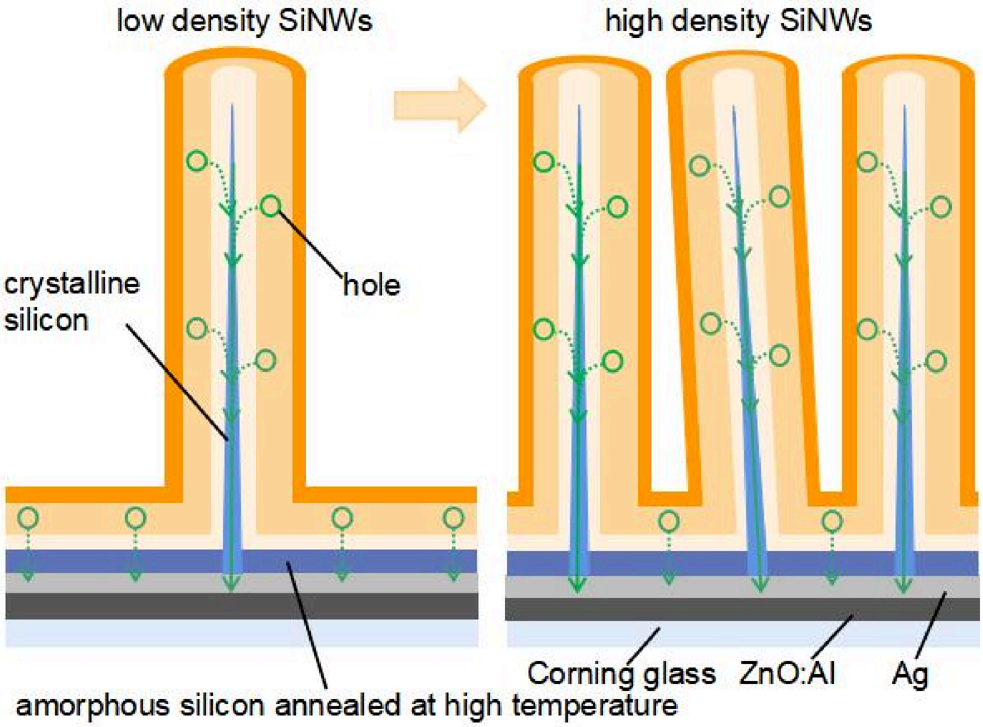

Figure 3.27 Representation of importance of NW density on preferred current path of photo-generated holes. As NW density increases, more carriers are produced in RJs and pass through the ohmic p type c-Si NW/ZnO:Al contact.

The S-shape observed in low SiNW density devices is caused by planar device growth making direct contact with the ZnO:Al and producing a non-ohmic contact, giving a lower limit to the density of NWs. A poor contact between ZnO:Al and p type a-Si:H deposited at 600 °C is formed in planar regions between NWs. We also measured the conductivity of p type a-Si:H deposited at 600 °C. It has low conductivity of 10^{-8} S/cm. This is important for this work as it is the lower densities of NWs that give the highest V_{OC} values.

3.5 SiNW solar cells: from single to double and triple junction

In this chapter, we now compare the best single, double, and triple junction solar cells made during the course of this thesis. We first compare planar junction devices before considering 3RJ devices. We will also compare the performance of the double and triple junctions to the maximum possible performance based on the performance of the single junction. According to the single diode model describing a solar cell, one can use the formula V_{OC}= nkT ln(J_{SC}/J_0) to describe the tendency of V_{OC} as a function of J_{SC}. All else remaining equal, if the current density becomes lower, the V_{OC} will also decrease. The J_{SC} can, at best, be equally divided between the junctions.

3.5.1 Single, double and triple junction planar solar cells

The single, double and triple junction planar solar cells are compared in Figure 3.28, and the associated solar cell parameters are shown in Table 3.11.

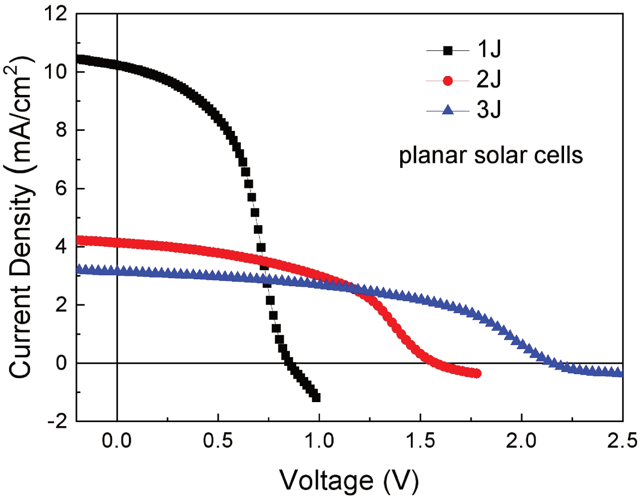

Figure 3.28 J-V characteristics of single, double and triple PIN junction planar solar cells

Table 3.11 The extracted parameters from J-V characteristics of single, double and triple PIN junction planar solar cells

Device	V_{OC} (V)	J_{SC} (mA/cm^2)	FF	η (%)
1J	0.85	10.23	0.51	4.44
2J	1.57	4.13	0.47	3.05
3J	2.17	3.13	0.49	3.33

The V_{OC} of the single, double and triple planar junction solar cells are 0.85 V, 1.57 V and 2.17 V, respectively. On the grounds of V_{OC}= nkT ln(J_{SC}/J_0) and using the parameters of the 1J, the ideal V_{OC} of a 2J would be 1.61~1.65 V, and that of a 3J around 2.27~2.46 V. So if we assume J_0 for each kind of solar cell is the same, the real V_{OC} of the 2J is very close to the highest possible expected value. Taking the value of J_{SC} and splitting ideally between solar cells, the maximum J_{SC} for 2J and 3J are 5.1 mA/cm^2 and 3.4 mA/cm^2, respectively. The real J_{SC} is significantly lower than the ideal J_{SC}. This may be because of poor current matching, or because maybe due to light absorption by the tunnel junction.

3.5.2 Single, double and triple SiNW solar cells

As shown in Figure 3.29 and Table 3.12, the V_{OC} values of the 1RJ, 2RJ, and 3RJ SiNW solar cells are 0.79 V, 1.34 V and 2.05 V, respectively. Using the above calculation, the expected V_{OC} for a double junction based on a single junction with 0.79V would be between 1.54 and 1.51V, depending on the value of n (n=1 or n=2), ignoring voltage losses in the tunnel junction. For a triple junction, the expected values would be between 2.11V and 2.28V, so in fact, the voltage in the triple junction is very close to the maximum achievable value if we assume constant values of J_0 for all the subcells.

The J_{SC} values compared to the expected maximum are not as impressive for the triple junction. The 14.8 mA/cm^2 of the single junction could be divided between two junctions giving 7.4 mA/cm^2 each (actually 7.1 mA/cm^2) or three junctions, giving 4.9 mA/cm^2 (actually 3.8 mA/cm^2). For the triple junction, some current balancing is obviously still necessary to improve the absolute efficiency. The FF deceases from 1

RJ to 3 RJ mainly due to an increase of series resistance. This is probably due to the tunnel junctions.

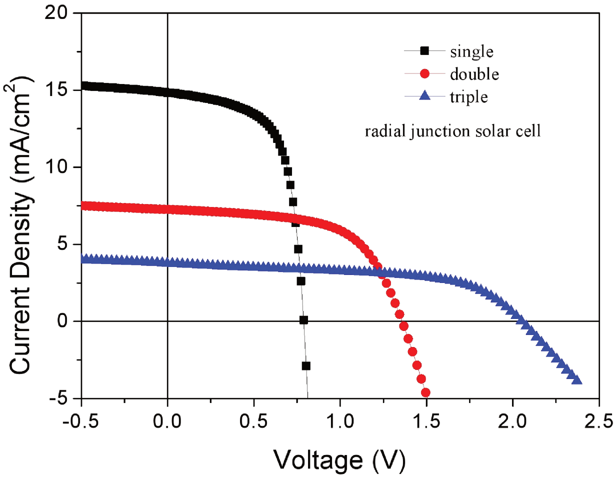

Figure 3.29 J-V characteristics of single, double and triple radial junction solar cells

Table 3.12 V_{OC}, J_{SC}, FF and power conversion efficiency (PCE) of single, double and triple junction SiNW solar cells.

Device	V_{OC} (V)	V_{MPP} (V)	J_{SC} (mA/cm^2)	FF	PCE (%)
1RJ	0.79	0.63	14.8	0.65	7.6%
2RJ	1.34	1.03	7.1	0.62	5.9%
3RJ	2.05	1.59	3.8	0.57	4.4%

3.5.3 Single, double and triple SiNW solar cells in dark

The 1RJ, 2RJ, and 3RJ solar cells have also been compared with their dark J-V parameters. Table 3.13 shows the parameters obtained from fitting the dark J-V characteristics of figure 3.30. The 1RJ solar cell has the smallest J_0. The n for 1RJ is 2.28, it means that there are many defects in the solar cell. For the 2RJ with an n of 5.23 and the 3RJ with an n of 7.78, compared with 1RJ, the n value has more than doubled and tripled. This shows that more recombination per junction occurs in the 2RJ and 3RJ.

Out of curiosity, the V_{OC} of 1RJ, 2RJ and 3RJ are also calculated by V_{OC}= nkT ln(J_{SC}/J_0). Comparing with V_{OC} measured by light J-V, the V_{OC} by equation is larger, but so many assumptions go into this calculation (identical cells, perfect current matching) that the validity of performing this calculation in this way remains open for debate.

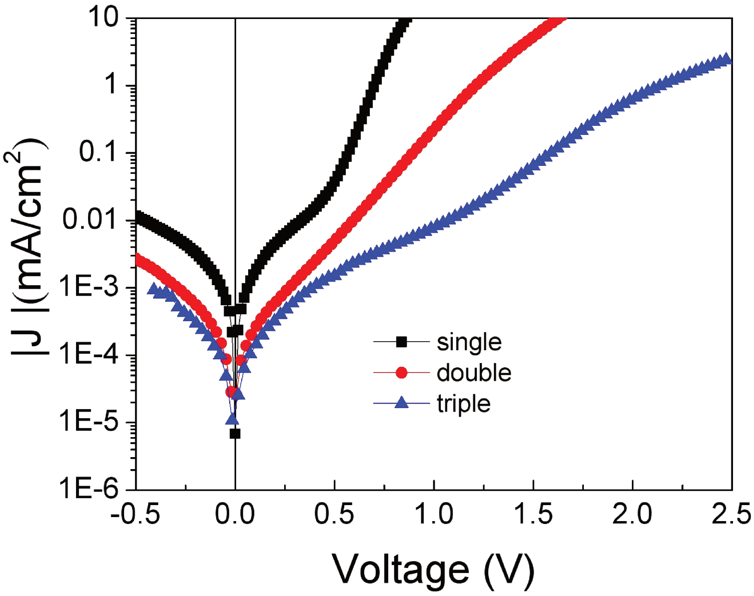

Figure 3.30 Dark J-V characteristics of 1RJ, 2RJ and 3RJ solar cells

Table 3.13 Extracted parameters from dark J-V characteristics of 1RJ, 2RJ and 3RJ solar cells

Device	**J_0 (mA/cm^2)**	**n**	**V_{OC} by equation (V)**	**V_{OC} by J-V (V)**	**J_{SC} (mA/cm^2)**
1RJ	6.87×10^{-6}	2.28	0.86	0.79	14.83
2RJ	1.35×10^{-4}	5.23	1.47	1.34	7.07
3RJ	3.7×10^{-5}	7.78	2.32	2.05	3.77

3.6 Conclusion

In this chapter, different strategies have been deployed to optimize and understand 1RJ, 2RJ and 3RJ SiNW solar cell performance. For the 1RJs, results using different layer doping (including gradients) as well as optimizing SiNW density were shown. The 1RJ solar cells with density of 3.3×10^8/cm^2 have the best efficiency. In addition, the cells were modelled to obtain V_{bi}, J_{ph} and V_{μ}. Comparing with light and dark J-V, the a-Si:H radial junction SiNW solar cells performance are limited by recombination in the i-layer.

The performance of 2RJ solar cells was also tried to be improved by several strategies: tunnel junction optimization, doped layer optimization, absorber layer thickness, and SiNW density. The 2RJ solar cells with NW density of $2.4\times10^8/cm^2$ have the best efficiency.

Next, 3RJs were fabricated on the basis of the single and double junction solar cells. Once again, the V_{OC} of the 3RJ depends on the NW density. When the NW density is below $2.5\times10^8/cm^2$, the V_{OC} is extremely sensitive to NW density. A density of $2.2\times10^8/cm^2$ shows the best efficiency of 4.4%, and solar cells with V_{OC} above 2 V are consistently produced. Sensitivities to relative layer thicknesses were also explored, showing that the V_{OC} values are quite robust.

The S shape that occurred in some J-V curves was also investigated. We find that the S shape is due to a poor contact between ZnO:Al and p type a-Si:H, as the S shape disappears when using FTO as substrate. The S shape is improved by a high density of SiNWs, because the contact between the p-a-Si:H and the ZnO:Al becomes limited.

Finally, we compare the best single, double and triple radial junction SiNW solar cells to each other; they show efficiencies of 7.6%, 5.9% and 4.4%, respectively, and for which the V_{OC} reaches 0.79 V, 1.34 V and 2.05 V, respectively. The triple radial junction solar cells therefore provide a V_{MPP} (1.59 V) that is sufficient for water-splitting, which is a main goal of this thesis. The next chapter will examine sources of randomness that arise during the production of 3RJ SiNW solar cells that lead to variations in the final performance despite what appears to be identical process conditions.

References

[1] F Edelman, A Chack, R Weil, R Beserman, Yu.L Khait, P Werner, B Rech, T Roschek, R Carius, H Wagner, W Beyer. *Structure of PECVD Si:H films for solar cell applications,* Solar Energy Materials and Solar Cells. 2003. **77**(2):p. 125-143.

[2] D. Pysch, C. Meinhardt, K. Ritzau, M. Bivour, K. Zimmermann, C. Schetter, M. Hermle, S. W. Glunz. *Comparison of intrinsic amorphous silicon buffer layers for silicon heterojunction solar cells deposited with different PECVD techniques,* IEEE Photovoltaic Specialists Conference. 2010.

[3] O. Gabriel, S. Kirner, C. Leendertz, M. Gerhardt, A. Heidelberg, H. Bloeß, R. Schlatmann, B. Rech. *Large area PECVD of a-Si:H/a-Si:H tandem solar cells,* Physica Status Solidi C, 2011, **8**(10):p. 2982-2985.

[4] S. Morrison, U Das, A. Madan. *Deposition of thin film silicon using the pulsed PECVD and HWCVD techniques,* Solar Energy Materials and Solar Cells, 2003, **76**(3):p. 281-291.

[5] M. I. Kabir, S. A. Shahahmadi, V. Lim, S. Zaidi, K. Sopian and N. Amin. *Amorphous silicon single-junction thin-film solar cell exceeding 10% efficiency by design optimization,* International Journal of Photoenergy, 2012, **2012** (1).

[6] W. Futako, S. Takeoka, C. Fortmann and I. Shimizu. *Fabrication of narrow-band-gap hydrogenated amorphous silicon by chemical annealing,* Journal of Applied Physics, 1998, **84**(3):p.1333-1339.

[7] C. R. Wronski, J. M. Pearce, R. J. Koval, A. S. Ferlauto, R. W. Collins. *Progress in Amorphous Silicon Based Solar Cell Technology,* RIO 02-World Climate & Energy Event, Rio de Janeiro, Brazil, 2002, p.67-72.

[8] E. Fefer, Y. Shapira, *Direct determination of the band-gap states in hydrogenated amorphous silicon using surface photovoltage spectroscopy,* Applied Physics Letters, 1995, **67**(3):p. 371-373.

[9] M. Stutzmann, *The defect density in amorphous silicon,* Philosophical Magazine B, 1989, **60** (4):p. 531-546.

[10] T. Uesugi, H. Ihara, H. Matsumura, *The Staebler-Wronski Effect in*

Hydro-Fluorinated Amorphous Silicon Prepared Using the Intermediate Species SiF$_2$, Japanese Journal of Applied Physics, 1985, **24** (8): p. 909.

[11] M. Meunier, T. Gattuso, D. Adler, and J. Haggerty, *Hydrogenated amorphous silicon produced by laser induced chemical vapor deposition of silane,* Applied Physics Letters, 1983, **43**(3):p. 273-275.

[12] M. Dua and S. Zhang.*Topological defects and the Staebler-Wronski effect in hydrogenated amorphous silicon,* Applied Physics Letters, 2005, **87**(19):p. 191903.

[13] M. Stutzmann, W. Jackson, C. Tsai. *Kinetics of the Staebler-Wronski effect in hydrogenated amorphous silicon,* Applied Physics Letters, 1984, 45(10):p. 1075-1077.

[14] T. Krüger. *On the origin of the Staebler-Wronski effect,* Journal of Applied Physics, 2006, **99** (6):p. 063509.

[15] A. Kazanskii,V. Kiselev, E. Silaev, V. Vavilov. *On the role of surface phenomena in the Staebler-Wronski effect,* Physica Status Solidi (a), 1983, **76**(1):p. 337-343.

[16] R. Prasad, S. Shenoy. *Staebler-Wronski effect in hydrogenated amorphous silicon,* Physics Letters A, 1996, 218 (1-2):p. 85-90.

[17] S. Misra, L. Yu, W. Chen, M. Foldyna, P. Roca i Cabarrocas, *A review on plasma-assisted VLS synthesis of silicon nanowires and radial junction solar cells,* Journal of Physics D: Applied Physics, 2014, **47** (39): p. 393001.

[18] Y. Kuang, M. D. Vece, J. K. Rath, L. van Dijk, REI Schropp, *Elongated nanostructures for radial junction solar cells,* Reports on Progress in Physics, 2013, **76**(10), p.106502.

[19] M. M. Adachi, M. P. Anantram, K. S. Karim, *Optical of properties of crystalline-amorphous core-shell siliocn nanowires,* Nano Letters, 2010, **10**(10): p.4093-4098.

[20] B. M. Kayes, H. A. Atwater, N. S. Lewis, *Comparsion of the device physics principles of planar and radial p-n junction nanorod solar cell,* Journal of Applied Physics, 2005, **97** (11):p. 114302.

[21] E. Garnett, P. Yang, *Light trapping in silicon nanowire solar cells,* Nano Letters, 2010, **10**(3), p.1082-1087.

[22] S. Benagli, D. Borrello, E. Vallat Sauvain, J. Meier, U. Kroll, J. Hoetzel, J. Bailat,

J. Steihnhauserm, M. Marmelo, G. Monteduro, L. Castens, *High-effciency amorphous silicon devices on LPCVD-ZnO TCO prepared in industrial KAITM-M R&d reactor,* in: 24th EUPVSEC, Hamburg Germany. 2009, p. 2293-2298.

[23] S. Misra, *Single and tandem radial junction silicon thin film solar cells based on PECVD grown crystalline silicon nanowire arrays,* PhD thesis, Ecole Polytechnique, 2015.

[24] L. Dai, *Silicon nanowire solar cells with μc-Si:H absorbers for tandem radial junction devices*, PhD thesis, Ecole Polytechnique, 2019.

[25] J. Tang, *From Silicon to Germanium Nanowires: growth processes and solar cell structures,* PhD thesis, Ecole Polytechnique, 2017.

[26] S. Misra, L. Yu, M. Foldyna, P. Roca i Cabarrocas, *High efficiency and stable hydrogenated amorphous silicon radial junction solar cells built on VLS-grown silicon nanowires,* Solar Energy Materials and Solar Cells, 2013, **118**: p. 90-95.

[27] Y. Cao, Z. Ge, X. Jiang, J. Xu, L. Xu,W. Li, L. Yu, K. Chen, *Light Harvesting and Enhanced Performance of Si Quantum Dot/Si Nanowire Heterojunction Solar Cells,* Particle & Particle Systems Characterization, 2016, **33**:p. 38-43.

[28] S. Shiu, S. Lin, S. Hung, C. Lin, *Influence of pre-surface treatment on the morphology of silicon nanowires fabricated by metal-assisted etching,* Applied Surface Science, 2011, **257**(6):p. 1829.

[29] W. Cheng, M. H. Richter, M. M. May, J. Ohlmann, D. Lackner, F. Dimroth, T. Hannappel, H. A. Atwater, H. Lewerenz, *Monolithic Photoelectrochemical Device for Direct Water Splitting with 19% Efficiency,* ACS Energy Letters, 2018, **3** (8):p. 1795-1800.

[30] J. Oh, H.C. Yuan, H. M. Branz, *An 18.2%-efficient black-silicon solar cell achieved through control of carrier recombination in nanostructures,* Nature Nanotechnology 2012, **7**:p.74-748.

[31] Y. Dan, Kwanyong Seo, Kuniharu Takei, Jhim H. Meza, Ali Javey, Kenneth B, Crozier, *Dramatic Reduction of Surface Recombination by in Situ Surface Passivation of Silicon Nanowires*, Nano Letters, 2011, **11**(6):p. 2527-2532.

[32] M. Gharghi, E. Fathi, B. Kante, S. Sivoththaman, X. Zhang, *Heterojunction*

silicon microwire solar cells, Nano Letter, 2012, **12**(12):p. 6278-6282.

[33] T. Repmann; J. Kirchhoff; W. Reetz; F. Birmans; J. Muller, B. Rech, *Investigations on the current matching of highly efficient tandem solar cells based on amorphous and microcrystalline silicon*, Proceedings of 3rd World Conference on Photovoltaic Energy Conversion, 2003, May, 11-18.

[34] R. S. Crandall, *Modeling of thin film solar cells: Uniform field approximation*, Journal of Applied Physics, 1983, **54**:p. 7176.

[35] E. Köhnen, M. Jošt, A. B. Morales-Vilches, P. Tockhorn, A. Al-Ashouri, B. Macco, L. Kegelmann, L. Korte, B. Rech, R. Schlatmann, B. Stannowski, S. Albrecht, *Highly efficient monolithic perovskite silicon tandem solar cells: analyzing the influence of current mismatch on device performance,* Sustainable Energy & Fuels, 2019, **3**:p. 1995.

[36] M. Bonnet-Eymard, M. Boccard, G. Bugnon, F. Sculati-Meillaud, M. Despeisse, C. Ballif, *Optimized short-circuit current mismatch in multi-junction solar cells,* Solar Energy Materials and Solar Cells, 2013, **117**: p.120-125.

[37] C. Ulbrich, C. Zahren, A. Gerber, B. Blank, T. Merdzhanova, A. Gordijn, and U. Rau, *Matching of Silicon Thin-Film Tandem Solar Cells for Maximum Power Output,* Interbational Journal of Photoenergy, 2013, **2013**:p.1.

[38] C. Charpentier, P. Prod'homme, I. Maurin, M. Chaigneau, P. Roca i Cabarrocas, *X-Ray diffraction and Raman spectroscopy for a better understanding of ZnO:Al growth process*, EPJ Photovoltaics, 2011, **2**: p. 25002.

Chapter 4 "Repeatable" Influence of NW Density on Solar Cell Performance

The NW density can be well controlled by a top-down patterning technology [1-6]. However, SiNWs grown using our VLS method (using PECVD) do not use lithography to define their position on the substrate [7]. Subsequently, for the 3RJ solar cells grown by PECVD based on those SiNWs, it is hard to achieve a narrow distribution of V_{OC} values; the V_{OC} can have variations within the same batch, as can be seen in the previous chapter. Because the V_{OC} of solar cell heavily depends on the NW density (see Figure 3.21 in chapter 3), we suspect that the variations in V_{OC} are mainly due to changes in the NW density, even when experimental conditions are carefully reproduced.

In this chapter, the origin of this NW density variability is explored by in-situ ellipsometry and SEM measurements. Furthermore, we will compare the characteristics of solar cells having similar values of V_{OC} in order to try to determine what are the reasons behind the variations in NW density.

4.1 What kinds of randomness are present?

To give an example of the randomness observed in our process, we present the following experimental results. In this experiment, the same nominal thickness of 0.1 nm Sn catalyst was deposited on the same batch of ZnO:Al/Ag/CG glass substrates. After Sn evaporation, the substrates are transferred into the PECVD chamber for SiNW and solar cell growth. The performance of three runs of 3RJ SiNW solar cells produced on the same batch of substrates and Sn evaporation are shown in Figure 4.1. In these experiments the only parameter varied was the deposition time of the absorber layer of the top cell; for a typical a-Si:H solar cell, we would expect an important variation in J_{SC}, but little change in V_{OC}. The solar cell parameters (V_{OC}, J_{SC}, FF and efficiency) are presented in Table 4.1. We can see that the V_{OC} and J_{SC} of these cells vary to a large degree. In particular, the V_{OC} of these solar cells are 1.83 V, 1.68 V and 1.59 V. As all the process parameters were the same, we suspect that the density of SiNWs changed from one run to another for some unknown reason, as we have shown in the previous chapter that the V_{OC} strongly depends on the NW density. Therefore, we start by taking SEM images of these same batch sample to support our conjecture.

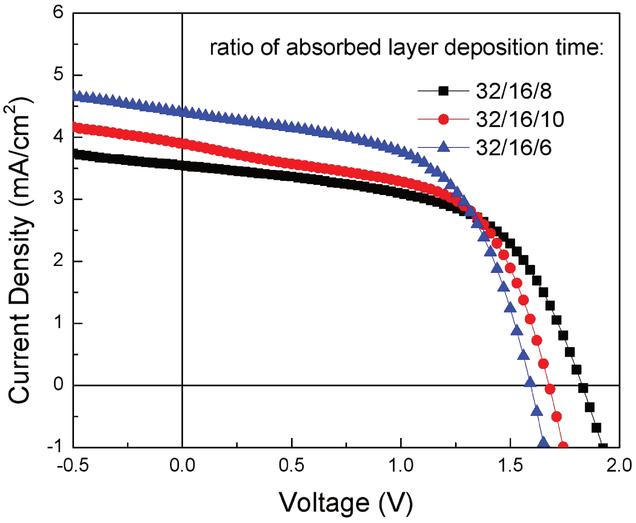

Figure 4.1 The J-V performance of 3RJ SiNW solar cells with different absorber layer thickness from the same batch of Sn catalyst deposition.

Table 4.1 V_{OC}, J_{SC}, FF and efficiency of 3RJ SiNW solar cells from figure 4.2.

Bottom/middle/top i layer deposition time (min)	**V_{OC} (V)**	**J_{SC} (mA/cm^2)**	**FF**	**Efficiency (%)**
32/16/6	1.59	4.4	0.57	3.99
32/16/8	1.83	3.55	0.56	3.64
32/16/10	1.68	3.91	0.57	3.74

Figure 4.2 shows SEM images from three samples of the same batch substrates and Sn evaporation after solar cell growth (samples from figure 4.1). As expected their NW density is different. The NW density is varying from $3.5\times10^8/\text{cm}^2$ to $4\times10^8/\text{cm}^2$. From the last chapter, we know that the SiNW solar cells performances (V_{OC} in particular) are influenced by SiNW density, hence we can attribute the V_{OC} variation in the same batch of samples to a variation in the NW density. Furthermore, because we deposit in theory the same nominal thickness of Sn on substrates, therefore we suppose that the NW density is not only determined by the nominal thickness of Sn catalyst.

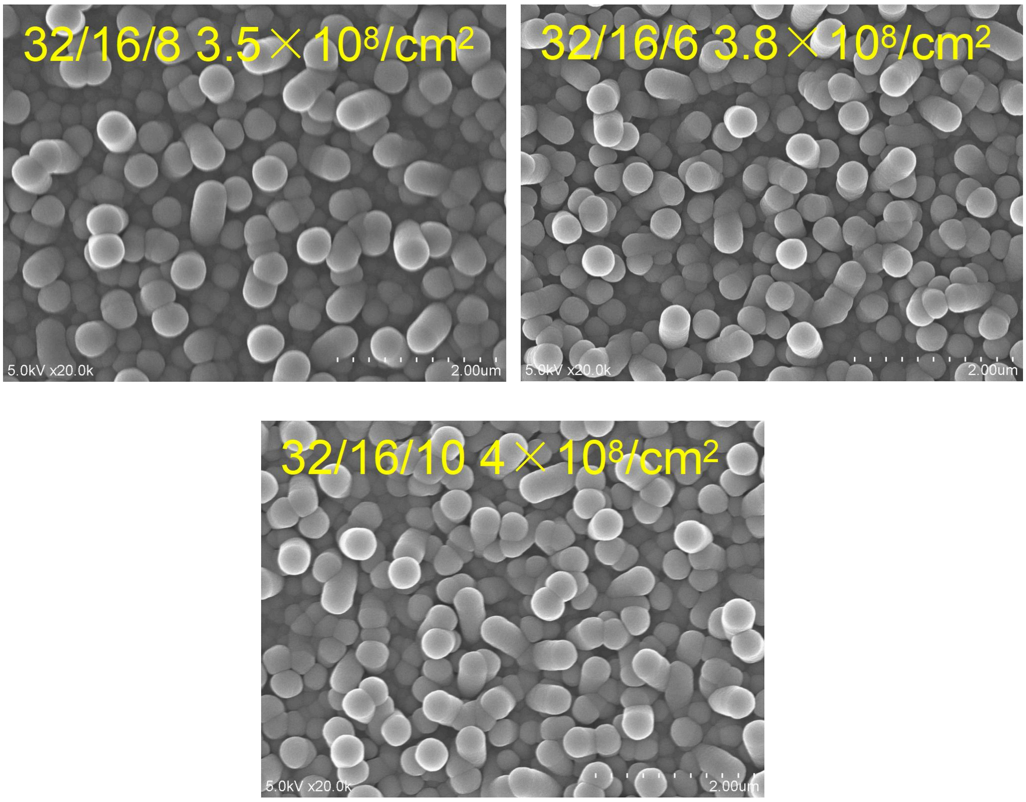

Figure. 4.2 Morphology of 3RJ SiNW solar cells obtained under the same nominal conditions, except for the deposition time of the top absorber layer (6, 8 and 10 minutes).

4.2 Where does the randomness come from?

In order to know where the randomness comes from, we use optical methods to investigate each step of the SiNW solar cell growth process. As shown in chapter 2, the SiNW solar cell growth process includes Sn evaporation, H_2 plasma treatment to form Sn drops, and NW growth. Therefore, we used: i) ex-situ ellipsometry to characterize the substrate before and after Sn evaporation and ii) in situ ellipsometry to characterize the effects of the H_2 plasma on the Sn layer and iii) in-situ elllipsometry to characterize the first stages of SiNW growth. Finally, SEM was used for investigating the SiNW radial junction density.

4.2.1 ZnO:Al substrate

The effect of changes in the surface of ZnO:Al substrates on the solar cell growth process is of great interest here. We placed a ZnO:Al/Ag/CG substrate into PECVD chamber and measured the in-situ ellipsometer spectra under vacuum at the same temperature as the processes for 3RJ SiNWs solar cell growth: at 250 °C for the H_2 treatment, and at 600 °C for SiNWs growth. As shown in Figure 4.3 (a), intensity as a function of time from in-situ ellipsometry spectra of ZnO:Al substrate, the intensity at 5.5 eV suddenly changes from 0.25 to 0.21 while the chamber goes to vacuum in the initial process. Then, as the temperature is increased up to 250 °C, the intensity further decreases from around 0.22 down to 0.19. Due to the inertia of the heating system, there is an overshoot above the nominal value and the temperature reaches 265 °C before stabilizing at 250 °C, therefore, the intensity will go back a little bit from 600 s to 1800 s. Afterwards, the temperature is raised up to 617 °C, and then goes back to 600 °C. But if keep annealing at 600 °C (this range is marked), it will make the intensity go down. Since 4100 s, the chamber cools down, the intensity rises up, but it will not go back as before. In a word, we can know that the vacuum and temperature both affect the signal intensity due to a change of the position of the sample in the chamber and due to possible change of the surface of ZnO:Al substrates.

To ensure that the surface is really changing (and that it is not just the alignment that is shifting), we also monitor the value of Δ during the heating steps. Δ is the phase change difference (refer to section 2.4.7). Figure 4.4 (b) shows the Δ changing as a function of time, the Δ increases from 30° to 33.4° as the temperature rising up to 617°C, then the Δ decreases and keep stable at 32° while the temperature goes down and keep stable at 600°. After that, the Δ decreases while chamber cooling down. Therefore, we can know that the cooling or heating of ZnO:Al sample will affect the ellipsometry spectra.

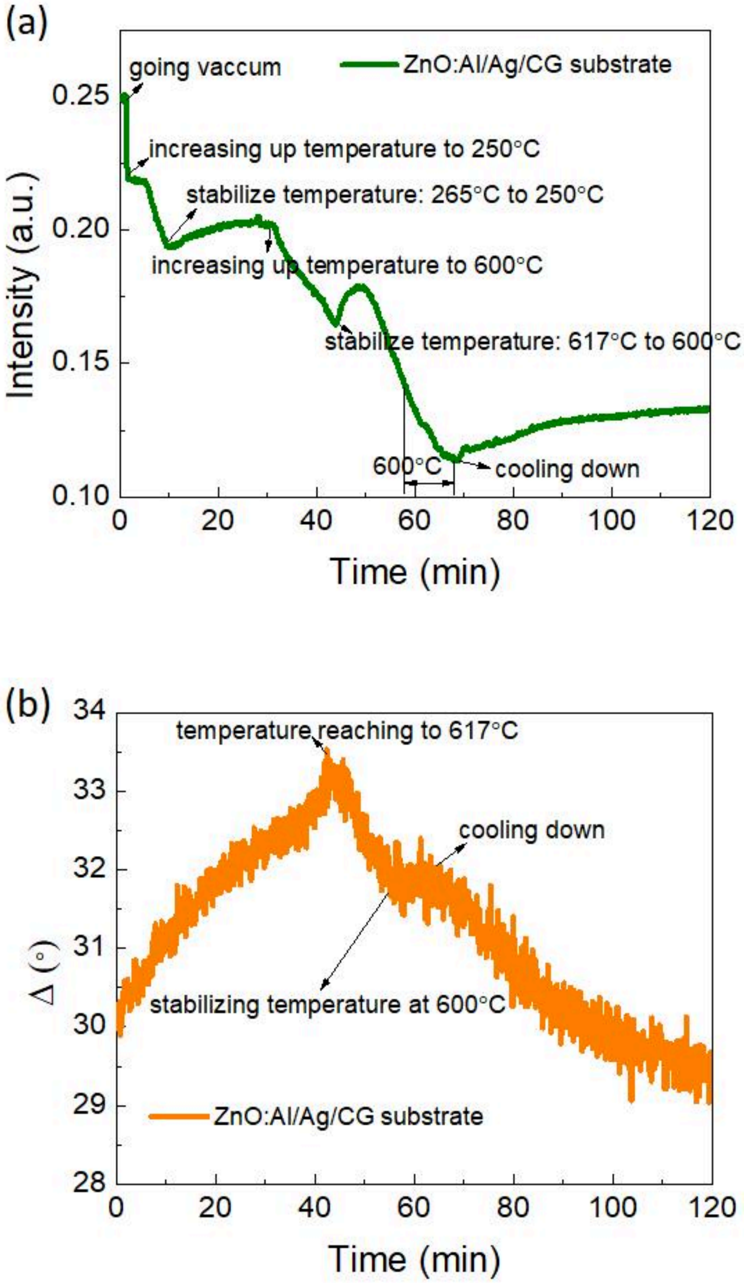

Figure 4.3 (a) Intensity at 5.5 eV as a function of time from in-situ ellipsometry of ZnO:Al substrate at the same temperature as the process for SiNWs growth under vacuum; (b) Delta as a function of time from in-situ ellipsometry of ZnO:Al substrate at the same temperature as the process for SiNWs growth under vacuum at 5.5 eV.

4.2.2 Sn evaporation

The next experiment investigates the randomness introduced by the steps involving Sn. First, four ZnO:Al/Ag/CG substrates are fabricated by sputtering in the same batch. After that, the four ZnO:Al/Ag/CG substrates are transferred into a thermal evaporator for Sn deposition, also in the same batch. The four 1”x1” substrates are placed close to each other to minimize thickness variation. Figure 4.4 (a) shows the ellipsometer angle Δ (sensitive to surface changes) as a function of photon energy for the four substrates [8-10]. We can see that the ellipsometer spectra of four ZnO:Al/Ag/CG substrates are almost the same. From Figure 4.4 (b), we can see that the value of Δ is around 35° at 4.5 eV. The roughness and thickness of the four samples are almost the same. The ZnO:Al/Ag/CG substrate has good repeatability in the same batch.

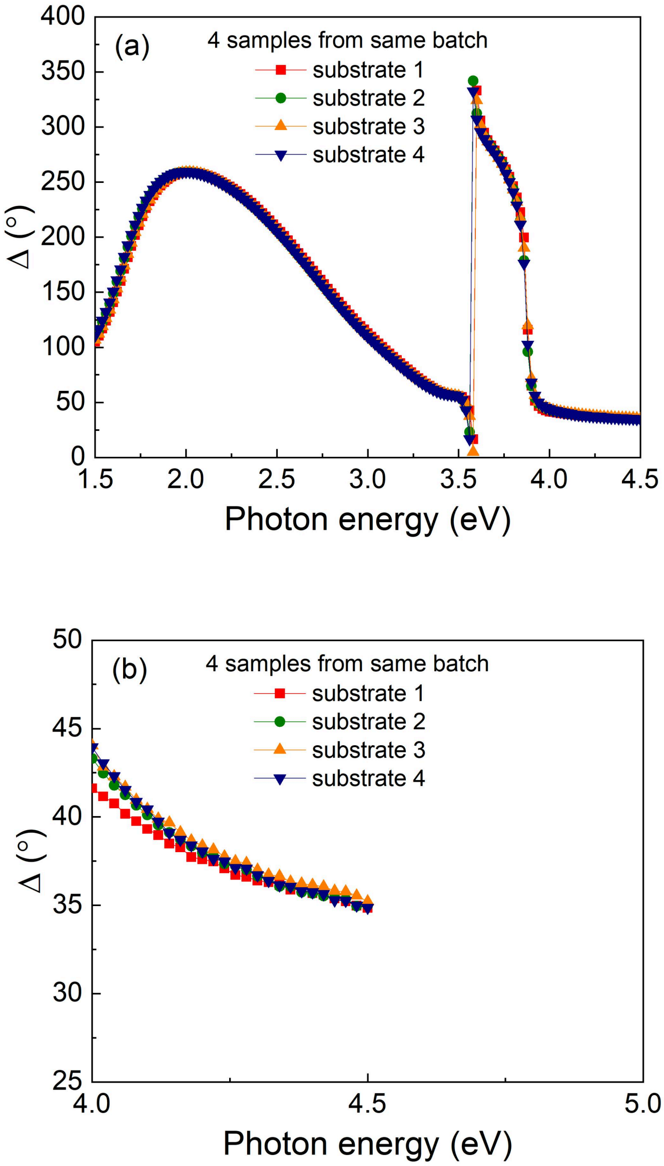

Figure 4.4 (a) Ellipsometry angle Δ measured in the range from1.5 to 4.5 eV of four ZnO:Al/Ag/CG substrates from the same batch; (b) Enlarged figure of (a) around 4.5 eV.

We repeated the same measurements on this set of substrates after the evaporation of the Sn layer. Figure 4.5 (a) shows the ellipsometer spectra of 0.1 nm Sn/ZnO:Al/Ag/CG from same batch substrate fabrication and same batch Sn deposition. These ellipsometer spectra are almost overlapping. Figure 4.5 (b) is the zoom-in spectra around 4.5 eV of (a). Δ change from 34.5° to 35.9° at 4.5 eV for these four samples. The 0.05 nm Sn/ZnO:Al/Ag/CG substrates from same batch do not have a detectable variation within the precision achievable with this ellipsometer.

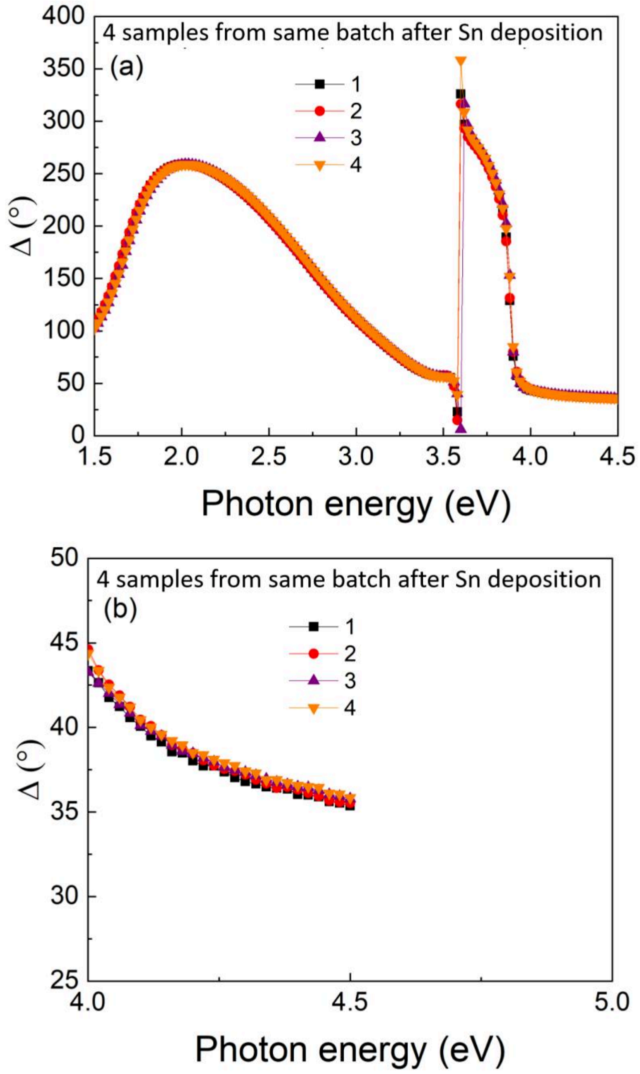

Figure 4.5 (a) Ellipsometry spectra from 0.1 nm Sn/ZnO:Al/Ag/CG substrates of same batch from 1.5 eV to 4.5 eV. (b) Enlarged figure of (a) around 4.5 eV.

4.2.3 H_2 plasma treatment

From 4.2.1, we can know that the 0.1 nm Sn/ZnO:Al/Ag/CG substrates are quite reproducible in terms of surface properties as indicated by the ellipsometer angle Δ.

Therefore, the spread in NW density may be due to other steps of their growth process. To check that, we transferred these samples into a PECVD chamber to grow SiNWs. During the transfer of the substrates from the thermal evaporator to the PECVD reactor the thin Sn layer will be oxidized. Hence before the SiNW growth, a H_2 plasma treatment process is used to reduce the SnO_2 shell to Sn. All the while, the in-situ ellipsometer is used to measure the angle Δ as a function of time while H_2 treatment.

We subsequently used SEM to observe the Sn droplets on the surface after H_2 plasma treatment. Figure 4.6 shows SEM images of Sn droplets formed on ZnO:Al/Ag/Cg substrate after H_2 plasma treatment of 4 samples in the same batch. Small particles are formed on the substrates. The number of Sn droplets can be counted manually from the images. The Sn droplet densities are $1.45 \pm 0.05 \times 10^{10}/cm^2$, $2.12 \pm 0.13 \times 10^{10}/cm^2$, $2.38 \pm 0.08 \times 10^{10}/cm^2$, $1.72 \pm 0.03 \times 10^{10}/cm^2$.

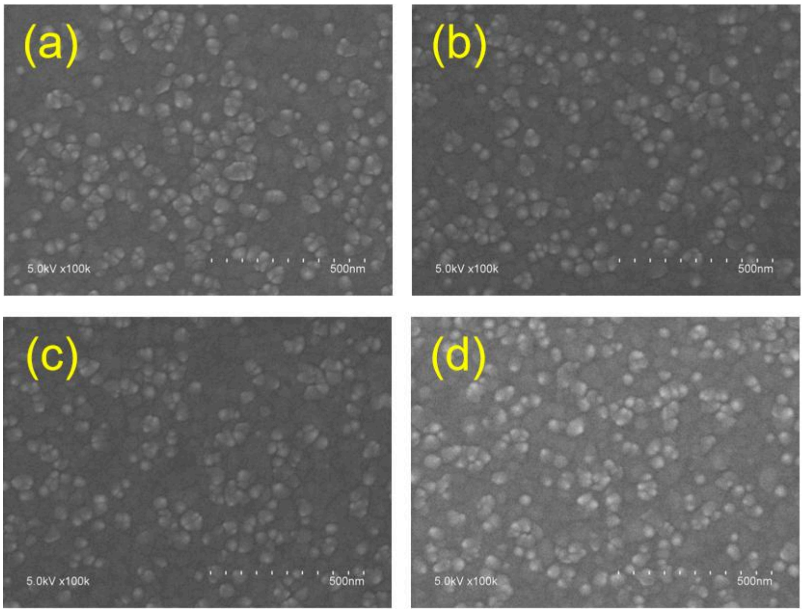

Figure 4.6 Sn droplet produced after H_2 plasma treatment from samples of same batch of substrate fabrication and Sn catalyst evaporation

Figure 4.7 shows the result of counting the Sn droplet density (white spots in the image) with uncertainty from figure 4.6 (a), (b), (c) and (d). One can observe that the droplet density on the same batch samples varies significantly (almost by a factor of 2). This is due to the process occurring during the H_2 plasma. When the temperature is above the melting point, the catalyst droplets (without their shells) prefer to coalesce and nanoparticles connect with each other [11]. This random nature of the Sn droplet formation process will result in different density of SiNWs and finally affect the SiNW solar cell performance.

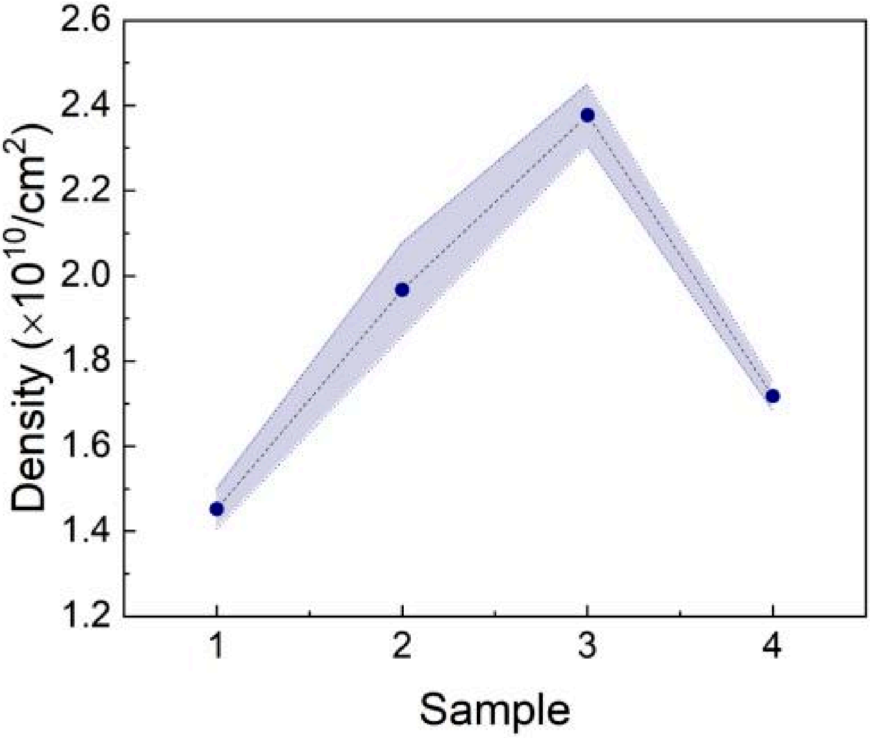

Figure 4.7 Sn droplet density with uncertainty of different samples.

4.2.4 SiNW growth

After Sn droplet formation, SiNWs are grown at a high temperature, given as 600°C on the heater controller, the actual temperature is around 400°C. It is interesting to measure the evolution of the ellipsometer angle Δ during SiNW growth. Therefore, for a new batch of samples, we also measure the in-situ ellipsometer spectra from H_2 plasma treatment to SiNWs growth. Figure 4.8 is the in-situ ellipsometer spectra of a new same batch of samples before and after H_2 plasma treatment. Table 4.2 summarized the extracted value of Δ from Figure 4.11. The values of Δ before H_2 plasma treatment are 28.8°, 27.3° and 26.7°. The values after H_2 plasma treatment are 30.2°, 28.7° and 28.2°. Once again, we can track the variation of Δ. The changes in Δ are 1.4°, 1.4° and 1.5°

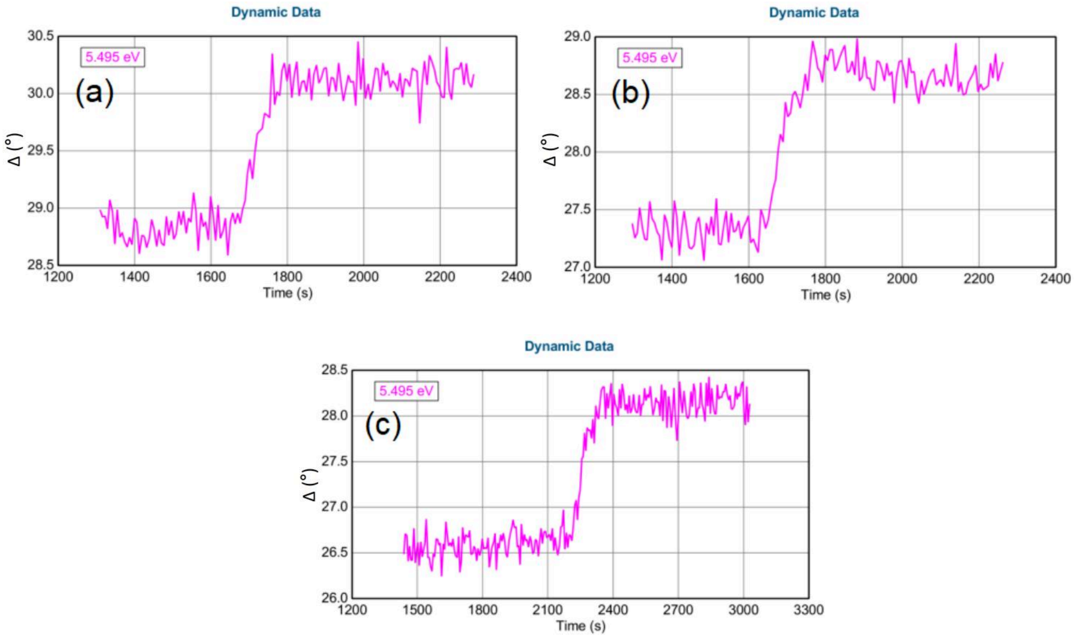

Figure 4.8 Delta as function of time of same batch sample before and after H_2 plasma treatment.

Table 4.2 The extracted value of delta from figure 4.9

Sample	Delta before H_2 plasma	Delta after H_2 plasma	Delta changing
1	28.8°	30.2°	1.4°
2	27.3°	28.7°	1.4°
3	26.7°	28.2°	1.5°

After the H_2 treatment, the temperature of the substrate is directly increased to 600 °C for SiNW growth. We first observe only the initial growth process of SiNWs to observe the density changing. Figure 4.9 shows the SEM images after the first 10 seconds of SiNW growth. We can see the morphology of SiNWs after 10s growth at 600°C, when they are very small. Figure 4.10 presents the density of SiNWs after 10s growth for 3 samples from the same substrate fabrication and Sn deposition batch. The density of SiNWs after 10s growth is $0.92 \pm 0.07 \times 10^{10}/cm^2$, $1.19 \pm 0.04 \times 10^{10}/cm^2$ and $1.29 \pm 0.1 \times 10^{10}/cm^2$. Compared with the Sn droplets after H_2 plasma treatment, the density has slightly decreased. This can be explained by the fact that a-Si:H coating of the substrates changes their surface energy and wettability for Sn, thus favoring the coalescence of Sn droplets. As presented by Tang, the Sn droplets experience a dramatic change in the triggering process of SiNWs growth [12]. The density decreases more in J. Tang's work, because we do not use the same Sn thickness. This random merging of low density Sn droplets might cause the difference on NW density and V_{OC} of the same batch samples.

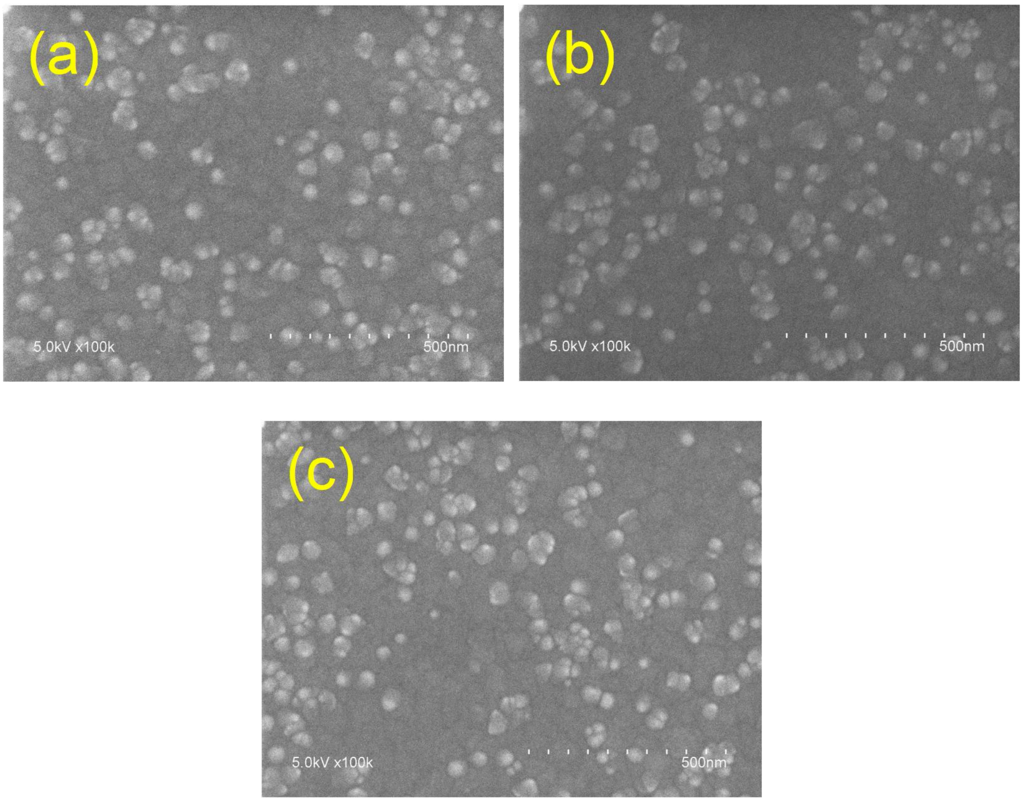

Figure 4.9 SEM images of three samples after H_2 plasma treatment at 250℃ and then 10s of SiNWs growth at 600℃.

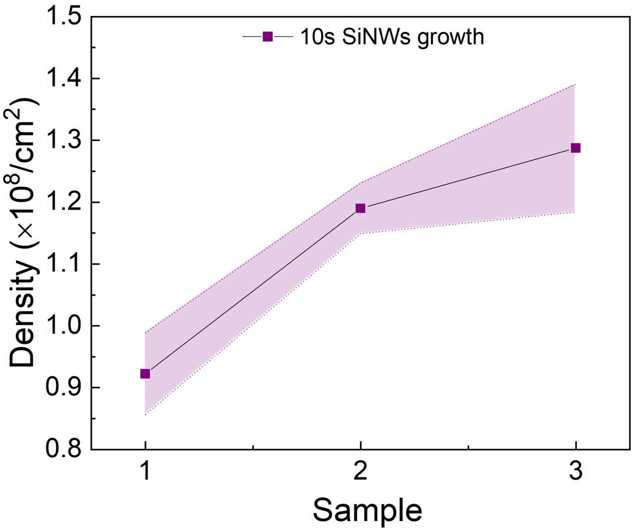

Figure 4.10 Density with uncertainty counted from figure 4.10 of 10s SiNWs growth of three samples.

Figure 4.11 shows an example of the typical evolution of the reflected intensity measured with in-situ ellipsometry as a function of time during SiNW growth and the intrinsic layer and n type layer deposition process. The time (t=45 s) is when the plasma has been turned on. The increase of the intensity of the signal is mainly due to the silicon radical deposition on the top surface of the substrate. It changes the reflectivity of the surface, as silicon is a high refractive index material with high absorption coefficient at photon energies of 5.5 eV. The intensity starts to decrease after 2 min deposition, because SiNWs start to grow and scatter the light. At 10 min of SiNW growth, the light scattering strength from SiNWs gradually increasing. The intensity changing of this part is due to the growth of SiNWs.

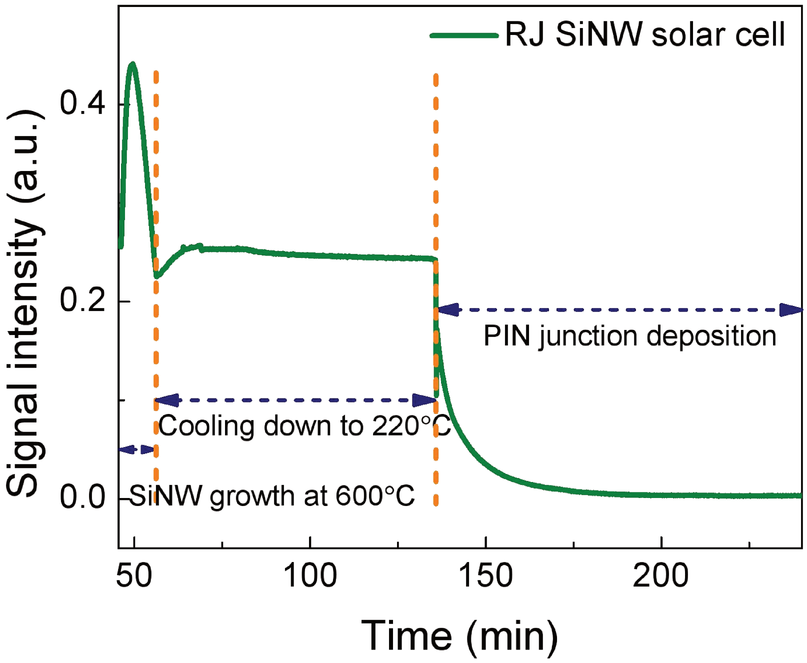

Figure 4.11 Evolution of the intensity of the ellipsometry signal (specular reflectivity) measured in-situ at a photon energy of 5.5 eV during SiNW solar cell growth.

The peak time is related to the transition when the light scattering from the SiNWs starts to strongly influence the detected signal. The scattering from the NWs is directly related to the NW length and density. Hence, we selected the SiNW growth process of different 3RJ SiNW solar cells having different values of V_{OC} and plot them together. Figure 4.12 shows the intensity as a function of time for different density

SiNW grown using the same growth conditions.

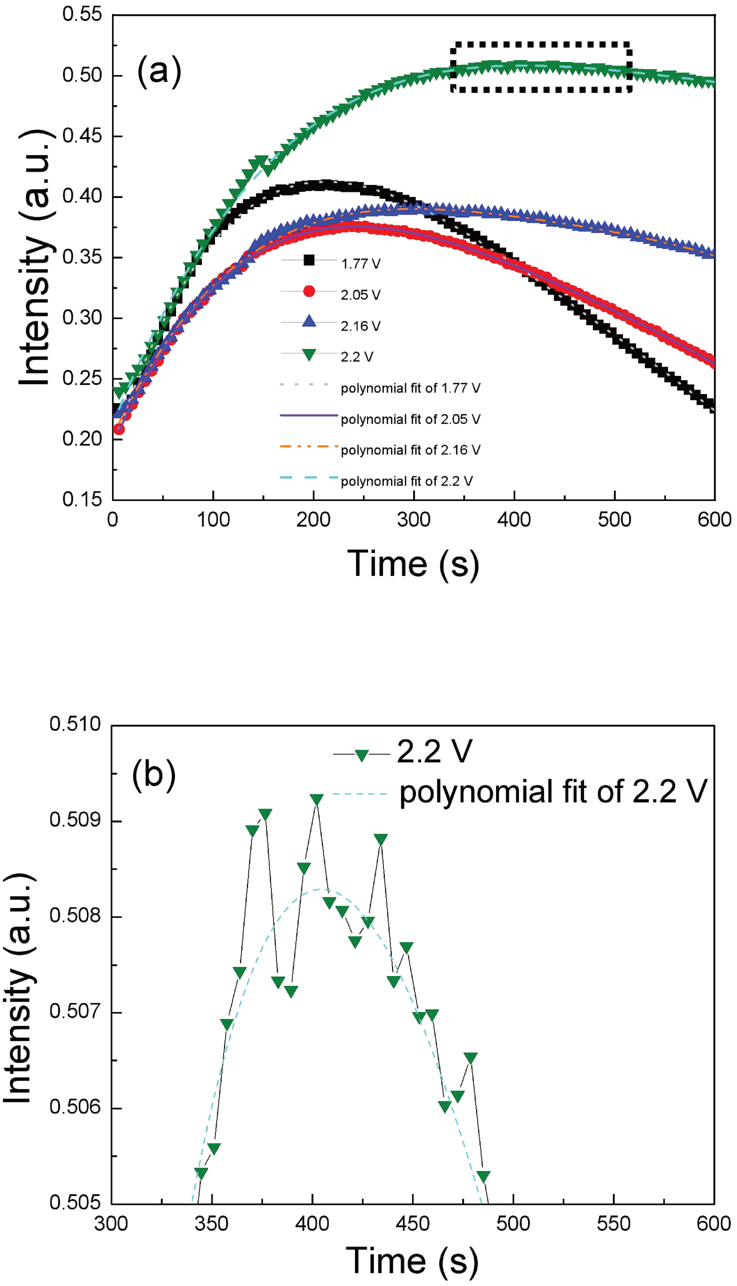

Figure 4.12 In-situ ellipsometer spectra (a) 3RJ SiNW solar cells processed under same nominal conditions and having different values of V_{OC}; (b) enlarged figure of (a).

After coating the a-Si:H PIN junction on the top of different SiNW, the 3RJ SiNW solar cells are finished, they have V_{OC} of 1.77, 2.05, 2.16, and 2.2 V. Polynomial fittings are also plotted in the same figure. Fig. 4.12(b) is a zoom of signal for 2.2 V 3RJ solar cell.

Figure 4.13 show the values of V_{OC} as a function of peak time. We can see that the different V_{OC} 3RJ solar cells have different peak time of intensity. A higher V_{OC} solar cell has systematically longer time for the peak to appear. The peak time is related to light scattering of SiNW. Under the assumption that the SiNW growth rate is the same, which is typically true for the same growth conditions and similar NW densities (especially for smaller NW densities), the light scattering can be related to the SiNW density, therefore, we can use in-situ ellipsometer to predict the SiNW density.

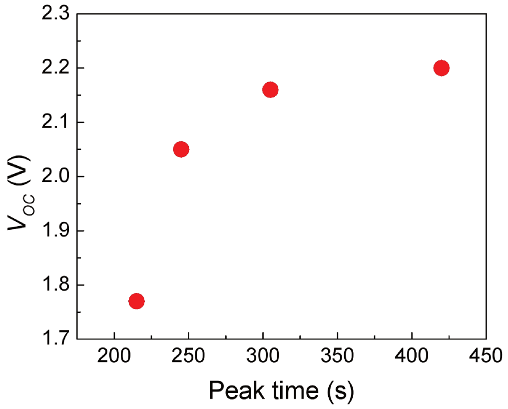

Figure 4.13 The relationship between V_{OC} and peak time.

Figure 4.14 shows SEM images of 3RJ SiNW solar cells having different values of V_{OC}: 1.77 V, 2.05 V, 2.16 V, 2.2 V corresponding to density of solar cells of $3.5 \times 10^8/\text{cm}^2$, $2.3 \times 10^8/\text{cm}^2$, $1.7 \times 10^8/\text{cm}^2$, and $1.2 \times 10^8/\text{cm}^2$, respectively. We can conclude that lower V_{OC} solar cell has higher SiNW density, which can be attributed to a more carrier recombination in high density NW solar cells because of their higher effective surface.

In a word, from SEM images and results from in-situ ellipsometer spectra, V_{OC} of 3RJ SiNW solar cell is related to 3RJ SiNW density and this has been related to the position of the intensity peak appearing in in-situ ellipsometry data. Hence we can use the in-situ ellipsometry as a guide to optimize SiNW solar cell density.

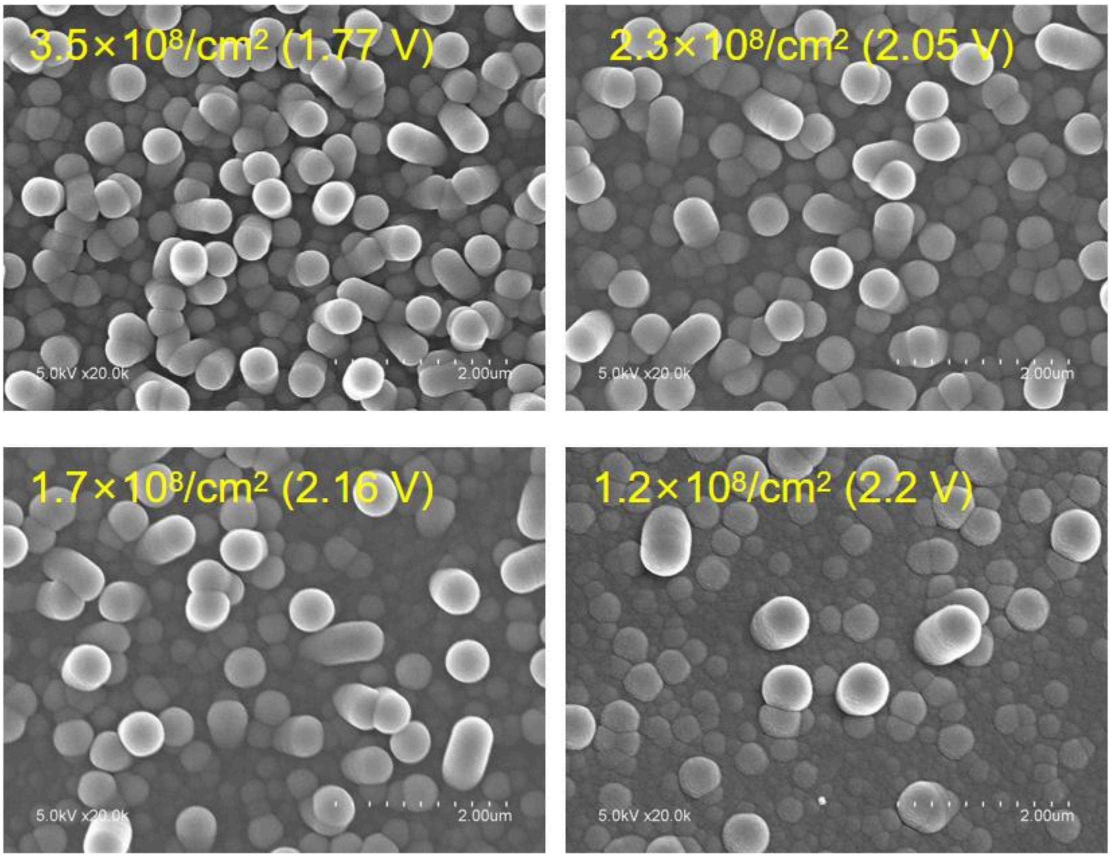

Figure 4.14 SEM images of 3RJ solar cells with different nanowire density.

4.3 Conclusion

In this chapter, we investigated origins of the apparent randomness in the same batch sample while growing the 3RJ SiNW solar cells. When V_{OC} of same batch samples are not the same, it means that the SiNW density varies as well. The process of SiNW growth is investigated step by step. It can be seen that the density of Sn catalyst is not the same, even in the same batch in some cases. After 10 s growing SiNWs, the density of SiNW is also not identical. The random merging of Sn droplet may cause the different SiNW density.

The surface of ZnO:Al/Ag/CG substrates can be affected by the vacuum and temperature. From the in-situ ellipsometer spectra of ZnO:Al/Ag/CG substrate, we have observed that the signal has changed when high substrate temperature was applied.

The position of the ellipsometry signal intensity peak in time has been studied for different density of SiNWs. The position of the peak can be used to determine the SiNW density, which is shown to correlate well with the value of V_{OC}. Hence in further work, the in-situ ellipsometer can be used to predict the NW density during the growth and further predict the V_{OC} of 3RJ SiNW solar cell for a given process conditions and fixed multijunction configuration.

References

[1] J. Choi, K. Cho, S. Kim, *Flexible Thermoelectric Generators Composed of n-and p-Type Silicon Nanowires Fabricated by Top-Down Method*, Advanced Energy Materials, 2017, **7**:p. 1602138.

[2] H. Phan, T. Kozeki, T. Dinh, T. Fujii, A. Qamar, Y. Zhu, T. Namazu, N. Nguyen, D. V. Dao, *Piezoresistive effect of p-type silicon nanowires fabricated by a top-down process using FIB implantation and wet etching*, RSC Advances, 2015, **5**:p. 82121-82126.

[3] W. K. Choi, T. H. Liew, M. K. Dawood, Henry I. Smith, C. V. Thompson, and M. H. Hong, *Synthesis of Silicon Nanowires and Nanofin Arrays Using Interference Lithography and Catalytic Etching,* Nano Letters, 2008, **8**(11):p. 3799-3802.

[4] P. C. McIntyre, A. Fontcuberta i Morral, *Semiconductor nanowires: to grow or not to grow?* Materials Today Nano, 2020, **9**:p. 100058.

[5] M. Zhang, K. Peng, X. Fan, J. Jie, R. Zhang, S. Lee, N. Wong, *Preparation of Large-Area Uniform Silicon Nanowires Arrays through Metal-Assisted Chemical Etching*, The Journal of Physical Chemistry C, 2008, **112** (12):p. 4444–4450.

[6] X. Han, G. Larrieu, E. Dubois, *Realization of Vertical Silicon Nanowire Networks with an Ultra High Density Using a Top – Down Approach*, Journal of Nanoscience and Nanotechnology, 2010, **10**:p. 1-5.

[7] S. Misra, L. Yu, W. Chen, M. Foldyna, P. Roca i Cabarrocas, *A review on plasma-assisted VLS synthesis of silicon nanowires and radial junction solar cells*, Journal of Physics D: Applied Physics, 2014, **47**:p. 393001.

[8] P. Roca i Cabarrocas, S. Kumar, B. Drevillon. *In-situ study of the thermal decomposition of B2H6 by combing spectroscopic ellipsometry and Kelvin probe measurements*, Journal of Applied Physics, 1989, **66**(7):p.3286-3292.

[9] V. Yakovlev, B. Dreillon, N. Layadi, P. Rota i Cabarrocas, *Real-time spectroellipsometry investigation of the interaction of silane with a Pd thin film: Formation of palladium silicides,* Journal of Applied Physics, 1993, **74**(4):p. 2535-2542.

[10] B. Drevillon, Satyendra Kumar, P. Roca i Cabarrocas, *In situ investigation of the optoelectronic properties of transparent conducting oxide amorphous sincon interfaces*, Applied Physics Letters, 1989, 54(21):p. 2088-2090.

[11] Z. Fan, J. Maurice, W. Chen, S. Guilet, E. Cambril, X. Lafosse, L. Couraud, K. Merghem, L. Yu, S. Bouchoule, P. Roca i Cabarrocas, *On the Mechanism of In Nanoparticle Formation by Exposing ITO Thin Films to Hydrogen Plasmas*, Langmuir, 2017, 33(43):p. 12114-12119.

[12] J. Tang, J. Maurice, W. Chen, S. Misra, M. Foldyna, E. V. Johnson, P. Roca i Cabarrocas, *Plasma-assisted growth of silicon nanowires by Sn catalyst: step-by-step observation*, Nanoscale Research Letters, 2016, 11: 455.

Chapter 5 “Stable” Unassisted solar water splitting with quadruple radial junction silicon nanowire solar cells

The main focus of this chapter is to investigate the performance of quadruple junction SiNW solar cells fabricated via one-pump-down PECVD process using FTO substrates as Sn source. The Sn catalyst can be directly reduced from FTO, which reduces the number of steps compared to Sn evaporation. Ni deposited by evaporation on the SiNW solar cell and their application as photocathode in PEC device is also evaluated.

5.1 Linear sweep voltammetry curves of water splitting

5.1.1 Different scan rate of linear sweep voltammetry curves of water splitting

Figure 5.1 presents the linear sweep voltammetry (LSV) curves of Ni cathode and Pt anode for water splitting in 0.1 M KOH electrolyte (pH=13.8) with different scanning speeds and different scan starting point (for the scanning from -2.5 V to 2.5 V, only the part from 0 V to 2.5 V is shown in the figure 5.1). Comparing with 1 V/s and 25 mV/s scanning speed, we can see that the faster scanning speed results in a higher current in the 1.5-2 Volts range. If the scanning speed is too high, the material has a background capacitance which generates current, masking the catalyst's kinetic current density and making the displayed activity artificially high. However, reducing the scan speed to 1 V/s is not enough if the scan range is too broad. As shown in Fig. 5.1, increasing the scan range from -2.5 V to 2.5 V still leads to an anomalous high current compared to the case where the range is reduced (0 to 2.5 V). These results show that the scan rate of water splitting test cannot be too high, otherwise it will mislead the results of current density. Therefore, in the following, the scan rate of 1 V/s will not be used. We adopted a scan rate of 25 mV/s.

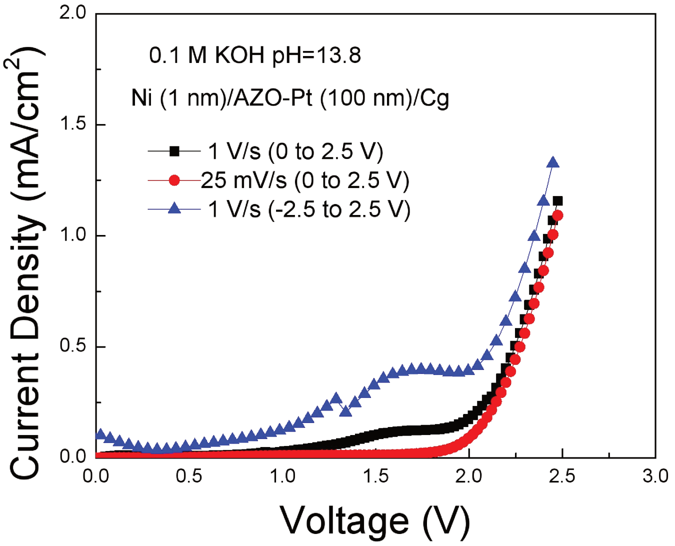

Figure 5.1 LSV curves of water splitting with Ni cathode for HER and Pt anode for OER with different scanning speed and scanning range in 0.1 M KOH. (The range from 0 V to 2.5 V shown in the figure)

5.1.2 Effect of electrolyte concentration on water splitting characteristics

Figure 5.2 shows the J-V curves of water splitting with symmetrical Pt electrodes measured in two electrolyte solutions: 0.1 M KOH (pH=13.2, 20 mS/cm) and 0.5 M KOH (pH=14, 256 mS/cm). It can be seen that the current density rises up quickly in 0.5 M KOH compared to 0.1 M KOH solution. As expected, the turn on voltage is almost the same in the case of symmetrical Pt electrodes, however we can see that the ON current is higher for 0.5 M, indicating that the current is limited by the resistance of the solution.

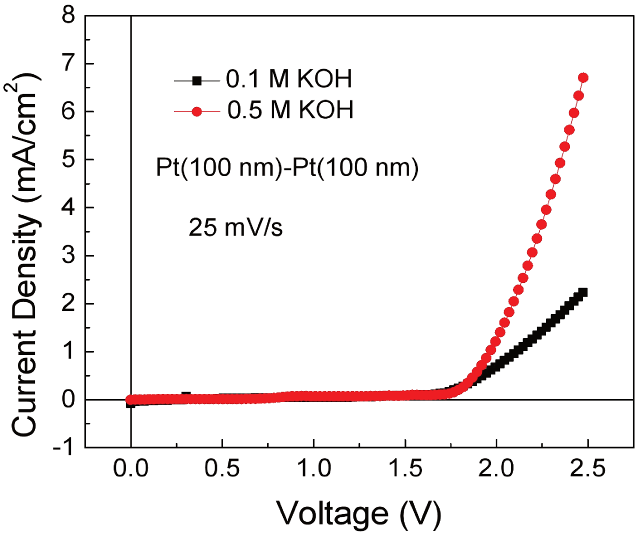

Figure 5.2 LSV curves of water splitting with Pt cathode for HER and Pt anode for OER in different electrolyte concentrations.

As presented in Figure 5.3, the Ni cathode and Pt anode have been tested for water splitting in different kinds of electrolyte, 0.1 M KOH and 1 M KBi. The electrodes in 0.1 M KOH (pH=13.2) have better performance than in the case of 1 M KBi. The potential of electrodes in 0.1 M KOH is lower than that of 1 M KBi electrolyte. It shows that the Ni cathode and Pt anode have better catalytic performance in KOH electrolyte.

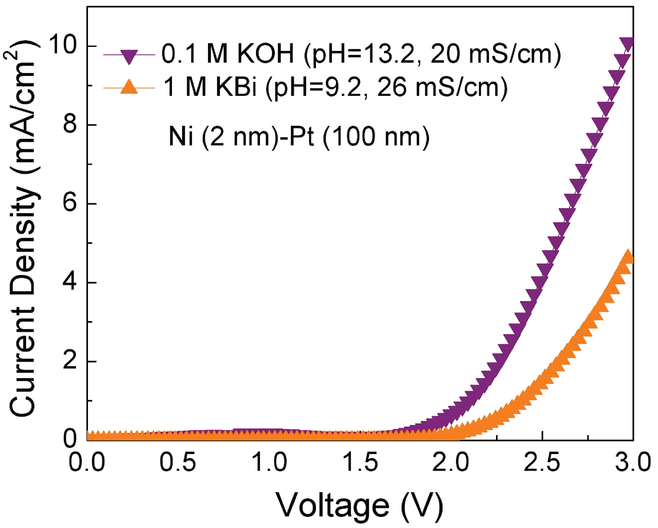

Figure 5.3 LSV curves of water splitting with Ni cathode for HER and Pt anode for OER in different electrolytes 0.1 M KOH and 1 M KBi.

5.1.3 Different distance between anode and cathode

As shown in Fig. 5.4, the conductivity of the electrolyte matters. As shown in Figure 5.4, the symmetrical Pt performance are measured in 1 M KBi electrolyte, but with different electrolyte distance, 5 cm, 2 cm and 1cm. The potential of these conditions are almost the same, however, shorter distance between two electrodes results in a higher current. This can be related to the reduction of the ohmic resistance from electrolyte when the two electrodes get closer. The distance between two electrodes affects the performance of water splitting. For the ideal measurement of water splitting, two electrodes should be very close.

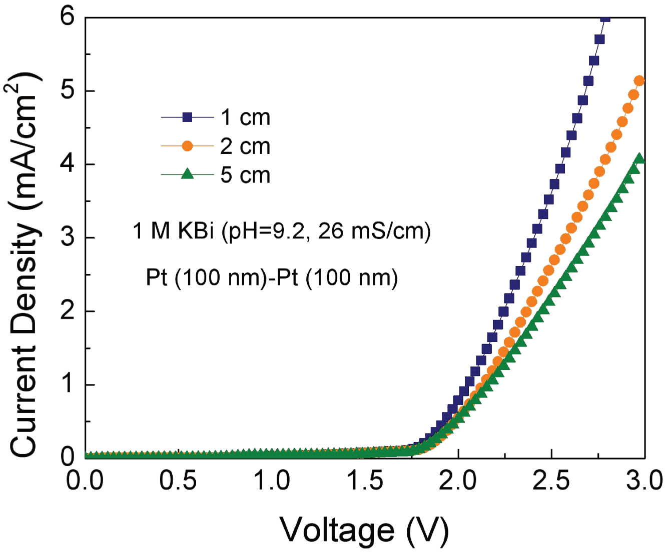

Figure 5.4 LSV curves of water splitting with Pt cathode for HER and Pt anode for OER with different electrode distance in 1 M KBi electrolyte.

5.1.4 J-V curves of solar cells versus LSV curve of water splitting

Figure 5.5 shows the comparison of J-V curves from 1RJ, 2RJ and 3RJ solar cells with LSV curves of Ni cathode and Pt anode and the best catalyst curve we got before. The current at the crossing point of the J-V curve of 3RJ and LSV curve of Ni-Pt is very low. Therefore, the potential of 3RJ solar cells is still not high enough for Ni electrode for HER and Pt electrode for OER in this configuration. For symmetrical 100 nm Pt, although it can generate more current for water splitting, it is not possible to deposit 100 nm Pt on RJ SiNW solar cell. In addition, 0.5 M KOH will seriously corrode the electrode. Therefore, we have extended the multijunction fabrication process to quadruple RJ SiNW solar cells, which should provide a higher current for unassisted water splitting.

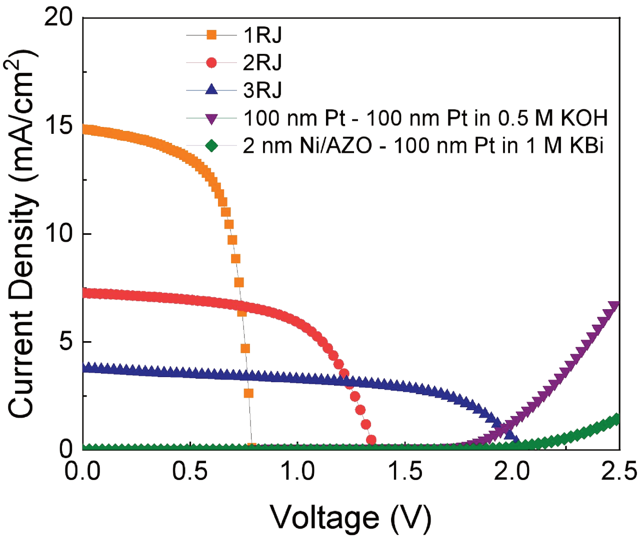

Figure 5.5 Comparison of J-V curves of 1RJ, 2RJ and 3RJ solar cells and LSV curve of water splitting by 2 nm Ni cathode and 100 nm Pt anode in 1 M KBi.

5.2 4RJ SiNW solar cells

5.2.1 4RJ SiNW solar cell fabrication

From Figure 5.5, we know that if we use Ni and Pt for HER and OER, respectively, the turn on potential is around 2 V. For efficient water splitting, the quadruple radial junction is investigated in this section. The fabrication process of 4RJ SiNW solar cells is shown in Figure 5.6 (a), (b) and (c). First, Sn drops are directly produced from the SnO_2 layer by H_2 plasma treatment in the PECVD chamber at 250 °C for different times (5 s, 20 s and 1 min) with H_2 gas flow of 100 sccm and pressure of 1.8 mbar. It should be noted that this is in contrast to the previous samples, where Sn was deposited by evaporation, which may impact the SiNW solar cell performance. Then, the substrate holder temperature is increased to the nominal value of 600 °C, and afterwards 10 sccm SiH_4, 100 sccm H_2, 1.5 sccm trimethylboron (1% TMB diluted in H_2) are flowed into PECVD chamber. The SiNWs start to grow by plasma-assisted vapor-liquid-solid method for 10 min while the plasma is ignited with a RF power of 2 W and a total pressure of 1.38 mbar. After SiNWs growth, the PECVD chamber is cooled down to 220 °C under H_2 atmosphere. For the first PIN junction, a graded doping p-type a-Si:H layer is firstly deposited on the SiNWs. After that, an undoped i-a-Si:H layer is deposited by closing the TMB gas. Then, a graded n-a-Si:H is deposited with PH_3 gas on i-a-Si:H layer. Highly doped n++ and p++ layers are further deposited in order to form a tunnel-recombination junction between each PIN junction. For the second PIN junction, a constant doping p-layer with flow rate of 5 sccm TMB gas is deposited after the tunnel junction. The i-a-Si:H layer and the n-a-Si:H are deposited with same parameters as described before, except for the i-layer deposition time. For the third PIN junction and fourth PIN junction, the p, i and n-layers are identical to the second PIN junction, except for the i-layer deposition time. The initial i-layer deposition time of first, second, third and fourth junction are choose equal to 32 min, 16 min, 8 min and 4 min, respectively. The pressure of all the p-layers deposition is shown in table 5.1. The temperature for the deposition of all PIN layers is 220 °C and the RF power 1 W.

Table 5.1 Parameters of different doping method for p layer

	Gradient doped layer			Constant doped layer
TMB (sccm)	3	2	1	5
Time (min)	3	1	1	5
P (mbar)	0.18	0.17	0.16	0.18

Figure 5.6 (e) and (f) are SEM images of the 4RJ SiNW solar cell before and after ITO sputtering. Indium Tin Oxide (ITO) transparent top contact pads are sputtered on the solar cells through a shadow mask after PECVD growth. The deposition is realized with 43 sccm Ar gas and 3 sccm O_2 gas flow at a RF power of 200 W, temperature of 180 °C and pressure of 4.4×10^{-3} mbar for 7 min. After ITO sputtering, the SiNW solar cells were annealed in air at 220 °C for 10 min before measuring them.

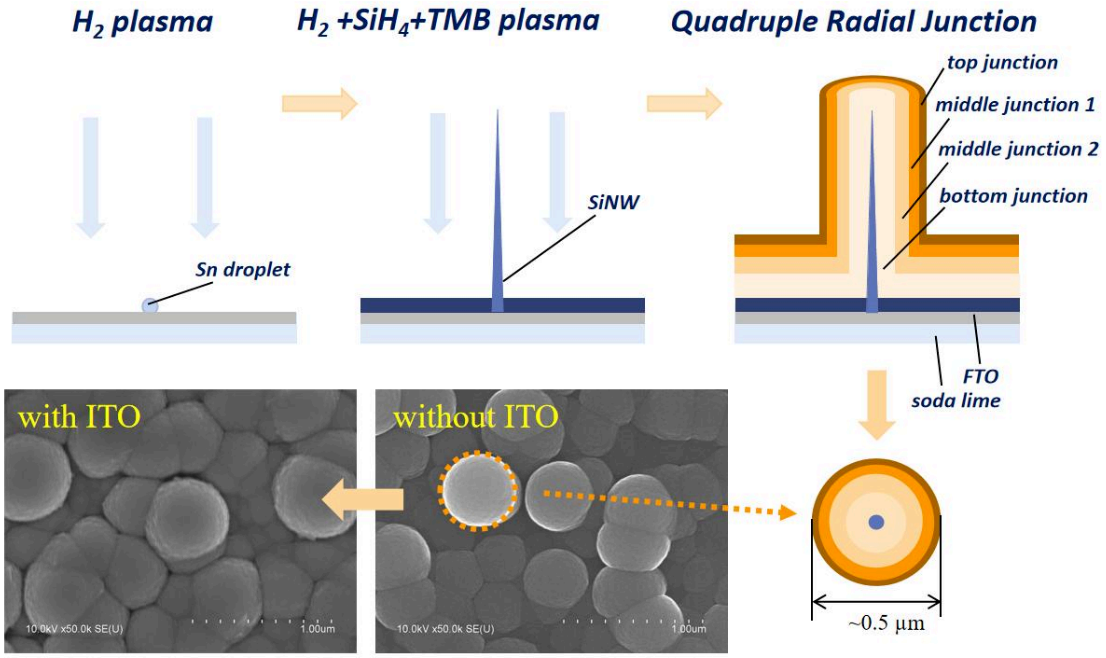

Figure 5.6. SiNW solar cell process flow. (a) H_2 plasma to produce Sn droplets from a FTO layer; (b) H_2, SiH_4 and TMB plasma to grow p-type c-Si SiNWs; (c) schematic of 4RJ multilayer stack; (d) schematic top view of 4RJ junction; (e) SEM image of top view of 4RJ; (f) 4RJ after ITO top contact sputtering.

5.2.2 4RJ SiNW solar cell performance

Figure 5.7 shows 4RJ SiNW solar cells fabricated in different densities varying from $0.4\times10^8/cm^2$ to $1.5\times10^8/cm^2$ by changing the H_2 plasma treatment time for reducing the SnO_2 to Sn. The density of SiNWs was calculated by counting the RJ without ITO top contact.

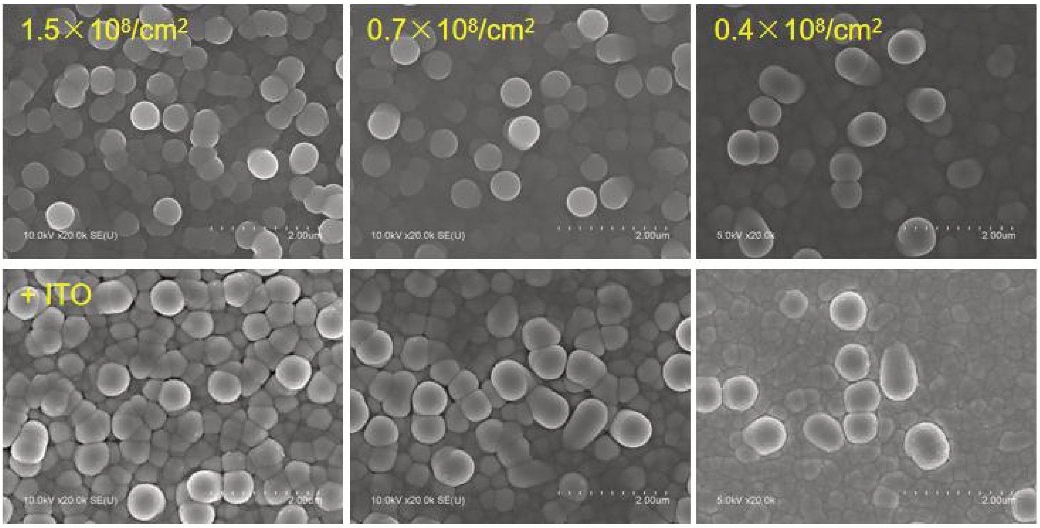

Figure 5.7 SEM images of 4RJ SiNW solar cells with different density varying from 0.4×10^8/cm^2 to 1.5×10^8/cm^2 by changing the H_2 plasma exposure time from 5 s to 20 s to 1 min (top view). The top row of the images shows the 4RJ without ITO top contact. The bottom row shows the 4RJ with ITO top contact.

In Figure 5.8, the density of SiNW is increasing from 0.4×10^8/cm^2 to 0.7×10^8/cm^2 to 1.5×10^8/cm^2 with H_2 plasma treatment time increasing from 5 s to 20s to 60 s. From the thesis of M. Ghzaiwat, the SiNW density is decreasing from 5.2 ×10^8/cm^2 to 4.3 ×10^8/cm^2 with H_2 treatment time is increasing from 2 min to 4 min. As treatment time is increasing from 2 min to 4 min, the Sn droplet diameter increases and the density decreases. Different amount of Sn catalyst is produced by changing the H_2 plasma treatment exposure time.

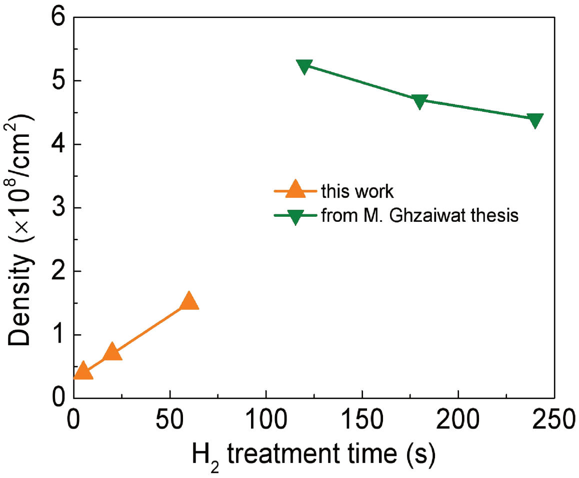

Figure 5.8 SiNW density as a function of H_2 plasma treatment time obtained in this thesis and obtained from thesis of M. Ghzaiwat [1].

As shown in Figure 5.9 and Table 5.2, the density of quadruple junction density varying from 0.4×10^8/cm^2 to 1.5×10^8/cm^2, it is notable that a V_{OC} as high as 2.75 V is achieved at the lowest density 0.4×10^8/cm^2. As the SiNW density increases to 1.5×10^8/cm^2, the V_{OC} of 4RJ solar cell decreases to 1.98 V. As discussed in Chapter 3, this can be related to the fact that with a larger surface area being generated in high density SiNW solar cells, more recombination will take place at the multiple interfaces [2-4]. For the J_{SC}, as the SiNW density increases from 0.4×10^8/cm^2 to 0.7×10^8/cm^2, the current density rises from 1.87 mA/cm^2 to 1.94 mA/cm^2 because a high density of SiNWs enhances the light trapping ability of the solar cell [5]. However, as the SiNW further increases to 1.5×10^8/cm^2, the J_{SC} of solar cell starts to decrease to 1.83 mA/cm^2, which can be attributed to the fact that the top of the SiNW solar cells start to overlap, changing the radial junction solar cell into a planar structure. The FF almost are the same. 4RJ SiNW solar cells with a density of 0.4×10^8/cm^2 have the best efficiency of 2.78% with a high V_{OC} of 2.75 V and V_{MPP} of 2.05 V.

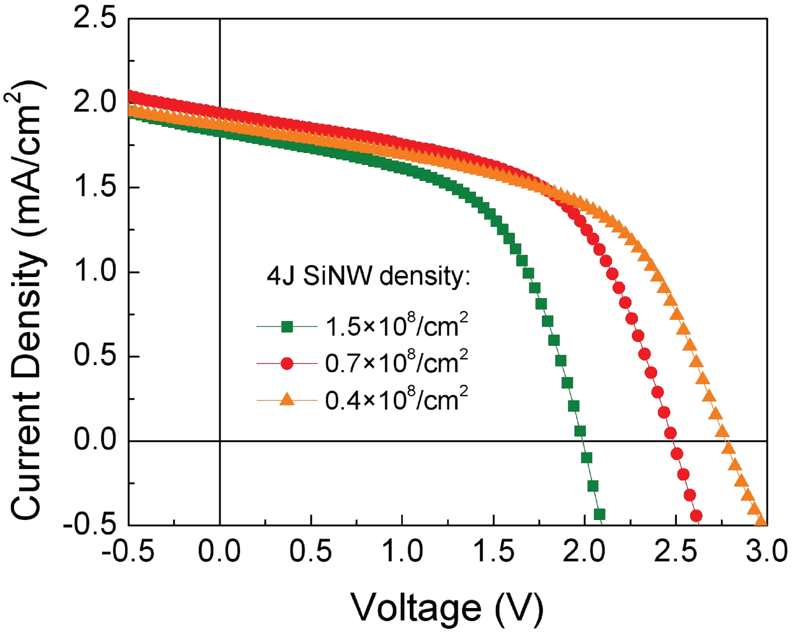

Figure 5.9 J-V characteristics of 4RJ SiNW solar cells with different SiNW density.

Table 5.2 Effect of the 4TRJ density on the solar cell parameter.

H_2 plasma treatment time (s)	4RJ Density	V_{OC} (V)	J_{SC} (mA/cm^2)	FF	Efficiency (%)
5	0.4×10^8/cm^2	2.75	1.87	0.54	2.78
20	0.7×10^8/cm^2	2.46	1.94	0.56	2.67
60	1.5×10^8/cm^2	1.97	1.83	0.55	1.99

5.2.3 Comparison of 4RJ SiNW and planar 4J solar cells

The J-V characteristics of a 4RJ SiNW solar cell and a four-junction (4J) solar cell grown on a planar substrate are compared in Figure 5.10. The 4J planar solar cell has a V_{OC} of 2.79 V, which is a bit higher than that of the 4J SiNW solar cell, again perhaps related to the fact that more recombination current is produced in the larger surface area SiNW solar cell. As expected, the J_{SC} increases from 1.73 mA/cm^2 for the planar device to 1.87 mA/cm^2 for the 4RJ Also, around V_{OC}, we can see that an S shape is present for the planar structure, as we have reported in chapter 3 for 3RJ. However, the S shape in the planar 4J may be due to not using the same batch of FTO substrates as for 3RJ. Overall, the efficiency of the 4RJ SiNW solar cell is 2.78%, compared to 2.46% for the planar device, a 13% improvement. However, this improvement is small, compared to variations within single batches of NW devices (see Figure 3.15). The improvement due to using the SiNW architecture should be confirmed on a larger set of samples in the future.

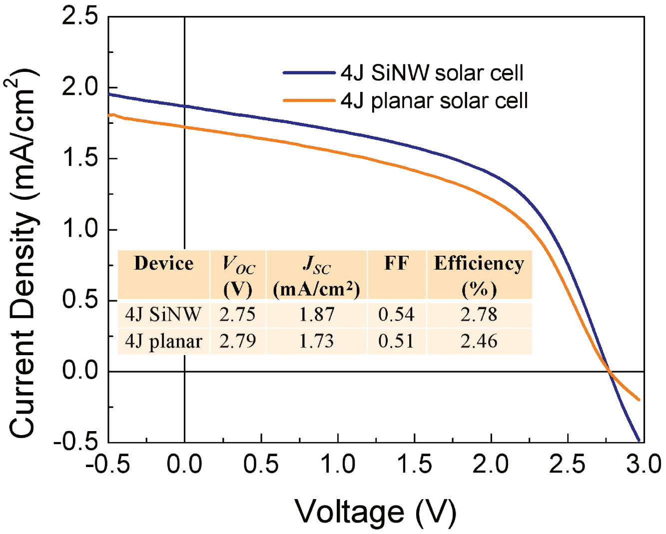

Device	V_{OC} (V)	J_{SC} (mA/cm^2)	FF	Efficiency (%)
4J SiNW	2.75	1.87	0.54	2.78
4J planar	2.79	1.73	0.51	2.46

Figure 5.10 J-V characteristics of 4RJ SiNW solar cell and planar 4J solar cell.

5.2.4 Light soaking of 4RJ SiNW solar cells

It has been shown that single RJ solar cells are more stable against light soaking when compared to planar devices. However, no report has been published for the multijunction RJ solar cells. Figure 5.11 shows the J(V) characteristics of a 4RJ solar cell after different light soaking times under standard AM 1.5G illumination at room temperature under open circuit conditions, with the solar cell parameters summarized in Table 5.3. One can see that there is a small degradation taking place during the first 2 hours of light-soaking and then the J(V) characteristics become stable. The current density decreases from 1.87 mA/cm^2 to 1.73 mA/cm^2 while V_{OC} drops by 30 mV. After 4 h light soaking test, the efficiency of 4RJ SiNW solar cell has changed from 2.78 % to 2.68 %. No obvious light induced degradation happens in the last 2 h of light soaking, confirming the interest of the RJ architecture with respect to the stability of the solar cells. However, one must also remark that these devices are composed of many thin layers, which are known to have reduced LID. A comparison with the degradation of 4J planar cells should be performed to confirm the effect of the SiNW architecture on the stability of 4J cells.

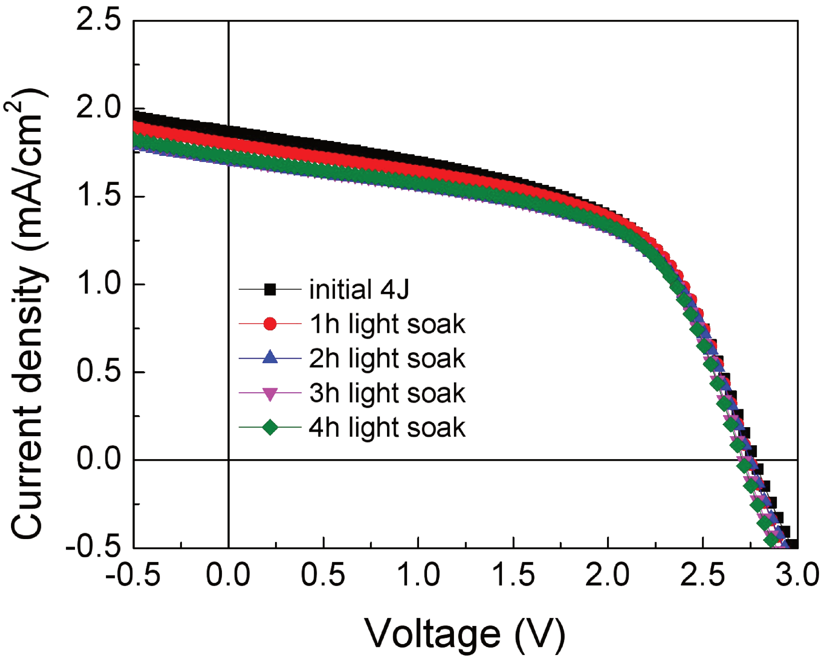

Figure 5.11 J-V characteristics measured after different times of light -soaking of 4RJ SiNW solar cell under AM1.5G spectrum.

Table 5.3 Comparison of extracted V_{OC}, J_{SC}, FF and efficiency from J-V characteristics of light soak test.

4RJ	V_{OC} (V)	J_{SC} (mA/cm^2)	FF	Efficiency (%)
Initial 4RJ	2.75	1.87	0.54	2.78
1h light-soak	2.75	1.8	0.56	2.77
2h light-soak	2.75	1.7	0.57	2.67
3h light-soak	2.72	1.72	0.57	2.67
4h light-soak	2.72	1.73	0.57	2.68

5.3 4RJ SiNW PEC cell

5.3.1 Setting up a 4RJ SiNW PEC cell

The top layer of our 4RJ SiNW solar cells is a n-type a-Si:H layer. Hence the 4RJ SiNW solar cell can be used as photocathode for HER reaction. For driving the HER reaction, the Ni catalyst is used. The SEM image of nominal thickness 2 nm Ni on n++ Si wafer is shown in Figure 5.12. At this scale the Ni deposition is uniform, as we cannot see any contrast in the image. Hence, AFM is used to investigate the morphology of Ni catalyst as shown in figure 5.13. From this image the size of the Ni particles is around 10 nm.

A TiO_2 layer deposited by atomic layer deposition is applied on the surface of the 4RJ solar cells to provide a conformal deposition of a protection layer to prevent corrosion [6]. In this thesis, 3 nm TiO_2-protection layer is deposited by thermal evaporation on the 4RJ SiNW solar cell. After that, 2 nm of Ni catalyst are evaporated as a cathode. 100 nm Pt thin film deposited on Corning glass is used as an anode. The PEC cell is installed for running the water splitting under 1 sun. The picture and configuration of PEC cell with SiNW photocathode for water splitting is shown in figure 5.14. Two solutions (0.1 M KOH and 1 M KBi) are used as electrolyte for water splitting. The 4 RJ SiNW solar cell cathode and Pt anode are fitted on the bottom of the reactor. The electrolyte is filled into the reactor from the holes on the reactor using a pipette.

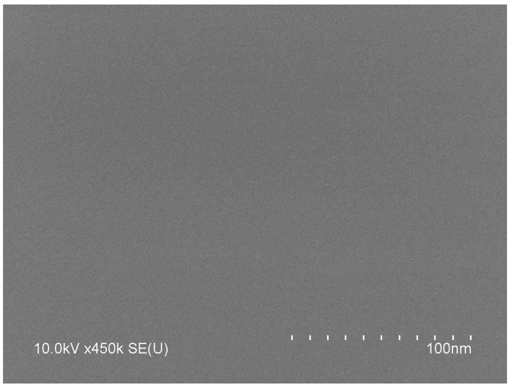

Figure 5.12 SEM Image of nominal thickness 2 nm Ni deposited on n++ Si wafer.

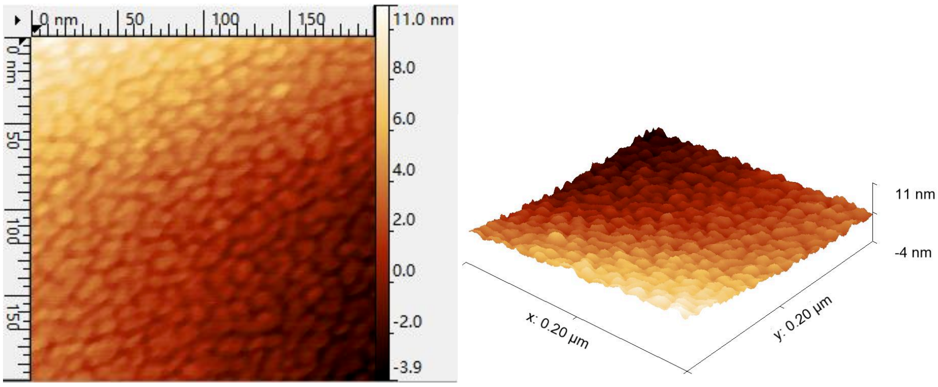

Figure 5.13 AFM images of a 2 nm Ni (nominal thickness) deposited on n++ c-Si wafer.

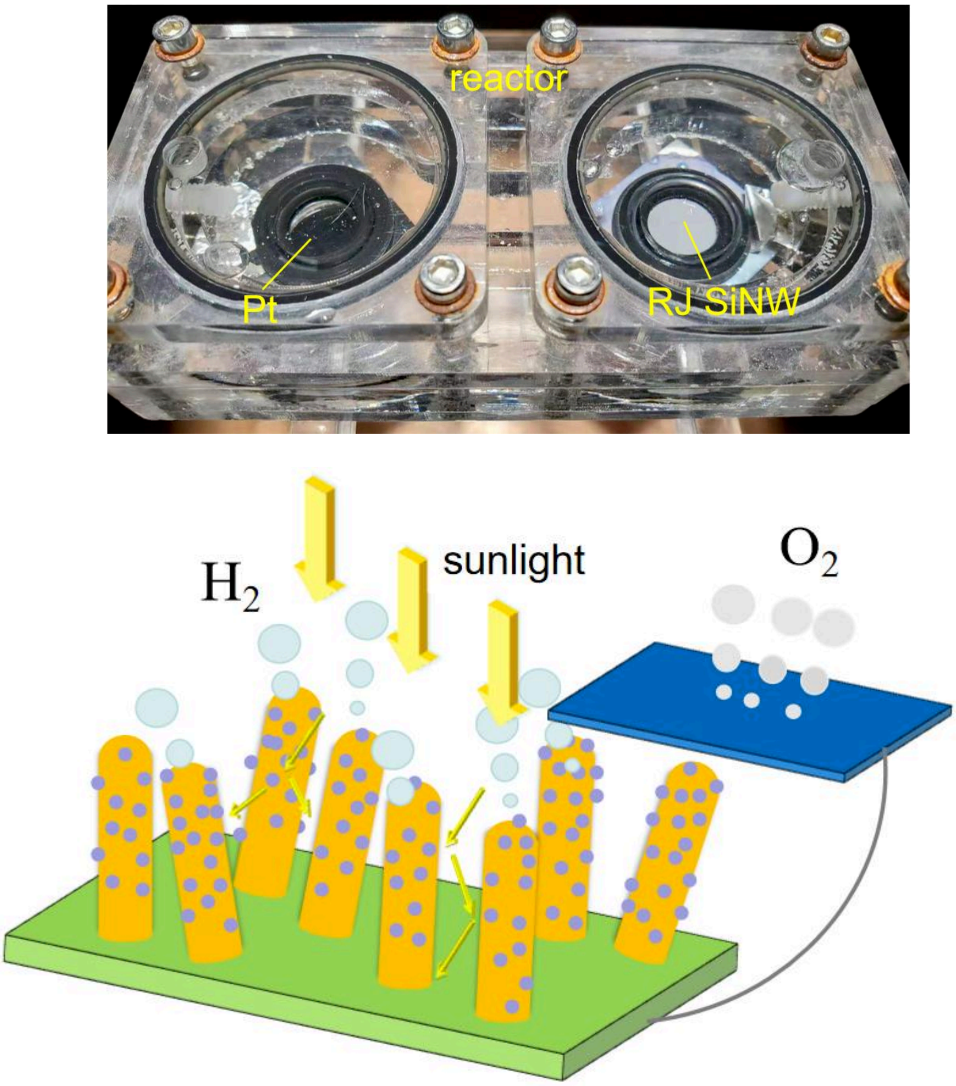

Figure 5.14 Configuration of our PEC cell with a 4RJ SiNW solar cell coated with Ni catalysts as a photocathode and a Pt thin film anode.

5.3.2 Stability of our PEC cell with 4RJ SiNW photocathode

The water splitting operation of our PEC cell without an external power supply is evaluated by using evaporated Ni catalyst on our 4RJ SiNW solar cell as a photocathode and Pt film/CG anode. Figure 5.15 shows the PEC cell performance. In 0.1 M KOH electrolyte, the PEC cell starts from 0.8 mA/cm^2, but the current strongly decreases during the first 30 min of electrolysis. On the contrary, the PEC cell keeps stable for 90 min at 0.35 mA/cm^2 in 1 M KBi electrolyte. The PEC with 1 M KBi electrolyte shows its potential ability for longtime running water splitting and sustained hydrogen production.

The solar to fuel efficiency for converting the light and water into hydrogen and oxygen can be calculated as follows:

$$\eta = \frac{J \cdot 1.23V}{P} \times 100\% \qquad (5\text{-}1)$$

η is the efficiency of solar cell, J is the current density at 0 V bias generated from PEC cell, 1.23 V is the potential for water splitting, P is the incident solar irradiance provided from AM 1.5 light source (100 mW/cm^2). This equation assumes that the Faraday efficiency is 100%. Therefore, the initial efficiency is 0.98% for PEC cell with 0.1 M KOH electrolyte and 0.43% for PEC cell with 1 M KBi electrolyte. Note that the light shines through the window of the reactor onto the photocathode and therefore some light maybe lost. Moreover, the Ohmic resistance losses from the electrolyte have an impact on the solar cell performance as shown in Figure 5.4. These losses can be reduced by adding other salts to increase the solution conductivity. Moreover, decreasing the distance between anode and cathode by redesigning the reactor also could help to reduce the Ohmic resistance. In addition, HER and OER catalysts such as RuO_2 and IrO_2 have better OER catalytic activity than Pt [7, 8] and could be used to enhance the water splitting performance.

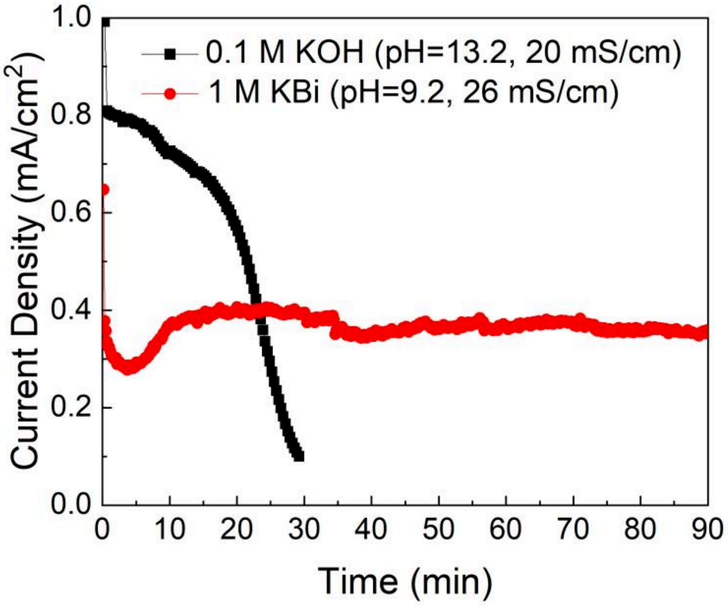

Figure 5.15 Current density as a function of time of our 4RJ SiNW solar cell in 0.1 M KOH and 1 M KBi electrolyte. Note the strong impact of the pH on the stability of the devices.

In order to characterize the effect of the pH on the stability of our 4RJ SiNW solar cells for water splitting, three kinds of buffer solution made from KOH, H_3BO_3, and KBi are chosen as electrolyte, having pH values of 13.2, 11 and 9.2 respectively. As illustrated in Figure 5.15, the PEC cell in 0.1 M KOH has a higher current than that of in 1 M KBi because the catalyst activity is better in higher pH value solution. However, the current density goes down very quickly in 30 min in 0.1 M KOH solution. To analyze the reason for the drop in current we performed SEM measurements on the 4RJ solar cells after their operation in the different solutions, as shown in Figure 5.16. Comparing figure 5.16 (a) and (b) with (c) and (d), SiNW before and after water splitting in KOH, the degradation can be related to the corrosion in 0.1 M KOH solution. From (e) and (f), we can see that the 4RJ SiNW solar cell also has corrosion in pH=11 buffer solution, but the degree of corrosion is reduced. To have a further look on (g) and (h), the 4RJ SiNW solar cell running in pH=9.2 electrolyte does not show such corrosion, which is consistent with the stable operation of the PEC reported in Figure 5.15.

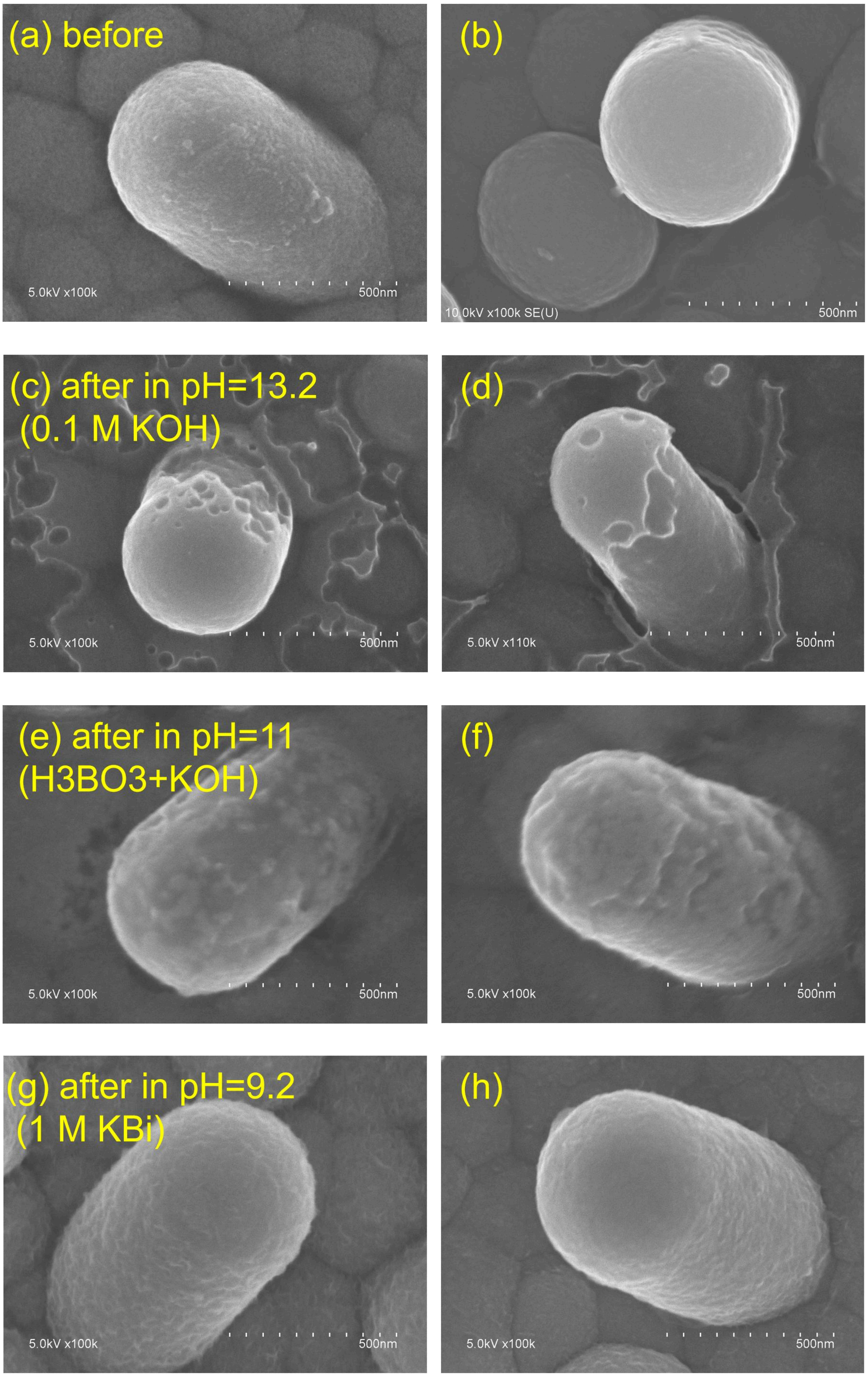

Figure 5.16 SEM images of 4RJ SiNW solar cells before water splitting (a) and (b); after running water splitting in different buffer solutions (made of KOH and H_3BO_3), pH=13.2(c) and (d); pH=11 (e) and (f); pH=9.2 (g) and (h).

As shown in Figure 5.17, the Pt/CG anode is on the left side of the reactor and the 4RJ SiNW solar cell photocathode is on the right side. Before water splitting, the reactor is filled with 1 M KBi electrolyte. After 2h water splitting, many bubbles are produced from cathode and anode in the chamber, showing the feasibility of 4RJ SiNW solar cells as a photocathode for solar to hydrogen conversion. The solar water splitting can be run by PEC cell with RJ SiNW solar cell cathode without any external power supply. However, the electrodes are 50 mm apart and are not even facing each other. Future improvement of the hydrogen conversion efficiency requires also designing an efficient reactor to test the water splitting performance.

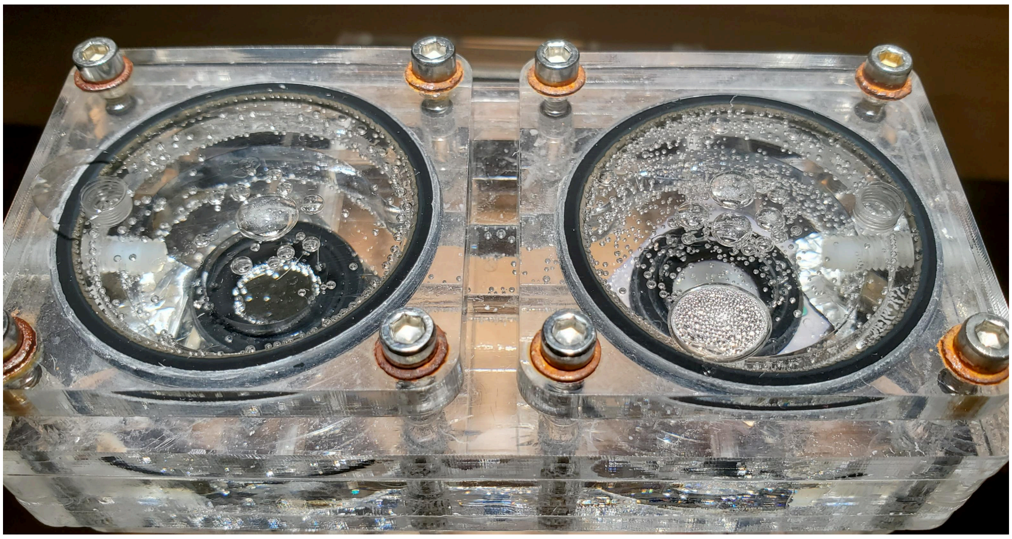

Figure 5.17 The reactor after water splitting in 1 M KBi solution.

5.4 Conclusion

In this chapter, 4RJ SiNW solar cells have been developed for the first time. A simple thermal evaporation method is applied for earth-abundant Ni catalyst deposition on the 4RJ SiNW solar cells for HER reaction. A stable solar to hydrogen and oxygen production has been demonstrated.

From the J-V curves of water splitting from catalyst, we have shown that a too high scan rate while measuring the J-V curves can mislead the current density values for water splitting. For both 100 nm Pt - 100 nm Pt system and 2 nm Ni - 100 nm Pt system, the water splitting has better performance in higher pH value alkaline electrolyte. The distance between two electrodes affect the water splitting. Shorter distance has better performance of water splitting.

The a-Si:H 4RJ NW solar cell is fabricated by one-pump-down process using standard PECVD. The FTO substrate is directly used as the Sn catalyst source for growing SiNWs. A record V_{OC} value of 2.75 V for a 4RJ SiNW solar cell has been obtained by optimizing the density of SiNWs. The 4RJ SiNW solar cell has been applied as the photocathode for photoelectrochemical cell for water splitting in combination with earth-abundant Ni – deposited by simple thermal evaporation. The photoelectrochemical cell efficiency reaches up to initial 0.98% in 0.1 M KOH electrolyte and stable 0.43% operation in 1 M KBi electrolyte. This work demonstrates the feasibility of low cost and high V_{OC} RJ SiNW solar cells as photocathode for unassisted water splitting.

References

[1] M. Ghzaiwat, Fabrication and study of solar cell modules based on silicon nanowire based radial junction solar cells, PhD Thesis, Ecole Polytechnique, 2018.

[2] A. Gudovskikh, D. Kudryashov, A. Baranov, A. Uvarov, I. Morozov, A. Maksimova, E. Vyacheslavova, D. Kirilenko, A. *Mozharov, Impact of Interface Recombination on Quantum Efficiency of a-Si:H/c-Si Solar Cells Based on Si Wires*, Physics Status Solidi A, 2021, **218**(22):p. 2100339.

[3] M. Gharghi, E. Fathi, B. Kante, S. Sivoththaman, X. Zhang, *Heterojunction Silicon Microwire Solar Cells*, Nano Letters, 2012, **12**(12):p. 6278-6282.

[4] J. Oh, H. Yuan, H. M. Branz, *An 18.2%-efficient black-silicon solar cell achieved through control of carrier recombination in nanostructures*, Nature Nanotechnology, 2012, **7**:p. 743-748.

[5] M. Foldyna, L. Yu, P. Roca i Cabarrocas, *Theoretical Short-circuit Current Density for Different Geometries and Organizations of Silicon Nanowires in Solar Cells*, Solar Energy Materials and Solar Cells,2013, **117**:p. 645-651.

[6] T. Cottre, K. Welter, E. Ronge, V. Smirnov, F. Finger, C. Jooss, B. Kaiser, W. Jaegermann, *Integrated Devices for Photoelectrochemical Water Splitting Using Adapted Silicon Based Multi-Junction Solar Cells Protected by ALD* TiO_2 *Coatings*, Zeitschrift für Physikalische Chemie, 2020, **234**(6):p. 1155-1169.

[7] T. D. Nguyen, G. G. Scherer, Z. J. Xu, *A Facile Synthesis of Size-Controllable* IrO_2 *and* RuO_2 *Nanoparticles for the Oxygen Evolution Reaction*, Electrocatalysis. 2016, **7**:p. 420-427.

[8] J. Wang, Y. Ji, R. Yin, Y. Li, Q. Shao, X. Huang, *Transition metal-doped ultrathin* RuO_2 *networked nanowires for efficient overall water splitting across a broad pH range*, Journal of Materials Chemistry A, 2019, **7**:p. 6411-6416.

.

Summary and perspectives

The general objective of this thesis was to develop multijunction solar cells able to supply a high enough voltage compatible with unassisted water splitting. Our strategy has been based on the development of a-Si:H based solar cells using an original architecture developed at LPICM, namely using silicon nanowires as a template for the growth of the multijunction devices. The use of a-Si:H as the unique material has the advantage of indeed allowing for a high V_{OC} (2.75 Volts demonstrated in this thesis) and a relatively simple material optimization. On the other hand, the radial junction architecture ensures a high carrier collection, improved stability with respect to planar structures and provides a large surface area for catalyst support and its interaction with the electrolyte. We summarize below the main results in terms of solar cell efficiency, reproducibility of the results and unassisted water splitting.

On solar cells

Building up on the single junction architecture studies in previous theses, I have shown a remarkable beneficial effect of introducing a gradient of doping in the top n-layer of the devices. Its main effect is an increase in both open circuit voltage and short circuit current of the cells which can be attributed to a reduction of defects between the i-layer and the n-layer. The V_{OC} of single junction solar cells is improved from 0.77 V to 0.79 V and the J_{SC} is improved from 13.43 mA/cm^2 to 14.83 mA/cm^2. The effect of NW density on RJ solar cell performance was also investigated. NW densities of 3.3×10^8/cm^2, 2.4×10^8/cm^2 and 2.2×10^8/cm^2 show the best efficiencies for single, double and triple RJ SiNW solar cells respectively. While the reduction of the NW density with increasing the number of junctions (diameter of the stack) is expected, the rather narrow range of optimal NW densities reveals the intrinsic difficulty in optimizing this type of devices. In the case of 3RJ NW solar cells we have shown that for a NW density below 2.2×10^8/cm^2, the V_{OC} is highly sensitive to NW density and a small variation of 3RJ NW density leads to a large change in $V_{OC.}$

Despite of this, 3RJ SiNW solar cells with V_{OC} above 2 V have been consistently produced. Another interesting result was the observation of an S shape appearing in the J-V characteristics of the devices. We have shown that the S shape is due to a poor contact between the ZnO:Al and p type a-Si:H layer deposited at 600 °C in the planar regions between the NWs. The S shape is suppressed when increasing the NW density, i.e. the fraction of planar regions. Indeed, the a-Si:H deposited at high temperature has a low conductivity of ~10^{-8} S/cm. In Figure 6.1 we compare the J-V characteristics of 1RJ, 2RJ and 3RJ. Interestingly the J_{SC} of the devices reduces proportionally to the number of junctions while the V_{OC} increases from 0.79 V, to 1.34 V and 2.05 V. However, as shown in chapter 5, the requirement for an unassisted water splitting device is not on the V_{OC} but on the V_{MPP}, which has lead us to develop quadruple radial junction solar cells.

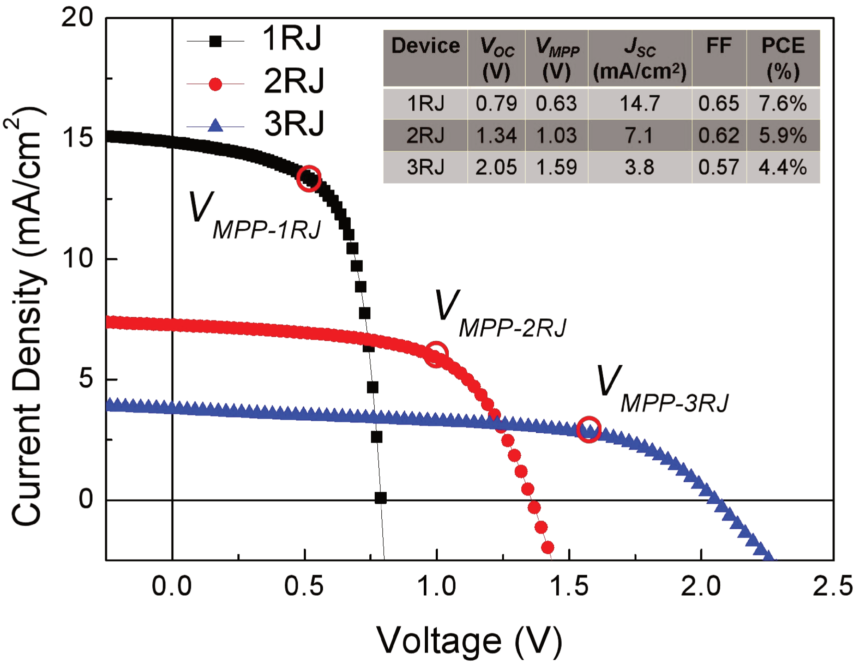

Device	V_{OC} (V)	V_{MPP} (V)	J_{SC} (mA/cm²)	FF	PCE (%)
1RJ	0.79	0.63	14.7	0.65	7.6%
2RJ	1.34	1.03	7.1	0.62	5.9%
3RJ	2.05	1.59	3.8	0.57	4.4%

Figure 6.1 J-V performance of 1RJ, 2RJ and 3RJ SiNW solar cells.

On the reproducibility of the radial junction production process

The bottom up approach to produce random arrays of SiNWs on top of which the multijunction solar cells are deposited is a simple, low cost and robust solution when compared to other approaches which require lithography to predetermine the position of the catalyst droplets or top down approaches also making use of lithography and etching. This simplicity comes at the cost of variations in the nanowire density and therefore on the V_{OC} of the devices. Thus, we have systematically addressed the possible reasons for the loss of reproducibility. Among them:

i) the surface chemistry/contamination of the ZnO:Al/Ag/CG substrate which is affected by the vacuum level and temperature;

ii) annealing time of substrate will also affect the substrate which can also modify the grain size and its surface;

iii) the Sn droplet density which is indirectly controlled via the nominal thickness of the evaporated Sn;

iv) the NW density which initial value should be controlled by the Sn layer thickness, but that can change during the H_2 plasma treatment and SiNW growth.

v) the interplay between these parameters, as the interaction of Sn atoms with the substrate will determine their diffusion, coalescence and nanodroplet diameter.

From a practical point of view, we have shown that the complexity of the processes determining the NW and RJ density can be mastered by measuring the intensity of the reflected signal as a function of time. Figure 6.2 shows the intensity of the ellipsometry signal as a function of time for different process conditions. There is a fast increase in the intensity, corresponding to an increase of the surface reflectivity as the substrate with the Sn nanoparticles is being covered with a-Si:H and NWs. As the NW length and density increase and the sample becomes diffusive, the intensity of the signal goes through a maximum and starts to decrease. Remarkably, the highest V_{OC} (optimal NW density) is achieved for the process conditions leading to a longer time for the maximum intensity.

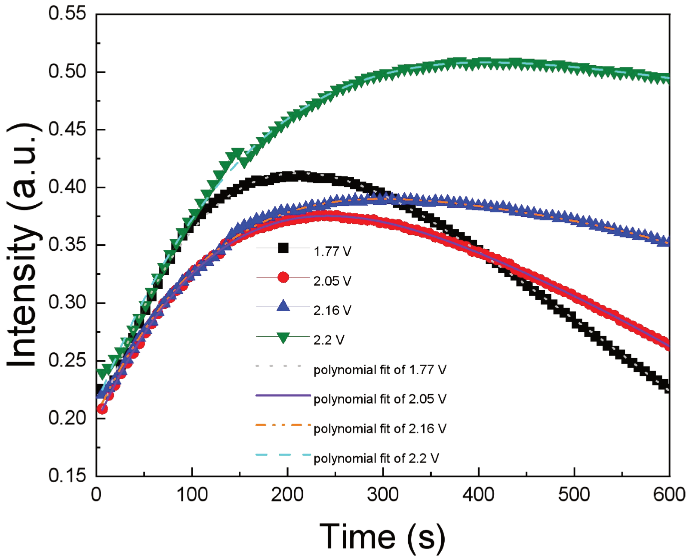

Figure 6.2 Intensity of the signal at 5.5 eV as function of time from in-situ ellipsometry of 3RJ SiNW solar cells processed under the same nominal conditions and having different values of V_{OC}.

On the unassisted water splitting

Comparing the J-V characteristics of the 3RJ SiNW solar cell with that of the electrolytic cell shows that the V_{MPP} is not enough to obtain an efficient solar-to-hydrogen production, which pushed us to develop 4RJ solar cells. Moreover, we have shown that a too fast scanning speed leads to unreliable results with hysteresis effects. For symmetrical Pt electrode and Ni electrode for HER with Pt electrode for OER systems, the water splitting has better performance in higher pH value alkaline electrolyte. Also, reducing the distance between anode and cathode has better performance of water splitting. 4RJ SiNW solar cells with 2.75 V V_{OC} have been fabricated for the first time. The 4RJ SiNW solar cell has been coated using standard thermal evaporation with earth-abundant Ni catalyst and used as the photocathode of the PEC cell for water splitting. For a PEC cell with Ni/Ti-protecting layer/4RJ SiNW solar cell photocathode and Pt anode, the efficiency reaches an initial value of 0.98% in 0.1 M KOH and 0.43% in 1 M KBi electrolyte. Moreover, a stable solar to fuel performance is realized by the 4RJ SiNW solar cell in 1 M KBi electrolyte, demonstrating the possibility of RJ SiNW solar cell for unassisted water splitting.

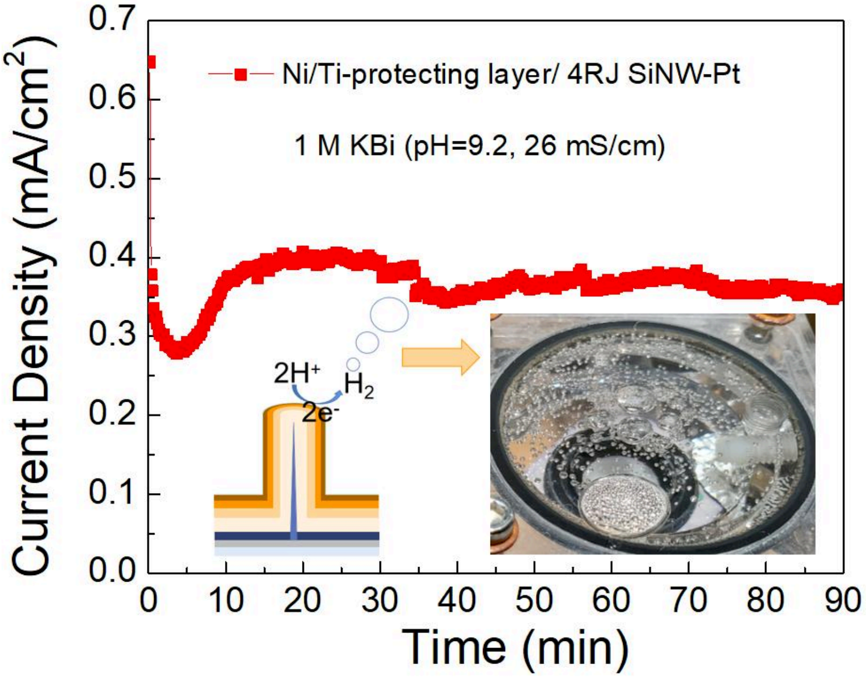

Figure 6.3 Unassisted stable water splitting by RJ SiNW PEC cell.

Perspectives

Intrinsic and doped a-Si:H layers have been used as the unique material to fabricate the multijunction devices during this thesis. As summarized in Fig. 6.1, increasing the number of junctions results in losses at the level of J_{SC} and V_{OC} (optical and electrical). A first increase in complexity would be to incorporate doped layers which are less absorbing while having a better conductivity, such as μc-Si:H and μc-SiO_x:H materials. In particular, one can further try μc-SiO_x:H as the top n layer for RJ SiNW solar cells. Moreover, applying μc-SiO_x:H as tunnel junction for double and triple junction SiNW solar cells will be also interesting to study.

For solar water splitting, the performance of the PEC cell depends on the solar cell characteristics as well as on the catalyst. The solar to fuel performance is limited by solar cell, HER and OER catalyst. It will be interesting to try different HER catalysts for the cathode. Moreover, the Pt anode can be changed into RuO_2, IrO_2 or stainless steel mesh, in order to obtain better catalytic activity and larger surface area for OER.

The RJ SiNW artificial leaf combines anode and cathode. The production of gases from artificial leaf can be measured by chromatography. Because of the ohmic loss between anode and cathode, a new PEC design that would reduce the distance that ions have to travel is also an important path for improvement.

The earth's ecological environment is being seriously damaged by the greenhouse effect. The most direct cause of the greenhouse effect is the increase in the amount of carbon dioxide in the atmosphere. The RJ SiNW solar cell for CO_2 reduction to produce high value-added fuel and chemical raw materials is a great promise.

Appendixes

A – Fits of dark J-V of different density 1RJ and 3RJ

B – Polynomial fit parameters of figure 4.12 (a)

C – More 1RJ Optimization

D – Conductivity and optical band gap of a-Si:H deposited at high temperature

A – Fits of dark J-V of different density 1RJ and 3RJ

V_{bi} , J_{ph} and V_{μ} of SiNW RJ solar cell

The carrier collection efficiency $\chi(V)$ can be introduced to describe the relation between photo current density I_{ph} and constant photo current density $I_{ph,\max}$ as follows:

$$I_{ph} = I_{ph,\max}\chi(V)$$

$$\chi(V) = \left({(V - V_{bi})}/{V_{\mu}} \right)\left(1 - e^{{V_{\mu}}/{(V - V_{bi})}} \right)$$

$$V_{\mu} = {d_i^2}/{\mu\tau_{eff}}$$

Where $\mu\tau_{eff}$ is the carrier mobility-lifetime, V_{bi} is internal built-in voltage, d_i is the absorber layer thickness. One should that $\mu\tau_{eff}$ and V_{bi} cannot be directly measured easily. But the J-V curve can be fitted by the last equation, then V_{bi} and V_{μ} can be obtained [34, 35]. V_{μ} is related to FF, higher V_{μ} is corresponding to lower FF.

Figure A1 shows the fitting curves of J-V of SiNW solar cells with density of $0.7\times10^8/\text{cm}^2$. Table A1 shows the fitting values of V_{bi}, J_{ph} and V_{μ} from J-V curves of different density SiNW solar cells. The J_{ph} is always higher than the J_{SC}. Because the value of current density of solar cell is photo current minus recombination. For the J_{ph} as function of SiNW density, the J_{ph} increases with the SiNW density. However, for the trend of J_{SC} as function of SiNW density, the J_{SC} goes down as the SiNW density rises up from $3.3\times10^8/\text{cm}^2$ to $4.8\times10^8/\text{cm}^2$. This is due to the J_0 rise up significantly as the SiNW density reach to $4.8\times10^8/\text{cm}^2$. The V_{μ} of SiNW solar cells with different density is all around 0.1.

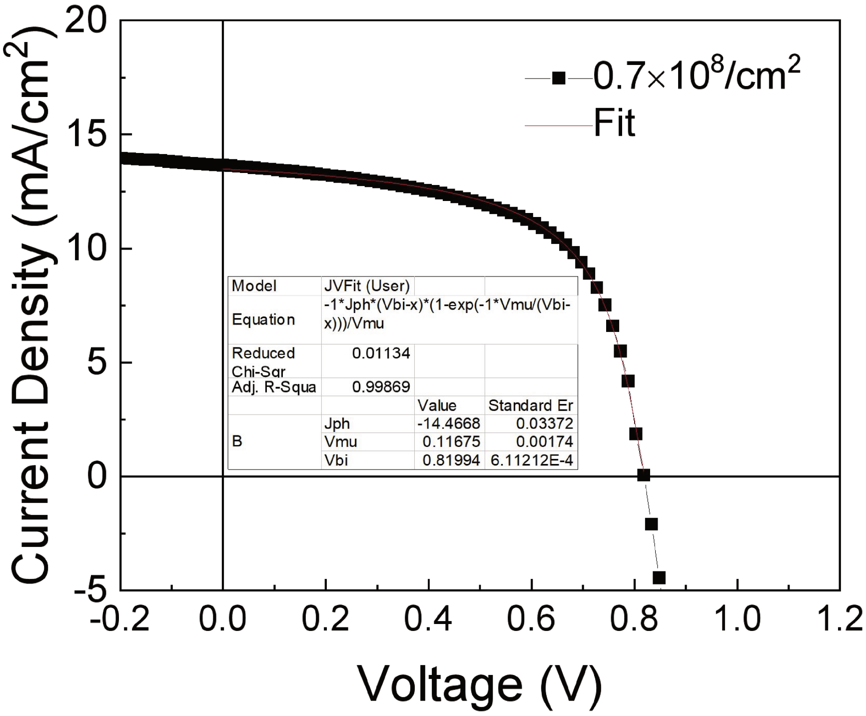

Model	JVFit (User)		
Equation	-1*Jph*(Vbi-x)*(1-exp(-1*Vmu/(Vbi-x)))/Vmu		
Reduced Chi-Sqr	0.01134		
Adj. R-Squa	0.99869		
		Value	Standard Er
B	Jph	-14.4668	0.03372
	Vmu	0.11675	0.00174
	Vbi	0.81994	6.11212E-4

Figure A1 Fitting curves of J-V characteristics of SiNW solar cell with density of 0.7×10^8/cm^2. Variances are marked in the tables in the curves.

Table A1 V_{bi} and V_μ from fitting curves of J-V characteristics of different density SiNW solar cells.

Nanowire density	V_{bi} **(V)**	J_{ph} **(mA/cm^2)**	V_μ **(V)**
0.7×10^8/cm^2	0.82	14.47	0.12
2.3×10^8/cm^2	0.81	14.6	0.11
3.3×10^8/cm^2	0.78	15.25	0.1
4.8×10^8/cm^2	0.65	15.4	0.15

Real R_s and R_p from dark J-V of different density SiNW solar cells

Solar cells can be assumed to be ideal diodes. The dark J-V curves of different density SiNW solar cells show the PIN diode performance. From fitting the dark J-V curve, we can know the R_s and R_p from the slope according to the equation:

$$I = I_{ph} - I_0[\exp(\frac{q(V+IR_S)}{nkT}) - 1] - \frac{V+IR_S}{R_P}$$

Figure A2 presents the dark J-V curves of SiNW solar cell with different density. Table A2 presents the R_{OC}, R_{SC} and R_s, R_p. R_{OC} is the resistance around V_{OC} in the light,

R_{SC} is the resistance around J_{SC} in the light. The R_s and R_p in the dark present the real resistance without light effect. The R_s in the dark is smaller than R_{OC} in the light. On the contrary, the R_p in the dark is larger than R_{SC} of in the light. For the R_s and R_p from the dark J-V, the solar cell with density of 4.8×10^8/cm^2 also has the largest R_s (14.74 Ω cm^2) and lowest R_p (1523 Ω cm^2). This causes the lowest FF of solar cell with density of 4.8×10^8/cm^2.

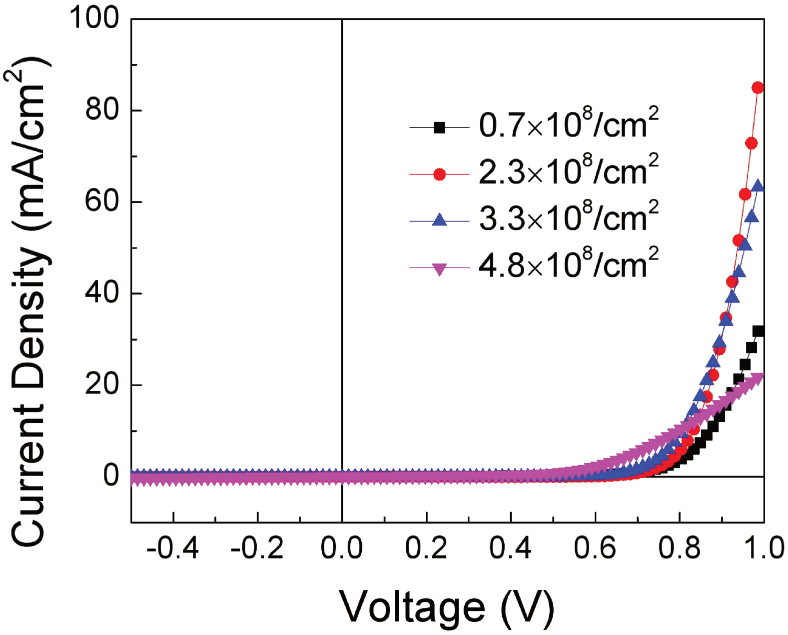

Figure A2 Dark J-V curves of different density SiNW solar cells.

Table A2 R_s and R_p of different density SiNW solar cells.

Nanowire Density	**R_{OC} (Ω cm^2)**	**R_{SC} (Ω cm^2)**	**R_s (dark) (Ω cm^2)**	**R_p (dark) (Ω cm^2)**
0.7×10^8/cm^2	10.1	497	4.31	5824
2.3×10^8/cm^2	8.54	431	1.36	223214
3.3×10^8/cm^2	8.58	539	2.43	54885
4.8×10^8/cm^2	20.2	335	14.74	1523

J_0 and n from the dark J-V of different density SiNW solar cell

Figure A3 shows the dark J-V measurement of SiNW solar cell with different NW density ($\log_{10}|J_{SC}|$ as a function of voltage). Table 3.6 gives the J_0 and n values from the fitting result. The diode ideality factor is used for evaluating how closely a diode follows the ideal diode equation as following

$$I = I_L - I_0[\exp(\frac{qV}{nkT}) - 1]$$

In this equation, the model assumes the recombination only happens in the band to band or via traps in the bulk areas, not in the junction. Under the circumstances, the diode ideality factor is equal to 1. But other recombination or recombination in the other areas makes the diode ideal factor far away from 1. The values of n shown in the table A3 are all above 1. This illustrates that the solar cells are away from ideal state. In comparison with the J_0 of solar cells with NW density of $2.3\times10^8/\text{cm}^2$ and $3.3\times10^8/\text{cm}^2$, the J_0 of solar cell with density of $0.7\times10^8/\text{cm}^2$ is higher. This may be due to the fact that a lower density of SiNWs will result in a larger area for the planar part in between the NWs, where a more defective p-type a-Si:H layer is deposited during NW growth high temperature (600 °C). For the SiNW solar cell with density of $4.8\times10^8/\text{cm}^2$, it shows the highest J_0 among all four samples, this is due to a larger surface area from high SiNW density sample creates more recombination.

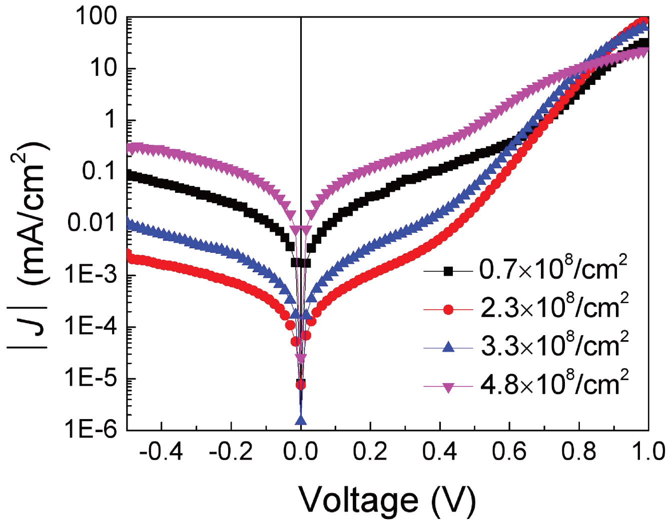

Figure A3 Dark J-V measurement of SiNW solar cells with different NW density.

Table A3 J_0 and n fitting from dark J-V curves of SiNW solar cells with different NW density.

Nanowire Density	J_0 (mA/cm^2)	n
0.7×10^8/cm^2	4.43×10^{-5}	1.9
2.3×10^8/cm^2	1.22×10^{-6}	1.4
3.3×10^8/cm^2	6.46×10^{-6}	1.5
4.8×10^8/cm^2	3.7×10^{-3}	2.5

V_{bi} , J_{ph} and V_μ of SiNW RJ solar cell

The carrier collection efficiency $\chi(V)$ can be introduced to describe the relation between photo current density I_{ph} and constant photo current density $I_{ph,\max}$ as follows:

$$I_{ph} = I_{ph,\max}\chi(V)$$

$$\chi(V) = \left({(V - V_{bi})}/{V_\mu} \right)\left(1 - e^{{V_\mu}/{(V - V_{bi})}} \right)$$

$$V_\mu = {d_i^2}/{\mu\tau_{eff}}$$

Where $\mu\tau_{eff}$ is the carrier mobility-lifetime, V_{bi} is internal built-in voltage, d_i is the absorber layer thickness. One should that $\mu\tau_{eff}$ and V_{bi} cannot be directly measured easily. But the J-V curve can be fitted by the last equation, then V_{bi} and V_μ can be obtained [34, 35]. V_μ is related to FF, higher V_μ is corresponding to lower FF.

Figure A4 shows the fitting curves of J-V of SiNW solar cells with density of 0.7×10^8/cm^2. Table A4 shows the fitting values of V_{bi}, J_{ph} and V_μ from J-V curves of different density SiNW solar cells. The J_{ph} is always higher than the J_{SC}. Because the value of current density of solar cell is photo current minus recombination. For the J_{ph} as function of SiNW density, the J_{ph} increases with the SiNW density. However, for the trend of J_{SC} as function of SiNW density, the J_{SC} goes down as the SiNW density rises up from 3.3×10^8/cm^2 to 4.8×10^8/cm^2. This is due to the J_0 rise up significantly as the SiNW density reach to 4.8×10^8/cm^2. The V_μ of SiNW solar cells with different density is all around 0.1.

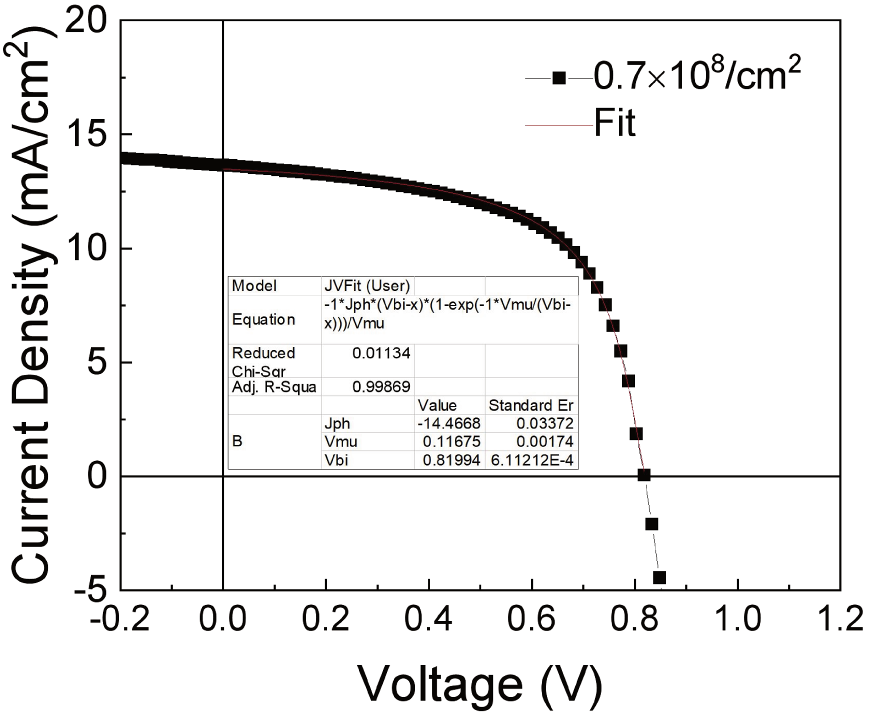

Model	JVFit (User)		
Equation	-1*Jph*(Vbi-x)*(1-exp(-1*Vmu/(Vbi-x)))/Vmu		
Reduced Chi-Sqr	0.01134		
Adj. R-Squa	0.99869		
		Value	Standard Er
B	Jph	-14.4668	0.03372
	Vmu	0.11675	0.00174
	Vbi	0.81994	6.11212E-4

Figure A4 Fitting curves of J-V characteristics of SiNW solar cell with density of 0.7×10^8/cm^2. Variances are marked in the tables in the curves.

Table A4 V_{bi} and V_{μ} from fitting curves of J-V characteristics of different density SiNW solar cells.

Nanowire density	V_{bi} **(V)**	J_{ph} **(mA/cm^2)**	V_{μ} **(V)**
0.7×10^8/cm^2	0.82	14.47	0.12
2.3×10^8/cm^2	0.81	14.6	0.11
3.3×10^8/cm^2	0.78	15.25	0.1
4.8×10^8/cm^2	0.65	15.4	0.15

Real R_s and R_p from dark J-V of different density SiNW solar cells

Solar cells can be assumed to be ideal diodes. The dark J-V curves of different density SiNW solar cells show the PIN diode performance. From fitting the dark J-V curve, we can know the R_s and R_p from the slope according to the equation:

$$I = I_{ph} - I_0[\exp(\frac{q(V+IR_S)}{nkT}) - 1] - \frac{V+IR_S}{R_P}$$

Figure A5 8 presents the dark J-V curves of SiNW solar cell with different density.

Table A5 presents the R_{OC}, R_{SC} and R_s, R_p. R_{OC} is the resistance around V_{OC} in the light, R_{SC} is the resistance around J_{SC} in the light. The R_s and R_p in the dark present the real resistance without light effect. The R_s in the dark is smaller than R_{OC} in the light. On the contrary, the R_p in the dark is larger than R_{SC} of in the light. For the R_s and R_p from the dark J-V, the solar cell with density of $4.8\times10^8/\text{cm}^2$ also has the largest R_s (14.74 Ω cm^2) and lowest R_p (1523 Ω cm^2). This causes the lowest FF of solar cell with density of $4.8\times10^8/\text{cm}^2$.

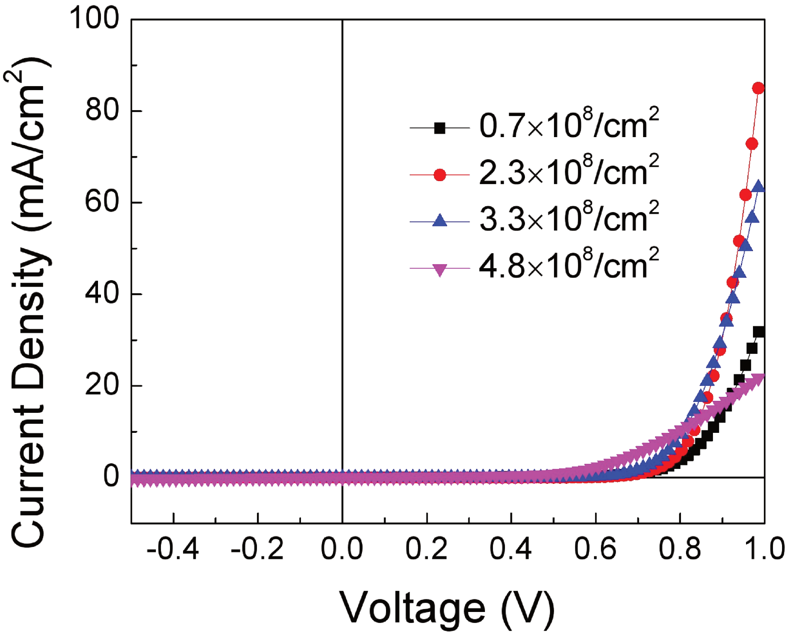

Figure A5 Dark J-V curves of different density SiNW solar cells.

Table A5 R_s and R_p of different density SiNW solar cells.

Nanowire Density	**R_{OC} (Ω cm^2)**	**R_{SC} (Ω cm^2)**	**R_s (dark) (Ω cm^2)**	**R_p (dark) (Ω cm^2)**
$0.7\times10^8/\text{cm}^2$	10.1	497	4.31	5824
$2.3\times10^8/\text{cm}^2$	8.54	431	1.36	223214
$3.3\times10^8/\text{cm}^2$	8.58	539	2.43	54885
$4.8\times10^8/\text{cm}^2$	20.2	335	14.74	1523

J_0 and n from the dark J-V of different density SiNW solar cell

Figure A6 shows the dark J-V measurement of SiNW solar cell with different NW density ($\log_{10}|J_{SC}|$ as a function of voltage). Table A6 gives the J_0 and n values from the fitting result. The diode ideality factor is used for evaluating how closely a diode follows the ideal diode equation as following

$$I = I_L - I_0[\exp(\frac{qV}{nkT}) - 1]$$

In this equation, the model assumes the recombination only happen in the band to band or via traps in the bulk areas, not in the junction. Under the circumstances, the diode ideality factor is equal to 1. But other recombination or recombination in the other areas makes the diode ideal factor far away from 1. The values of n shown in the table 3.6 are all above 1. This illustrates that the solar cells are away from ideal state. In comparison with the J_0 of solar cells with NW density of $2.3\times10^8/\text{cm}^2$ and $3.3\times10^8/\text{cm}^2$, the J_0 of solar cell with density of $0.7\times10^8/\text{cm}^2$ is higher. This may be due to the fact that a lower density of SiNWs will result in a larger area for the planar part in between the NWs, where a more defective p-type a-Si:H layer is deposited during NW growth high temperature (600 °C). For the SiNW solar cell with density of $4.8\times10^8/\text{cm}^2$, it shows the highest J_0 among all four samples, this is due to a larger surface area from high SiNW density sample creates more recombination.

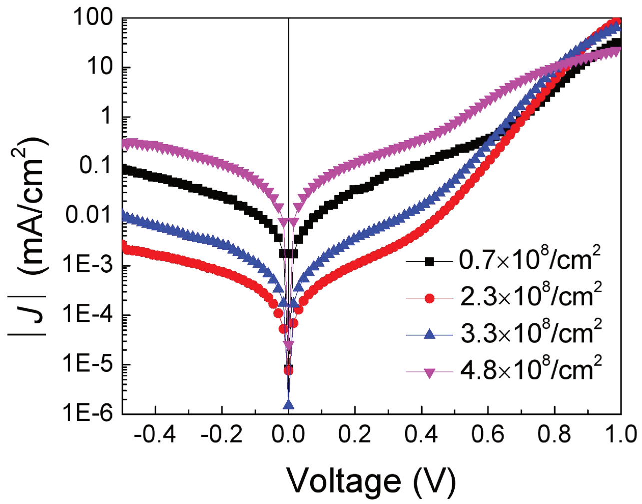

Figure A6 Dark J-V measurement of SiNW solar cells with different NW density.

Table A6 J_0 and n fitting from dark J-V curves of SiNW solar cells with different NW density.

Nanowire Density	**J_0 (mA/cm^2)**	**n**
0.7×10^8/cm^2	4.43×10^{-5}	1.9
2.3×10^8/cm^2	1.22×10^{-6}	1.4
3.3×10^8/cm^2	6.46×10^{-6}	1.5
4.8×10^8/cm^2	3.7×10^{-3}	2.5

R_s and R_p from the dark J-V curves

It is interesting to know the true values of the series (R_s) and parallel resistances (R_p), which can be obtained by fitting the slope of the dark J-V curves and comparing these to the values obtained by fitting the slopes of the light J-V curves at V_{OC} and J_{SC} (R_{OC} and R_{SC}, respectively). Results are presented in Table A7.

Whether calculated from the light J-V or from the dark J-V, the R_{OC} and R_S decreases as the nanowire density rises up. For the R_{OC}, this is an artefact, as this can be attributed to the S shape and it makes the solar cell appear to have larger R_{OC} than it would in reality.

Finally, if we compare the values of the real R_p in the dark to those of R_{SC} measured in the light, we notice that the real R_p is many orders of magnitude higher (except for the samples with the highest SiNW density). This is because R_{OC} is reflecting other phenomena (recombination or lack of current matching), and also shows that R_P is not limiting the performance of the cells in any way.

Table A7 The fitting of R_s and R_p from dark and light J-V curves.

Nanowire Density	**1.2×10^8/cm^2**	**1.7×10^8/cm^2**	**2.2×10^8/cm^2**	**3.5×10^8/cm^2**	**4.3×10^8/cm^2**
$R_s/\Omega\cdot\text{cm}^{-2}$ (from dark J-V)	3198	257.8	92.4	11.8	8.5
$R_{OC}/\Omega\cdot\text{cm}^{-2}$ (from light J-V)	321.2	116.7	87.1	78.9	62.5
$R_p/\Omega\cdot\text{cm}^{-2}$ (from dark J-V)	1.4×10^6	1.4×10^6	1.3×10^6	4.4×10^5	575.9
$R_{SC}/\Omega\cdot\text{cm}^{-2}$ (from light J-V)	3900	2340	2170	1826	3818

Figure A7 shows the dark J-V curves of the solar cells in a linear log plot. Table A8 shows the fitting result from the dark J-V curves of 3RJ solar cells with different densities of SiNWs, fit for the part of the curve that replicates the diode equation (linear when plotted as ln *J*). The value of lnJ_0 can be obtained from the intersection with the y axis when fitting the curves. The J_0 increases as SiNW density increases from 1.7×10^8/cm^2 to 4.3×10^8/cm^2, it means more recombination/saturation current is generated in a higher density 3RJ SiNW solar cell. The ideality factor, *n*, can be obtained from the slope of the fitting curves, and the solar cell with a SiNW density of 1.7×10^8/cm^2 has smallest n of 6.81.

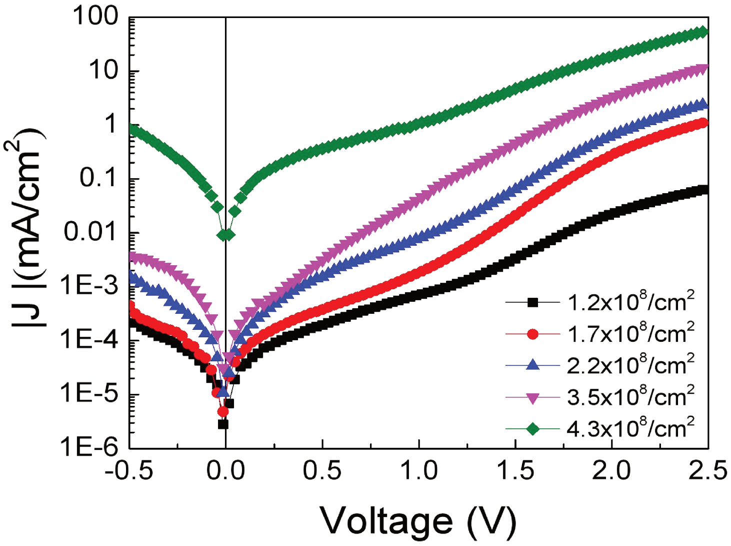

Figure A7 Dark J-V curve of different density SiNW 3RJ solar cells. (|J| as a function of voltage, NW density ranging from 1.2×10^8/cm^2 to 4.3×10^8/cm^2)

Table A8 The J_0, n and V_{OC} values calculated from equation of different density 3RJ solar cells.

Density	J_0 **(mA/cm^2)**	**n**	V_{OC} **by equation (V)**	V_{OC} **by J-V (V)**	J_{SC} **(mA/cm^2)**
1.2×10^8/cm^2	6.39× 10^{-6}	9.27	2.94	2.2	2.97
1.7×10^8/cm^2	4.59×10^{-6}	6.81	2.4	2.17	3.44
2.2×10^8/cm^2	3.7×10^{-5}	7.78	2.32	2.05	3.77
3.5×10^8/cm^2	7.58×10^{-4}	9.08	2	1.77	3.86
4.3×10^8/cm^2	4.93×10^{-2}	12.77	1.44	1.35	3.9

Finally, the V_{OC} can be calculated from the fitting J_0 and n, and using the real value of J_{SC}, as $V_{OC} = nkT \ln(J_{SC} / J_0)$. Calculated this way, all the V_{OC} values are higher than the V_{OC} measured from the J-V characteristic, which is to be expected as the diode equation does not account for V_{OC} loses due imperfections on the device as well as to voltage loses at contacts. Nevertheless, the trend versus SiNW density for calculated V_{OC} is the same as that of measured V_{OC}.

Fits of dark J-V of different density 3RJ for *J_0* and n

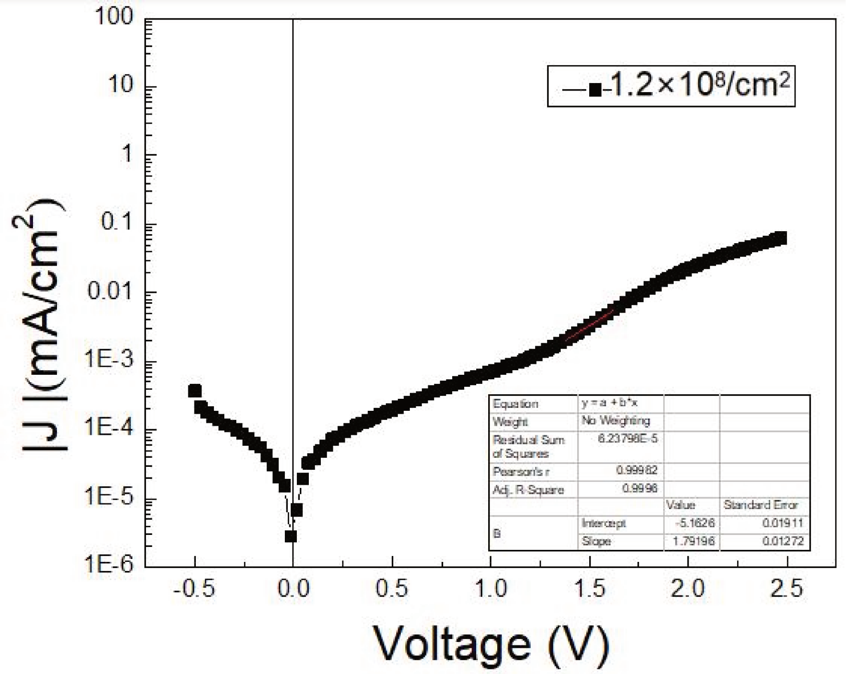

Equation	y = a + b*x		
Weight	No Weighting		
Residual Sum of Squares	6.23798E-5		
Pearson's r	0.99982		
Adj. R-Square	0.9996		
		Value	Standard Error
B	Intercept	-5.1626	0.01911
	Slope	1.79196	0.01272

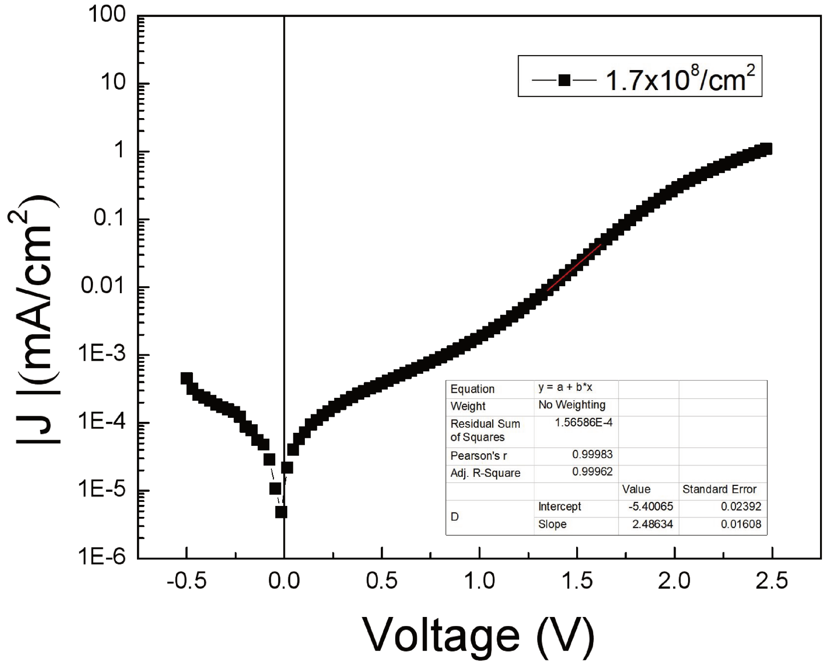

Equation	y = a + b*x		
Weight	No Weighting		
Residual Sum of Squares	1.56586E-4		
Pearson's r	0.99983		
Adj. R-Square	0.99962		
		Value	Standard Error
D	Intercept	-5.40065	0.02392
	Slope	2.48634	0.01608

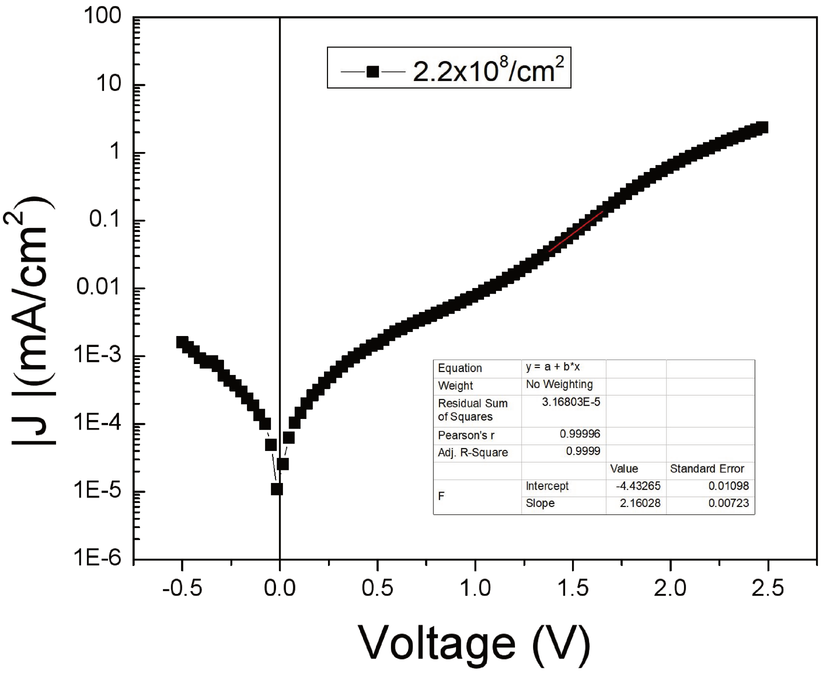
100
10
1
0.1
0.01
1E-3
1E-4
1E-5
1E-6
|J |(mA/cm^2)
-0.5
0.0
0.5
1.0
1.5
2.0
2.5
Voltage (V)
2.2x10^8/cm^2
Equation
y = a + b*x
Weight
No Weighting
Residual Sum of Squares
3.16803E-5
Pearson's r
0.99996
Adj. R-Square
0.9999
Value
Standard Error
F
Intercept
-4.43265
0.01098
Slope
2.16028
0.00723

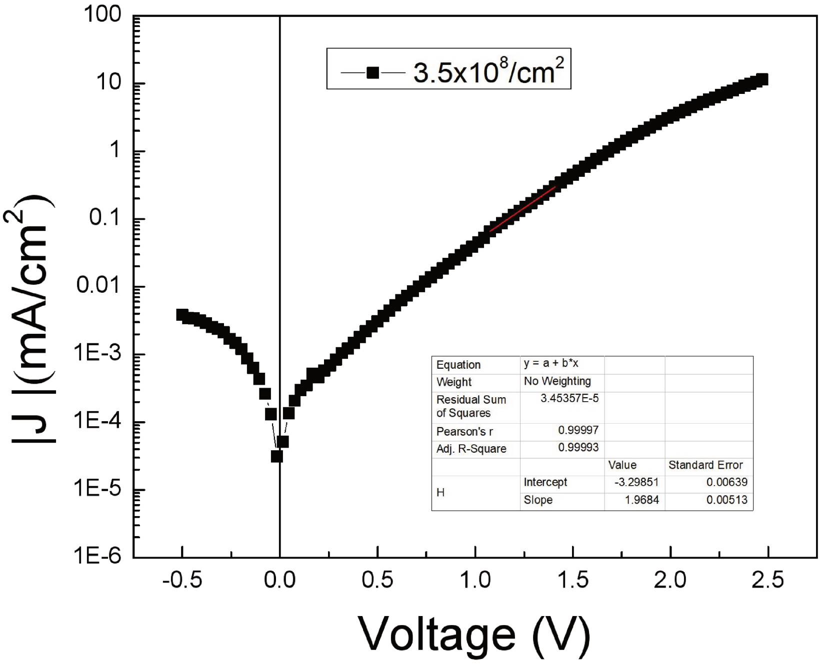
100
10
1
0.1
0.01
1E-3
1E-4
1E-5
1E-6
|J |(mA/cm^2)
-0.5
0.0
0.5
1.0
1.5
2.0
2.5
Voltage (V)
3.5x10^8/cm^2
Equation
y = a + b*x
Weight
No Weighting
Residual Sum of Squares
3.45357E-5
Pearson's r
0.99997
Adj. R-Square
0.99993
Value
Standard Error
H
Intercept
-3.29851
0.00639
Slope
1.9684
0.00513

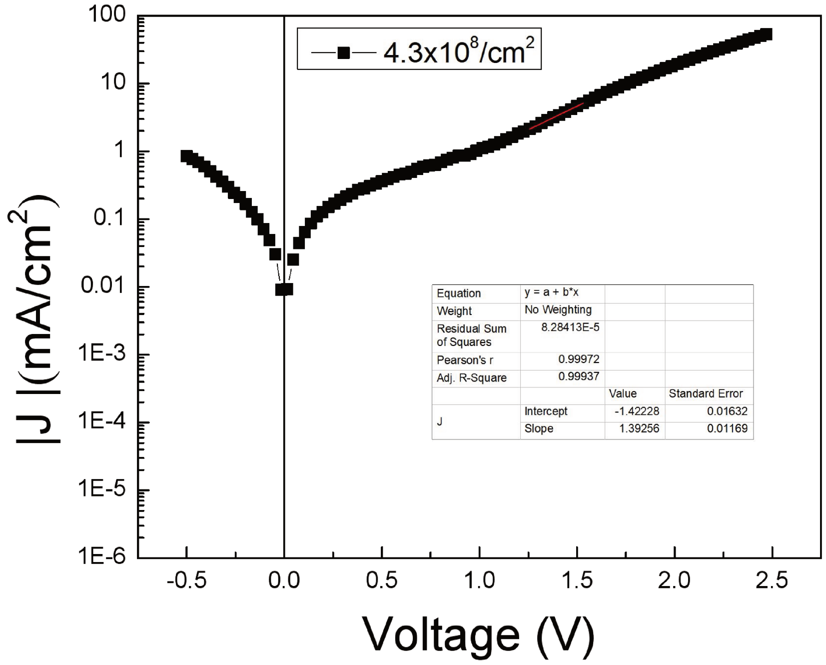

Equation	y = a + b*x		
Weight	No Weighting		
Residual Sum of Squares	8.28413E-5		
Pearson's r	0.99972		
Adj. R-Square	0.99937		
		Value	Standard Error
J	Intercept	-1.42228	0.01632
	Slope	1.39256	0.01169

Appendix B – Polynomial fit parameters of figure 4.12 (a)

The equation of the used polynomial fit is $Y=intercept+B_1\times X+B_2\times X_2+B_3\times X_3+B_4\times X_4$, this polynom shows good fitting for figure 4.12 (a). The specific indexes are shown in table A9. Y is intensity, X is time. B_1, B_2, B_3 and B_4 are primary term, quadratic, cubic and quartic coefficients.

Table B1 Polynomial fit parameters of figure 4.12 (a)

Y	1.77 V	2.05 V	2.16 V	2.2 V
intercept	0.19275	0.19594	0.20267	0.21201
B_1	$0.00252\pm3.97735\times10^{-5}$	$0.00183\pm1.00303\times10^{-5}$	$0.00174\pm2.33111\times10^{-5}$	$0.00207\pm4.37687\times10^{-5}$
B_2	$-9.37674\times10^{-6}\pm2.64753\times10^{-7}$	$-6.20763\times10^{-6}\pm6.67672\times10^{-8}$	$-5.75605\times10^{-6}\pm1.55171\times10^{-7}$	$-5.16805\times10^{-6}\pm2.91347\times10^{-7}$
B_3	$1.27057\times10^{-8}\pm6.54436\times10^{-10}$	$7.95303\times10^{-9}\pm1.6504\times10^{-10}$	$8.1497\times10^{-9}\pm3.8356\times10^{-10}$	$5.53957\times10^{-9}\pm7.20174\times10^{-10}$
B_4	$-6.53653\times10^{-12}\pm5.3556\times10^{-13}$	$-3.99267\times10^{-12}\pm1.35061\times10^{-13}$	$-4.50012\times10^{-12}\pm3.1389\times10^{-13}$	$-2.26129\times10^{-12}\pm5.89356\times10^{-13}$
R^2	0.99738	0.99965	0.99808	0.99798

Appendix C – More 1RJ Optimization

As growing the PIN structure solar cell, when the deposition layer changes from p layer to i layer or changes from i layer to n layer, the defects are produced. The electron accumulate in the interface. A gradient doping n layer or p layer can reduce the defects and makes the electrons and holes transfer more smoothly. The improvement on V_{OC} is not obvious as shown in figure C1, which maybe due to the S shape. The improvement on current density can be contribute to a thinner p or n layer. For a thinner n layer, if shine light through n layer, less light will be absorbed by n layer, but also works for p layer. More light can go through and absorbed by i layer. The gradient doping n layer can help the solar cell performance. The current density is improved from 8.33 mA/cm^2 with constant doping to 9.46 mA/cm^2 with n gradient doping to 10.23 mA/cm^2 with p and n both in gradient doping.

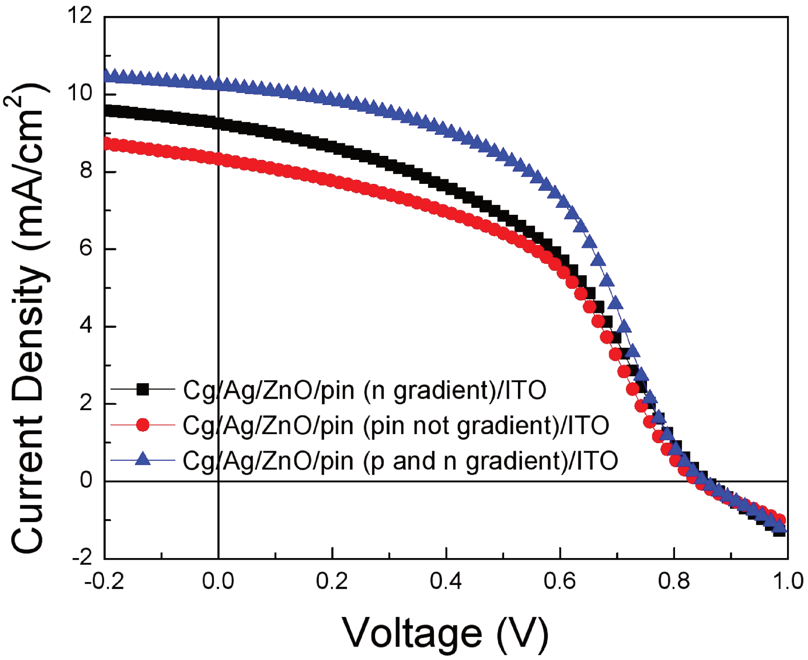

Figure C1 J-V characteristics of planar solar cells with and without gradient doped layer.

Table C1 The extracted parameters of planar solar cells with different thickness ZnO:Al substrate form figure 3.24.

Type	V_{OC} (V)	J_{SC} (mA/cm^2)	FF	η (%)
Cg/Ag/ZnO/pin/ITO	0.85	8.33	0.47	3.33
Cg/Ag/ZnO/pin (n gradient)/ITO	0.85	9.46	0.46	3.7
Cg/Ag/ZnO/pin (p and n gradient)/ITO	0.85	10.23	0.51	4.44

Figure C2 shows the J-V characteristics of NIP junction planar solar cells with CG/ZnO:Al substrate and FTO substrate. The NIP structure solar cell has current density of 12.22 mA/cm^2 with commercial FTO substrate and 9.1 mA/cm^2 with CG/ZnO:Al substrate. The current density enhancement may be due to the light absorption improvement, due on a contribution to the roughness of FTO substrate. The enhancement on J_{SC} causes the efficiency increasing from 3.85% to 4.8% by changing the CG/ZnO:Al to FTO. Both the small S shape around V_{OC} maybe come from the p layer connection with ITO. Because the ITO is n type.

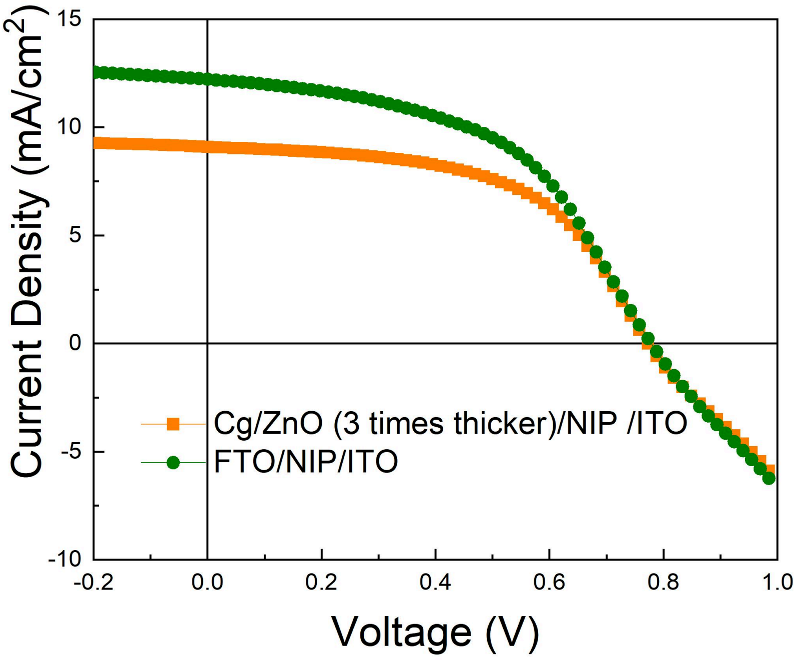

Figure C2 J-V characteristics of planar NIP junction solar cells with different substrates

Table C2 The extracted parameters of planar NIP junction solar cells with different substrates from figure 3.26

Type	V_{OC} (V)	J_{SC} (mA/cm^2)	FF	η (%)
FTO/NIP/ITO	0.77	12.22	0.51	4.8
Cg/ZnO:Al (3 times thicker) /NIP/ITO	0.77	9.1	0.55	3.85

Figure C3 presents the J-V characteristics of planar solar cell with different back reflectors, the J_{SC} is improved from 9.1 mA/cm^2 to 9.5 mA/cm^2 by applying Al minor. But the V_{OC} and FF are decreased by using Al minor. However, by changing the minor from Al to Ag, the Ag back reflector can further enhanced the current density to 9.73 mA/cm^2 and FF is improved from 0.55 to 0.59. As a consequence, the efficiency of solar cell with Ag back reflector is increased from 3.85% to 4.42%. Comparing to Al, the Ag is more suitable as back reflector for solar cell. On the other hand, the S shape will also affected by back reflector, The Ag/ZnO:Al shows the best contact for solar cell. It not only reduces the S shape, but also enhance the efficiency.

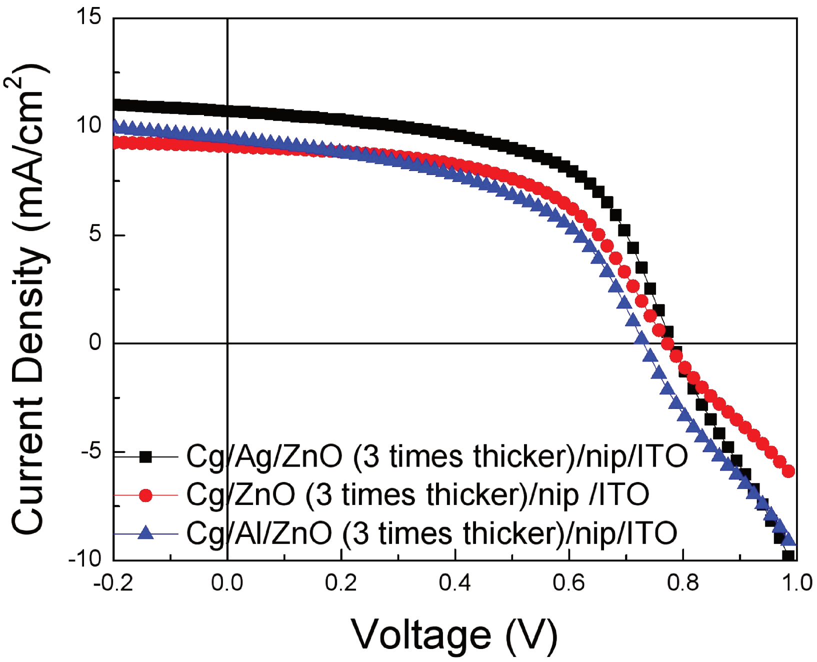

Figure C3 J-V characteristics of planar solar cells with different back reflector

Table C3 The extracted parameters of planar solar cells with different thickness ZnO:Al substrate from figure 3.27

Type	V_{OC} (V)	J_{SC} (mA/cm^2)	FF	η (%)
Cg/ZnO (3 times thicker) /nip/ITO	0.77	9.1	0.55	3.85
Cg/Al/ZnO (3 times thicker) /nip/ITO	0.73	9.5	0.5	3.47
Cg/Ag/ZnO (3 times thicker) /nip/ITO	0.77	9.73	0.59	4.42

Appendix D – Conductivity and optical band gap of a-Si:H deposited at high temperature

We find that the problem of S shape is from the non-ohmic contact between substrate and p type a-Si:H. In the planar part of SiNW solar cell, the a-Si:H is deposited on CG and non-ohmic contact is formed. Hence, it is interesting to know the conductivity of a-Si:H layer deposited at higher temperature. The temperature for p type a-Si:H thin film deposition is 600°C, which is the same temperature used for SiNW growth. The Al contact is deposited by evaporation. To be sure that the Al can be used as a good contact, 200 nm thickness Al is deposited on a-Si:H layer by evaporation. The conductivity is measured by meter in the dark.

According to the equation,

$$\sigma = \frac{1}{\mathrm{R}} \cdot \frac{L}{S} = \frac{1}{\mathrm{R}} \cdot \frac{L}{tW}$$

σ is the conductivity of a-Si:H layer, L is the distance between two Al pads layer, W is the width of the Al contact layer, t is the thickness of a-Si:H, R is the resistance calculated from the voltage and current density from the meter. Therefore, the conductivity of p type a-Si:H deposited at high temperature is 1.5×10^{-8} S/cm. That is lower than that of normal p type a-Si:H. The low conductivity can be contribute to the poor contact for solar cell.

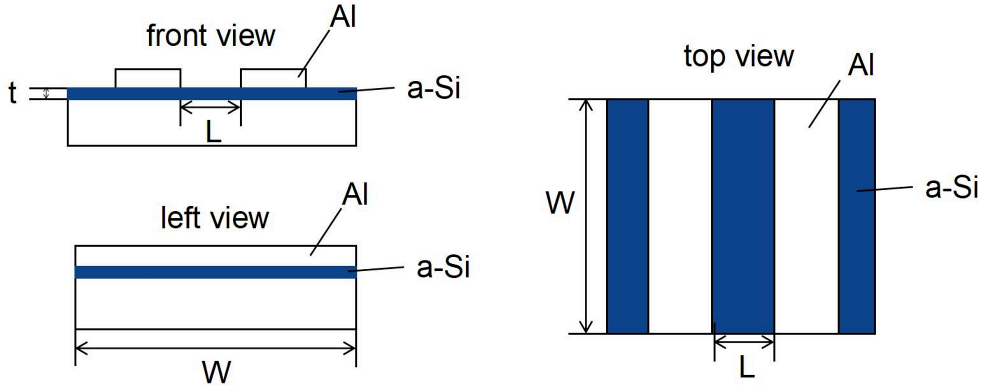

Figure D1 Configuration of the sample for conductivity measurement

In addition to the conductivity of a-Si:H, the thickness and optical band gap is measured by ellipsometer. A simple two layers model is used for fitting the ellipsometry spectra. In the model, the top layer is 50% a-Si:H and 50% void, the second layer is the a bulk p type a-Si:H layer. The substrate is glass. The part of under the glass substrate is void. From figure D2, the ellipsomety spectra of a-Si:H, we can know the surface roughness, the fitting curve is overlapping with the curves measured by ellipsometer. The top layer thickness is 3 nm, the second layer thickness is 33 nm. The optical band gap is 1.52 eV, because a-Si:H is deposited at 600℃. High temperature makes a-Si:H has a narrower band gap. C is 2.43, A is 202.6, E_0 is 3.69 from Tauc-Lorentz model fitting.

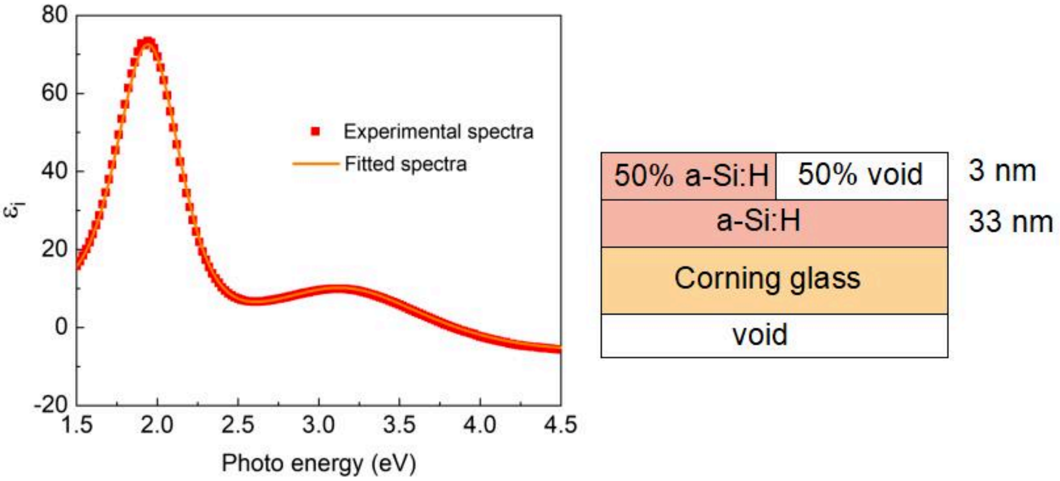

Figure D2 Ellipsometer spectra and its fitting mode of a-Si:H deposited at 600℃.

List of Publications

Peer reviewed articles:

- **Chaoqi Wang**, Martin Foldyna, Erik V. Johnson and Pere Roca i Cabarrocas, "Triple Radial Junction Hydrogenated Amorphous Silicon Solar Cells with >2 V Open-Circuit Voltage", Solar RRL, DOI:10.1002/solr.202200248, Frontispiece.
- **Chaoqi Wang**, Martin Foldyna, Pere Roca i Cabarrocas, Erik V. Johnson, "Repeatable Influence of NW Density on Solar Cell Performance", (to be submitted).
- **Chaoqi Wang**, Pere Roca i Cabarrocas, Erik V. Johnson and Martin Foldyna, "Unassisted Solar Water Splitting with Radial Junction Silicon Nanowire Photoelectrochemical Cell", (to be submitted).

Conference:

- **Chaoqi Wang**, Pere Roca i Cabarrocas, Erik V. Johnson and Martin Foldyna, "Triple Radial Junction Silicon Nanowire Solar Cells with 2.2 V Open Circuit Voltage", Poster, Nanowire Week 2022, April, 2022, Chamonix, France.
- **Chaoqi Wang**, Martin Foldyna, Pere Roca i Cabarrocas and Erik V. Johnson, "Radial Junction Hydrogenated Amorphous Silicon Solar Cells for Unassisted Solar Water Splitting", Oral, The 29th International Conference on Amorphous and Nano-crystalline Semiconductors, August, 2022, Nanjing, China.

ECOLE
DOCTORALE

Titre : Cellules solaires à base de nanofils de silicium: depuis les simple et double jonctions vers des triple et quadruple jonctions radiales pour l'électrolyse de l'eau

Mots clés : jonction radiale; nanofils; cellule solaire quadruple jonction; cellule photoélectrochimique

Résumé : Les cellules photo-électrochimiques (PEC) sont des dispositifs prometteurs pour convertir via l'électrolyse de l'eau l'énergie solaire en énergie chimique que l'on peut stocker. Les cellules solaires à base de nanofils de silicium (SiNW) à jonction radiale (JR) simple et double ont été étudiées précédemment au LPICM. Dans cette thèse, et pour la première fois, des cellules triple et quadruple jonction radiales (3JR, 4JR) ont été réalisées. Nous avons étudié l'effet de la densité de JR sur le rendement des cellules 3JR et montré que le V_{OC} est inversement corrélé à la densité. Un V_{OC} de 2.05 V et un rendement de 4.4% ont été obtenus pour une densité de 2.2x10^8 JR/cm^2.

Afin de savoir d'où vient le caractère aléatoire des performances des cellules solaires, leur processus de croissance a été analysé étape par étape. Nous avons constaté que la mesure de l'intensité du signal d'ellipsométrie en fonction du temps peut être utilisé pour optimiser la densité de NWs et predire le V_{OC} des cellules. Un pic plus tardif correspondant à une densité NW plus faible et à un V_{OC} plus élevé.

Afin d'obtenir un V_{OC} suffisant pour l'electrolyse non assitée de l'eau, nous avons optimisé des cellules 4JR, nous permettant d'atteindre un V_{OC} de 2,75 V. Avec du Ni comme catalyseur evaporé sur les 4JR (photocathode) et du Pt comme photoanode, nous avons demontré un fonctionnement stable de la cellule PEC pendant 90 min dans 1M KBi. L'efficacité de la PEC a une valeur initiale de 0,98% avec 0,1 M KOH comme électrolyte, et une valeur stabilisée de 0,43% avec de 1 M KBi.

Title : Silicon nanowire solar cells: from single and double to triple and quadruple radial junctions for unassisted water splitting

Keywords : radial junction; nanowires; quadruple junction solar cell; photoelectrochemical cell

Abstract : Water splitting in a Photo-electrochemical (PEC) cell allows to convert solar energy to chemical energy which can be stored. Single and double radial junction (RJ) silicon nanowire (SiNW) solar cells have been previously studied at LPICM. In this thesis, and for the first time, triple and quadruple junctions (3RJ, 4RJ) have been realized. We investigated the effect of NW density on 3RJ solar cell performance, showing that a higher V_{OC} correlates with a lower NW density. A V_{OC} of 2.05 V and a conversion efficiency of 4.4% is achieved for a 3RJ having 2.2x10^8 RJ/cm^2.

In order to determine the origin of the randomness in V_{OC}, the growth process of SiNW solar cells has been checked step-by-step. We have found that the measurement of the intensity of the ellipsometric signal as a function of time can be used to optimize the NW density and predict final V_{OC} of the RJ solar cell. A later peak time corresponding to lower NW density and a higher V_{OC}.

Finally, in order to achieve a voltage high enough for water splitting, we have optimized 4RJ SiNW solar cells, which allowed us to reach a V_{OC} of 2.75 V. Using Ni catalyst evaporated on the 4RJ (photocathode) and a Pt photoanode, we have demonstrated a stable unassisted water splitting for 90 min in 1M KBi electrolyte. The PEC efficiency has an initial value of 0.98% when using 0.1 M KOH as electrolyte, and a stabilized value of 0.43% when using 1 M KBi.

Institut Polytechnique de Paris
91120 Palaiseau, France